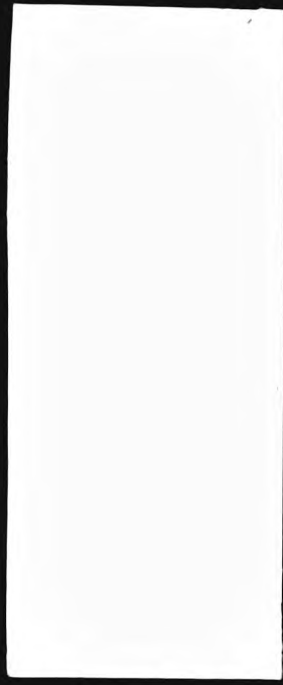


This PDF was created from the British Library's microfilm copy of the original thesis. As such the images are greyscale and no colour was captured.

Due to the scanning process, an area greater than the page area is recorded and extraneous details can be captured.

This is the best available copy



DX



172356



**ELECTRICAL BREAKDOWN AND STRUCTURAL
CHARACTERIZATION IN SYNTHETIC RESINS
USING OPTICAL TECHNIQUES**

by

STEPHEN JOHN DODD

**A thesis submitted in partial fulfilment of the
requirements of the Council for National Academic Awards
for the degree of Doctor of Philosophy**

September 1992

**Department of Physics
City of London Polytechnic**

ELECTRICAL BREAKDOWN AND STRUCTURAL
CHARACTERIZATION IN SYNTHETIC RESINS
USING OPTICAL TECHNIQUES

by

STEPHEN JOHN DODD

ABSTRACT

As part of a National Power/National Grid funded collaborative project on electrical breakdown in synthetic resins, various non-evasive optical techniques were developed to quantitatively characterise resin microstructure and residual internal mechanical stress (RIMS) and to study the physical processes occurring during electrical tree initiation and tree growth in the pin-plane geometry.

Light scattering measurements have been used to determine the origins and magnitudes of the microstructure content (MC) of the Epoxy (CT200) and unsaturated polyester resins, and in conjunction with FTIR spectroscopy, the polyester resin cure reaction kinetics have been established.

Polarisation microscopy with the aid of an interpretive fictive force model have enabled the RIMS to be quantified for the first time. It is shown that the RIMS relaxes with a time constant of some four years for CT200 and polyester resins and is associated with structural relaxation (physical ageing). The large variations of MC and RIMS depend on the supplied material, preparation procedures, sample age etc., and have important ramifications for any study of electrical tree initiation and growth.

Light emission measurements, using phase synchronous photon counting and CCD imaging during tree initiation and growth shows that three distinct types of emission occur. Type A; associated with charge injection processes which may be explained in terms of a deep trap charge recombination model. Type B; associated with microdischarges as a prelude to tree propagation and Type C; associated with the conventional partial discharge activity in growing tree channels. Electrical tree initiation follows slow material degradation and debonding of the metal/polymer interface with the formation of the first microchannels.

A study of tree initiation and growth in the CY1311 epoxy resin details some of the many factors that influence electrical breakdown in resins. The early tree growth is shown to be driven by the high electrical field near the pin tip, which is itself dependent on the pin-plane electrode separation as well as the applied voltage. Significantly, at least two different tree growth mechanisms occur and compressive mechanical stress acts to retard tree initiation. Tree growth may also be impeded by high compressive or tensile mechanical stress and a region of zero RIMS may completely passivate a growing tree.

ACKNOWLEDGEMENTS

I would like to thank my supervisors, Dr. J.V. Champion, of the City of London Polytechnic, and Dr. G.C. Stevens of National Power PLC, for their support, encouragement, and advice throughout the course of this work.

I would also like to thank I. Sutherland (for help with FTIR sample preparation), E. Stonnard (Peltier cooled CCD camera), R. Hare (permission to reproduce his current density-phase graph), all of National Power, D. Hooper (SEM pin characterization) of National Grid Co., and J. Wright (liquid nitrogen cooled CCD camera) of Wrights Instruments Ltd.

Finally I wish to thank my family for their support, Miss Ann Mary Halsey for her patience and understanding during the writing up this work, and to National Power PLC and the City of London Polytechnic for their financial support.

CONTENTS

<u>CHAPTER 1: Introduction</u>	1
1.1. Electrical Tree Initiation Studies	1
1.2. Electrical Tree Growth Studies	2
1.3. Factors Influencing Tree Initiation and Growth	3
1.4. NP/NG Collaborative Research Program	4
1.5. Scope of the Work Undertaken at the City of London Polytechnic	6
1.6. Aims of the Work Undertaken in this Thesis	6
1.6.1. Resin Microstructure	7
1.6.2. Residual Internal Mechanical Stress	7
1.6.3. Optical Detection of the Light Emission during Tree Initiation	8
1.6.4. Optical Studies of Tree Initiation and Growth in CY1311 Epoxy Resin	8
1.7. Presentation of the Work in this Thesis	9
<u>CHAPTER 2: Materials</u>	10
2.1. CT200/HT901 Epoxy Resin System	10
2.2. Unsaturated Polyester Resin System	12
2.3. Material Preparation	12
2.3.1. Material Filtration	14
2.3.2. Cure Schedules	14
2.4. CY1311/HY1300 Epoxy Resin System	15
2.5. Pin Supply, Manufacture and Characterization	15
2.5.1. Tungsten Pin Manufacture	16
2.6. Pin-Plane Sample Manufacture	18
<u>CHAPTER 3: Material Characterization - Resin Microstructure using Light Scattering Techniques</u>	20
3.1. Introduction	20
3.1.1. Evidence for Microstructure in Synthetic Resins	21
3.1.2. Formation of Network Structure	22
3.1.3. Use of Light Scattering Techniques	24
3.2. Light Scattering Theory	24
3.2.1. Applicability of Rayleigh Theory	25
3.2.2. Applicability of Mie Theory	25
3.3. Experimental Arrangement	26
3.3.1. Data Collection and Calibration	28
3.3.2. System Appraisal	29
3.4. Data Analysis and Computation	31
3.4.1. Fitting a Single Size of Scatterer	33
3.4.2. Fitting to a Size Distribution of Scatterers	34
3.4.3. Microstructure Characterization Procedure	41
3.5. CT200 Epoxy Resin Characterization Results	41
3.5.1. Fully Cured CT200 Epoxy Resin	42

3.5.2. Formation of Microstructure in CT200 Epoxy Resin	47
3.5.3. Discussion	49
3.6. Unsaturated Polyester Resin Characterization Results	50
3.6.1. Fully Cured Unsaturated Polyester Resin	50
3.6.2. Microstructure in the Pre-cured Materials	55
3.6.3. Formation of Microstructure during the Cure of Unsaturated Polyester Resin	56
3.7. Measurement of the Reaction Kinetics of Unsaturated Polyester Resin using Fourier Transform Infra Red Techniques	58
3.7.1. Introduction	58
3.7.2. Measurement of Infra Red Spectra during the Cure of Unsaturated Polyester Resin	60
3.7.3. Analysis of the Infra Red Spectra	61
3.7.4. Polyester Reaction Kinetics	64
3.7.5. Refractive Index Measurements	67
3.7.6. Measurement of Gel Time	67
3.7.7. Correlation with Light Scattering Measurements	69
3.8. Comparison Between the Microstructure in CT200 Epoxy and Unsaturated Polyester Resin	70
3.9. Conclusions	72
<u>CHAPTER 4: Material Characterization - Residual Internal Mechanical Stress using Optical Birefringence</u>	75
4.1. Introduction	75
4.2. Theory	77
4.3. Experimental	79
4.3.1. Samples	79
4.3.2. Experimental Arrangement	79
4.3.3. Application of an Applied Mechanical Stress	81
4.4. System Appraisal - Brewster Constant Measurements	82
4.5. Results and Analysis	83
4.5.1. CT200 Epoxy Resin	83
4.5.2. Unsaturated Polyester Resin	87
4.5.3. CY1311 Epoxy Resin	88
4.5.4. Sample Reconditioning	89
4.5.5. RIMS of Samples with Ogura Steel or Etched Tungsten Pins	89
4.5.6. Applied Mechanical Stress	89
4.6. Discussion	92
4.7. Conclusions	94
<u>CHAPTER 5: Quantitative Study of Light Emission During Electrical Tree Initiation and the Early Stages of Tree Growth</u>	95
5.1. Introduction	95
5.2. Experimental	96
5.2.1. Light Collection Optics	97
5.2.2. Experimental Arrangement	97
5.2.3. Mains Synchronous Photon Counter	101

5.2.4. Detection System Performance	103
5.3. Step Ramp Light Emission Results	105
5.3.1. Type A Emission - Field Limiting Space Charge Model	108
5.3.2. Type A Emission - Charge Carrier Injection Mechanisms	111
5.3.3. Type B Emission	114
5.3.4. Type C Emission	117
5.3.5. Discussion - Step Ramp Results	117
5.4. Long Term Voltage Stressing Tests	120
5.4.1. Experimental	121
5.4.2. Light Emission Results	121
5.4.3. Long Term Voltage Stressing - Discussion	127
5.5. Simultaneous CCD-Photomultiplier Measurement of the Light Emission	129
5.5.1. Experimental	129
5.5.2. Step Ramp Tests	130
5.5.3. Long Term Stressing	130
5.5.4. Light Emission from Tree Channels	130
5.6. Discussion	135
5.6.1. Electronic States in an Synthetic Resin	135
5.6.2. Shallow Trap Transport and the Phase Relationship of the Electroluminescence	135
5.6.3. Deep Trap Recombination Model	137
5.6.4. Deep Trap Recombination Model - Discussion	140
5.7. Conclusions	142
<u>CHAPTER 6: Tree Initiation and Growth in CY1311 Epoxy Resin</u>	146
6.1. Introduction	146
6.1.1. Background	147
6.2. Effect of Material Age on Tree Growth Behaviour	149
6.3. Detailed Tree Growth Study using Video Recording Techniques	150
6.3.1. Experimental	152
6.3.2. Results	153
6.3.3. Discussion	153
6.4. Effect of RIMS and Externally Applied Mechanical Stress on Tree Initiation and Growth	158
6.4.1. Experimental	158
6.4.2. Results	159
6.4.3. Discussion	159
6.5. The Effect of Voltage and Pin-Plane Spacing on Tree Initiation and Growth in CY1311 Resin	161
6.5.1. Experimental	161
6.5.2. Results	162
6.5.3. Discussion	162
6.6. CCD Imaging of Light Emission during Tree Growth	170
6.6.1. Experimental	170
6.6.2. Results	171
6.6.3. Discussion	176
6.7. Conclusions	178

<u>CHAPTER 7: Final Discussion and Overall Conclusions</u>	180
7.1. Material Characterization	180
7.1.1. Resin Microstructure	180
7.1.2. Residual Internal Mechanical Stress	181
7.2. Electrical Breakdown Studies	182
7.2.1. Electrical Tree Initiation in CT200 Epoxy and Polyester Resin	183
7.2.2. Tree Growth in CY1311 Epoxy Resin	184
7.3. Concluding Remarks	185
REFERENCES	186
Appendix 1: Rayleigh Theory	192
Appendix 2: Mie Theory	194
Appendix 3: Calibration of the Light Scattering Equipment	197
Appendix 4: Laser Speckle Reduction	200
Appendix 5: Computation of Mie Formulae	204
Appendix 6: Least Squares Fitting	206
Appendix 7: Charge Carrier Injection Mechanisms and the Field Limiting Space Charge Model	208

Chapter 1

Introduction

Crosslinked polyester and epoxy resins and their composites constitute the most widely used class of thermosetting polymers in electrical insulation systems and in service, they are required to support both high electrical and mechanical stresses for some considerable time, possibly at elevated temperatures.

Electrical treeing is the main long term insulation failure process. Void formation at a region of local electrical stress enhancement (tree initiation), is followed by the growth of fine erosion channels (tree growth stage) driven by partial discharges. Once the tree structure has crossed the inter-electrode space, high discharge currents can flow causing catastrophic failure of the insulator. Little is known of the physical processes which lead to void formation and tree growth. However, electrical field enhancement is likely to occur around material defects, such as voids, conducting impurities, or moulded-in metal inserts and this enhancement drives the process. Much of the published data on electrical treeing breakdown uses the pin-plane geometry to model a simple conducting defect and to produce the high electrical fields necessary for quick tree initiation. Some of the techniques used to investigate tree initiation and growth will be summarised below.

1.1. Electrical Tree Initiation Studies

Tree initiation in synthetic resins occurs at the microscopic level beginning with the injection and extraction of charge carriers. Direct observation of the tree initiation stage is therefore impossible, and because of this, the physical mechanisms leading to tree initiation are not well understood. Many workers have attempted indirect methods to elucidate the processes involved. Hibma and Zeller [1], have claimed to have measured the charge injection into the resin directly. They then identify material dependent voltage thresholds for charge injection and use this as the basis of their field limiting space charge model. This is a very difficult technique as the charge injected is many orders of magnitude lower than the capacitive charge associated with the pin-plane electrode arrangement. Guarded pins are required, and even then, after

bridge balancing to subtract the residual capacitance, a computer deconvolution of the measured data is required to remove additional resin polarisation effects to recover the charge injected into the resin. More promising investigations have used sensitive light detection techniques to measure the light emission at the pin-tip during the tree initiation phase before the onset of partial discharge activity. Here, the characteristics of the light emitted with respect to applied voltage, waveform, phase and spectral characteristics have been used to determine material degradation mechanisms that lead to void formation and tree growth. Several electrical tree initiation mechanisms have been proposed. Shibuya et al. [2], suggest that hot electron collisions with the resin matrix cause bond breakage, Bamji et al. [3], suggest that UV electroluminescence photo-degrades the resin at the pin-tip whilst Zeller and Schneider [4], propose an electrofracture process.

1.2. Electrical Tree Growth Studies

Tree growth in transparent resins can be observed directly using optical methods. Although essentially driven by partial discharge activity, the mechanisms of tree growth are not fully understood. Observation of tree growth has prompted authors to propose various models for tree extension. These include, ballistic erosion of material at the pin-tip [5], induced electron avalanches in the resin adjacent to the tree [6] and electrofracture of the resin [4]. The random nature of tree extension and branching has led some, i.e. Dissado and Sweeney [7], to develop stochastic models for tree growth, where the growth process is essentially a random process. Random parameters that can be built into the model include charge distribution within the tree to randomly modify the local electric field within the tree after each partial discharge and resin inhomogeneity. A key result from this analysis is that tree branching is very difficult to achieve unless a stochastic element is incorporated into the model. Hence, simple deterministic models alone are unlikely to succeed in explaining electrical tree growth. Given the wide range of tree structures that are found to occur (even with samples made from the same material), a universal tree growth model will require both deterministic and stochastic elements.

Partial discharge activity is often monitored by direct measurement of the current flowing in the high voltage test circuit [2]. Partial discharge activity can be separated from the capacitive current by filtration leaving just the high frequency components. The characteristics of the partial discharge activity with stressing voltage depend on the type of defect, i.e. electrical tree, voids etc. and may be useful for diagnosing faults in filled resin insulation where direct observation is not possible [8].

Although useful, partial discharge detection is of limited value for determining tree growth mechanisms as it is a measure of the integrated discharge activity throughout the tree. Spatial measurement of the partial discharge activity within the growing tree would be far more instructive. This has been attempted by very few authors, however Shibuya [2], and Laurent and Mayoux [6] have demonstrated that this can be done by measurement of the light emission within the tree channels using image intensifier tubes.

1.3. Factors Influencing Tree Initiation and Growth

Previous workers studying electrical breakdown have highlighted many factors that can influence electrical breakdown in resin materials. This has been comprehensively reviewed recently by Dissado and Fothergill [9]. Such factors may include resin chemistry, cure conditions and reaction completion, crosslink density, glass transition temperature [10], resin morphology [11], mechanical and residual internal stress [12], fracture toughness [4], temperature [13], applied voltage and frequency [14], voltage waveform, impulse voltages, polarity reversal [15], sample geometry, sharpness of the high voltage electrode, shape of the ground (earth) electrode [12], cleanliness of the electrodes, inter-electrode gap, electric field enhancement [16], sample aging [17], gas, water and oxygen absorption [18] etc. Any serious experimental study must take these and possibly many others into account before reaching any final conclusions. The situation is further complicated as the factors listed above are not all mutually independent. For example, residual mechanical internal stress will depend on resin chemistry, glass transition temperature, crosslink density, temperature etc. and may be affected by material aging, absorption of water vapour and air. As another example, testing say, at elevated temperatures, will also change the residual

internal stress, fracture toughness, and the amount of water and air absorption. Hence, arriving at clear conclusions as to the effect of a change in one parameter is difficult and account must be taken of the associated changes in other parameters.

The situation can be redeemed somewhat, by standardisation of the sample preparation techniques and testing methodology. It is also possible to determine quantitatively such factors as reaction completion, glass transition temperature, fracture toughness etc. However to date, no quantitative techniques have existed to determine resin morphology or residual internal mechanical stress.

1.4. NP/NG Collaborative Research Programme

The electrical treeing failure process is of interest to the electrical generation and distribution industries as it is a possible cause of insulation failure in electrical machines, cables, switch-gear and gas insulated substations. Prediction of insulator service life time, is essential for efficient servicing of insulation systems and minimising electrical generation and supply disruption. Further, an understanding of this process will enable the design and manufacture of insulators, (materials, manufacture process and quality control), to be optimised for increased reliability and maximum lifetime.

To address all this, a collaborative research programme has been set up by National Power (NP), and National Grid (NG) to investigate electrical breakdown in resin systems and involves a number of academic institutions. The work concentrates on two resin systems, CT200 epoxy resin (widely used in insulation systems) and unsaturated polyester resin. Both these resin systems, have been studied extensively in terms of their reaction chemistry, have high optical transparency and are easy to prepare. The majority of the work used the pin-plane electrode configuration to accelerate in particular, the formative stage (tree initiation stage) of electrical breakdown, requiring only moderate high voltages 5-10kV to be applied to the samples.

As background to the work undertaken in this thesis, a brief overview of the collaborative project, consisting of a list of collaborators and the scope of their work is summarised below.

National Power:-

Study of partial discharge phenomena.

National Power & Bristol University:-

Numerical computer simulation of charge injection from a pin-tip into resin insulator using the pin-plane geometry.

King's College and National Power:-

Stochastic numerical modelling of the tree growth and relation between fractal geometry and statistics of tree growth.

King's College London:-

Computer simulation of physics of electrical treeing and cumulative damage.
Numerical computer simulation of charge injection using the plane-plane geometry.

National Grid & Manchester University:-

Experimental study of tree growth in CT200 epoxy and polyester resins.
Characterization of electrical trees.
Influence of barriers on electrical treeing.

Glasgow Collage of Technology:-

Partial discharge detection, analysis and diagnostics.

City of London Polytechnic:-

Material supply and characterization.
Experimental investigation of tree initiation and growth.

City of London Polytechnic and National Power:-

Video and charge coupled device camera observations of tree growth in real time.

1.5. Scope of the Work Undertaken at the City of London Polytechnic

In order to reduce variation in the quality and physical properties of pin-plane samples, which may occur through slightly different production techniques employed at the different establishments, it was decided to centralise sample manufacture at the City of London Polytechnic.

An early objective, was to develop non-evasive optical techniques of material characterization which would allow a quantitative assessment of the resin microstructure (inhomogeneity) and internal mechanical stress to be made for the first time. As the resins are transparent, non-evasive optical techniques were chosen having the advantage that no special or destructive sample preparation techniques are required that may modify the sample characteristics or make interpretation difficult. This would then enable well characterized pin-plane samples, superior to those used in previous studies, to be used to investigate the formative and propagation stages of electrical breakdown in these materials.

These early objectives were then extended to develop other non-evasive optical techniques, to investigate both the formative and propagation stages of electrical breakdown. Running parallel with this, other resin systems were assessed to identify further 'model' resin systems to complement the study of CT200 epoxy resin and unsaturated polyester. One such resin system, the CY1311/H1300 from Ciba Geigy was used extensively for the tree growth study.

1.6. Aims of the Work Undertaken in this Thesis

Due to the wide range of activities documented in the thesis, the aims and tasks of each area of study as it appears in the thesis, are given below.

1.6.1. Resin Microstructure

Prior to this work no reliable techniques existed to quantitatively determine the amount of microstructure present in resin materials. The aim was to develop a non-evasive optical technique based on light scattering to quantitatively measure the microstructure content of resin samples. This would then allow different samples to be ranked in terms of their microstructure content for possible future electrical breakdown studies on the effect of resin morphology.

Light scattering is a sensitive probe of the small density fluctuations that may occur in these resin materials. It also has the advantage that it is theoretically well understood. Having its basis in Maxwell's equations, Mie [19] in 1909, solved the scattering problem for isotropic spheres. The task here, once a reliable method of measuring the angular distribution of scattered light is developed, is to invert this data to obtain information on the nature, size distribution and concentration of scatterers present in the resin material.

1.6.2. Residual Internal Mechanical Stress

Residual internal mechanical stress is always present in pin-plane samples. It arises due to resin shrinkage during cure and the difference between the thermal contraction of the resin and metal pin as the sample cools after post cure [12]. Mechanical stress is known to influence tree initiation and growth, yet to date, no quantitative study has been undertaken. The aim in this part of the work was to develop a non-evasive optical technique to quantitatively determine the residual internal mechanical stress in pin-plane resin samples.

Polarised light when passing through a mechanically stressed material suffers a optical retardation which is proportional to the mechanical stress and the optical path length. If the sample were stressed homogeneously, a simple analysis of the polarised light emerging from the sample would suffice to determine the mechanical stress, however in pin-plane samples this is not the case and the observed optical retardation must be related to the integral of the stress distribution over the optical path. A

method of quantitatively determining the mechanical stress distribution from optical retardation measurements in pin-plane specimens was developed. This was then extended to include the more general case of time dependent residual internal mechanical stress as well as externally applied mechanical stress.

1.6.3. Optical Detection of the Light Emission during Tree Initiation

The physical processes involved in tree initiation are unclear. Before the onset of partial discharge activity, a low intensity light emission is observed associated with charge injection and electroluminescence. In this part of the work, an ultra sensitive synchronous light detection system based on photon counting techniques was developed. An ultra sensitive photomultiplier tube and high efficiency light collection optics were used providing an order of magnitude increase in sensitivity compared with previous investigations. This was then used to elucidate the mechanisms responsible for electroluminescence and to investigate tree initiation in CT200 epoxy resin and unsaturated polyester. Recently, extremely sensitive liquid nitrogen cooled charge coupled device (CCD) cameras have become available, offering even greater sensitivity with the additional advantage of being able to spatially resolve the light emission. A camera, hired from Wrights Instruments Ltd. was used to complement some of the key results of the photomultiplier work.

1.6.4. Optical Studies of Tree Initiation and Growth in CY1311 Epoxy Resin

The aim of this section of work was to investigate tree growth in CY1311 epoxy resin using various non-evasive optical techniques, to identify factors which may influence tree initiation and growth and to determine the partial discharge activity within growing trees. Tree growth was studied over a range of stressing voltage, pin-plane separation and mechanical stress. Partial discharge activity was recorded by monitoring the light emission using a Peltier cooled CCD camera.

1.7. Presentation of the Work in this Thesis

The wide range of subject areas are arranged into a number of self contained chapters. Chapter 2 introduces the resin materials studied and describes the cure procedures and sample preparation. Chapters 3 and 4 concentrate on the development of material characterization techniques, for the determination of resin microstructure and residual internal mechanical stress respectively. The optical investigation of tree initiation in CT200 and polyester resin is described in chapter 5. Chapter 6 describes the tree initiation and growth study using optical techniques in CY1311 epoxy resin. The final discussion and conclusion, chapter 7, will link all this work together and discuss overall achievements.

Chapter 2

Materials

The two resin materials used throughout this work are the CT200/HT901 epoxy resin system from Ciba Geigy and the unsaturated polyester resin C from Strand. A brief description of their chemistry and cure methods are given in the following sections. During the course of this work a further resin system was utilised, mainly for the tree growth studies. This resin system is the araldite CY1311/HY1300 epoxy resin system from Ciba Geigy.

Two types of pins were used, commercially available steel pins from Ogura Jewel Co. Japan, and electrochemically etched tungsten. The manufacture technique for the tungsten pins will be described in detail in this section along with the production of standard pin-plane specimens and samples for light scattering.

2.1. CT200/HT901 Epoxy Resin System

The CT200 epoxy prepolymer is a diglycidyl ether of bisphenol A (DGEBA) resin which is cured with HT901 phthalic anhydride (PA) hardener. The chemical structure of these two components has been examined by Stevens and Richardson [20] and are shown in figure 2.1. The DGEBA molecule forms hindered and rod-like diepoxide monomer and oligomers, with a repeat unit, n , having an average value of 1.7 and comparable $n=0$ to 4 fractions.

The crosslinking reactions, shown in figure 2.2, occur when the resin and hardener are mixed and these have been discussed in detail by Stevens [21]. Both addition esterification and the slower addition etherification reaction leads to branching and crosslinking. The addition esterification reaction consists of two steps, the DGEBA free hydroxyl groups ring open the anhydride forming a monoester linkage and a reactive carboxyl group before a diester crosslink can be formed. Etherification is promoted in the presence of PA and carboxylic acid groups and little or no etherification is observed in the pure DGEBA resin even when heated to 120°C [22].

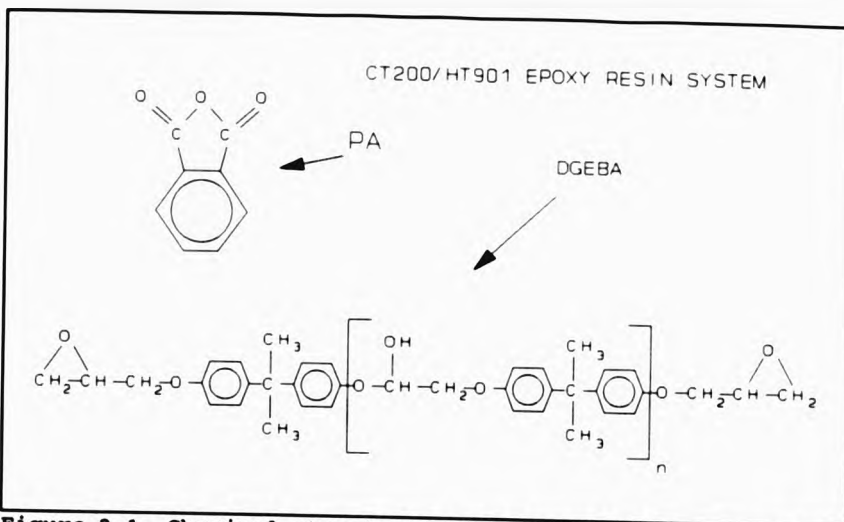


Figure 2.1. Chemical structure of the CT200/HT901 epoxy resin system.

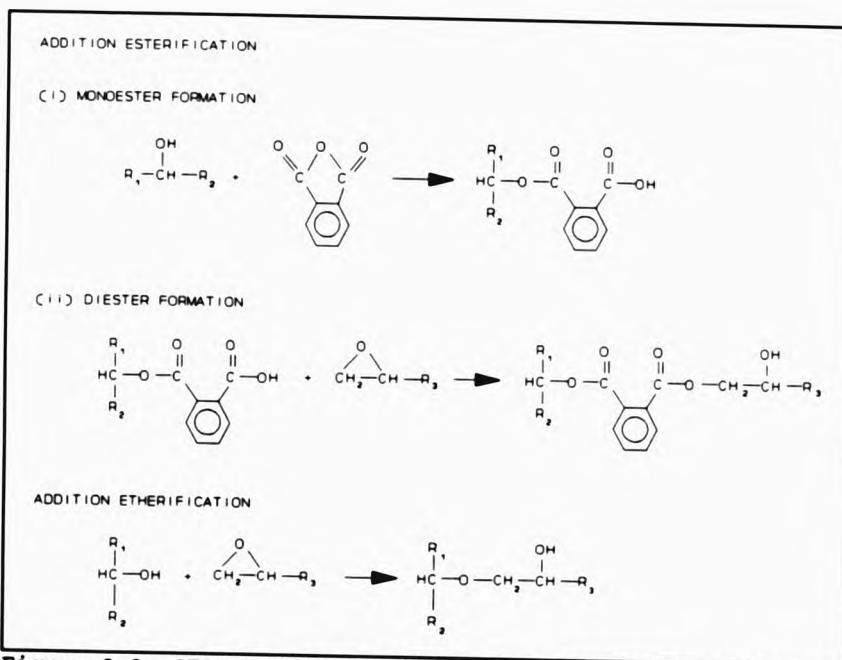


Figure 2.2. CT200/HT901 possible crosslinking reactions.

2.2. Unsaturated Polyester Resin System

The polyester resin used consists of unsaturated polyester linear molecules in styrene monomer. Unsaturated polyesters are usually formed from the fusion of propylene glycol, phthalic anhydride and maleic anhydride to give chain structures similar to that shown in figure 2.3 [10]. The resin should be supplied containing 40% styrene corresponding to a stoichiometric ratio of two styrene double bonds for each polyester double bond [23]. However, in most cases excess styrene is present to account for inefficient use of styrene and competing styrene homopolymerization reaction. An inhibitor is usually added by the manufacturer to prevent oxygen initiated free-radical polymerization during storage.

Addition of methylethylketone hydroperoxide (MEKP) catalyst causes a free-radical crosslinking reaction to take place between the polyester and styrene molecules via their carbon double bonds. Possible chemical reactions during cure have been reviewed by Yang and Lee [24] and are shown in figure 2.4. Crosslinking occurs between different growing polyester chains (intermolecular crosslinking) either directly or more likely involving styrene molecules if they are available; these reactions are responsible for macroscopic gelation. Because of the high flexibility of the polyester chains before gelation, intramolecular crosslinks can form (cyclisation), either directly or involving styrene. Styrene homopolymerization can also occur if the local styrene concentration is high compared with the availability of polyester double bonds.

2.3. Material Preparation

In order to produce resin samples with high conformity and maximum stability, a standard cure schedule is required which ensures a complete cure reaction. Standard cure schedules for both CT200 epoxy and polyester resins will be given in section 2.3.2. Resin samples were prepared with 2 levels of purity, i) 'as received' where the resin and hardener were used as supplied by the manufacturer and ii) 'ultra clean' where the resin and hardener were first filtered before use.

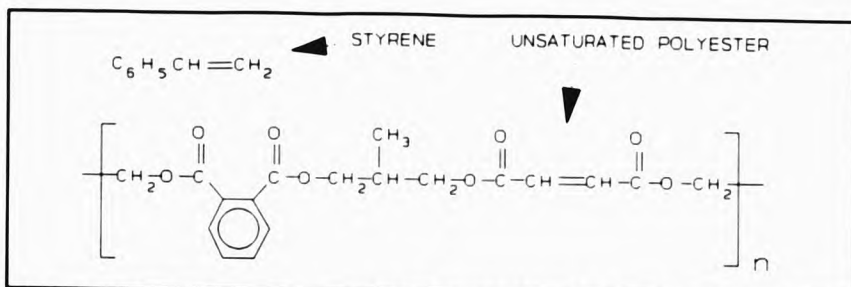


Figure 2.3. Chemical structure of unsaturated polyester resin.

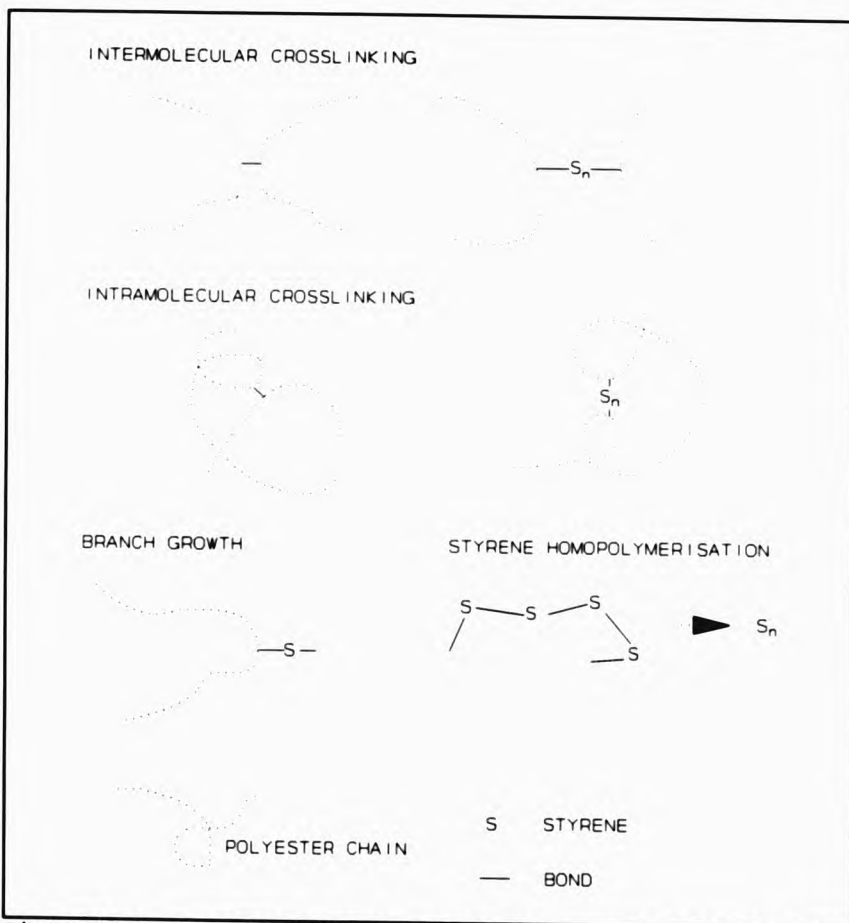


Figure 2.4. Unsaturated polyester resin - possible chemical reactions during cure.

2.3.1. Material Filtration

CT200 epoxy resin and HT901 hardener are supplied in a solid form. The HT901 hardener was first heated to 140°C to first melt the hardener before passing through two 0.2µm PTFE filters. Two different filtration techniques were employed for the CT200 resin.

- a) CT200 passed through three 0.2µm PTFE filters at 140°C in its liquid form.
- b) CT200 resin was first dissolved in butanone at 60°C, (volume of butanone added in ml = 1.5 x mass of CT200 in grammes). The dissolved resin was then passed through 0.2µm PTFE filters at 60°C, then the butanone was removed by evaporation at 80°C under vacuum.

Further details of the filtration techniques and equipment can be found in the thesis by Perkins [25].

The unsaturated polyester resin and MEKP catalyst are supplied in liquid form. These were filtered by passing through two 0.2µm PTFE filters at room temperature (18 to 22°C).

2.3.2. Cure Schedules

Cure schedules for the CT200 epoxy resin and unsaturated polyester resin are given in table 2.1. These follow Stevens and Richardson [20] and Perkins [25] for the CT200 epoxy resin and Cooper and Stevens [10] for the polyester resin to ensure cure reaction completion and hence, maximum stability of the cured resin. After mixing CT200 epoxy resin with the HT901 hardener, the mixture was degassed for 10 minutes under vacuum to reduce the possibility of microvoids in the fully cured resin. The polyester resin was not degassed to prevent substantial styrene loss. Experience has shown that a slow cool rate of 2.5°C per hour is required to produce the highest yield of pin-plane samples with good interfaces and to minimise internal

mechanical stress. A more detailed description of the cure technique and reaction vessels required are given in reference [25].

Table 2.1. CT200 and polyester cure schedules

SAMPLE	CT200 EPOXY RESIN	UNSATURATED POLYESTER
RESIN	Ciba Geigy CT200* (100 PARTS)	Strand RESIN C* (100 PARTS)
HARDENER	Ciba Geigy HT901** (30 PARTS BY WEIGHT)	Strand MEKP** (1 PART BY VOLUME)
CURE TEMP.	125°C	ROOM TEMP.
CURE TIME	48 HOURS	48 HOURS
POST CURE TEMP.	150°C	70°C
POST CURE TIME	8 HOURS	8 HOURS
SLOW COOL RATE	2.5°C PER HOUR	2.5°C PER HOUR
* Diglycidyl ether of bisphenol A. ** Phthalic anhydride. + Unsaturated polyester resin in styrene monomer. ++ Methyl ethyl ketone peroxide.		

2.4. CY1311/HY1300 Epoxy Resin System

Araldite CY1311 is a modified and flexibilised bisphenol-A epoxy which is reacted with an aliphatic polyamine hardener, HY1300 [26]. Before mixing, the resin and hardener are degassed for 1 hour in a vacuum oven at 40°C. After mixing for 10 minutes (using a high speed magnetic stirrer), the mixture was further degassed at 40°C for 10 minutes before pouring into preheated moulds. This procedure reduces considerably the population of microbubbles, however, it does not completely eliminate them. The resin is cured for 7 days at room temperature (18-22°C).

2.5. Pin Supply, Manufacture and Characterization

The commercially supplied Ogura steel pins having a shank diameter of 1mm and pin-tip radius ranging from 2 to 5µm, were first polished and cleaned before characterization at National Grid PLC. Tungsten pins were manufactured using the technique described in section 2.5.1. at the City of London Polytechnic. For



characterization of each pin, the scanning electron microscope (SEM) facility at NG PLC was used, to obtain high quality, high resolution images. All pins having attached dirt or non-spherical tip were rejected. Pin-tip radius was measured directly from the SEM micrographs. The characterized pins were stored individually in glass vessels and to prevent rusting, the Ogura pins were coated with a light oil.

2.5.1. Tungsten Pin Manufacture

Tungsten pins were prepared from 0.4mm diameter tungsten wire using a electrochemical etching technique and is based on the technique used by Shibuya [2]. The experimental arrangement is shown in figure 2.5. A 20% by weight aqueous solution of potassium hydroxide (KOH) is floated on top of insulating carbon tetrachloride (CCl_4) in a glass vessel, such that the two layers each have a depth of 1cm. A negative electrode made from tungsten wire is positioned such that its end extends into the CCl_4 layer. The positive electrode, which will be etched to form the pin, is placed into the etching solution in a similar manner but arranged such that it is lowered slowly at a rate of 0.1mm per minute into the etching fluid using a modified travelling microscope and electric motor with gearbox. This was done to form a gradual tapering cone and prevent a sharp shoulder from forming near the pin-tip.

The positive electrode starts to etch as soon as the 6V potential is applied. An ammeter in the circuit is used to monitor the current during the etching process. Typically, after an initial surge, the current quickly settles down to between 80 and 100mA. Over a period of approximately 15 minutes, the current falls to around 20 to 30mA as the wire is etched, until the lower section of the wire drops off, leaving a tip at the etching fluid surface. Once this occurs and for the finest pin-tips, the etching current is interrupted using the switch. For pin-tips of larger radius, greater than $0.1\mu\text{m}$, the etching current is allowed to continue for a 'post etch' period before interruption. Figure 2.6 shows the dependence of pin-tip radius on post etch time and can therefore be used as a guide (with an accuracy of $\pm 50\%$) for producing pins over a wide range of radius. The pins are then cleaned using distilled water, propanol and chloroform.

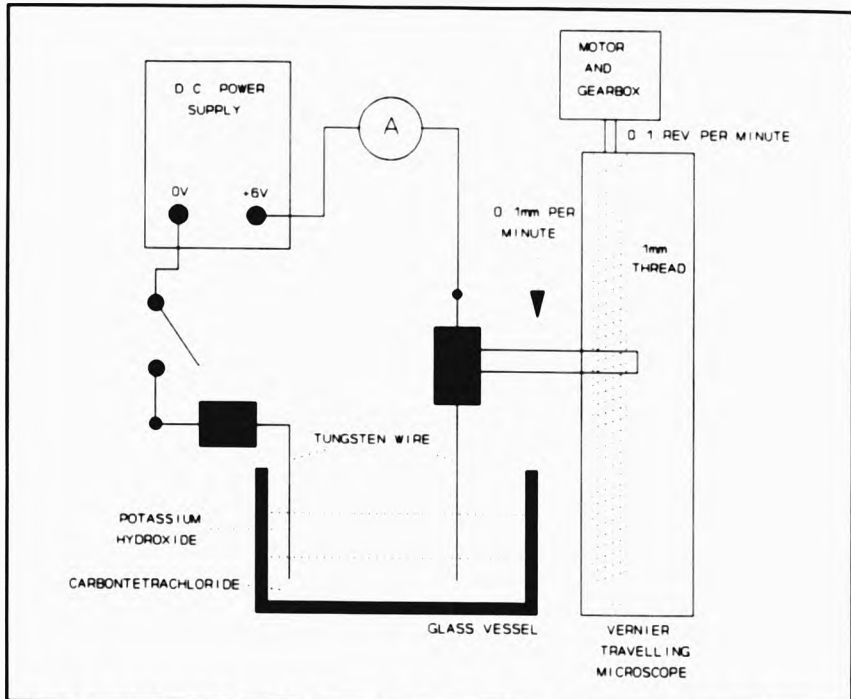


Figure 2.5. Tungsten pin manufacture - experimental arrangement.

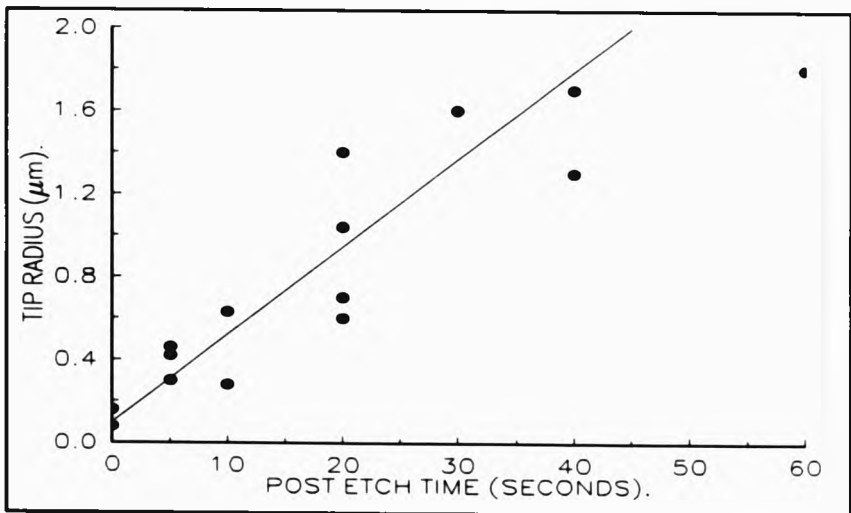


Figure 2.6. Dependence of pin-tip radius on post etch time.



2.6. Pin-Plane Sample Manufacture

Pin-plane CT200 epoxy and polyester resin samples were cast in sets of 10 using a stainless steel mould as shown in figure 2.7. Small groves in the inner surfaces of both the top and bottom part of the mould help to locate and clamp the pins in place. Once the pins have been set in place the top and bottom parts of the mould is then clamped together. Once the pin-plane resin samples have cured, they are individually cut to produce standard pin-plane samples as shown in figure 2.8. For the light scattering measurements, glass cylindrical moulds were used having an inner diameter of 25mm and 50mm high.

For the CY1311 epoxy resin, silicone rubber moulds were used to produce standard pin-plane samples. This had an additional benefit of producing samples with high optical quality surfaces without the need to polish, which is difficult due to the rubbery nature of this material.

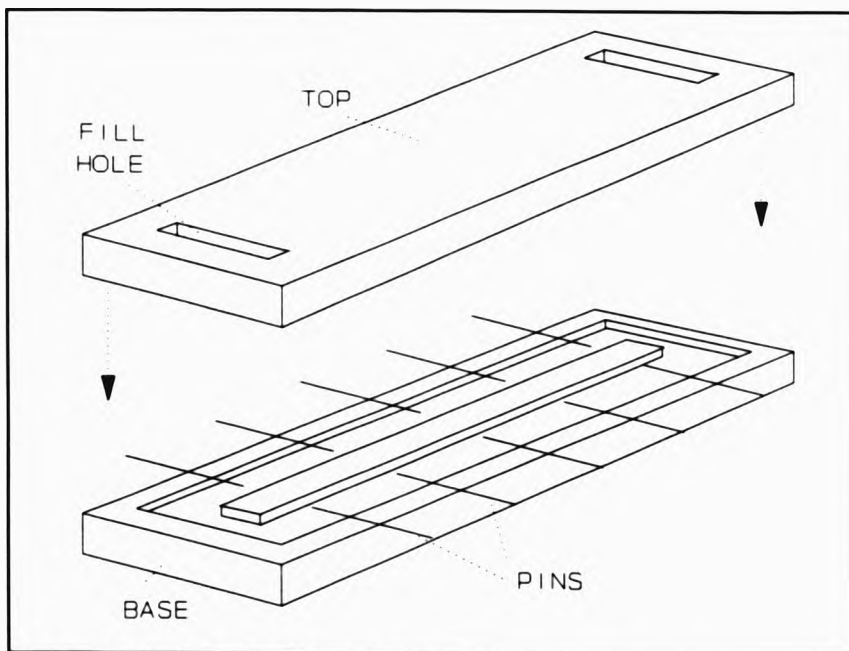


Figure 2.7. Pin-plane sample mould.

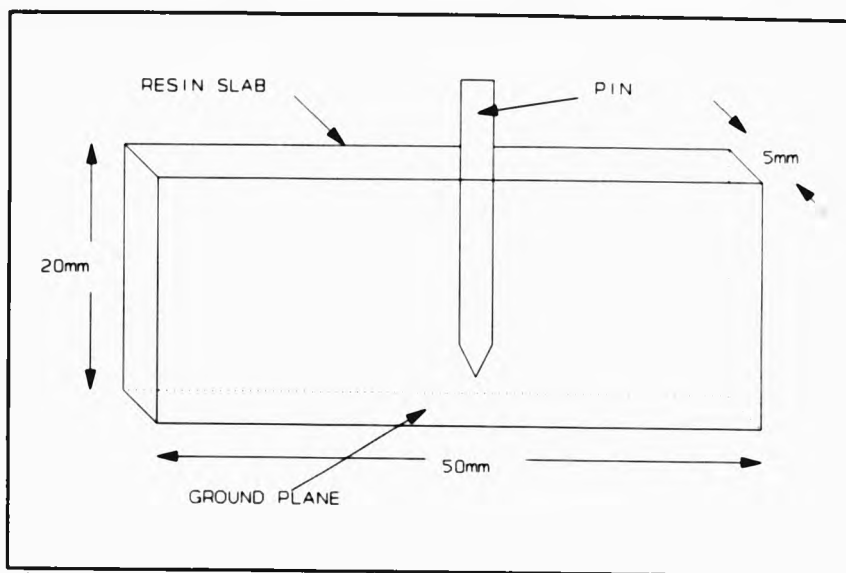


Figure 2.8. Standard pin-plane sample.

Chapter 3

Material Characterization - Resin Microstructure using Light Scattering Techniques

3.1. Introduction

Although controversial and contradictory, evidence for the existence of microstructure in cross-linked amorphous resins has been found using many techniques. These include, small angle x-ray scattering, (SAXS), small angle neutron scattering, (SANS), electron microscopy, (EM), and light scattering, (LS), and these will be reviewed in the next section. It has been suggested that microstructure i.e. density fluctuations with sizes in the region 10nm to 1000nm in these resins can affect their mechanical properties [21,27,28,29,30,31], however, few clear correlations have been proved. One recent study [32], using Epoxy resin in which the preparation procedure was modified to increase the microstructure, characterized using SAXS, found a factor of 2 increase in the fracture toughness when the magnitude of the density fluctuations is increased by a factor of 40.

Zeller [4], has proposed an electro-fracture process for electrical breakdown and hence, it is conceivable that the network structure of these resins may also influence their electrical breakdown properties. However, very few studies have been undertaken to investigate this, possibly due to the difficulty in the characterization of microstructure in these resins. Stevens et al. [33], have used light scattering in epoxy resin to explore the relationship between network structure and mechanisms of void formation, under both mechanical and electrical stress. Most other studies on the influence of resin morphology on electrical breakdown, for example, Hozumi et al. [11] and Tanaka et al. [34], have used polyethylene, which is semi-crystalline, and where the resin morphology is more clearly understood.

The electronic properties of these resins may be directly influenced by microstructure [35], which can affect electrical conduction and charge trapping processes. Microstructure will also control free volume, voids or areas of low crosslink density which may act to increase the mean free path of charge carriers in these regions and enhance the effect of electrical erosion processes [36].

In order to be able to confirm or refute these assertions, quantitative methods of microstructure characterization will be required. In this chapter, a quantitative method for determining the microstructure content of these resins will be described, using light scattering techniques.

3.1.1. Evidence for Microstructure in Synthetic Resins

Most evidence for microstructure in cross-linked resins has come from EM studies of etched or un-etched fracture surfaces or surface replicas. Mijovic and Koutsky [37] using transmission EM, Aspbury and Wake [38] using EM, and Gupta et al. [39] using scanning, transmission and scanning transmission EM, have shown that a nodular structure exists on the surfaces of epoxy resins, with a nodule size generally in the range 10-100nm. Gupta et al. [39], have also shown a correspondence of nodule size with resin stoichiometry and that these nodules are attributed to regions of higher cross-link density dispersed in a lower cross-link density matrix. Stevens [21] claims to have seen this also. Yang and Lee [40] using scanning EM, observe microgel particles of sizes between $1\mu\text{m}$ and $10\mu\text{m}$ in unsaturated polyester resin, with differing styrene-polyester molar ratios.

Dusek et al. [41], has compared the nodular structure that appears on fracture surfaces using EM with bulk measurements of the microstructure using SAXS. They find that the nodular structure of DGEBA epoxy with hexamethylenediamine curing agent (chosen for its homogeneous reaction chemistry), is similar to that of PMMA or polystyrene, having a nodule size 20-40nm. The SAXS results were found to be consistent with thermal density fluctuations, but at lower scattering angles the excess scattering is consistent with inhomogeneities of colloid dimensions ($\sim 100\text{nm}$). However, swelling in a solvent of lower electron density was found not to increase the low angle scattering and it was concluded that the physical structure of the epoxy resin does not essentially differ from that of common amorphous polymers and are therefore essentially homogeneous. Matyi et al [42], using SAXS on epoxy resins, has found a similar low angle excess scattering consistent with inhomogeneity sizes up to 400nm. They also note that the SAXS results are inconsistent with TEM observations of the concentration and size of nodular structure. Uhlmann [43], has

suggested that this inconsistency may be due to imaging of surfaces at high resolution, leading to a 'pepper and salt' structure, similar to the speckle observed in laser light. Defocussing of the electron microscope leads to a change in the scale of the 'salt and pepper' structure.

Wu and Bauer [44], have used SANS to elucidate the network structure of partially deuterated DGEBA epoxy resins cured with di and tri-amines. They find evidence for intra-network correlation and hence, network structure. However, Bai [45] using DGEBA resin cured with deuterated di-amine, found that the crosslinks are distributed uniformly throughout the epoxy network.

Few light scattering studies of microstructure in cross-linked resins have been undertaken. Bogdanova et al. [46] using LS and epoxy resin, found that the scattered light increases during cure, due to a inhomogeneous cure reaction. The extent of the inhomogeneities depend on the cure chemistry and cure temperature, having values ranging from 40 to 100nm, which correlate with inhomogeneity sizes obtained from EM observations. Stevens et al. [47], using LS, have shown that molecular aggregates exist in unreacted CT200 and CY207 epoxy resin with sizes up to 70nm. The molecular aggregate size, number and stability are related to the epoxide/hydroxyl ratio of the resins and the degree of intermolecular hydrogen bonding.

3.1.2. Formation of Network Structure

Formation of network structure in crosslinked resins has been extensively reviewed by Stevens [21]. For an ideal network, random intermolecular crosslinking occurs during cure. With increasing degree of branching, the molecular weight distribution broadens and at the gel point, an infinite network forms extending over the macroscopic dimensions of the sample. If the reaction is able to continue beyond the gel point, the unreacted monomer will become attached to the infinite network as the reaction proceeds to completion.

In the case of real networks, structural imperfections or defects may exist ranging from local network configurational order at the molecular level, up to the macroscopic dimensions of the sample. Dusek and Prins [48], have identified four basic types of defect which will result in the formation of network structure. These are,

- i) pre-existing order in the uncured materials,
- ii) network defects such as unreacted functional groups, loop formation and permanent chain entanglements.
- iii) inhomogeneous network formation due to an inhomogeneous cure reaction,
- iv) Phase separation.

Of these, pre-existing structure and inhomogeneous network formation are likely to be the most important for the two crosslinked resin systems, CT200 epoxy and unsaturated polyester under study in this work.

Stevens et al [47], using LS have found evidence for pre-existing order in unreacted CT200 epoxy resin, (see previous section). Zimm et al. [49], Dusek et al. [50] and Funke [51] have suggested that intramolecular reactions are favoured during the early stages of the cure of unsaturated polyester resins, due to the high flexibility of the growing polymer chain. Intramolecular cyclisation occurs at the onset of the free radical co-polymerisation reaction, leading to the formation of compact internally crosslinked particles (microgel). Microgel formation continues until macroscopic gelation occurs. This inhomogeneous reaction therefore results in a network with non-uniform network structure. This process is unlikely to occur in CT200 due to the rigidity of the DGEBA monomer chains.

Network structure may form due to insufficient mixing of the pre-cured resin components. Ghaemy et al. [52], using ultra violet microscopy on amine cured epoxy, have shown that inadequate mixing can lead to locally high amine

concentrations and incomplete crosslinking. Bell [53], found that increasing the mixing effectiveness of amine cured epoxy, decreased the size and number of nodules observed on fracture surfaces using EM. A corresponding increase in the glass transition temperature and ultimate tensile strength was also found.

3.1.3. Use of Light Scattering Techniques

The existence of local variations in the density and therefore in the refractive index of these resins, will scatter light out of the incident light direction. Measurement of this scattered light, coupled with a knowledge of theoretical models for the light scattering process will enable information on the physical structure of the scattering entities to be elucidated. A method of microstructure characterization using light scattering techniques will be described in the following sections. This technique will then be used to assess and characterize the microstructure present in CT200 epoxy and unsaturated polyester resins and to determine the origin of the observed microstructure.

3.2. Light Scattering Theory

Only those theories, namely Rayleigh and Mie theory which are directly related to this work will be given here. Derivation from the basic principles will not be given as excellent reviews already exist in the literature [54,55,56,57].

An account of Rayleigh and Mie Theory is given in appendices 1 and 2 respectively. It is also necessary to define the scattering parameters such as scattering angle, polarisation etc. which are related to the actual light scattering apparatus used. These are shown in figure 3.1 below.

The scattering plane is defined by the plane in which the detector arm moves and is the horizontal plane. The scattering angle, θ , is the angle between the direction of the incident light and the position of the detector arm. The incident light polarisation direction is vertical and hence perpendicular to the scattering plane. The x and y axis

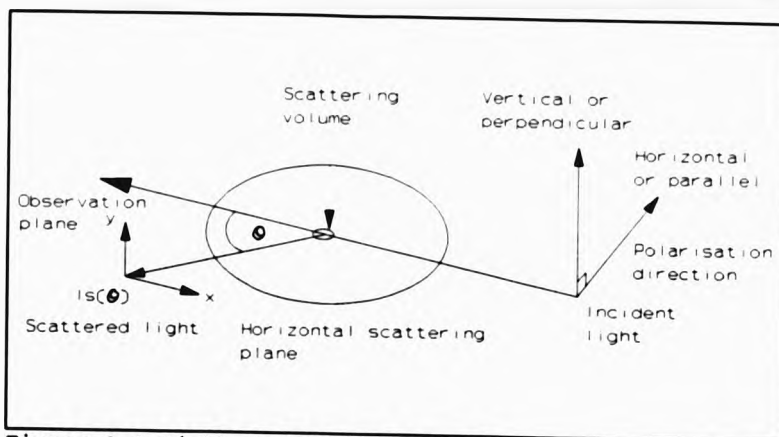


Figure 3.1 Light Scattering Geometry.

define the observation plane, the detector aperture at this surface measures the unpolarised scattered light intensity.

3.2.1. Applicability of Rayleigh Theory

Rayleigh theory (as described in appendix 1) is only valid for scatterer sizes up to $\lambda/20$, where λ is the wavelength of the incident light. This will not be applicable for the analysis of the light scattered from resins which may have inhomogeneity of sizes up to $1\mu\text{m}$ or more. However, Rayleigh theory accurately describes the scattering from liquids and hence, will be used for the calibration of the light scattering equipment.

3.2.2. Applicability of Mie Theory

Although Mie theory (as described in appendix 2) is exact for homogeneous spheres of arbitrary size, it would be unrealistic to assume that such entities exist as microstructure in crosslinked resins. In real systems, the relative refractive index is likely to vary over the spatial range of the microstructure. In addition, they may also be non-spherical in shape and have random orientation. A complete review and study of the applicability of Mie theory for the situation described above, would be a project in its own right and therefore lies outside the scope of this work. However,



some evidence exists in the literature, suggesting that Mie theory can be used to approximate to this non-ideal situation and these will be summarised below.

The solution of Maxwell's equations for homogeneous spheroidal particles have been formulated by Asano and Yamamoto [58]. Asano and Sato [59] computed the light scattering behaviour for randomly orientated spheroidal particles and found that the scattered light in the forward direction (scattering angle less than 70°) is comparable to that of equivalent area spheres, calculated using Mie theory. In the case of a polydisperse collection of scatterers, the scattered light envelope will be dominated by the individual intense forward scattering lobes of the individual scatterers, this suggests that Mie theory should give a reasonable approximation. Also, Holland and Gagne [60] and Pinnick et al. [61], have shown experimentally that for monodisperse and polydisperse, randomly orientated collection of non-spherical particles, Mie theory can be used as a good approximation, particularly for particles with a size parameter less than 5.

3.3. Experimental Arrangement

A schematic of the light scattering measurement system is shown in figure 3.2, and is based around a light scattering goniometer capable of measuring the scattered light intensity over an angle range of 10° to 105° in the horizontal scattering plane. The system was developed to allow simultaneous mechanical or electrical stressing of the sample whilst taking light scattering measurements. For a more complete description of the light scattering measurement system, see reference [25]. The sample sits at the centre of the scattering cell which is filled with index matching fluid of the same refractive index as the sample to reduce spurious reflections at the sample surface. The light source is a 10mW HeNe laser of wavelength 632.8nm and its polarisation set vertically. The scattered light collection optics consist of two 0.6mm pinholes separated by 300mm, and defines a scattering area of 0.2mm x 0.2mm at the scattering volume. Two photomultipliers, one measuring a fraction of the incident light intensity and the second, mounted on the goniometer arm measuring the scattered intensity. A two channel Brookdeal 5C1 photon counter was used to simultaneously count photons detected at the two photomultipliers over

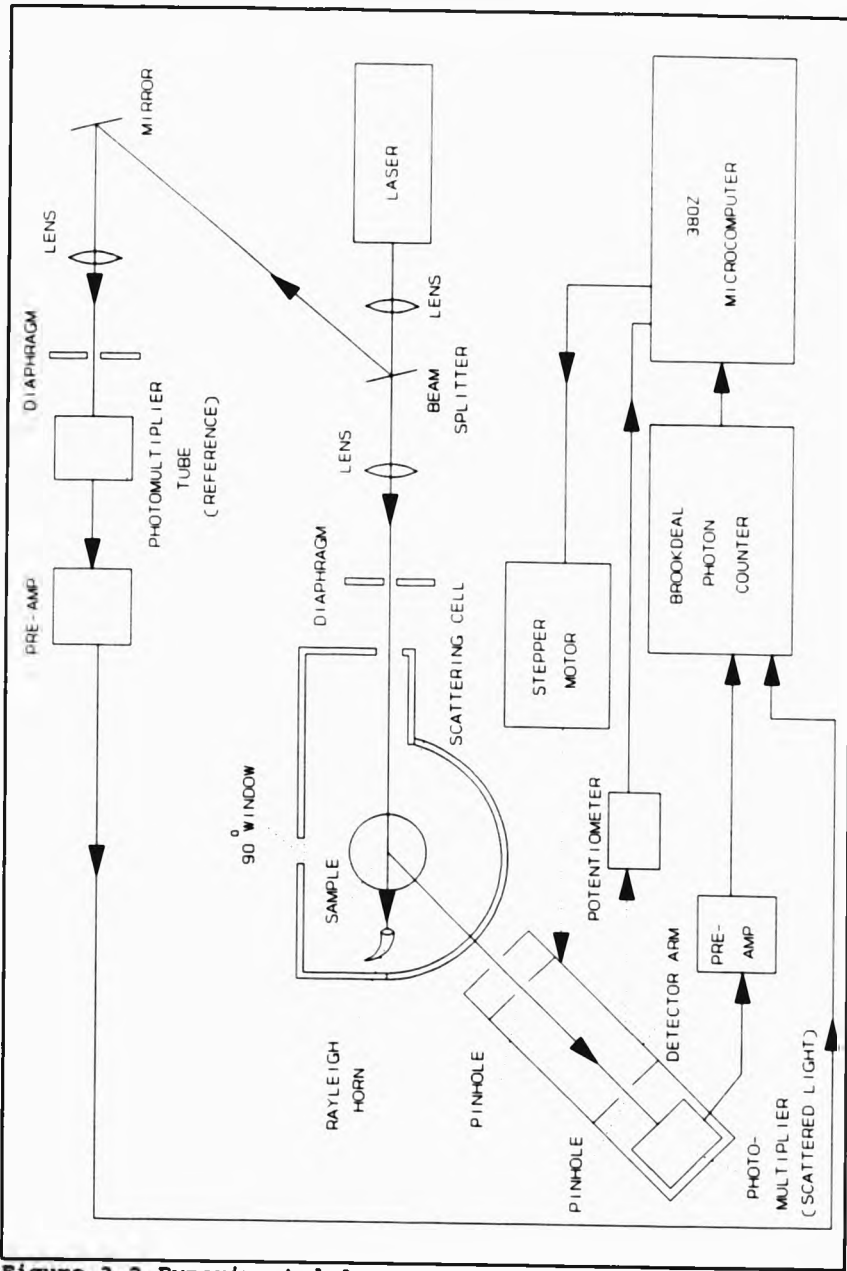


Figure 3.2 Experimental Arrangement.

an adjustable time interval. A Research Machines 380Z microcomputer controls the system, setting the detector arm angle using a stepper motor and potentiometer, and recording intensity measurements at these angles from the photon counter.

3.3.1. Data Collection and Calibration

Data collection is fully automated, the computer program written for the 380Z allows the initial, final and total number of scattering angles to be set. It also allows a set number of intensity measurements to be taken at each scattering angle, so that mean and standard deviation values can be calculated at each angle. A further feature of this program is that a whole set of angular intensity measurements can be repeated a set number of times.

The only other control on data collection is the photon counter integration time over which it counts photons from the two photomultipliers. This has to be long enough so that a reasonable number of photons are detected for each measurement such that the statistical error associated with photon counting (standard deviation = square root of the total number of photons detected) is acceptable. Given the low intensity of scattered light, a count time of at least 10 seconds is found to be necessary.

In this work, light scattering measurements were taken over the angle range 20° to 100°, with a total of 32 angles. The lower angle limit of 20° was chosen so that surface scattering, and scattering from foreign bodies in the index matching fluid do not contribute to the measured scattered intensities. Data is automatically stored on floppy disk for later data analysis.

Calibration of the light scattering measurement system is described in appendix 3. Standard liquids with known light scattering properties were used.



3.3.2. System Appraisal

The scattering by solids of highly coherent laser light, reveals the existence of speckle in the scattered light which has the effect of superimposing noise on the measured data. With no speckle reduction technique employed, the signal to noise ratio of the measured data could be as low as 1:1. A technique to reduce the speckle noise and increase the signal to noise ratio to 10:1 was developed and is described in appendix 4.

Before using the light scattering system to measure the scattered light from resin samples, some tests were performed to ensure correct operation of the system. Figure 3.3, shows the measured scattered light intensity with angle for toluene. Over the angle range 20° to 100°, the scattered light is isotropic as expected and no peaks due to spurious reflections of the incident light are observed.

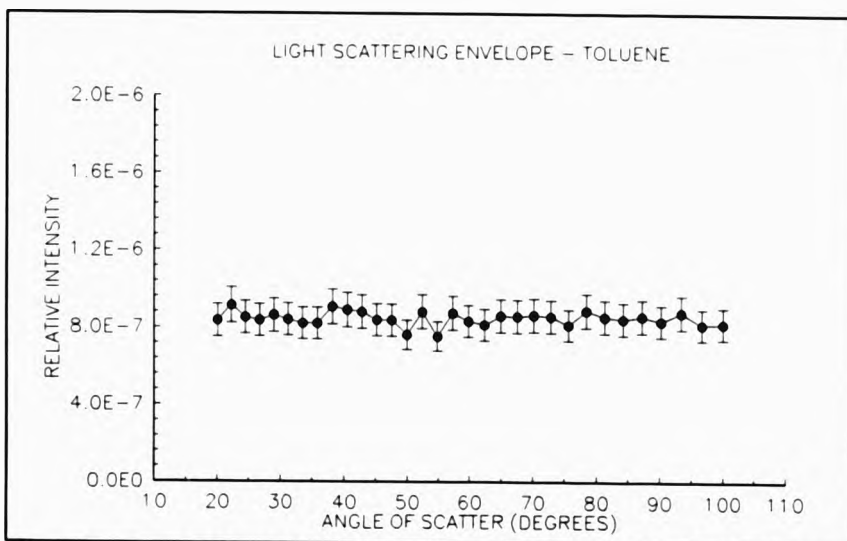


Figure 3.3 Angular Light Scattering Measurements for Toluene.

Light scattering measurements were taken on dilute aqueous solutions of polystyrene latex spheres of known diameter, refractive index and concentration. Using the

technique described in section 3.4.1 to fit theoretical data for a single size scatterer (using Mie theory) to the measured data, the size and concentration of the polystyrene spheres may be determined. The results are shown in table 3.1 together with the diameter given by the manufacturer and concentration determined assuming that the measured size rather than the manufacturer's size is correct.

TABLE 3.1 Determination of Size and Concentration of Polystyrene Spheres from Light Scattering Measurements

Manufacturer and Diameter (μm)	Concentration (cm^{-3})	Measured Dia. (μm)	Measured concentration (cm^{-3})
Polysciences 0.37	0.25×10^8	0.332 ± 0.001	$(0.29 \pm 0.05) \times 10^8$
Polysciences 0.54	0.77×10^7	0.491 ± 0.002	$(0.60 \pm 0.10) \times 10^7$
Polysciences 0.77	0.50×10^7	0.566 ± 0.002	$(0.43 \pm 0.08) \times 10^7$
Sigma 0.33	0.52×10^8	0.327 ± 0.001	$(0.60 \pm 0.08) \times 10^8$

Good agreement is found for the concentration of scatterers. However, only for the Sigma $0.33\mu\text{m}$ spheres was good agreement found in the scatterer size. For the Polysciences spheres, large differences are found between the manufacturer's size and that found from light scattering measurements. To investigate this, scanning electron micrographs were obtained for the Sigma $0.33\mu\text{m}$ spheres and the Polysciences $0.77\mu\text{m}$ spheres. The sizes (diameters) obtained from the micrographs are given in table 3.2 below.

TABLE 3.2 Size of Polystyrene Spheres from SEM Measurements

Manufacturer and size (μm)	Size from SEM Measurements (μm)
Polysciences 0.77	0.55 ± 0.03
Sigma 0.33	0.30 ± 0.03

The scanning electron microscope measurements agree with the sizes obtained using light scattering and therefore cast doubt on the sizing technique employed by the manufacturer. These results therefore confirm the calibration of the light scattering system.

3.4. Data Analysis and Computation

Light scattering measurements for three different CT200 epoxy resin samples are shown plotted against scattering angle in figure 3.4. Although the intensities of the scattered light differ significantly, the shape of the light scattering envelope is similar for all three samples. Also noticeable is a lack of lobe structure indicating that a distribution of scatterer size exists. The scattered light intensity is observed to increase sharply at angles less than 30° suggesting that scatterers of size greater than $1\mu\text{m}$ are present.

Many different techniques of inversion of the measured scattered light to determine size, concentration, size distribution of scatterers etc. have been used by various workers. These include least squares fitting [67,68,69], the Phillips-Twomey inversion method [70,71,72] and the Backus-Gilbert inversion method [73,74].

Least squares fitting is perhaps the most useful. Although an *a priori* assumption of the size distribution is required, the comparison of the fitted sum of squares allows decisions to be made as to the most likely size distribution or family of distributions compatible with the measured data and experimental error. This technique has a further advantage in that an estimate of the error (standard deviation) of the fitted parameters can be obtained.

Both the Phillips-Twomey and Backus-Gilbert inversion methods do not rely on an *a priori* assumption of the size distribution. A comparison of these two techniques by Chow and Tien [72], reveals that the latter method gives solutions which are not as stable as the former method and hence the Backus-Gilbert method was not considered further. In use, the Phillips-Twomey method (using light scattering measurements from resin samples) allows solutions involving negative concentrations. To overcome this, it is necessary to pre-weight the theoretical Mie data which is equivalent to assuming a size distribution. Hence, this technique offers no real advantage over the method of least squares and was not considered further.

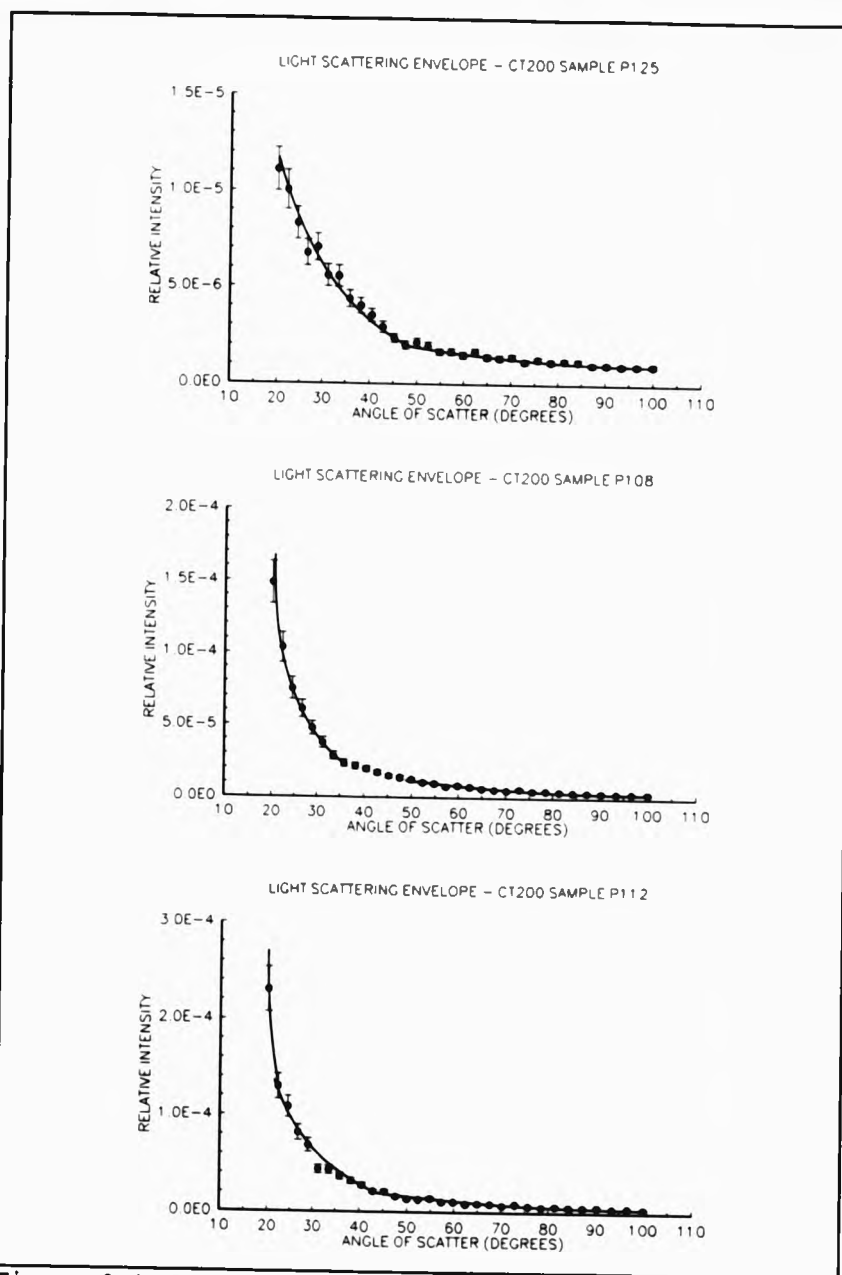


Figure 3.4 Scattered Light from 3 Different CT200 Resin Samples.

The method of least squares was therefore chosen to invert the light scattering measurements and to obtain information on the size and concentration of scatterers. Three different size distributions were considered, single size, normal distribution and log-normal distribution. These will be considered in the following sections along with the value for the relative refractive index of the scatterer.

The computation of the Mie formulae require some care to prevent round-off errors from accumulating and yielding erroneous results. The techniques followed are given in appendix 5.

The method of least squares along with the procedure for estimating the errors in the fitted parameters are given in appendix 6.

3.4.1. Fitting a Single Size of Scatterer

The scatterer diameter and concentration (cm^3) was chosen as parameters in the least squares fitting analysis. Mie theory was used to compute the theoretical data to be compared with the measured data. The relative refractive index of the scatterers is chosen at the start and remained fixed during the analysis.

For a known scatterer relative refractive index, as is the case with the aqueous solutions of polystyrene latex spheres, the analysis program directly determines the size and concentration of scatterers present. This has been successfully used to confirm the calibration of the light scattering measurement system (see section 3.3.2.).

For samples with unknown relative refractive index, repeated analysis for a range of relative refractive indexes, will yield different values for the fitted ^{Sum of Squares} χ^2 . The correct value for the relative refractive index may then be identified from the lowest value of χ^2 . This will only be true however if it is known that all the scatterers present in the sample have the same diameter. Plotted in figure 3.5 is the fitted sum of squares against relative refractive index for CT200 epoxy resin sample P108. A minimum is observed in the fitted sum of squares, having a minimum value of

approximately 200, at a relative refractive index of 0.66 which is close to that of a void (0.629). This would seem to suggest that the scatterers present are voids all of a single size.

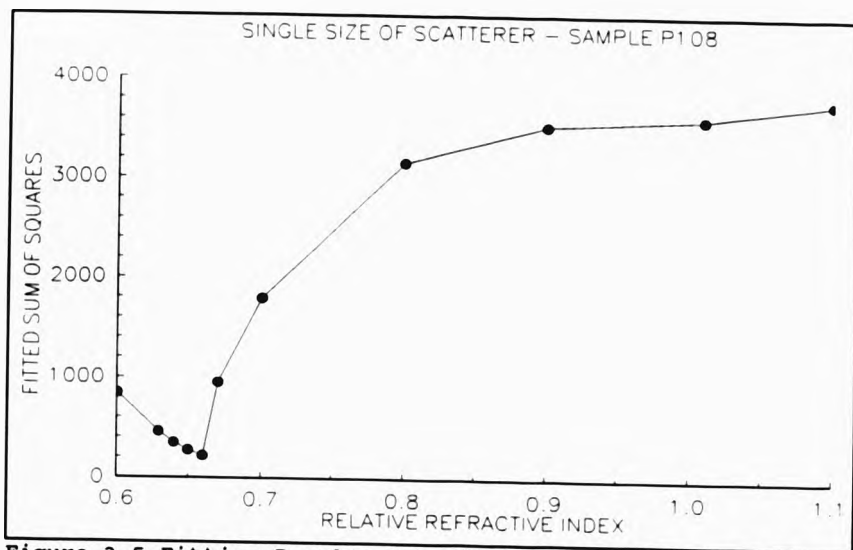


Figure 3.5 Fitting Results for Single Size of Scatterer.

3.4.2. Fitting to a Size Distribution of Scatterers

Microstructure in synthetic resins is likely to have a distribution of scatterer sizes. For instance, Stevens [21], has found using SEM that the inhomogeneities in CT200 epoxy resin have a log-normal size distribution with a modal diameter of 150nm and inhomogeneity sizes up to 400nm were observed. To allow for this, the analysis program was modified to take into account different size distributions. Two distribution functions were considered, normal and log-normal.

The normal distribution function [54] is defined as

$$P(a) = \frac{1}{(2\pi)^{1/2}\sigma} \cdot \exp\left[-\frac{(a-\bar{a})^2}{2\sigma^2}\right] \quad (3.1)$$

where a is the effective diameter of the scatterer, \bar{a} is the mean scatterer diameter and σ the standard deviation. The pre-exponential factor normalizes the expression such that

$$\int_{-\infty}^{\infty} P(a) da = 1. \quad (3.2)$$

In order to allow for a concentration variation, the distribution function is modified by including a factor C , representing the total number of scatterers in the distribution, as shown below.

$$N(a) = \frac{C}{(2\pi)^{1/2} \sigma} \cdot \exp\left[-\frac{(a-\bar{a})^2}{2\sigma^2}\right]. \quad (3.3)$$

Similarly, the log-normal distribution function [54] is defined as

$$N(a) = \frac{C}{(2\pi)^{1/2} \sigma_g a} \cdot \exp\left[-\frac{(\log a - \log a_m)^2}{2\sigma_g^2}\right], \quad (3.4)$$

where $\log(a_m)$ is the mean value of $\log(a)$ and a_m is therefore both the median and the geometric mean value of a . σ_g is the standard deviation of $\log(a)$ and is termed the geometric mean standard deviation. The mode a_M , median a_m , and the mean \bar{a} , of the distribution are related to the geometric mean a_g , by, [54],

$$\ln a_M = \ln a_g - \sigma_g^2, \quad (3.5)$$

$$\ln a_m = \ln a_g, \quad (3.6)$$

$$\ln \bar{a} = \ln a_g + 0.5 \sigma_g^2. \quad (3.7)$$

Equations 3.3 and 3.4, along with Mie theory can be used to obtain theoretical light scattering data for scatterers with a distribution of sizes, to compare with the measured data using the method of least squares. The range of scatterer sizes that needs to be considered in the analysis is limited by both Mie theory and the angle

range of the measured data. Mie theory shows that the scattered light is essentially isotropic for scatterer sizes below $0.1\mu\text{m}$ diameter. As the scatterer size increases, more of the incident light is scattered into a lobe in the forward direction i.e. in the low angle range. The angular width of this lobe decreases with increasing scatterer size. Light scattering measurements are taken over the angle range 20° to 100° and so the largest scatterer diameter that can be considered in the analysis is $1.3\mu\text{m}$.

The theoretical data for a distribution of scatterer sizes is calculated by computing from Mie theory, the scattering envelopes for a range of scatterer diameters, $0.01\mu\text{m}$ then $0.1\mu\text{m}$ to $1.3\mu\text{m}$ in $0.1\mu\text{m}$ steps, for a given relative refractive index. Each of these, is then multiplied by the corresponding value of the distribution function, $N(a)$, for the given values of the distribution parameters, before summing each of the now weighted scattering envelopes. This procedure is shown mathematically below.

$$I_\theta = \sum_{a=0.01, 0.1, 0.2, \dots, 1.3\mu\text{m}} N(a) \cdot I_{\theta, a} \quad (3.8)$$

where I_θ is the theoretical data for the distribution of scatterer size for each angle θ , and $I_{\theta, a}$ are the individual scattering envelopes for each of the scatterer diameters, a , ranging from $0.01\mu\text{m}$ to $1.3\mu\text{m}$.

The two fitting parameters used in the least squares fitting analysis were the concentration parameter C (cm^{-3}), and the geometric mean standard deviation, henceforth called the 'width' parameter. For the normal distribution analysis, the relative refractive index and the distribution mean diameter were fixed at the start of the analysis. By repeated analysis using different values for these two values, and comparing the fitted sum of squares, estimates of their real values can be made.

For the log-normal distribution, the relative refractive index and the modal diameter of the distribution are fixed at the start of the analysis. Preliminary analysis using the log-normal size distribution on CT200 and polyester data, and by comparing the fitted sum of squares, has shown that the modal value must be less than $0.01\mu\text{m}$ for the distribution to be compatible with the measured scattered light data. As the light scattering envelopes of scatterers less than $0.01\mu\text{m}$ are isotropic, no further information can be gained and so the model value of the distribution was fixed at

0.01 μ m in all subsequent analysis. This value is also consistent with other light scattering studies [47] on CT200 resin where hydrogen bonded aggregates were observed of approximately this size.

Figure 3.6 shows the variation in the fitted sum of squares for a log-normal distribution of scatterers plotted against relative refractive index for CT200 sample P111. A minimum in the fitted sum of squares is obtained, having a value of 48, for a relative refractive index of approximately 1.01, the actual value being difficult to gauge as no sharply defined minimum exists. Similar results are found for the polyester resin. However, this method of analysis supports the hypothesis that the scatterers present are inhomogeneities having a log-normal size distribution, rather than voids all of a single size, see section 3.4.1..

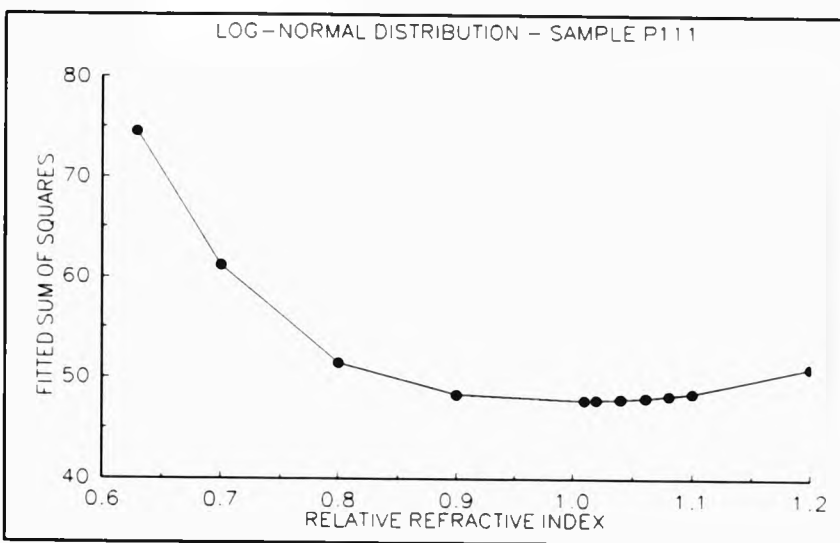


Figure 3.6 Fitting Results for a Log-Normal Distribution of Inhomogeneities.

If a normal distribution of inhomogeneities of relative refractive index 1.01 is fitted to the same experimental data (CT200 sample P111), a minimum is obtained in the value of the fitted sum of squares, of value 130, when the mean size of the distribution is zero, as shown in figure 3.7. The fitted standard deviation of the normal distribution was found to depend on the mean value, preset at the start of the

analysis. For mean sizes above $0.65\mu\text{m}$, the fitted standard deviations have values of approximately $20\mu\text{m}$, corresponding to a flat distribution where all the scatterer sizes considered in the analysis have similar populations. The fitted standard deviation parameter tends to zero for a distribution mean size of $0.3\mu\text{m}$, corresponding to a monodisperse distribution of inhomogeneities. At the sum of squares minimum, (distribution mean value of zero), the fitted standard

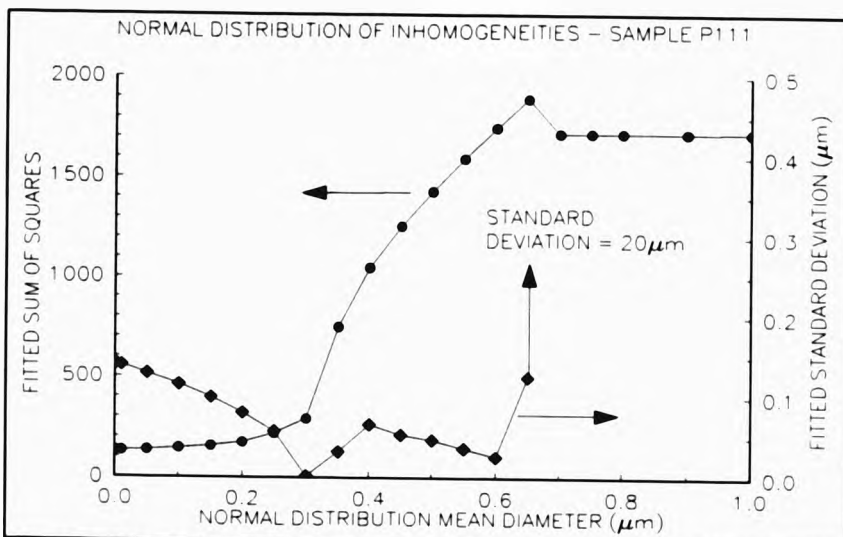


Figure 3.7 Fitting Results for a Normal Distribution of Scatterers.

deviation has a value $0.14\mu\text{m}$. Considering just the positive sizes in the distribution, the fitted distribution approximates to the fitted log-normal distribution but having a higher fitted sum of squares value of 130. Fitting a normal distribution of voids, having a relative refractive index of 0.629, a similar result is obtained, but having a sum of squares minima of 104.

Comparing the fitted sum of squares values, for all data analysis methods, it is found that the log-normal distribution of inhomogeneities gives the best fit to the measured scattered light data. Subsequent analysis on all resin samples will use this method of analysis in order to characterize the microstructure in these resins.



Values of the relative refractive index and modal value of the distribution were fixed to 1.01 and $0.01\mu\text{m}$ respectively for all samples in order to standardize the characterization procedure, as from Mie theory it can be seen that small changes in the relative refractive index, lead to large changes in the scattered intensity. However, the shape of the scattering envelope is fairly insensitive to changes in the refractive index.

The measured and fitted light scattering envelopes for CT200 sample P111 are plotted in figure 3.8, showing the good agreement obtained when fitting to a log-normal distribution of inhomogeneities. The fitted log-normal distribution for polyester sample RC7 is shown in figure 3.9 along with the calculated 68% and 95% confidence limits. The logarithm of the concentration (per cm^3) is plotted against the inhomogeneity diameter to show the large range of concentration for the individual scatterer sizes in the distribution. In figure 3.10, the fitted log-normal distributions of 8 consecutive measurements of the scattered light were taken at various positions within the sample, The spread in the 8 fitted distributions, is approximately the same as the 95% confidence limits shown in figure 3.9. This suggests that the analysis

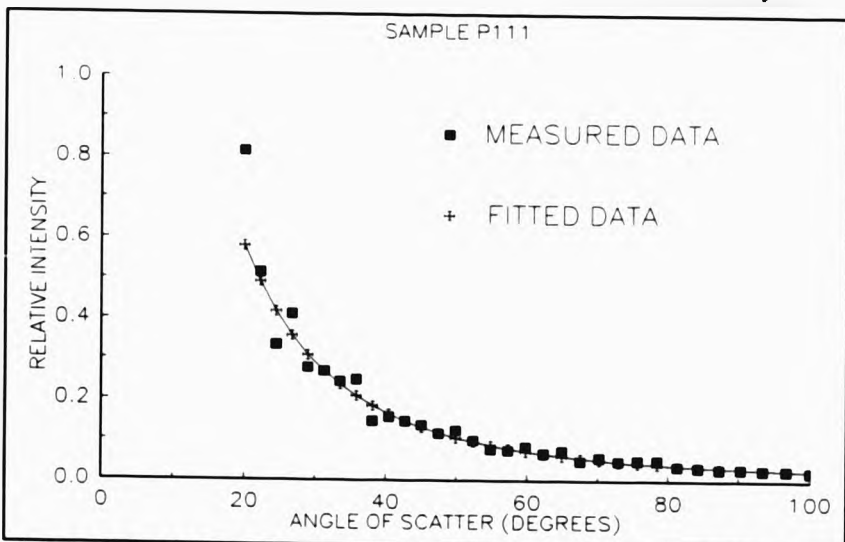


Figure 3.8 Measured and Fitted Light Scattering Envelope for a Log-Normal Distribution of Inhomogeneities.

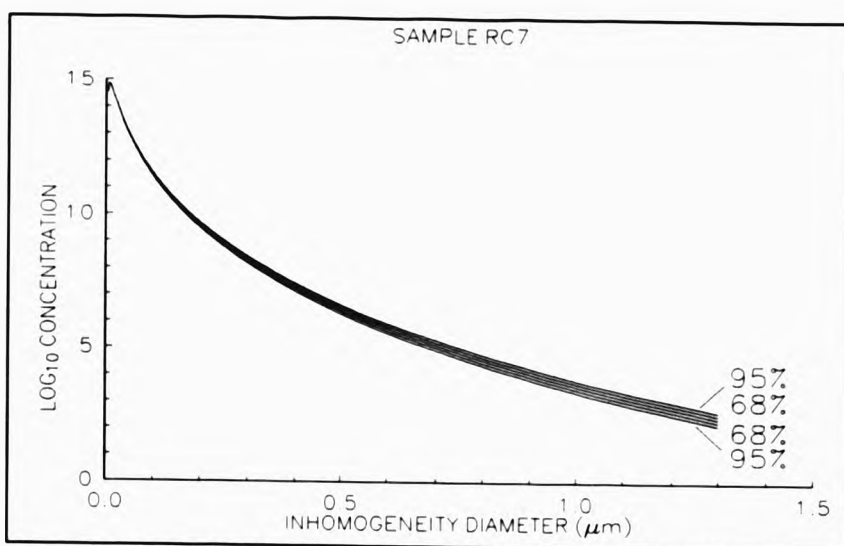


Figure 3.9 Fitted log-normal distribution showing the 68% and 95% confidence Limits for polyester resin sample RC7. Concentration is per cm^3 and the logarithm of base 10 taken.

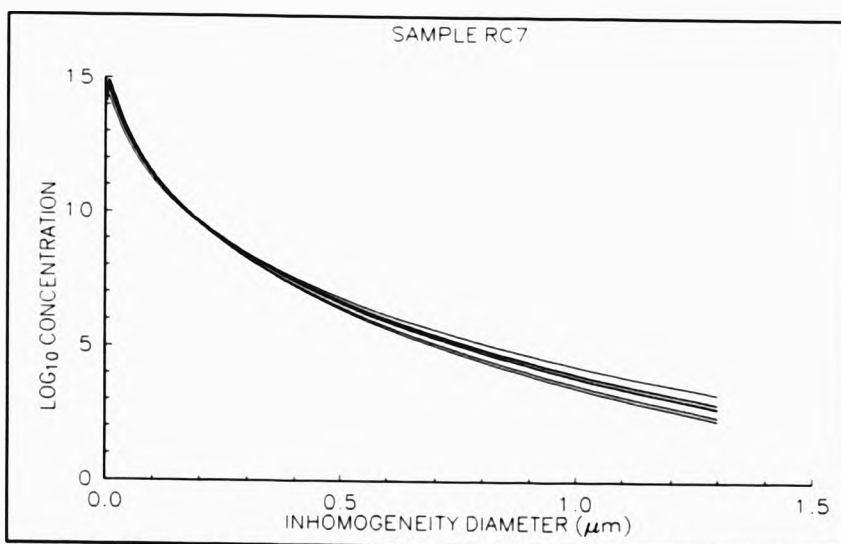


Figure 3.10 Log-normal distributions obtained from 8 consecutive measurements of the scattered light from sample RC7.

procedure is repeatable and that the microstructure concentration and size distribution does not change significantly within different regions in the sample.

3.4.3. Microstructure Characterization Procedure

A log-normal size distribution is fitted to the measured scattered light envelope as described in the previous section along with the error analysis to determine the standard deviation in each of the fitted parameters.

In order to obtain a figure of merit describing the amount of microstructure each sample contains, the following procedure was adopted. For each fitted log-normal distribution, the area under the distribution curve is calculated over the size range $0.25\mu\text{m}$ to $1.3\mu\text{m}$. The figure obtained, here after called the 'microstructure content' corresponds to the number of scatterers per cm^3 present within this size range. The lower limit was set due to the uncertainty in the distribution below $0.2\mu\text{m}$. This uncertainty is due mainly to the isotropic scattering behaviour of the small scatterers (less than $0.1\mu\text{m}$) and the arbitrary choice for the modal value of the distribution. The upper limit set by the largest scatterer size used in the analysis.

Errors for the microstructure content (number of scatterers present per cm^3 , of sizes between $0.25\mu\text{m}$ and $1.3\mu\text{m}$), are calculated by taking into account the standard deviations in the fitted distribution parameters, 65% confidence limits were calculated.

3.5. CT200 Epoxy Resin Characterization Results

Light scattering measurements were obtained for a number of 'as received' and 'ultra clean' CT200 samples. Filtration of the uncured resin (for the 'ultra clean' samples) followed the two techniques described in section 2.3.1., i.e. with or without the use of butanone. The uncured resin of two of the 'as received' samples were subjected to a special treatment. For these two samples, the unfiltered resin was dissolved in butanone which was then evaporated from the resin at 80°C .

Additional light scattering measurements were taken on the uncured resin in order to determine the origin, type and amount of microstructure found in the various cured resin preparations.

3.5.1. Fully Cured CT200 Epoxy Resin

The fitted log-normal distributions for the 'as received' samples are shown in figure 3.11, the distributions labelled B refer to the butanone treated samples. The fitted distributions are very similar and the butanone treated samples having the higher microstructure concentration. The log-normal distributions for the 'ultra clean' samples are shown in figure 3.12. A wide range of microstructure concentration is found for these samples. The distributions labelled U refer to samples prepared without using butanone.

The characterization results for the fully cured CT200 samples are given in table 3.3 below. Tabulated are the preparation procedure, the fitted width and concentration parameters of the log-normal distribution and the microstructure content (the number per cm^3 of scatterers between $0.25\mu\text{m}$ and $1.3\mu\text{m}$ in size). Two or three light scattering measurements were taken on each sample and the analysis results for each are given. The samples are ranked in increasing values for the microstructure content. The amount of microstructure can vary by up to 2 orders of magnitude depending on the sample preparation technique. Repeated measurements of the microstructure content on the same sample agree within the calculated 65% confidence limits, whilst the fitted log-normal width and concentration parameters do not. This suggests that the characterization technique is stable, the width and concentration parameters compensate each other such that the calculated microstructure content agrees from measurement to measurement. Hence the characterization technique is not significantly affected by measurement error such as the speckle noise on the scattered light data. (see appendix 4).

The 'as received' samples have similar microstructure content having values in the range 8.5×10^7 to $1.0 \times 10^8 \text{ cm}^{-3}$. The 'as received' resins treated with butanone, (AR+B), have a higher microstructure content than the 'as received' samples and

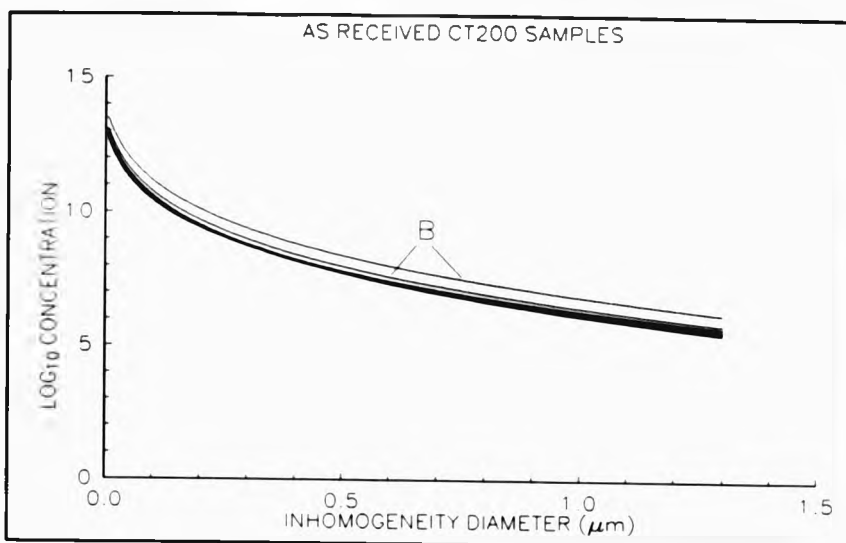


Figure 3.11 Fitted log-normal distributions for the fully cured 'as received' CT200 samples. B - resin butanone treated.

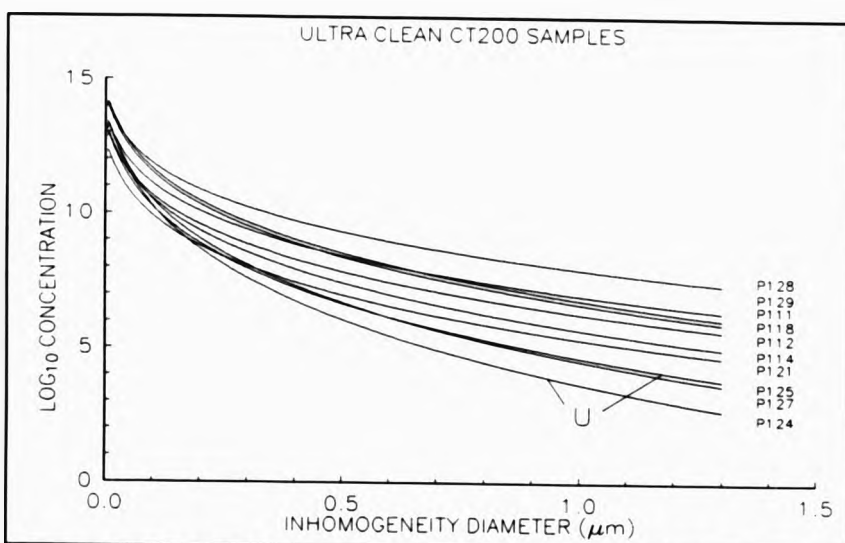


Figure 3.12 Fitted log-normal distributions for the fully cured 'ultra clean' CT200 samples. u - resin filtered without butanone.

TABLE 3.3 Fully Cured CT200 Epoxy Resin Characterization Results

SAMPLE	PREPARATION PROCEDURE	FITTED WIDTH PARAMETER	FITTED CONCENTRATION PARAMETER (cm ³)	MICROSTRUCTURE CONTENT (cm ³)
P124	UC	0.777+/-0.003	(3.00+/-0.05)x10 ¹¹	(5.2+/-0.5)x10 ⁶
		0.795+/-0.003	(2.21+/-0.04)x10 ¹¹	(5.6+/-0.5)x10 ⁶
		0.786+/-0.003	(2.65+/-0.05)x10 ¹¹	(5.6+/-0.5)x10 ⁶
P125	UC	0.879+/-0.003	(1.09+/-0.02)x10 ¹¹	(1.4+/-0.1)x10 ⁷
		0.874+/-0.003	(1.15+/-0.02)x10 ¹¹	(1.3+/-0.1)x10 ⁷
		0.868+/-0.003	(1.25+/-0.02)x10 ¹¹	(1.3+/-0.1)x10 ⁷
P121	UC+B	0.983+/-0.003	(3.12+/-0.06)x10 ¹⁰	(1.6+/-0.1)x10 ⁷
		0.982+/-0.003	(3.09+/-0.06)x10 ¹⁰	(1.6+/-0.1)x10 ⁷
		0.985+/-0.003	(3.00+/-0.05)x10 ¹⁰	(1.6+/-0.1)x10 ⁷
P127	UC+B	0.834+/-0.003	(2.99+/-0.05)x10 ¹¹	(1.7+/-0.1)x10 ⁷
		0.827+/-0.003	(3.19+/-0.06)x10 ¹¹	(1.6+/-0.1)x10 ⁷
P114	UC+B	0.941+/-0.003	(1.70+/-0.03)x10 ¹¹	(5.3+/-0.3)x10 ⁷
		0.948+/-0.003	(1.55+/-0.03)x10 ¹¹	(5.3+/-0.3)x10 ⁷
		0.955+/-0.003	(1.41+/-0.03)x10 ¹¹	(5.3+/-0.3)x10 ⁷
P108	AR	1.028+/-0.004	(1.02+/-0.02)x10 ¹¹	(8.9+/-0.5)x10 ⁷
		1.007+/-0.003	(1.23+/-0.02)x10 ¹¹	(8.6+/-0.5)x10 ⁷
		1.022+/-0.004	(1.04+/-0.02)x10 ¹¹	(8.5+/-0.5)x10 ⁷

Table 3.3 continued.

P122	AR	1.065+/-0.004 1.062+/-0.004 1.056+/-0.004	(6.9+/-0.1)x10 ¹⁰ (7.3+/-0.1)x10 ¹⁰ (7.6+/-0.1)x10 ¹⁰	(8.7+/-0.5)x10 ⁷ (8.9+/-0.5)x10 ⁷ (8.8+/-0.5)x10 ⁷
P119	AR	1.001+/-0.003 1.007+/-0.003 1.001+/-0.003	(1.38+/-0.02)x10 ¹¹ (1.29+/-0.02)x10 ¹¹ (1.40+/-0.03)x10 ¹¹	(9.0+/-0.5)x10 ⁷ (9.0+/-0.5)x10 ⁷ (9.1+/-0.5)x10 ⁷
P116	AR	1.049+/-0.004 1.045+/-0.004 1.045+/-0.004	(8.5+/-0.2)x10 ¹⁰ (8.8+/-0.2)x10 ¹⁰ (8.7+/-0.1)x10 ¹⁰	(9.1+/-0.5)x10 ⁷ (9.1+/-0.5)x10 ⁷ (9.0+/-0.5)x10 ⁷
P120	AR	1.018+/-0.004 1.028+/-0.004 1.032+/-0.004	(1.14+/-0.02)x10 ¹¹ (1.04+/-0.02)x10 ¹¹ (9.8+/-0.2)x10 ¹⁰	(8.9+/-0.5)x10 ⁷ (9.1+/-0.5)x10 ⁷ (8.8+/-0.5)x10 ⁷
P105	AR	1.011+/-0.004 1.007+/-0.003	(1.23+/-0.02)x10 ¹¹ (1.37+/-0.02)x10 ¹¹	(9.0+/-0.5)x10 ⁷ (9.5+/-0.5)x10 ⁷
P115	AR	1.043+/-0.004 1.041+/-0.004	(9.3+/-0.1)x10 ¹⁰ (9.6+/-0.2)x10 ¹⁰	(9.4+/-0.5)x10 ⁷ (9.5+/-0.5)x10 ⁷
P123	AR	1.019+/-0.004 1.020+/-0.004 1.031+/-0.004	(1.25+/-0.02)x10 ¹¹ (1.24+/-0.02)x10 ¹¹ (1.13+/-0.02)x10 ¹¹	(9.9+/-0.6)x10 ⁷ (1.0+/-0.1)x10 ⁸ (1.0+/-0.1)x10 ⁸
P112	UC+B	1.012+/-0.004 1.010+/-0.004	(1.52+/-0.03)x10 ¹¹ (1.61+/-0.03)x10 ¹¹	(1.1+/-0.1)x10 ⁸ (1.2+/-0.1)x10 ⁸

Table 3.3 continued.

P110	AR+B	1.021+/-0.004 1.017+/-0.004	(1.87+/-0.03) x10 ¹¹ (1.96+/-0.04) x10 ¹¹	(1.5+/-0.1) x10 ⁸ (1.5+/-0.1) x10 ⁸
P129	UC+B	1.049+/-0.004 1.055+/-0.004	(3.65+/-0.07) x10 ¹¹ (3.37+/-0.06) x10 ¹¹	(3.9+/-0.2) x10 ⁸ (3.8+/-0.2) x10 ⁸
P113	AR+B	1.022+/-0.004 1.031+/-0.004	(4.70+/-0.08) x10 ¹¹ (4.38+/-0.08) x10 ¹¹	(3.8+/-0.2) x10 ⁸ (3.7+/-0.2) x10 ⁸
P118	UC+B	0.945+/-0.003 0.940+/-0.003	(1.51+/-0.03) x10 ¹² (1.67+/-0.03) x10 ¹²	(5.0+/-0.3) x10 ⁸ (5.2+/-0.3) x10 ⁸
P111	UC+B	0.947+/-0.003 0.955+/-0.003 0.948+/-0.003	(2.01+/-0.04) x10 ¹² (1.84+/-0.03) x10 ¹² (2.07+/-0.04) x10 ¹²	(6.8+/-0.4) x10 ⁸ (6.9+/-0.4) x10 ⁸ (7.1+/-0.4) x10 ⁸
P128	UC+B	1.089+/-0.004 1.089+/-0.004	(1.78+/-0.03) x10 ¹² (1.79+/-0.03) x10 ¹²	(2.8+/-0.2) x10 ⁹ (2.8+/-0.2) x10 ⁹

PREPARATION PROCEDURE - AR - AS RECEIVED
 UC - ULTRA CLEAN
 AR+B - AS RECEIVED RESIN BUTANONE TREATED
 UC+B - ULTRA CLEAN RESIN BUTANONE FILTERED

suggests that the butanone treatment increases the microstructure in the uncured resin.

The 'ultra clean' samples show considerable variation in their microstructure content. The 'ultra clean' samples with the lowest microstructure content, P124 and P125, were prepared by filtration at 140°C without butanone. These results again suggest that butanone is involved in the formation of microstructure.

3.5.2. Formation of Microstructure in CT200 Epoxy Resin

In order to investigate when and how the microstructure forms during the preparation of the samples, light scattering measurements were made on the uncured resin at different stages of the 'ultra clean' preparation technique. This was then repeated using a fresh batch of 'as received' material.

Light scattering measurements were taken at 3 stages of the preparation of the pre-cured resin.

- A) The 'as received' resin.
- B) After filtration of the resin through 0.2 μ m filters at 140°C.
- C) The resin from stage B, after filtration through 0.2 μ m filters using butanone as a solvent and removal of the butanone at 80°C.

The microstructure content measured at the three stages are given in table 3.4 below. Label (1) refers to the original and (2), repeat measurements on fresh 'as received' resin.

The 'as received' pre-cured resin has microstructure content (1.4 x 10⁸ cm⁻³) comparable to the fully cured 'as received' samples (9 x 10⁷ cm⁻³) if the volume of hardener is taken into account. After filtration at 140°C without butanone, the concentration of microstructure drops by approximately two orders of magnitude, indicating that

TABLE 3.4 Microstructure at Various Stages of Resin Preparation

PREPARATION STAGE	MICROSTRUCTURE CONTENT (cm ⁻³)
(A1)	(1.4 +/- 0.1) x 10 ⁸
(B1)	(2.9 +/- 0.1) x 10 ⁶
(C1)	(1.4 +/- 0.1) x 10 ⁸
(A2)	(1.4 +/- 0.1) x 10 ⁸
(B2)	(2.2 +/- 0.1) x 10 ⁶
(C2)	(2.2 +/- 0.1) x 10 ⁶

filtration can remove most of the microstructure present in the 'as received' resin. After filtering the resin at 80°C using butanone, the microstructure increases to the level found in the 'as received' material (1.4 x 10⁸ cm⁻³), and for the repeat measurement, approximately one order of magnitude greater than this (2.2 x 10⁹ cm⁻³).

In order to determine whether any additional microstructure forms during the cure of the CT200 resin, light scattering measurements were taken on uncured resin which was filtered without butanone. The same filtered resin was then cured by the addition of filtered hardener, and light scattering measurements taken on the cured sample (P125). The characterization results are given in table 3.5. During the cure of the resin, the microstructure content was found to increase by a factor of approximately 3, suggesting that some microstructure forms during resin cure. However, the microstructure content found in the fully cured sample P124, see table 3.3, has a microstructure content similar to the filtered resin, and so microstructure formation during cure is not conclusive. This increase is small compared with the microstructure concentration found in the 'as received' samples.

TABLE 3.5 Microstructure Formation During Cure of CT200 Resin

PREPARATION STAGE	MICROSTRUCTURE CONTENT (cm ⁻³)
Before cure	(4.7 +/- 0.4) x 10 ⁶
After cure	(1.25 +/- 0.08) x 10 ⁷

3.5.3. Discussion

Light scattering measurements taken on the uncured CT200 resin showed that significant microstructure exists in the 'as received' resin supplied by the manufacturer. Microstructure greater than the pore size of the filter could be removed from the resin by filtration, suggesting that the microstructure is of a particulate nature. It was found that microstructure could reform when the butanone solvent was removed from the resin at 80°C after filtration.

It is concluded that this microstructure is due to the formation of microgel during the removal of butanone. It is suggested that microgel particles form by homopolymerization of the resin with the butanone acting as a catalyst at 80°C. The butanone, through hydrogen bonding, may facilitate opening of epoxide rings of the DGEBA molecules, allowing etherification reactions with DGEBA hydroxyl groups. Etherification of the pure resin is found not to occur even when the resin is heated to 120°C [22].

The fully cured 'ultra clean' samples filtered using butanone were found to have microstructure concentrations which varied by up to two orders of magnitude. The amount of microstructure was found to depend on the length of time and temperature of the butanone removal. Of these samples, the lowest concentration of microstructure was obtained if the majority of the butanone was removed at room temperature. Only when most of the butanone was removed, was the temperature increased to 80°C. The 'ultra clean' samples with the highest concentration of microstructure were obtained when the temperature was carefully maintained at 80°C throughout the butanone removal. For the other 'ultra clean' samples, where butanone was used, evaporation of the butanone caused the temperature of the resin butanone mixture to drop (depending on the rate of evaporation) and therefore to suppress microgelation. This is consistent with a thermal activated etherification reaction and explains the large variation observed in the microstructure concentration in these samples.

To prepare 'ultra clean' samples with the minimum amount of microstructure it was found necessary to filter the resin at 140°C without butanone. The two butanone treated 'as received' samples showed an increase in the amount of microstructure compared with untreated 'as received' samples, supporting the above conclusions.

Comparing the amount of microstructure present in the 'ultra clean' uncured resin (filtered at 140°C without butanone), with the same resin fully cured, suggests that some additional microstructure may form during the cure reaction. The amount of additional microstructure formed is small and much less than that present in the 'as received' samples. The microstructure in these samples is therefore due primarily to pre-existing microgel in the uncured resin supplied by the manufacturer. The origin of this microstructure must be in the resin manufacturing process employed by the manufacturer and probably results from etherification crosslinking reactions.

3.6. Unsaturated Polyester Resin Characterization Results

Light scattering measurements were taken on a number of fully cured 'as received' and 'ultra clean' polyester samples. As this particular resin cures at room temperature, it is possible to take light scattering measurements at all stages of the resin cure. These results, along with results from the measurement of the reaction kinetics using FTIR techniques, refractive index and gel point, will be used to explain the origin, type and amount of microstructure found in the various resin preparations.

3.6.1. Fully Cured Unsaturated Polyester Resin

The log-normal inhomogeneity distributions obtained for the fully cured 'as received' polyester samples are shown in figure 3.13. Two distinct distributions are obtained. Those labelled (1), the earlier samples, have less microstructure than the latter samples labelled (2). The difference is due to a different batch of resin being used in the sample preparation.

The 'ultra clean' samples have similar log-normal distributions as shown in figure 3.14. They have less microstructure than the 'as received' preparations suggesting at

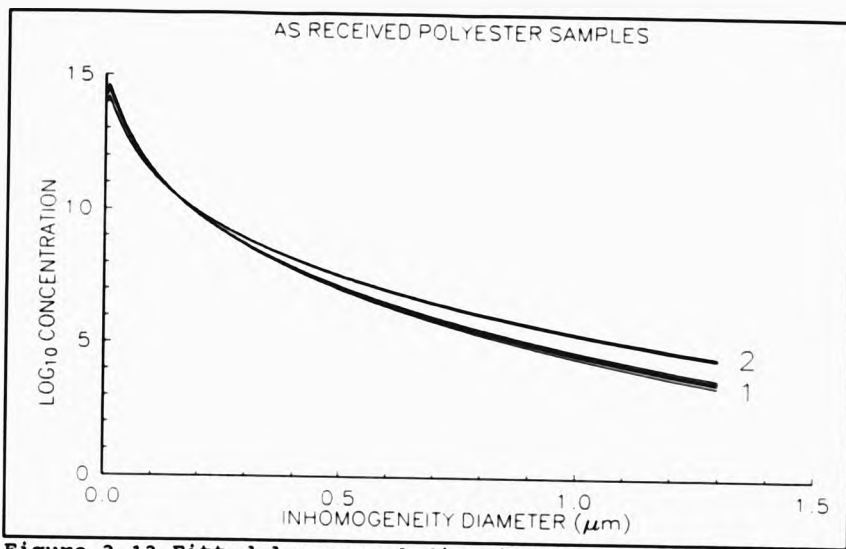


Figure 3.13 Fitted log-normal distributions, 1) four samples from an earlier batch and 2) five samples from a later batch of fully cured 'as received' polyester resin.

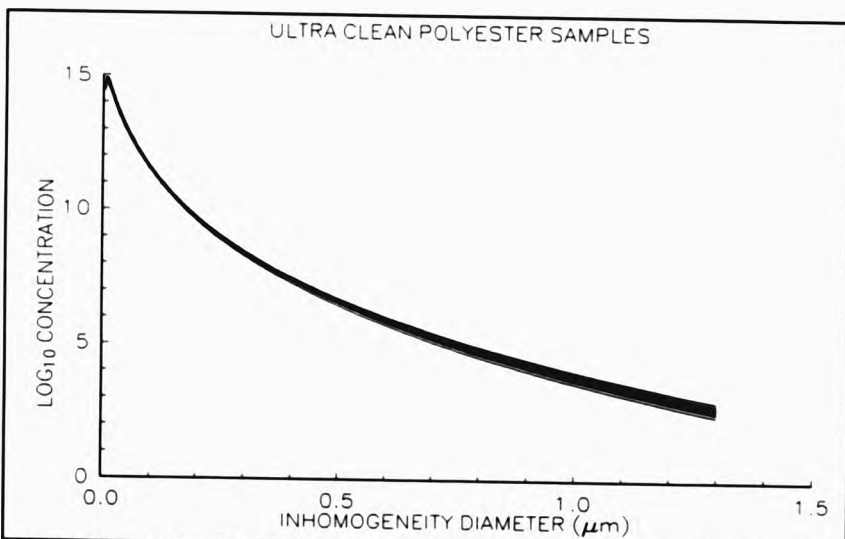


Figure 3.14 Fitted log-normal distributions for 16 fully cured 'ultra clean' polyester resin samples.

TABLE 3.6 Fully Cured Unsaturated Polyester Characterization Results

SAMPLE	PREPARATION PROCEDURE	FITTED WIDTH PARAMETER	FITTED CONCENTRATION PARAMETER (cm ³)	MICROSTRUCTURE CONTENT (cm ³)
RC7	UC	0.710+/-0.004 0.703+/-0.004 0.726+/-0.003	(9.7+/-0.2)x10 ¹² (1.11+/-0.02)x10 ¹³ (7.5+/-0.1)x10 ¹²	(2.8+/-0.4)x10 ⁷ (2.6+/-0.4)x10 ⁷ (3.4+/-0.4)x10 ⁷
RC17	UC	0.719+/-0.004 0.719+/-0.004 0.713+/-0.004	(8.3+/-0.1)x10 ¹² (8.4+/-0.2)x10 ¹² (9.4+/-0.2)x10 ¹²	(3.1+/-0.4)x10 ⁷ (3.2+/-0.4)x10 ⁷ (3.0+/-0.4)x10 ⁷
RC20	UC	0.694+/-0.004 0.706+/-0.004	(1.72+/-0.03)x10 ¹³ (1.33+/-0.02)x10 ¹³	(3.1+/-0.5)x10 ⁷ (3.4+/-0.5)x10 ⁷
RC23	UC	0.714+/-0.004 0.714+/-0.004	(1.01+/-0.02)x10 ¹³ (1.02+/-0.02)x10 ¹³	(3.3+/-0.5)x10 ⁷ (3.3+/-0.5)x10 ⁷
RC18	UC	0.719+/-0.004 0.701+/-0.004 0.712+/-0.004	(9.2+/-0.2)x10 ¹² (1.39+/-0.02)x10 ¹³ (1.10+/-0.02)x10 ¹³	(3.5+/-0.5)x10 ⁷ (3.0+/-0.5)x10 ⁷ (3.4+/-0.5)x10 ⁷
RC13	UC	0.718+/-0.004 0.724+/-0.003 0.722+/-0.003	(8.9+/-0.2)x10 ¹² (8.1+/-0.1)x10 ¹² (8.5+/-0.2)x10 ¹²	(3.3+/-0.4)x10 ⁷ (3.5+/-0.4)x10 ⁷ (3.5+/-0.4)x10 ⁷
RC21	UC	0.709+/-0.004 0.695+/-0.004	(1.22+/-0.02)x10 ¹³ (1.64+/-0.03)x10 ¹³	(3.5+/-0.5)x10 ⁷ (3.0+/-0.5)x10 ⁷
RC24	UC	0.712+/-0.004 0.713+/-0.004	(1.13+/-0.02)x10 ¹³ (1.10+/-0.02)x10 ¹³	(3.5+/-0.5)x10 ⁷ (3.5+/-0.5)x10 ⁷
RC3	UC	0.723+/-0.003 0.726+/-0.003 0.730+/-0.003	(8.6+/-0.2)x10 ¹² (8.1+/-0.2)x10 ¹² (7.7+/-0.1)x10 ¹²	(3.6+/-0.4)x10 ⁷ (3.7+/-0.5)x10 ⁷ (4.0+/-0.5)x10 ⁷

Table 3.6 continued.

RC4	UC	0.722+/-0.004 0.727+/-0.003 0.732+/-0.003	(9.7+/-0.2) x10 ¹² (8.7+/-0.2) x10 ¹² (7.9+/-0.1) x10 ¹²	(3.9+/-0.5) x10 ⁷ (4.2+/-0.5) x10 ⁷ (4.4+/-0.5) x10 ⁷
RC28	UC	0.729+/-0.003 0.734+/-0.003	(7.8+/-0.1) x10 ¹² (7.0+/-0.1) x10 ¹²	(3.9+/-0.5) x10 ⁷ (4.1+/-0.5) x10 ⁷
RC25	UC	0.738+/-0.003 0.735+/-0.003	(6.4+/-0.1) x10 ¹² (6.7+/-0.1) x10 ¹²	(4.1+/-0.5) x10 ⁷ (4.1+/-0.5) x10 ⁷
RC27	UC	0.739+/-0.003 0.744+/-0.003	(6.1+/-0.1) x10 ¹² (6.0+/-0.1) x10 ¹²	(4.1+/-0.5) x10 ⁷ (4.5+/-0.5) x10 ⁷
RC26	UC	0.715+/-0.004 0.706+/-0.004	(1.22+/-0.02) x10 ¹³ (1.50+/-0.03) x10 ¹³	(4.2+/-0.6) x10 ⁷ (3.9+/-0.6) x10 ⁷
RC6	UC	0.726+/-0.003 0.716+/-0.004 0.734+/-0.003	(9.4+/-0.2) x10 ¹² (1.20+/-0.02) x10 ¹³ (8.4+/-0.1) x10 ¹²	(4.3+/-0.5) x10 ⁷ (4.2+/-0.6) x10 ⁷ (4.8+/-0.6) x10 ⁷
RC22	UC	0.718+/-0.004 0.702+/-0.004	(1.17+/-0.02) x10 ¹³ (1.56+/-0.03) x10 ¹³	(4.3+/-0.6) x10 ⁷ (3.5+/-0.6) x10 ⁷
RC8	AR	0.758+/-0.003 0.771+/-0.003 0.758+/-0.003	(6.0+/-0.1) x10 ¹² (4.71+/-0.08) x10 ¹² (6.0+/-0.1) x10 ¹²	(6.4+/-0.6) x10 ⁷ (6.9+/-0.6) x10 ⁷ (6.5+/-0.6) x10 ⁷
RC11	AR	0.766+/-0.003 0.763+/-0.003 0.775+/-0.003	(5.2+/-0.1) x10 ¹² (5.4+/-0.1) x10 ¹² (4.40+/-0.08) x10 ¹²	(6.8+/-0.6) x10 ⁷ (6.6+/-0.6) x10 ⁷ (7.1+/-0.6) x10 ⁷
RC5	AR	0.780+/-0.003 0.780+/-0.003 0.774+/-0.003	(3.82+/-0.07) x10 ¹² (3.78+/-0.07) x10 ¹² (4.28+/-0.08) x10 ¹²	(7.0+/-0.6) x10 ⁷ (7.0+/-0.6) x10 ⁷ (6.8+/-0.6) x10 ⁷

Table 3.6 continued.

RC2	AR	0.774+/-0.003 0.765+/-0.003 0.770+/-0.003	(4.20+/-0.07) x10 ¹² (5.06+/-0.09) x10 ¹² (4.83+/-0.09) x10 ¹²	(6.7+/-0.6) x10 ⁷ (6.5+/-0.6) x10 ⁷ (7.1+/-0.6) x10 ⁷
RC10	AR	0.769+/-0.003 0.765+/-0.003 0.772+/-0.003	(5.3+/-0.1) x10 ¹² (5.5+/-0.1) x10 ¹² (5.2+/-0.1) x10 ¹²	(7.6+/-0.7) x10 ⁷ (7.2+/-0.7) x10 ⁷ (8.0+/-0.7) x10 ⁷
RC14	AR	0.837+/-0.003 0.836+/-0.003 0.831+/-0.003	(1.89+/-0.03) x10 ¹² (1.95+/-0.03) x10 ¹² (2.15+/-0.04) x10 ¹²	(1.1+/-0.1) x10 ⁸ (1.1+/-0.1) x10 ⁸ (1.1+/-0.1) x10 ⁸
RC16	AR	0.830+/-0.003 0.830+/-0.003 0.834+/-0.003	(2.27+/-0.04) x10 ¹² (2.29+/-0.04) x10 ¹² (2.16+/-0.04) x10 ¹²	(1.2+/-0.1) x10 ⁸ (1.2+/-0.1) x10 ⁸ (1.2+/-0.1) x10 ⁸
RC12	AR	0.833+/-0.003 0.831+/-0.003 0.835+/-0.003	(2.14+/-0.04) x10 ¹² (2.20+/-0.04) x10 ¹² (2.00+/-0.04) x10 ¹²	(1.2+/-0.1) x10 ⁸ (1.2+/-0.1) x10 ⁸ (1.2+/-0.1) x10 ⁸
RC15	AR	0.840+/-0.003 0.837+/-0.003 0.834+/-0.003	(1.94+/-0.03) x10 ¹² (2.07+/-0.04) x10 ¹² (2.14+/-0.04) x10 ¹²	(1.2+/-0.1) x10 ⁸ (1.2+/-0.1) x10 ⁸ (1.2+/-0.1) x10 ⁸

PREPARATION PROCEDURE - AR - AS RECEIVED
UC - ULTRA CLEAN

least some of the microstructure in the 'as received' samples is due to pre-existing microstructure present in the pre-cured materials.

The characterization results are shown in table 3.6, where the samples are ranked in increasing values of the microstructure content. Tabulated for each sample is the preparation procedure, the log-normal width and concentration parameters and the microstructure content, (the number of scatterers between $0.25\mu\text{m}$ and $1.3\mu\text{m}$ per cm^3). Where several light scattering measurements were taken on each sample, the value of the microstructure content agrees within the calculated 68% confidence limits. The samples are found to fall into 3 groups. The first group with the least amount of microstructure are the 'ultra clean' samples. The second and third groups are the 'as received' samples which were prepared from two different batches of polyester resin. The samples made from the earlier batch of polyester resin have approximately twice the amount of microstructure as the 'ultra clean' samples, while the later 'as received' samples have approximately 3 times the amount of microstructure as the 'ultra clean' samples. Hence, the amount of microstructure in the 'as received' samples depends on the resin batch and possibly the storage conditions.

3.6.2. Microstructure in the Pre-cured Materials

The microstructure content for the unfiltered 'as received' and filtered 'ultra clean' un-cured resin and MEKP hardener are tabulated in table 3.7 below.

TABLE 3.7 Microstructure in Uncured Polyester Resin and Hardener

SAMPLE	MICROSTRUCTURE CONTENT (cm^{-3})
'As Received' Polyester Resin	$(4.3 \pm 0.3) \times 10^7$
'Ultra Clean' Polyester Resin	$(2.6 \pm 4.0) \times 10^3$
'As Received' MEKP Hardener	$(1.1 \pm 0.5) \times 10^6$
'Ultra Clean' MEKP Hardener	$(1.3 \pm 3.2) \times 10^5$

The amount of microstructure present in the 'as received' resin and hardener is reduced considerably as expected when the resin and hardener are filtered. This



suggests a particulate nature for the microstructure, microgel can form by styrene homopolymerization (see section 2.2) and hence, the amount will depend on resin batch and the storage conditions. Large errors in the 'ultra clean' results are due to the lack of large scatterers present compared with the number of smaller scatterers ($<0.1\mu\text{m}$), resulting in a near isotropic scattering envelope. The errors will however, give the upper limit for the microstructure concentration compatible with the errors in the scattered light data.

As only 1% by volume of hardener is used to cure the resin, its intrinsic microstructure is not likely to contribute significantly to the microstructure present in the fully cured resin. Comparing the microstructure content value for the uncured 'ultra clean' resin with the values for the fully cured 'ultra clean' resin samples, suggests that significant microstructure forms during the cure reaction.

3.6.3. Formation of Microstructure during the Cure of Unsaturated Polyester Resin

An 'ultra clean' resin preparation was made. After adding the hardener and stirring for 10 minutes, the resin was poured into a glass cylindrical cell which had been cleaned but not treated with release agent (to avoid spurious surface scattering). The glass cell was then placed into the light scattering goniometer and at 15 minute intervals, light scattering measurements were taken over the scattering angle range of 20° to 100° , each full angular range taking 10 minutes to complete.

Figure 3.15 shows the scattered light intensity at 90° as a function of time since the addition of the hardener. An induction period of approximately 50 minutes is observed where the scattered light remains constant. After the inhibitor, used to prevent oxygen initiated free-radical polymerisation during storage [23], has been neutralised, the scattered light steadily increases with time. A similar behaviour is observed with the scattered light measured at 30° , as shown in figure 3.16. These results show that microstructure starts to form approximately 50 minutes after the addition of the hardener.

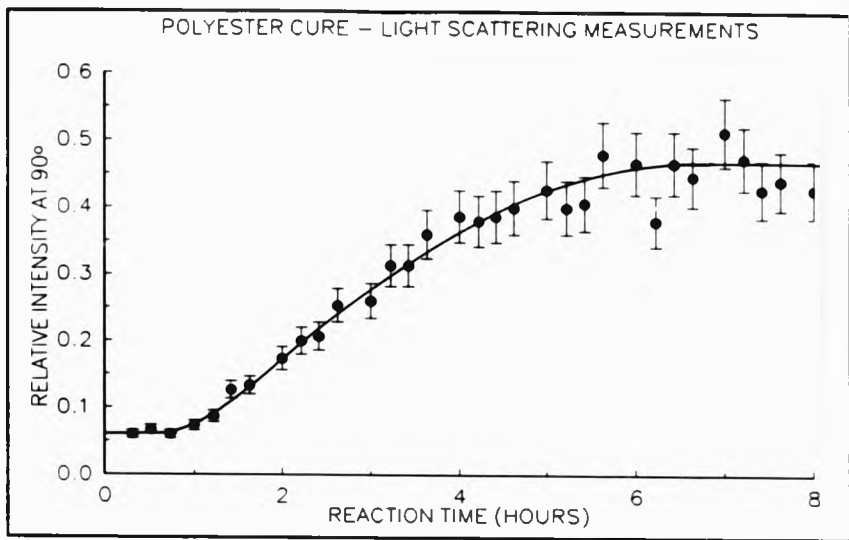


Figure 3.15 90° scattered light intensity during the cure of polyester resin.

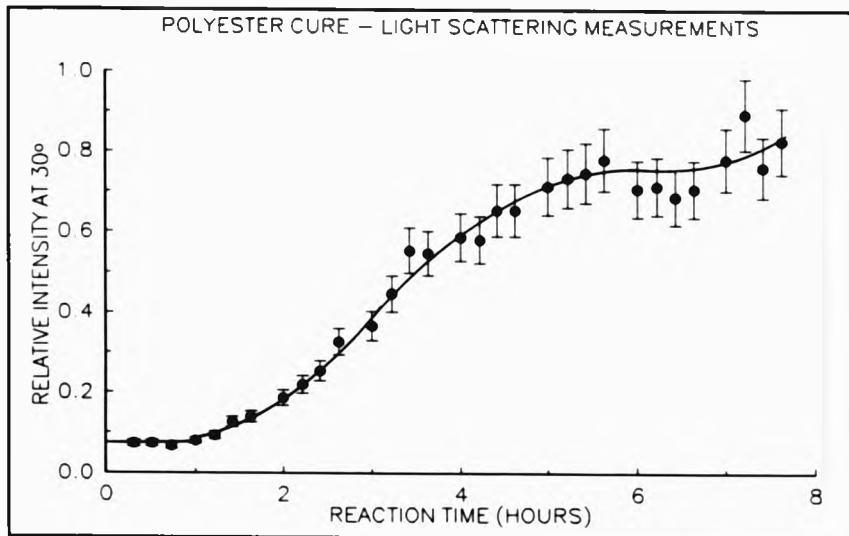


Figure 3.16 30° scattered light intensity during the cure of polyester resin.



Figure 3.17 shows the fitted log-normal width parameter over the same time interval as the previous measurements. The width parameter remains constant for the first 2 hours of the cure reaction and corresponds to a near isotropic scattering envelope. The microstructure that forms after 50 minutes must therefore be less than $0.1\mu\text{m}$. A sharp increase in the distribution width occurs between 2 to 3 hours after the addition of the hardener, indicating that larger inhomogeneous structures are being formed. The width parameter then remains constant until, after 6-7 hours, another increase in the width parameter is observed to within the range found for the fully cured samples.

The microstructure content, shown plotted against reaction time in figure 3.18, increases initially, reflecting the initial formation of small inhomogeneities, then increasing sharply over the time range 2 to 3 hours, corresponding to where the width parameter was observed to increase sharply. After 3 hours the microstructure content remains constant until between 6 to 8 hours, when it starts to increase again. Hence it would appear that microstructure formation occurs at three distinct stages during the first 8 hours of the polyester cure reaction.

The long term scattered light behaviour at 30° is shown in figure 3.19. The scattered intensity increases to a maximum after the first day, then slowly decreases over a period of a few weeks, down to the value obtained for a fully cured sample. Applying a post cure to the sample will accelerate this process. These long term changes are probably due to changes in the relative refractive index of the microstructure, due to shrinkage of the sample and to any remaining styrene within the sample polymerising.

3.7. Measurement of the Reaction Kinetics of Unsaturated Polyester Resin using Fourier Transform Infra Red Techniques

3.7.1. Introduction

Light scattering measurements taken during the cure of unsaturated polyester resin has shown that significant microstructure forms during several stages of the cure

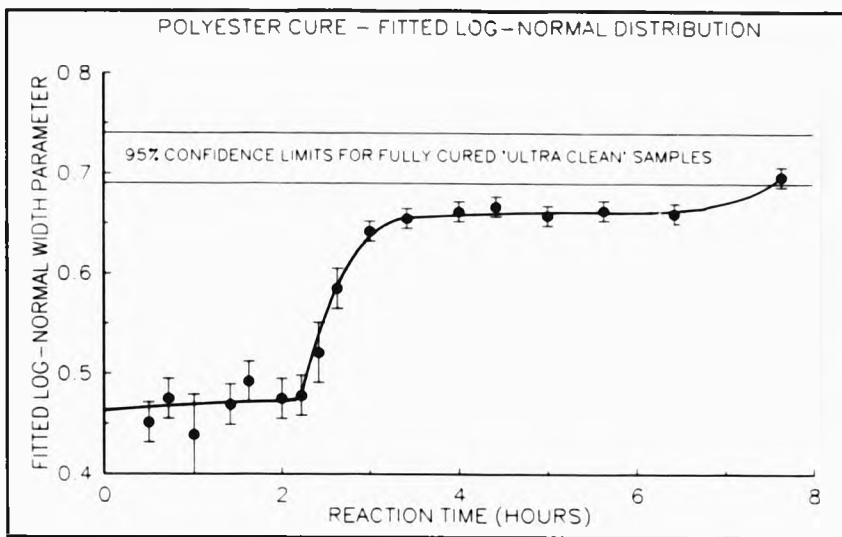


Figure 3.17 Fitted log-normal width parameter during the cure reaction of polyester resin.

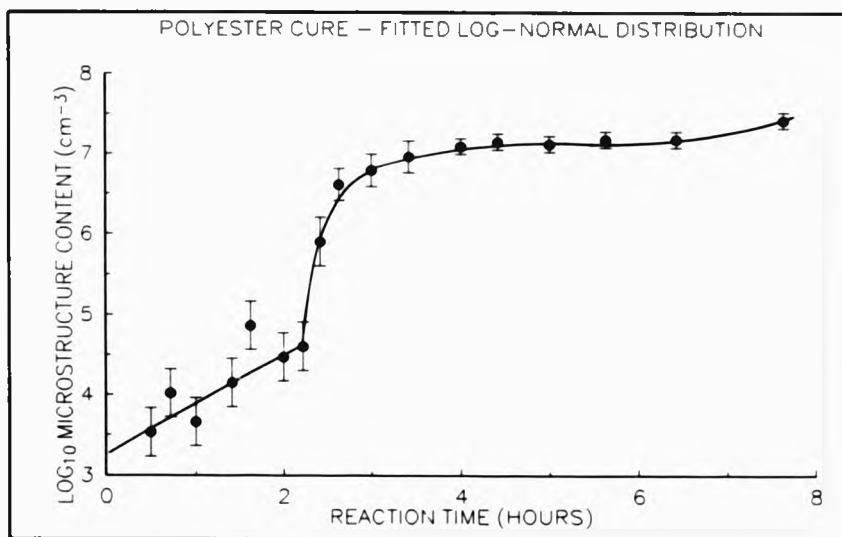


Figure 3.18 Logarithm of the microstructure content during the cure reaction of polyester resin.

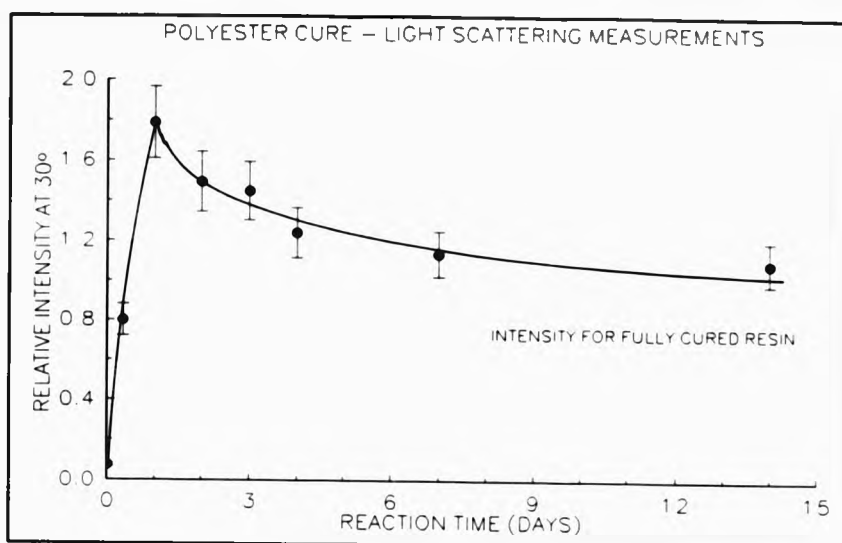


Figure 3.19 Long term light scattering behaviour during the cure of polyester resin.

reaction. In order to correlate the light scattering results with particular stages of the cure reaction, the reaction kinetics for the polyester cure reaction were monitored using FTIR techniques. Both thin film and bulk sample measurements were taken, the thin film data giving detailed information on the cure kinetics whilst the bulk samples were used to assess the differences between thin film and bulk cure. To compliment these and the light scattering results, detailed measurements of the refractive index during cure and the gelation time were also undertaken.

3.7.2. Measurement of Infra Red Spectra during the Cure of Unsaturated Polyester Resin

To start the cure reaction 1% volume of MEKP hardener was added to the 'as received' polyester resin and stirred for 10 minutes. A small quantity of the resin was then placed between two KBr plates separated using a 12 μ m thick Melinex spacer. The two KBr plates were then clamped together into a spectrometer sample holder ready for measurement of infra-red absorption spectra. The rest of the curing polyester was then poured into glass sample cells (1 inch diameter, 2 inches high) for

bulk samples. Once these had gelled, suitable samples were made by cutting thin (approx. $12\mu\text{m}$) layers from the centre of these samples, using a Reichert Jung microtome with a glass blade, which were then sandwiched between KBr plates.

Infra red absorption spectra were taken using a Perkin Elmer 1720-X IRFT spectrometer with a resolution of 4 cm^{-1} . An average of 20 scans were recorded for each measurement taking 1.5 minutes to complete. All spectra were stored on floppy disk for latter analysis. Examples of the infra red spectra are shown in figure 3.20 (a), for uncured polyester resin and (b) for the fully cured resin. The absorption peaks of interest are shown labelled. The peaks were identified using reference [76].

3.7.3. Analysis of the Infra Red Spectra

The analysis follows Yang and Lee [24], with some modifications. Their technique uses four absorption peaks listed below.

- 1) Polyester double bonds at 982 cm^{-1}
- 2) Styrene double bonds at 992 cm^{-1}
- 3) Styrene double bonds at 912 cm^{-1}
- 4) Total number of C-H bonds at 2942 cm^{-1}

For a given quantity of polyester resin the number of C-H bonds will remain constant during the cure reaction. This peak can therefore be used to normalise all the absorption data to correct for thickness changes and shrinkage of the resin during cure. However, it is found that the shape and fine structure of this peak changes during cure and is therefore unsuitable for normalisation purposes. Instead the styrene benzene ring peak at 697 cm^{-1} can be used instead assuming no styrene loss during cure.

The measured spectra have a resolution of 4 cm^{-1} and hence the 982 and 992 cm^{-1} peaks will overlap, as shown in figure 3.21, where the $992/982\text{ cm}^{-1}$ and 912 cm^{-1} are shown at various stages of resin cure. In order to separate these two peaks it is necessary to determine the styrene contribution to the measured double peak $982/992$

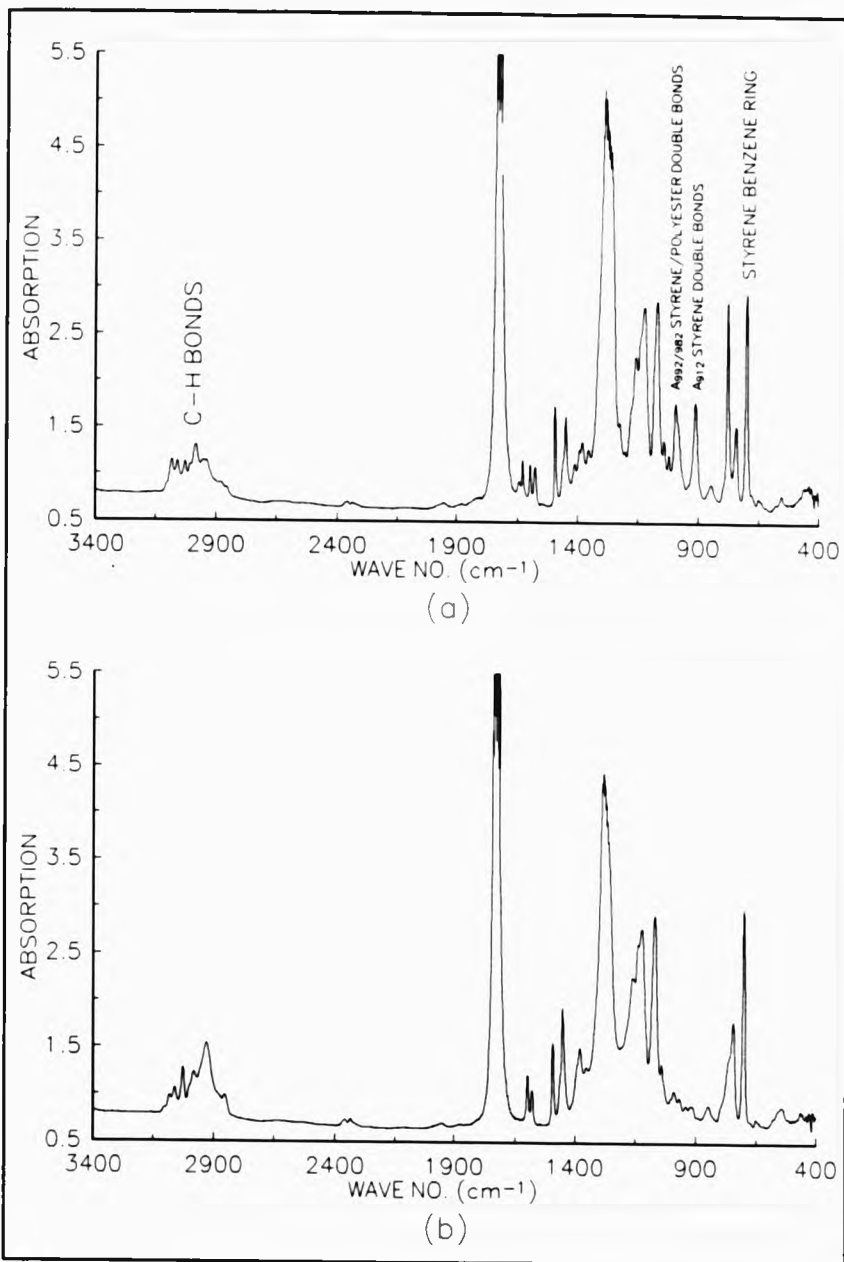


Figure 3.20 Infra red spectra of unsaturated polyester resin. (a) before cure, (b) after post cure.

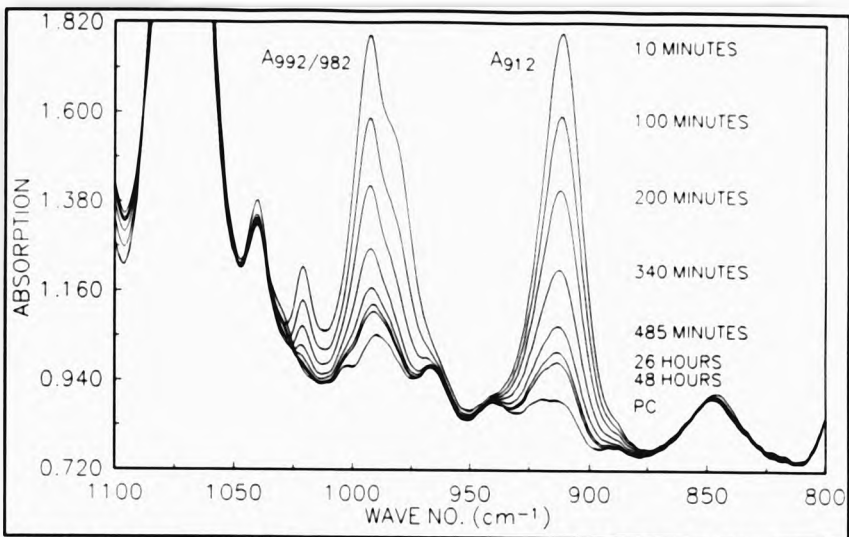


Figure 3.21 The overlapping styrene/polyester absorption peak at 982/992 cm^{-1} and the styrene absorption peak at 912 cm^{-1} at various times during the cure reaction.

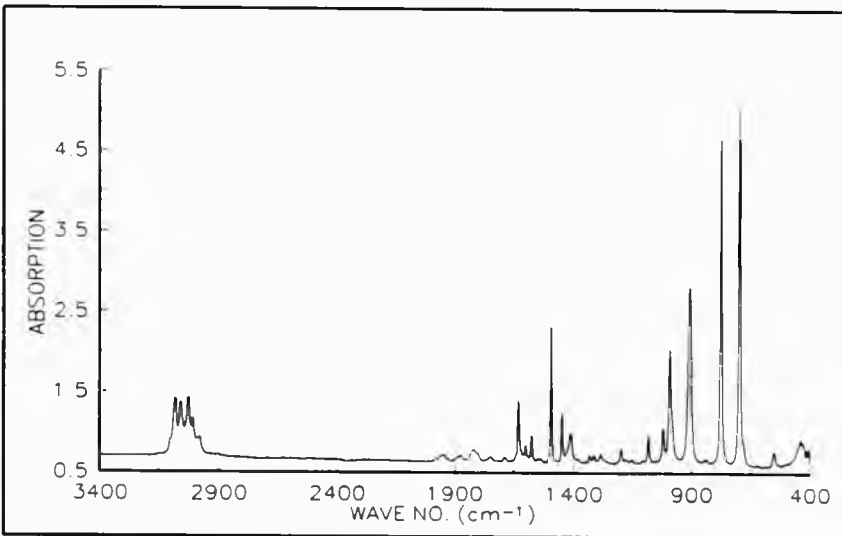


Figure 3.22 Infra red spectra of pure styrene.

cm⁻¹. This was done by first measuring the absorption spectra of pure styrene, as shown in figure 3.22. The relative areas of the two styrene peaks can be found such that

$$A_{992} = C \times A_{912} \quad (3.9)$$

Hence for the polyester resin spectra, the contribution of the styrene peak to the measured double peak $A_{992/982}$ is given by C times the measured absorption peak A_{912} . The polyester contribution is therefore found from

$$A_{982} = A_{992/982} - C \times A_{912} \quad (3.10)$$

The styrene and polyester conversions, α_s and α_p , during the cure reaction at time, t, can therefore be calculated from

$$\alpha_s = 1 - A_{912}(t) / A_{912}(t=0) \quad (3.11)$$

$$\alpha_p = 1 - A_{982}(t) / A_{982}(t=0) \quad (3.12)$$

A computer program was written to read the spectral data files and calculate peak areas. The base line correction for each of the spectra was performed by subtracting from each of the spectra, the spectra for the fully cured resin. A correction was made to all peak areas for the residual styrene and polyester peaks in the background spectra. This was found to be the best method of base line correction.

3.7.4. Polyester Reaction Kinetics

The styrene and polyester conversions for the first 500 minutes of the cure reaction are shown plotted against time in figures 3.23 and 3.24 respectively. An induction period is observed (the first 30 minutes) where the inhibitor, used to prevent oxygen initiated free-radical polymerisation during storage [23], is neutralised. The conversion rates increase significantly after this time.

Figure 3.25 shows the result of plotting styrene conversion, α_s , against polyester conversion, α_p . During the early stages of cure a styrene/polyester crosslinking

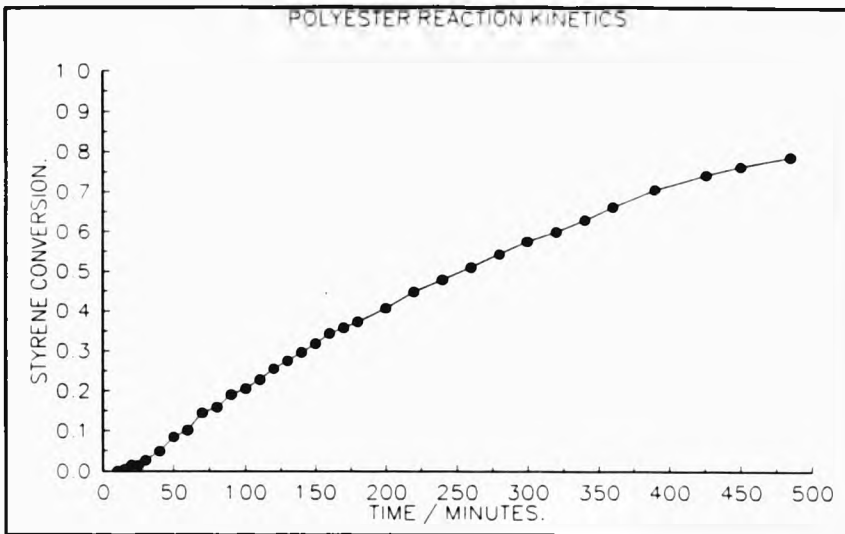


Figure 3.23 Styrene conversion during the first 8 hours of the cure reaction.

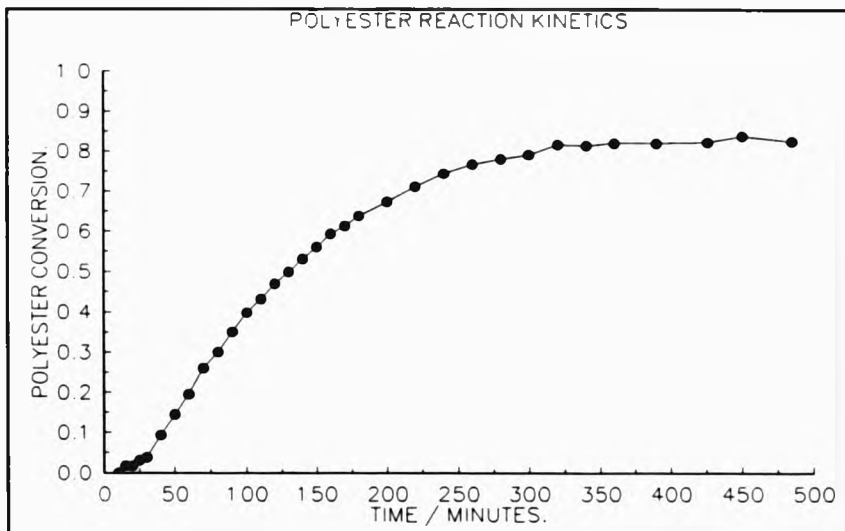


Figure 3.24 Polyester conversion during the first 8 hours of the cure reaction.

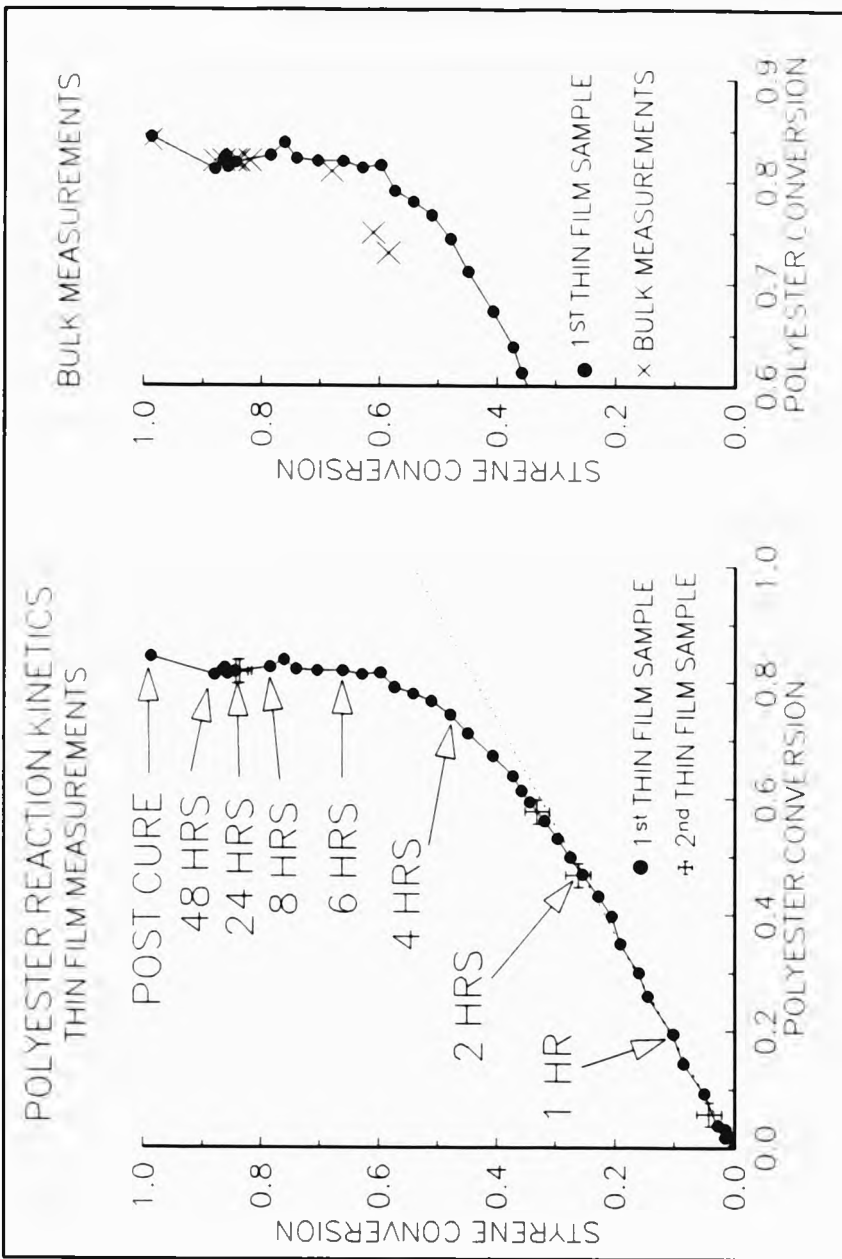


Figure 3.25 Polyester and styrene conversion during the cure reaction. Also shown are the results from a second thin film sample and the bulk samples.

occurs, shown by the dashed line (assuming that the ratio of styrene double bonds to polyester double bonds is approximately 2:1). After 90 minutes, the polyester conversion slows, as shown by the ^{increasing} gradient in the reaction curve, probably due to the lower mobility of the polyester monomer in the gelled resin network. As the cure reaction proceeds, the ratio of styrene/polyester reaction increases with increasing styrene homopolymerization occurring until after 8 hours the polyester reaction is essentially complete, whilst free styrene in the network continues to react. A post cure procedure ensures virtual completion of the styrene reaction. Measurements from another thin film sample and from the bulk samples, also plotted in figure 3.25, show identical behaviour (except for the early bulk samples where significant styrene loss occurred during the preparation of the samples) and suggests that there is no difference in the reaction kinetics in the thin film and bulk samples.

3.7.5. Refractive Index Measurements

Refractive index measurements during the cure reaction were taken using a Abbe refractometer. A sample cell made from CT200 epoxy resin and glass ensures that a higher refractive index material separates the polyester from the refractometer prism, otherwise measurement is not possible.

Refractive index measurements of the curing polyester resin are shown in figure 3.26, plotted against styrene conversion. It is found that the refractive index measurements follow the styrene conversion over a limited range. Temperature rise is responsible for the initial drop in refractive index and shrinkage of the curing polyester responsible for the large step between 8 and 24 hours.

3.7.6. Measurement of Gel Time

The gelation time of the polyester resin was determined by noting the time the reaction had proceeded where an abrupt increase in the viscosity was observed. The viscosity was determined by measurement of the terminal velocity, v , of small steel

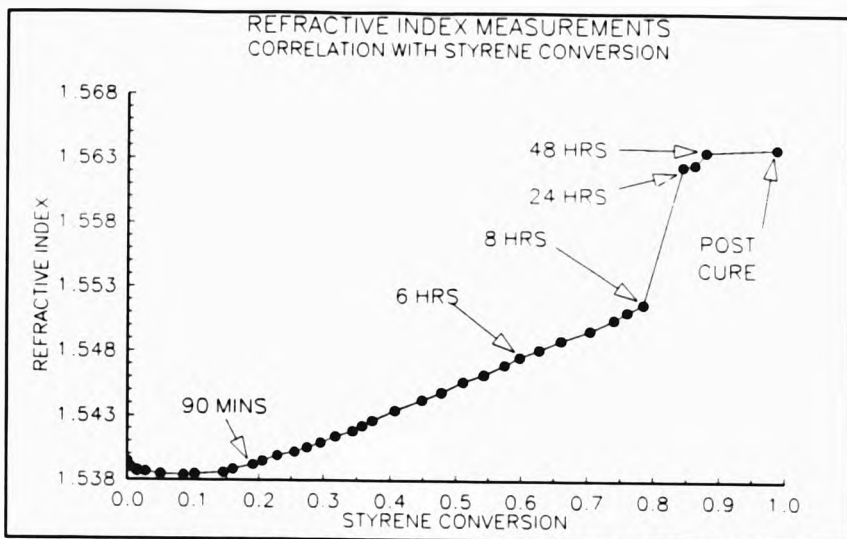


Figure 3.26 Correlation between refractive index and styrene conversion during the cure of polyester resin.

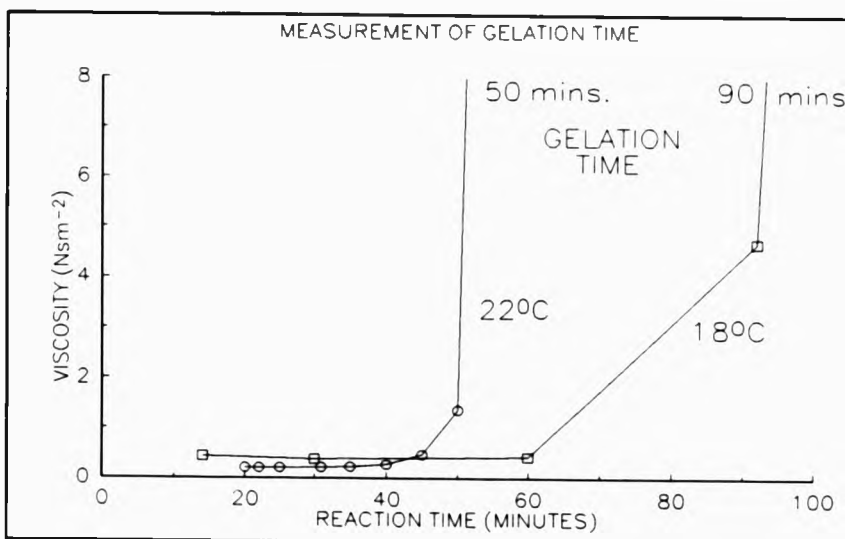


Figure 3.27 Gelation time measurements for polyester resin at 18°C and 22°.

spheres, of radius, r , which were dropped periodically into the curing resin. The viscosity, η , can be calculated [77] from,

$$\eta = \frac{2}{9} \frac{(\rho - \sigma) r^2 g}{v}, \quad (3.13)$$

where, ρ is the density of the sphere, σ is the density of the resin and g is the acceleration due to gravity. This expression is valid provided that, $\nu r \ll \eta$, [77]. It was also assumed that $(\rho - \sigma)$ was constant during the reaction.

Viscosity measurements were taken at two ambient temperatures, at 18°C, corresponding to the temperature of the light scattering measurements, and at 22°C, corresponding to the FTIR study of the reaction kinetics. The results are shown in figure 3.27, where viscosity of the curing resin is plotted against cure time. A sharp increase in the viscosity and hence gelation is found after a cure time of 90 minutes for the 18°C measurements and 50 minutes for the 22°C measurements. This difference must be taken into account when correlating the light scattering results with the cure reaction kinetics.

3.7.7. Correlation with Light Scattering Measurements

Before a comparison can be made between the light scattering measurements and the FTIR measurements of the cure reaction kinetics, the reaction temperature of the two different sets of measurements must be taken into account. From the gelation time measurements, the reaction rate of the FTIR reaction kinetic samples is approximately 1.8 times faster than that for the light scattering samples. In the following discussion, all reaction times quoted refer to the light scattering experiment.

The light scattering measurements taken during the cure of the 'ultra clean' sample suggests that microstructure starts to form after 50 minutes into the cure reaction, and agrees with the induction period of 30 minutes found from the FTIR measurements. Before this time the inhibitor in the resin was neutralised. Two competing reactions, styrene-polyester crosslinking and styrene homopolymerization proceed after this time leading to an increase in the isotropic light scattering.



After 90 minutes, the resin gels with the polymerised polyester and styrene forming a 3-dimensional network throughout the sample. At this stage, only approximately 8% of the styrene and 15% of the polyester monomer has polymerised. After gelation, a sharp increase in the log-normal size distribution width parameter and microstructure content occurs. As the 3-D network matures, spatial segregation of the homopolymerized styrene and the crosslinked styrene-polyester network may account for this.

The polyester-styrene crosslinking and styrene homopolymerization reactions continue until after approximately 7 hours into the reaction. The width parameter then slowly increases to that found in the fully cured samples. This is associated with a decrease in the rate of the polyester crosslinking reactions, due to the reduced mobility of the polyester in the now dense network. The styrene reaction rate is less affected due to the smaller size of the styrene monomer. The 3-D network is fully defined and is identical to the fully cured resin once the polyester crosslinking reaction reaches completion, after 14 hours.

The styrene homopolymerization reaction continues (over several days), a post cure being required to ensure styrene completion. The long term light scattering observations, as shown in figure 3.19, is due to the free styrene within the resin network. (The refractive index of the curing resin was found to follow the styrene conversion, see section 3.7.5.). This will have the effect of increasing the relative refractive index contrast, between the styrene rich lower refractive index regions and the higher refractive index microstructure. As the amount of free styrene diminishes in time, the relative refractive index of the scatterers falls leading to a reduction in the scattered light intensity. From Mie theory, a relative refractive index reduction of 1.013 to 1.01 would account for the excess scattering behaviour.

3.8. Comparison Between the Microstructure in CT200 Epoxy and Unsaturated Polyester Resin

Before the characterization results for the two resin systems can be compared, it must be remembered that the choice for the inhomogeneity refractive index used in the

analysis of 1.01 is arbitrary. Changing the refractive index from 1.01 to 1.02 will reduce the fitted concentration parameter by a factor of 4, (from Mie theory). As the exact relative refractive index of the inhomogeneities is not known for either material, only orders of magnitude comparisons of the microstructure concentrations can be made. The width parameters however, can be directly compared.

The percentage volume occupied by inhomogeneities of sizes between 0.25 μ m and 1.3 μ m, i.e. those sizes considered in the calculation of the microstructure content, for typical and extreme cases for both the CT200 and polyester resins are given in table 3.8. For the CT200 samples, the percentage volume ranges over 2 orders of magnitude, while the polyester samples were found to range over a factor of 4. The 'ultra clean' resin preparation techniques were responsible for the large microstructure concentration variation in the CT200 samples. Microstructure in the 'ultra clean' CT200 preparation filtered without butanone has a percentage volume 5 times less than for the 'ultra clean' polyester samples and suggests that a more inhomogeneous cure reaction occurs for the polyester resin compared with CT200 resin. The 'as received' CT200 and polyester samples are found to have similar percentage volume of inhomogeneity.

TABLE 3.8 Percentage Volume Occupied by Inhomogeneities of Sizes Between 0.25 μ m and 1.3 μ m

RESIN	PREPARATION	PERCENTAGE VOLUME OF INHOMOGENEITIES BETWEEN 0.25 μ m AND 1.3 μ m
CT200	UC	(1.2 \pm 0.2) $\times 10^{-5}$
CT200	AR	(2.7 \pm 0.2) $\times 10^{-4}$
CT200	UC+B	(1.7 \pm 0.1) $\times 10^{-3}$
POLYESTER	UC	(5.1 \pm 0.6) $\times 10^{-5}$
POLYESTER	AR	(1.1 \pm 0.1) $\times 10^{-4}$
POLYESTER	AR	(2.3 \pm 0.2) $\times 10^{-4}$

Due to the log-normal size distribution, the main contribution to the percentage volume, is from the smaller sizes in the distribution (<0.25 μ m) which were not

considered in the calculation. Hence, care must be used when comparing these results with results from other studies.

3.9. Conclusions

Light scattering measurements and subsequent analysis has shown that microstructure exists in both resins under study and that a reliable quantitative characterization of the resin microstructure can be made. This technique was then used successfully to determine the origin of the observed microstructure. In both resin systems, the microstructure was found to be inhomogeneities having a log-normal size distribution with a modal diameter of $0.01\mu\text{m}$ and geometric mean standard deviations ranging from 0.7 to 1.0. This is in agreement with the type of structure observed by Stevens [21], using electron microscopy of CT200 and CY207 epoxy resin fracture surfaces. Due to the insensitivity of the angular dependence of light scattering with relative refractive index, it was not possible to accurately determine the actual value for the inhomogeneity relative refractive index and hence, the absolute concentration of microstructure. Instead, the relative refractive index was standardised in the analysis, having a value of 1.01. This makes comparison between different resin systems difficult, due to differences in their inhomogeneity relative refractive index. However, this will still allow samples made with one resin system to be ranked in terms of their microstructure content. It is also worth comparing the size distribution obtained for epoxy resin using light scattering with the size distribution obtained by Matyi and Uhlmann [42], for Epon 828 epoxy resin cured with triethylenetetramine, using small angle x-ray scattering.

This comparison is shown in table 3.9. Surprisingly, the absolute concentrations, which depend on the assumed values for the relative refractive index and electron density variation, are in good agreement.

The fully cured 'as received' CT200 epoxy resin samples were found to contain significant microstructure and all having similar concentrations. This microstructure was due primarily to microgel in the uncured 'as received' resin being frozen into the fully cured resin matrix. Microstructure concentration in the fully cured 'ultra clean'

TABLE 3.9 Inhomogeneity size distribution for Epoxy Resin Obtained Using Light Scattering and SAXS

INHOMOGENEITY RADIUS / μm	CONCENTRATION FROM LS / cm^3	CONCENTRATION FROM SAXS / cm^3
0.0075	-	4.6×10^{14}
0.01	1.25×10^{14}	-
0.025	-	3.5×10^{12}
0.05	5.0×10^{12}	6.5×10^{11}
0.15	8.0×10^{10}	5.2×10^{10}
0.4	1.2×10^9	1.2×10^9

CT200 epoxy resin samples, varied over two orders of magnitude. This is due to the filtration technique used, where homopolymerization of the filtered resin occurs leading to the formation of microgel as the butanone solvent was removed from the resin at 80°C. The concentration of microgel formed depends on the time and temperature of butanone removal. Hence, by controlling these factors, fully cured 'ultra clean' resins may be made, covering a large range of microstructure concentration. This will be useful for correlating microstructure concentration with the mechanical and electrical properties of this resin. 'Ultra clean' samples with the lowest microstructure, were prepared by filtration of the resin at 140°C without butanone. The log-normal size distributions for the 'ultra clean' and 'as received' samples are found to be similar. This suggests that butanone or a similar solvent, or perhaps a process which is prone to resin microgelation, may have been used during the manufacture of the resin. If this is the case then the microstructure present in different batches of 'as received' resin supplied by the manufacturer, may also vary by a similar amount. This may have important consequences for industry where large quantities are used, as the amount of microstructure in the material may influence its mechanical and electrical properties.

Significant microstructure was also found in the fully cured polyester samples. The 'ultra clean' samples were found to have the lowest microstructure concentration. Measurements of the light scattering, and reaction kinetics using FTIR techniques has

shown that this microstructure forms as a result of a complex inhomogeneous cure reaction. Microstructure forms due to the competitive polyester-styrene crosslinking and styrene homopolymerization reactions. The 'as received' polyester samples were found to have significant additional microstructure compared with the 'ultra clean' samples. This is due to microgel, present in the uncured 'as received' resin, being frozen in to the fully cured network and will vary from batch to batch. The microgel forms due to styrene homopolymerization during storage of the resin.

Chapter 4

Material Characterization - Residual Internal Mechanical Stress using Optical Birefringence

4.1. Introduction

There have been many investigations during the last twenty years of the electrical breakdown in synthetic polymer resin insulators and that mechanical stresses in the resin can markedly influence the breakdown characteristics. For example, Schirr [12] has shown for epoxy resin samples that a reduction of 40% in the electrical tree initiation voltage occurs when subjected to a 20 MN/m² tensile stress, and a 16% reduction occurs for a 60 MN/m² compressive stress. He acknowledges that when using the pin-plane electrode geometry to produce enhanced electric fields, a large residual internal mechanical stress (RIMS) develops during sample preparation due to resin shrinkage during cure and subsequent cooling to room temperature. Nakanishi et al [78] have qualitatively reported the effect of RIMS in the epoxy CT200 (Ciba-Geigy) on tree initiation voltage, being unable to quantify the magnitudes of the stress distribution. They conclude that micro-cracks caused by the high stresses in the pin-tip region lead to premature tree initiation.

More recently Campoccia and Schifani [79] reported the strong effect of the RIMS in the epoxy resin system CY225 (Ciba-Geigy) on the time to electrical breakdown. Qualitatively reducing the RIMS by heating the sample close to the glass transition temperature, increases the median time to breakdown by a factor of two. Billing and Groves [80] have stated that for cable quality polyethylene, a 20% decrease in tree initiation voltage occurs when bending a sample to induce a 33 MN/m² tensile stress, and the initiation time in general is approximately proportional to the applied mechanical stress. They recognise the results only serve as a guide due to the simple analysis used of a complex stress distribution. Densley [81] has also stated that in XLPE cable insulation, increasing the mechanical tensile strain to 30% reduces the time to breakdown by as much as two orders of magnitude.

Arbab and Auckland [82] have examined the influence of mechanical stress on tree growth using polyester resin bars with embedded electrodes. They state that for a bending stress of 34 MN/m^2 , tree initiation times are reduced by 60%, whilst the tree growth rate increases five-fold. Auckland et al [83] find that the polyester resin insulation contains some RIMS due to differential cooling during sample manufacture. They have also qualitatively used coloured isochromatics produced by a circular polariscope to describe the changes in the internal stress due to vibrational electrostatic forces.

Shibuya [2] attempted to quantify the RIMS by proposing a fictive force model (see below), but found that for the CT200 epoxy resin in which a large RIMS occurs, the maximum mechanical stress at the pin-tip unreconcilably exceeded the resin compressive strength by a factor of four. His work highlights the problems associated with photoelastic stress analysis. Firstly, quantitative analysis of a three dimensional stress distribution is difficult as the measured optical phase retardation is the integral value along the light path, and can only be simply related to the integral of the difference in the principal stress perpendicular to the light path [84]. To fully quantify a three dimensional stress distribution, further experiments such as observing the light scattering envelope along the light path [85], are required. Secondly, using a plane/circular polariscope to produce isoclinic/isochromatic fringes, does not enable the absolute value of the fringe order to be determined unless a zero order fringe occurs within the sample. It was this latter fact that introduced the unreconcilable magnitudes of the maximum stresses found by Shibuya [2].

The aim of this section of work was to determine a method by which the magnitude and distribution of the RIMS within the pin-plane region of cast transparent synthetic resins containing a test electrode may be quantified. With this, the effect of age of the material λ ^{on the RIMS} can be assessed and may be important for long term electrical tests, if the RIMS changes appreciably with time. Then to extend this method to monitor the *additional* contribution of externally applied mechanical stress. This will then enable a *full* quantitative assessment of the effect of mechanical stress on electrical tree initiation and growth to be undertaken for the first time.

4.2 Theory

As stated above, detailed analysis of a three dimensional stress distribution from photoelastic observations is in general not possible as the observed optical retardation (and hence birefringence) is the integral value over the light path through the sample. However the symmetry of the slab samples used produces a principal axes of RIMS (and birefringence) along the pin axis in the pin-plane region. Hence along this axis (z) the integrated birefringence $\int (n_x - n_y) \cdot dL$ may be directly related to the integrated principal stress difference $\int (\sigma_x - \sigma_y) \cdot dL$ via the stress optical (Brewster) constant. The axes designations are shown in figure 4.1. Conventionally, if $(\sigma_x - \sigma_y) > 0$ the material is in tension along the z axis and for $(\sigma_x - \sigma_y) < 0$ it is in compression. The magnitude and sign of the Brewster constant is a material function, with a positive value when $\sigma_x > \sigma_y$ and $n_x > n_y$.

In order to determine the stress distribution in the region of the pin-tip Shibuya [2] proposed a fictive force model having found that the RIMS distribution in the pin-plane sample geometry is cylindrically symmetric about the pin axis z . The model assumes a homogeneous stress distribution and that the set of forces in the material (compressional in the case of CT200) produce equal and opposite reaction forces single fictive force P , directed along the pin axis and acting from the surface of the embedded pin. These reaction forces are replaced by a acting at a distance z_p from the position of the pin-tip, as illustrated in figure 4.1. Analytic expressions for the components of stress in cylindrical coordinates σ_r, σ_θ and σ_z due to a force P in an infinite solid have been derived by Timoshenko and Goodier [86], i.e.,

$$\sigma_r = B [(1-2\nu) z (r^2+z^2)^{-3/2} - 3r^2 z (r^2+z^2)^{-5/2}] , \quad (4.1)$$

$$\sigma_\theta = B(1-2\nu) z (r^2+z^2)^{-3/2} , \quad (4.2)$$

$$\sigma_z = -B [(1-2\nu) z (r^2+z^2)^{-3/2} + 3z^3 (r^2+z^2)^{-5/2}] , \quad (4.3)$$

$$\tau_{rz} = -B [(1-2\nu) r (r^2+z^2)^{-3/2} + 3rz^2 (r^2+z^2)^{-5/2}] , \quad (4.4)$$

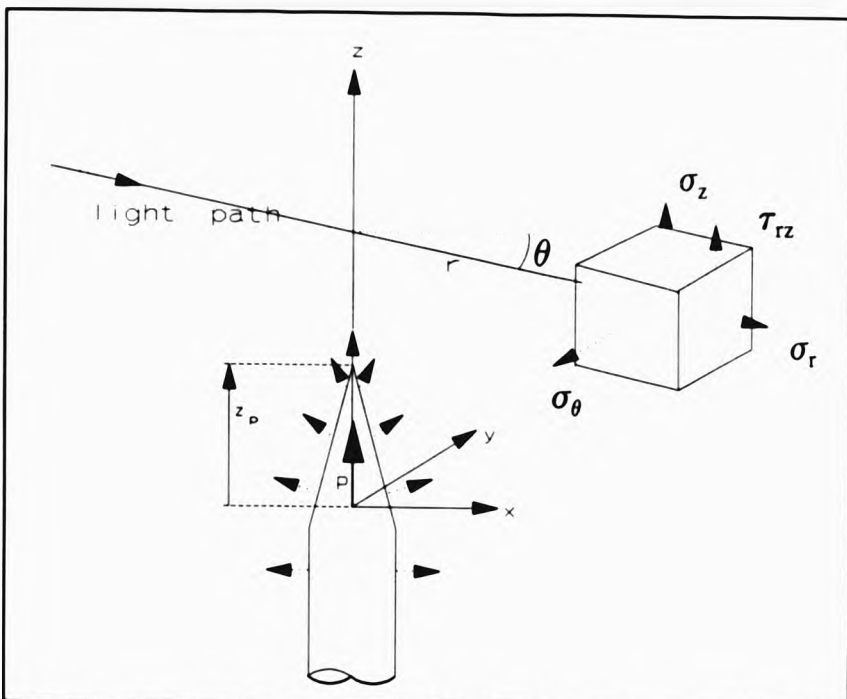


Figure 4.1. The Shibuya model fictive force P exerted by the embedded pin electrode, and the components of stress.

where each stress component is illustrated in figure 4.1, ν is the Poisson ratio and $B = P/8\pi(1-\nu)$.

Shibuya integrated these expressions over an optical path (the r axis) that passes through and perpendicular to the pin axis in the pin-plane space, i.e., the total optical retardation in terms of numbers of wavelengths (λ),

$$n\lambda = c \int_{-\infty}^{\infty} (\sigma_r - \sigma_\theta) \cdot dr. \quad (4.5)$$

He obtained the expression

$$z(n) = (CP/\pi\lambda) (1/n) - z_p, \quad (4.6)$$

where $z(n)$ is the axial position from the pin-tip of an optical retardation of n wavelengths, and C is the Brewster constant. The stresses at the pin-tip may be obtained by putting $r=0$ and $z=z_p$ in the above equations giving

$$\sigma_r = \sigma_\theta = -\sigma_z(1-2\nu)/2(2-\nu), \text{ and } \tau_{rz} = 0. \quad (4.7)$$

As $\nu \approx 0.35$ for the fully reacted epoxy resin CT200 [87] then $\sigma_r = -10\sigma_z$, and an estimate of the maximum mechanical stress $S(\max)$ at the position of the pin-tip and in the z -direction may be obtained from the expression

$$S(\max) = P(2-\nu)/(4\pi(1-\nu)z_p^2). \quad (4.8)$$

Using equation 4.6 a linear plot of $z(n)$ versus $1/n$ enables P and z_p to be determined and then using equation 4.8, $S(\max)$ can be obtained.

4.3. Experimental

4.3.1. Samples

Ogura steel pins of 1mm shank diameter and $5\mu\text{m}$ tip radius or laboratory produced etched tungsten pins of 0.4mm shank diameter and $0.1\mu\text{m}$ tip radius were embedded in three resin materials, CT200 and CY1311 epoxy and polyester, (see chapter 2 for the sample fabrication process), forming standard pin-plane specimens 5mm thick, 20mm high and 50mm long. The age of the samples is taken from the end of the whole cure process.

4.3.2. Experimental Arrangement

Initially and for the CT200 samples, an optical bench circular polariscope ^{was used as} shown in figure 4.2 (a), having a 16mm objective lens and magnification at the screen of X50. With a mercury arc lamp and Wratten 77a filter to isolate the mercury green line ($\lambda = 546 \text{ nm}$); this was used to produce the isochromatic fringe pattern of the RIMS. Photographic records of the fringe pattern were taken using a polaroid camera and

with a knowledge of the optical magnification, each of the fringe positions may be determined. This technique was found not to be suitable for the CY1311 epoxy and polyester resin samples as no fringe pattern is observed.

To measure the RIMS of samples with low internal stress or Brewster constant, where no isochromatic fringe pattern is observed, the sample was mounted on a precision traverse movable along the z axis with its position with respect to the pin-tip determinable to $\pm 1\mu\text{m}$. This is mounted in an X50 magnification optical bench polarising microscope with a 16mm objective lens and a X10 magnification Babinet compensator eyepiece, see figure 4.2(b), to measure the optical retardation, (see Longhurst [88] for a detailed description of the Babinet compensator and its use). This enabled long working distances, a magnification of X500 and small beam divergence through the sample to be achieved. An optical resolution of $2\mu\text{m}$ is obtainable, the limiting factor being essentially the optical quality of the sample. The Babinet compensator has a range of $\pm 4\lambda$ retardation at $\lambda = 546\text{nm}$ and a setting

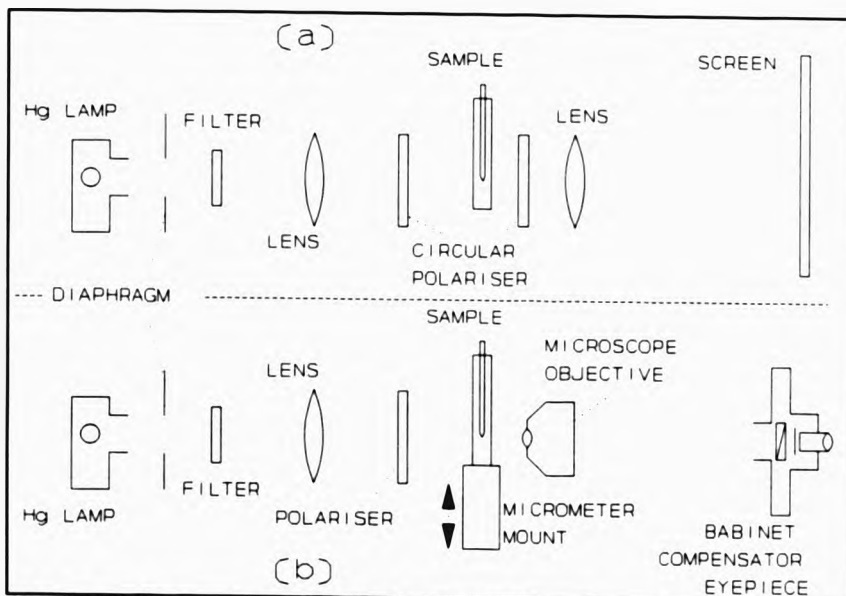


Figure 4.2. Experimental arrangement. (a) circular polariscope, (b) using Babinet compensator eyepiece.

reproducibility of better than ± 0.02 fringe. The ability of the Babinet compensator to measure both the sign and magnitude of the optical retardation, enables the sign of the stress to be determined once the sign of the Brewster constant for the material under test is known. Using fringe counting, retardations of up to $\pm 10\lambda$ may be measured. Hence, this method is also suitable for CT200 samples, providing the minimum retardation (usually at the sample edge) is 3λ or less. Retardations greater than this are difficult to measure due to mismatch of the optical dispersion of the sample material and the quartz wedges of the compensator, causing fringe jumping.

4.3.3. Application of an Applied Mechanical Stress

The external application of a mechanical stress to an already present RIMS must maintain a principal axis of stress along the pin axis direction if the stress distribution along this axis is to be determined. Preliminary tests have shown that a uniaxial tensional or compressional stress does not produce this condition, whilst an applied bending moment symmetric about the pin axis and in the plane of the sample does. Figure 4.3 shows schematically the arrangement, and with appropriate choice of the separation of the double supports, a known tensional or compressive stress distribution may be applied along the pin axis direction. The complete system could be traversed in the polarising microscope with the same precision as above. For symmetric bending of a beam with no embedded pin then, assuming the stress distribution is determined solely by the applied bending moment, it is easily shown (from beam bending theory [78,86]), that the optical retardation due to the added stress, $n - n_0$, (n_0 being the retardation with zero applied stress), is related to the applied load, F , by,

$$(n - n_0) = \frac{6CFgYd}{b^3\lambda}, \quad (4.9)$$

where, C is the Brewster constant, λ the wavelength of light used, d is distance measured from the central neutral axis of bending, and the remaining parameters defined in figure 4.3. Provision has been made for simultaneous mechanical and electrical stressing of samples as shown in figure 4.3.

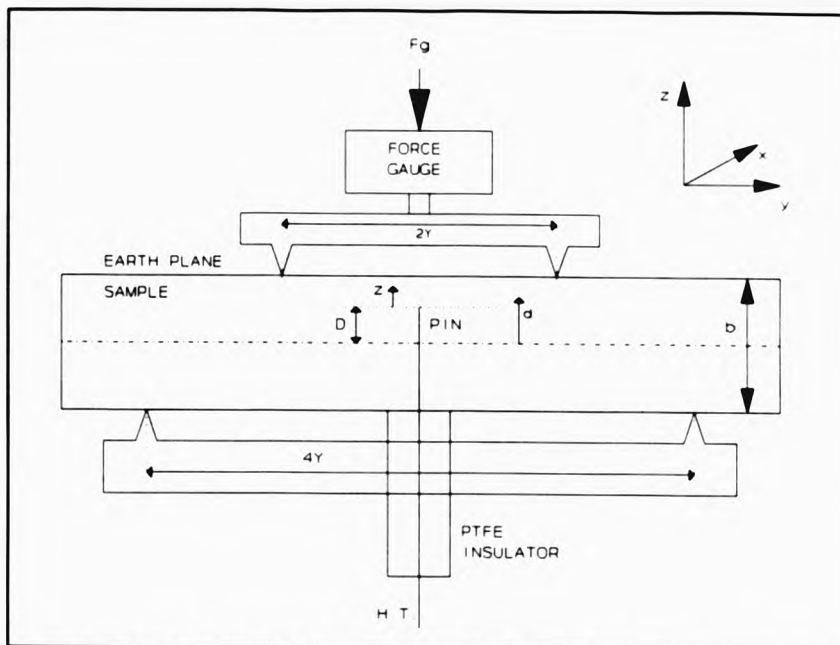


Figure 4.3. Application of mechanical stress.

4.4. System Appraisal - Brewster Constant Measurements

As the above analysis requires knowledge of the Brewster constant, C , for each of the materials, the polarising microscope and mechanical stressing system were used to measure the Brewster constant for a range of materials for which literature values are available as well as the resin materials used in this work. Both standard dogbone samples subjected to uniaxial tension or compression and bent beam samples were tested. A summary of the measured data is given in table 4.1.

From the literature, polystyrene [89] has a Brewster constant of $+9 \times 10^{-12} \text{m}^2/\text{N}$, PMMA [89] has a value of $-3.8 \times 10^{-12} \text{m}^2/\text{N}$ and CT200 [84] has a Brewster constant of $+56.1 \times 10^{-12} \text{m}^2/\text{N}$. Good agreement is therefore found between these and the measured values. It is also shown in table 4.1 that the

Table 4.1. Measurement of Brewster constant for a range of materials.

MATERIALS	METHOD	STRESS FORM	BREWSTER CONSTANT $m^2/N \times 10^{-12}$
Polystyrene	Dogbone	Tension	+8.7 +/- 0.2
PMMA	Dogbone	Tension	-3.9 +/- 0.2
CT200	Dogbone	Tension	+56.5 +/- 0.5
	Bending	Tension	+56.1 +/- 0.5
	Bending	Compression	+55.6 +/- 0.5
Polyester	Dogbone	Tension	+19.1 +/- 0.3
	Dogbone	Compression	-18.7 +/- 0.3
CY1311	Dogbone	Tension	+1880 +/- 50
	Dogbone	Compression	-2010 +/- 50
	Bending	Tension	+1960 +/- 60
	Bending	Compression	-1920 +/- 60

value of the Brewster constant shows good correspondence for the different methods used.

4.5. Results and Analysis

4.5.1. CT200 Epoxy Resin

The isochromatic fringes were found to very slowly collapse towards the embedded pin with time. A typical fringe distribution at a x13.5 magnification is shown in figure 4.4 for a 83 day old sample. This changing distribution may be characterised by measuring the distance $z(n)$ of the centres of the fringes from the pin-tip along the pin axis direction; the results are shown in figure 4.5. Two fringes very close to the pin-tip are not plotted for the sake of clarity. It can be seen after about 70 days that a new fringe appears at the plane surface, and after 320 days the fringes are still relaxing towards the pin. It was not possible to assign an absolute value to the fringe order as no zero-order fringe appeared.

The Shibuya model described above predicts a linear relationship between $z(n)$ and $1/n$ (equation 4.6). A set of such plots are shown in figures 4.6 and 4.7, where the fringe nearest the sample plane surface (the "border" fringe) is assumed to have



Figure 4.4. The isochromatic fringe distribution for a 83 days old sample.

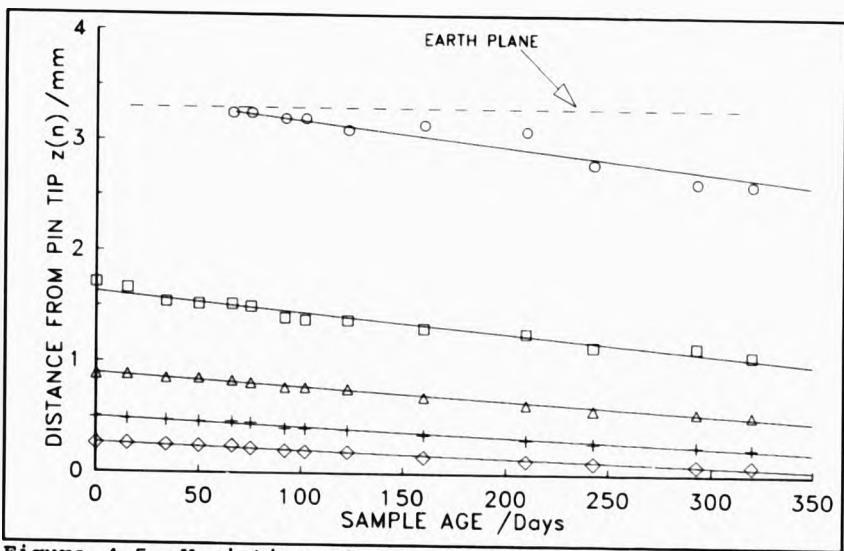


Figure 4.5. Variation of the position of the isochromatic fringes with time.

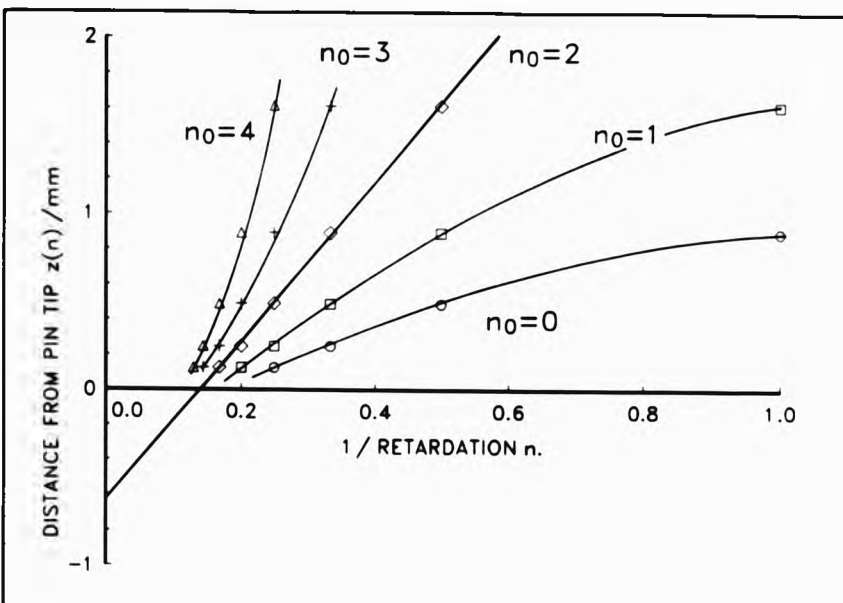


Figure 4.6. Shibuya model plot for different orders assigned to the boarder fringe. Sample age = 0 days.

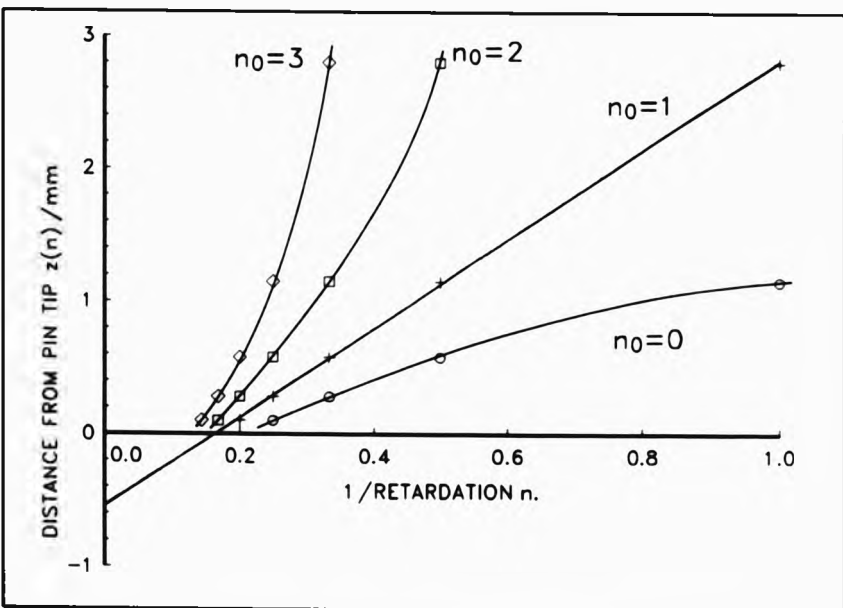


Figure 4.7. As figure 4.6 but with sample age=243 days.

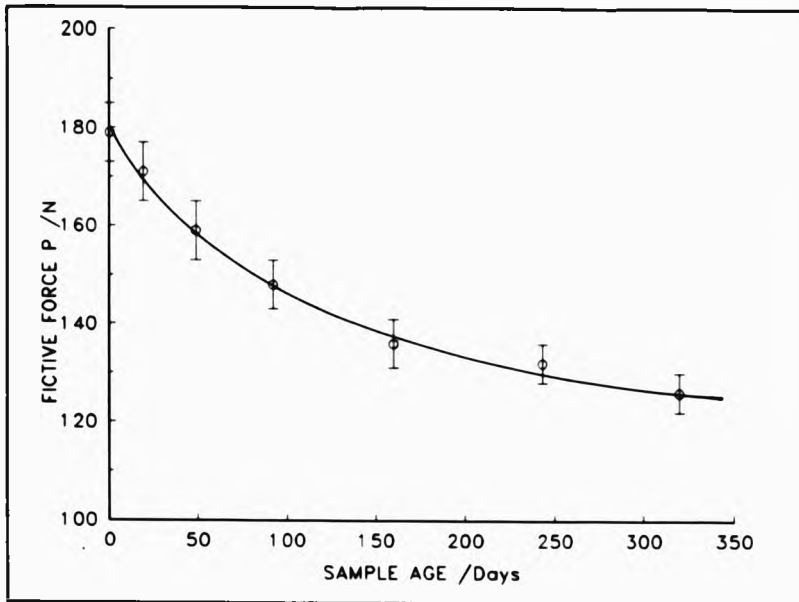


Figure 4.8. The variation of the fictive force P with time.

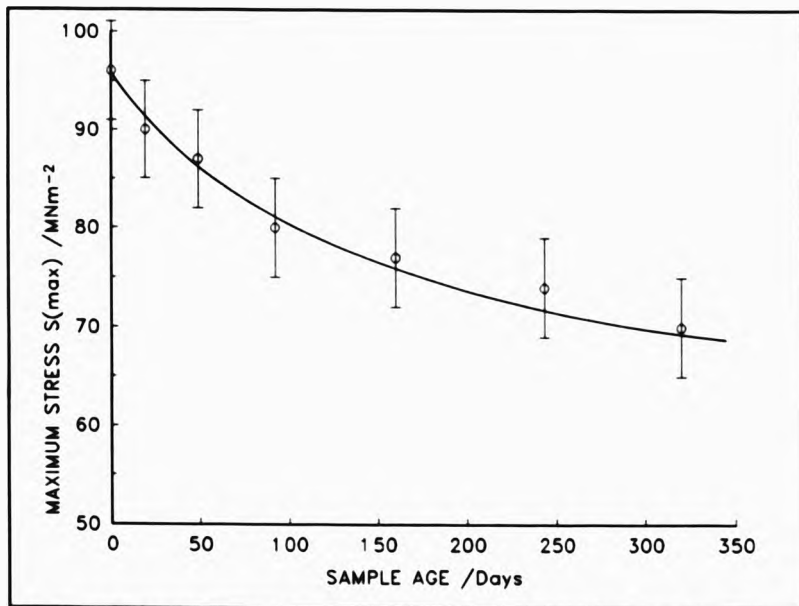


Figure 4.9. The variation of the maximum stress S(max) at the pin tip with time.

different values n_0 for its absolute order. In figure 4.6, for a sample of 0 days age, a linear plot occurs when the "border" fringe has an absolute order of $n_0 = 2$, whilst in figure 4.7 for a sample of age 243 days, linearity only occurs when $n_0 = 1$. This change in n_0 corresponds to the appearance of a new fringe after some 70 days. Thus it is concluded that varying the absolute fringe-order of the "border" fringe to obtain a linear fit to equation 4.6 is an appropriate method for determining the absolute fringe-order for the complete fringe set, and that the Shibuya model is applicable to our data.

The values of the fictive force P and the maximum stress at the pin-tip $S(\max)$ derived from Shibuya model plots, are shown as a function of sample age in figures 4.8 and 4.9 respectively, using a value for the Poisson ratio, $\nu=0.35$ [87]. The large error bars in figure 4.9 are due to the uncertainty in the extrapolation required to determine the negative intercept z_p .

Figure 4.9 shows that the CT200 resin initially has a large compressive stress at the pin-tip which approaches the compressive strength (125 MN/m^2 [2]) of the material which relaxes in time. Assuming that the changes in both P and $S(\max)$ may be simply described by a single exponential decay, they have time constants of 3 to 4 years. This corresponds well with the value of a 3 year stress relaxation time estimated from the data of Kong et al. [90] for essentially the same epoxy resin (EPON-828,Shell).

4.5.2. Unsaturated Polyester Resin

Figure 4.10 shows how $S(\max)$ changes with time for polyester resins with embedded Ogura pins, where $S(\max)$ is calculated from the slope and intercepts of the Shibuya model plots as described above and assuming the same value for the Poisson ratio, $\nu=0.35$. Points close to the plane surface (20% of the pin-plane spacing) were neglected as surface effects, possibly due to absorption of water vapour, are appreciable. However, linearity remains in the pin-tip region (80% of the pin-plane spacing), and after 300 days, the stress relaxes to a homogeneous distribution and linearity in the Shibuya plot is maintained across the whole of the pin-plane spacing.

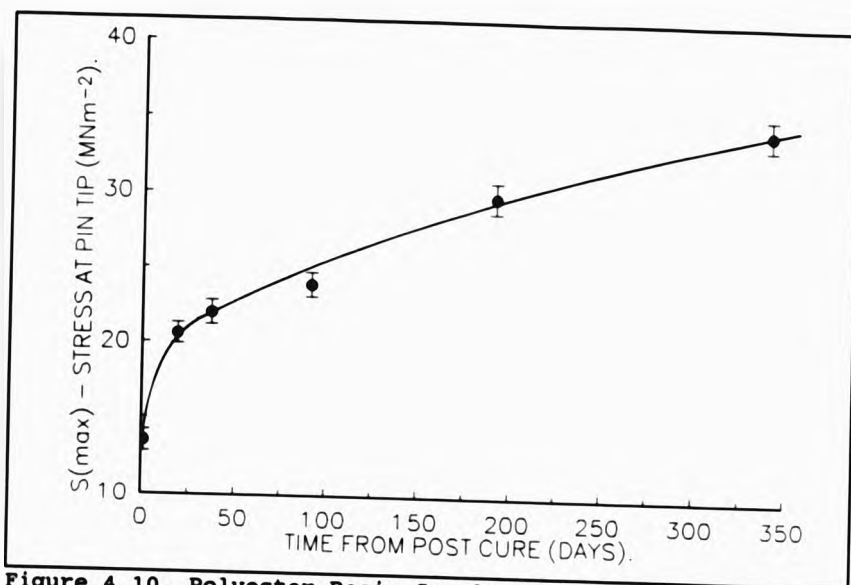


Figure 4.10. Polyester Resin Sample Ageing.

The maximum stress at the pin-tip is tensile and rapidly increases by 100% within 50 days of completion of post cure.

4.5.3. CY1311 Epoxy Resin

The RIMS changes significantly with the age of the sample. Initially the material is in compression in the pin-plane region and λ increases for some 25 days. The stress at the earth plane surface then starts to relax so that in a further 20 days the surface region is then in tension, producing a band of zero RIMS within the pin-plane region. The magnitude and extent of this tension increases with time moving the position of zero RIMS towards the pin, and at a total of some 100 days the whole of the pin-plane region is in tension. Vacuum desiccation of the sample for 7 days removes the surface region of tension returning it to a compressive state, with these changes being reproducible and reversible on multiple repeated cycling of the external conditions. This suggests that the original compressional RIMS is due to resin cure, and the long term change to tension is due to absorption of water vapour.



As the RIMS is dominated by the surface effects, the Shibuya model is not applicable. However, comparing the magnitude of the measured retardations in this resin, the RIMS is much less than that found in CT200 epoxy or polyester resin.

4.5.4. Sample Reconditioning

Reconditioning the resin samples, by repeating the post cure thermal procedures, drives the RIMS back to its original state found after the original post cure, irrespective of the sample age at reconditioning. This suggests that reversible structural relaxation (physical ageing) alone controls the change.

4.5.5. RIMS of Samples with Ogura Steel or Etched Tungsten Pins

Using etched tungsten pins of smaller shank diameter, rather than the larger shank diameter Ogura pins, reduces the RIMS in both resins by some 30% but showing the same characteristic behaviour in time. The probability of pin- tip/resin interface failure during manufacture is therefore less for the tungsten pins compared with using Ogura pins.

4.5.6. Applied Mechanical Stress

The external application of a mechanical stress to an already present RIMS should maintain a principle stress axis along the pin axis direction in the pin-plane region if the measured birefringence and mechanical stress are to be correlated. In practice, an additional homogenous stress distribution in the pin-plane region along the pin axis is required, even in the presence of an embedded pin. Tests have shown that an applied uniaxial tension or compression did not produce this condition, whilst an applied symmetrical bending moment does. Figure 4.3 shows the experimental arrangement used. By appropriate choice of the separation of the double supports, a tensional or compressional stress may be applied along the pin axis. The whole system could be moved in the polarising microscope along the pin axis direction with a precision of $5\mu\text{m}$ whilst both mechanical and electrical stresses are applied.



The mechanical stressing system was tested by applying a range of loads, F , to a CY1311 epoxy resin sample with embedded tungsten pin. At each value of the applied load, the optical retardation, n , was measured along the pin axis. Figure 4.11 shows the optical retardation as a function of distance z from the pin-tip, when a tensional stress is added to the wholly compressional RIMS of the sample.

Figure 4.12 illustrates the retardation due to the added stress ($n-n_0$), (n_0 , the retardation due to RIMS, i.e. when $F=0$), as a function of z . This shows that a homogenous stress distribution is induced into the pin-plane space except in the region close ($\sim 200\mu\text{m}$) to the pin-tip. Figure 4.13 shows a plot of the slopes of the lines in figure 4.12 versus the magnitude of the applied load F . The straight line obtained passes through the origin and suggests that the applied stress is additive to the original RIMS and can simply be described by symmetric beam bending. For symmetric bending of a beam with no embedded pin, then from equation 4.9,

$$(n - n_0) = \frac{6CFgY}{b^3\lambda} (z + D), \quad (4.10)$$

where D is the distance from the central neutral axis to the pin-tip and z is the distance from the pin-tip along the pin axis in the pin-plane space (see figure 4.3). The theoretical value for the slope of the line in figure 4.12 is therefore $6CgY/b^3\lambda$.

For the sample considered here, $b=1.8 \times 10^{-2}\text{m}$, $C=1.9 \times 10^{-9}\text{m}^2/\text{N}$, and with $Y=1.5 \times 10^7\text{N/m}^2$, gives a theoretical value for the slope of 0.54 ± 0.02 , compared with the measured value from figure 4.12, of 0.45 ± 0.02 . Hence, the tungsten pin of shank diameter 0.4mm modifies the applied stress distribution by only some 20%.

From the negative intercepts of the lines in figure 4.11 an average value of $D=6.1 \pm 0.5\text{mm}$ is obtained. With a pin-plane spacing of 2.4mm in this sample, the neutral axis of the bent beam appears to be centrally placed even in the presence of an embedded pin.

When a compressional stress is applied to a similar sample, an equivalent set of data and corresponding results are obtained. However, it was consistently found that when an Ogura pin of shank diameter 1.0mm was used, an essentially constant value of

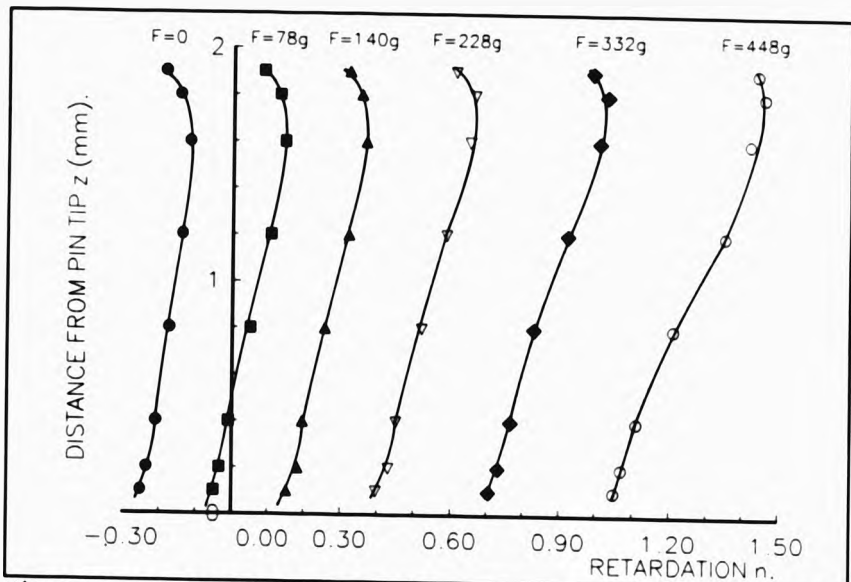


Figure 4.11. Measured retardation across the pin-plane region for different applied loads.

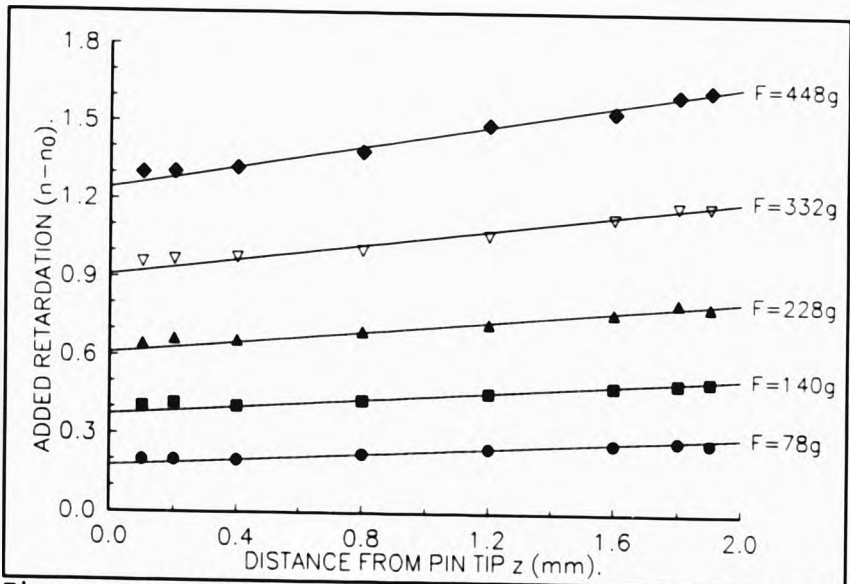


Figure 4.12. Additional retardation across pin-plane region for different applied loads.

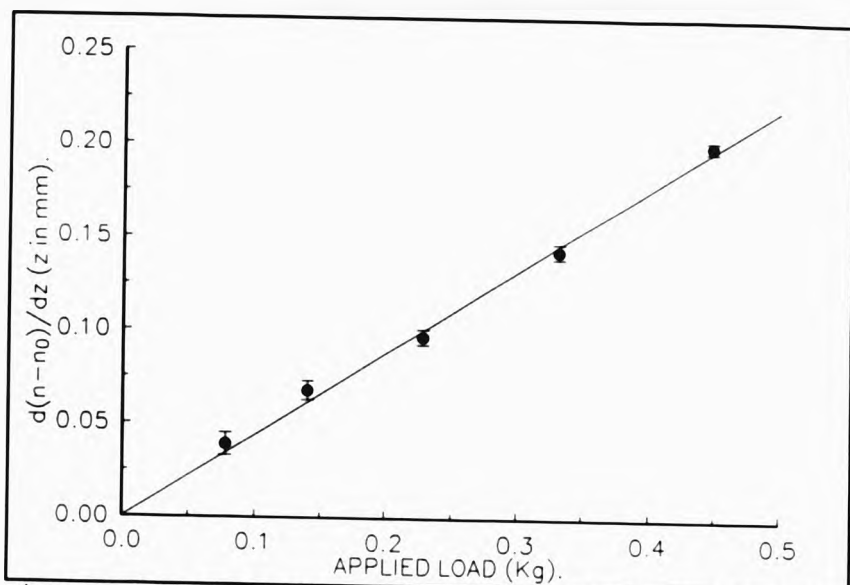


Figure 4.13. Retardation gradient across the pin-plane region for different values of the applied load.

$(n-n_0)$ occurs in the pin-plane region for a given applied load F , showing that the simple bending analysis and/or the additivity of the stresses is no longer applicable.

4.6. Discussion

A linear plot of $z(n)$ against $1/n$, see equation 4.6, extending from the pin-tip to the free surface substantiates the model of Shibuya [2], i.e. a homogeneous distribution of stress in a perfectly elastic material induced by a point force. Such behaviour exists in both the CT200 epoxy and polyester resin after some 300 days from postcure. Departure from linearity occurs in the region approaching the free surface for samples less than 300 days old and is due to an additional stress component that arises with the absorption of water vapour. This behaviour is most apparent in the CY1311 epoxy resin samples that have minimal RIMS. Vacuum desiccation of these samples returns the surface stress from tension back to its original compressive state. Careful examination of the data of Shibuya [2] for CT200 resin suggests that he assumed $n_0=1$ for the fringe nearest the sample plane. Replotting his data using $n_0=2$,



and the above values for ν and C , one obtains $S(\max) = 115 \text{ MN/m}^2$ instead of his value of 450 MN/m^2 , implying his observations were made on a sample less than 70 days old.

The CT200 resin has initially a large compressive stress at the pin-tip which approaches the compressive strength (125 MN/m^2 [2]) of the material. It is found in practise that nearly all CT200 samples containing Ogura pins had pin- tip/resin interface failure in the form of 2μ cracks, suggesting that local stress relief has occurred at the tip during the manufacturing process. Assuming the data can be represented by a single exponential decay, the relaxation has a time constant of some four years.

In the polyester resin the maximum stress at the pin-tip is tensile and rapidly increases by 100% within 50 days of completion of manufacture. Hence, large changes in RIMS is likely during electrical breakdown tests, particularly if the electrical stressing is of a similar time span. Also for short term electrical tests the age of the resin from postcure should also be taken into account. A very low percentage yield is found for the manufacture of pin-plane specimens with good pin-resin interfaces as pin-tip/resin interface failure has occurred by this time, probably due to the tensile nature of the RIMS, which is having the effect of pulling the resin from the pin-tip. For these reasons, the polyester resin is not ideally suited for electrical breakdown studies.

The flexible room temperature cured resin system, CY1311, has been examined as the RIMS is smaller than in either resin described above. This is due to bulk contraction of the resin during cure occurring whilst the resin is still in the liquid state, and no elevated temperature postcure introducing differential thermal contraction of the resin and pin. Hence embedding either Ogura or etched tungsten pins produce good quality pin-tip/resin interfaces suitable for electrical stressing experiments to study tree initiation and growth.

The symmetric bending technique described above can be used to induce homogeneous compressional or tensional stress distributions in embedded pin

samples. When the pin shank diameter is less than approximately 7% of the sample thickness, the total (RIMS plus added) integrated principle stress difference throughout the pin-plane space may be determined from optical birefringence measurements. For larger pin shank diameters, the residual and applied stresses are not simply additive.

4.7. Conclusions

The optical bench polarising microscope and Babinet compensator eyepiece have both the spatial and retardation resolution to allow detailed examination of the RIMS in pin-plane geometry samples that are used in electrical breakdown tests. The Shibuya fictive force model [2] provides an appropriate method of describing the magnitude of the mechanical stress that occurs at the pin-tip and its distribution in the pin-plane region. Additional externally applied mechanical stress (either tensional or compressional) can be applied using the symmetric beam bending technique. The total (RIMS plus applied) mechanical stress in the pin-plane region may then be quantified by analysis of the measured birefringence data provided that the pin shank diameter is less than 7% of the sample thickness. These techniques will enable a quantitative investigation of electrical tree initiation and growth to be undertaken for the first time.

The RIMS has a relaxation time of about four years in CT200 resin, whilst for polyester resin the RIMS increases by 100% after the first 50 days. These changes are associated with structural relaxation (physical ageing) of the materials. As this stress is known to influence the electrical breakdown characteristics of pin-plane test samples [12,78,79], its magnitude and time dependence should be taken into account in electrical breakdown studies.

Chapter 5

Quantitative Study of Light Emission During Electrical Tree Initiation and the Early Stages of Tree Growth

5.1. Introduction

Electrical treeing is a primary long term insulation failure process in which void formation at a region of high electrical stress enhancement (tree initiation) is followed by the growth of fine erosion channels due to partial discharge activity (tree growth). Little is known of the physical processes which lead to void formation. However, electrical field enhancement is likely to occur around material defects, conducting impurities or moulded-in metal inserts and this acts to drive defect formation. Much of the published data on electrical treeing breakdown uses the pin-plane geometry to model a simple conducting defect and to produce the high electrical fields necessary for quick tree initiation.

Light emission during treeing has been considered by several authors. Kojima et al. [91], studied polyethylene terephthalate using impulse voltages, Shibuya et al. [5], considered epoxy resin under 50Hz a.c. stress, Laurent et al. [92], examined polyethylene under 50Hz a.c. stress, Bamji et al. [3], considered it under 60Hz a.c. stress, and Baumann et al. [93] studied epoxy resin under both a.c. and impulse voltages. All have found that light is emitted from a region of high electrical stress at the pin-tip before the onset of partial discharge activity. This light emission is thought to be due to the injection of charge into the insulator material resulting in electroluminescence either by hot electron processes [5], or excitation of the host resin molecules [91], or charge carrier recombination [92]. In the case of a.c. voltage stressing, a phase relationship has been found between the emitted light and the stressing voltage [5,92,94] and has been used to distinguish between the emission due to partial discharges and that due to electroluminescence [5].

The characteristics of the electroluminescence on the applied stressing voltage has been used to postulate various mechanisms of initial failure of the insulator and to obtain a threshold or critical electrical stress for the initiation of breakdown. Space

charge formation and the mechanisms of electroluminescence and how these relate to failure are the subject of current debate in the literature. Hibma and Zeller [4], proposed a electro-fracture process for the initial failure, while Shibuya et al. [5], suggest that initial failure is caused by bond breakage due to hot electron bombardment of resin molecules. A more indirect process has been proposed by Bamji et al. [3], where UV electroluminescence is responsible for the initial failure via photo-degradation. The use of light emission data to obtain threshold stress values has been explored by some authors. Baumann et al. [93], determine threshold values by extrapolating to zero intensity the $\sqrt{\text{light intensity}}$ -voltage characteristic, whereas Bamji et al. [94], and Lebey et al. [95], determine thresholds by noting the voltage for the first appearance of light emission. In these latter cases, threshold values are likely to depend on the limit of detection (noise level) of the measurement system.

The aim of the work reported here was to quantitatively investigate the light emission during the initiation and early growth stages of electrical treeing in CT200 epoxy and unsaturated polyester resins in order to gain insight into the processes responsible for tree initiation and growth. Mains synchronous photon detection techniques were developed, comprising of an ultra sensitive photomultiplier and large light collection optics, was used to measure the low level light emission and its phase relationship with respect to the a.c. stressing voltage, from pin-plane samples subjected to 50Hz a.c. step ramp electrical stress. The data was also used to critically assess the field limited space charge (FLSC) model of Hibma and Zeller [1], as well as the Schottky and Fowler-Nordheim charge injection mechanisms. The existence or otherwise of threshold fields or voltages will also be addressed as these are often used in the determination of electrical breakdown statistics.

5.2. Experimental

Both CT200 and polyester resin were prepared with two levels of purity, 1) 'as received' 2) 'ultra clean', as described in chapter 2. Standard pin-plane samples were made by casting either Ogura steel pins or electrochemically etched tungsten of radii ranging from $0.08\mu\text{m}$ to $5\mu\text{m}$ (characterised using SEM) in resin slabs of size 50mm wide, 20mm high and 5mm thick, (see chapter 2). The pin-plane separation of all

samples was close to 3mm and to obtain an intimate plane contact, the bottom surface of the samples were coated with silver conductive paint.

5.2.1. Light Collection Optics

The light emission collection optics is shown in detail in figure 5.1. The pin-plane sample is clamped onto an earth plane inside a light tight metal box. Light emitted at the pin-tip is collected by a large diameter lens to maximise the light collection efficiency (gathering 5% of the total emitted light) and focused onto the photocathode of an ultra-sensitive photomultiplier tube (EMI 9789B). This photomultiplier was selected by the manufacturer for a low dark count of 1.2 photon counts per second.

5.2.2. Experimental Arrangement

A schematic of the mains synchronous photon counting system is shown in figure 5.2. The stressing voltage and synchronisation are both derived from the 240V 50Hz mains. A variac allows the EHT stressing voltage to be varied continuously from 0 to 15kV rms. The stressing voltage is monitored using a digital voltmeter and a 1000:1 probe and its waveform displayed on a Tektronix 468 digital storage oscilloscope via a 1000:1 potential divider. The stressing voltage is applied directly to the sample pin with no current limiting resistor.

A Nuclear Enterprises photon counter was used to amplify and threshold select the photon pulses from the photomultiplier using the fast discriminator. The internal counter and rate meter can be used to display the total count or rate of photons detected. The threshold selected photon pulses are also displayed on the second channel of the storage oscilloscope. With the oscilloscope set to envelope mode the phase distribution of the detected photon pulses can be built up in time.

The discriminator output is also connected to the mains synchronous photon counter (which will be described in detail in the next section). This consists of 4 separate counters each time gated to one of the 4 quadrants of the mains cycle as shown in

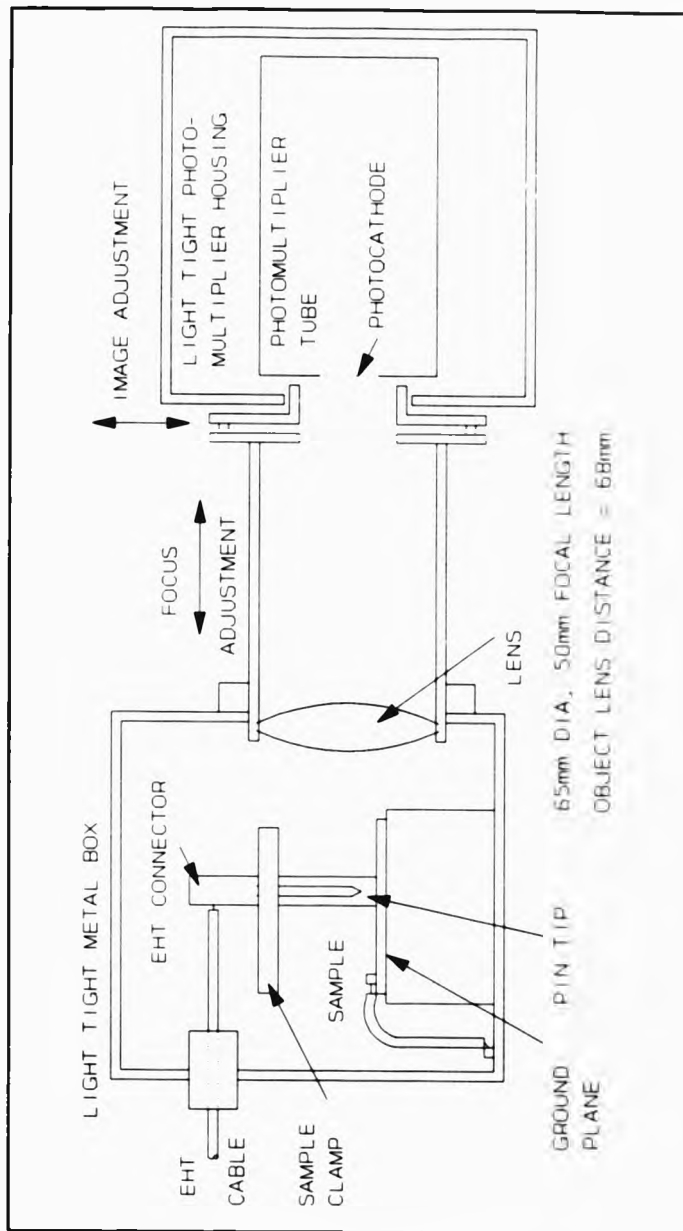


Figure 5.1. Light emission experimental arrangement.

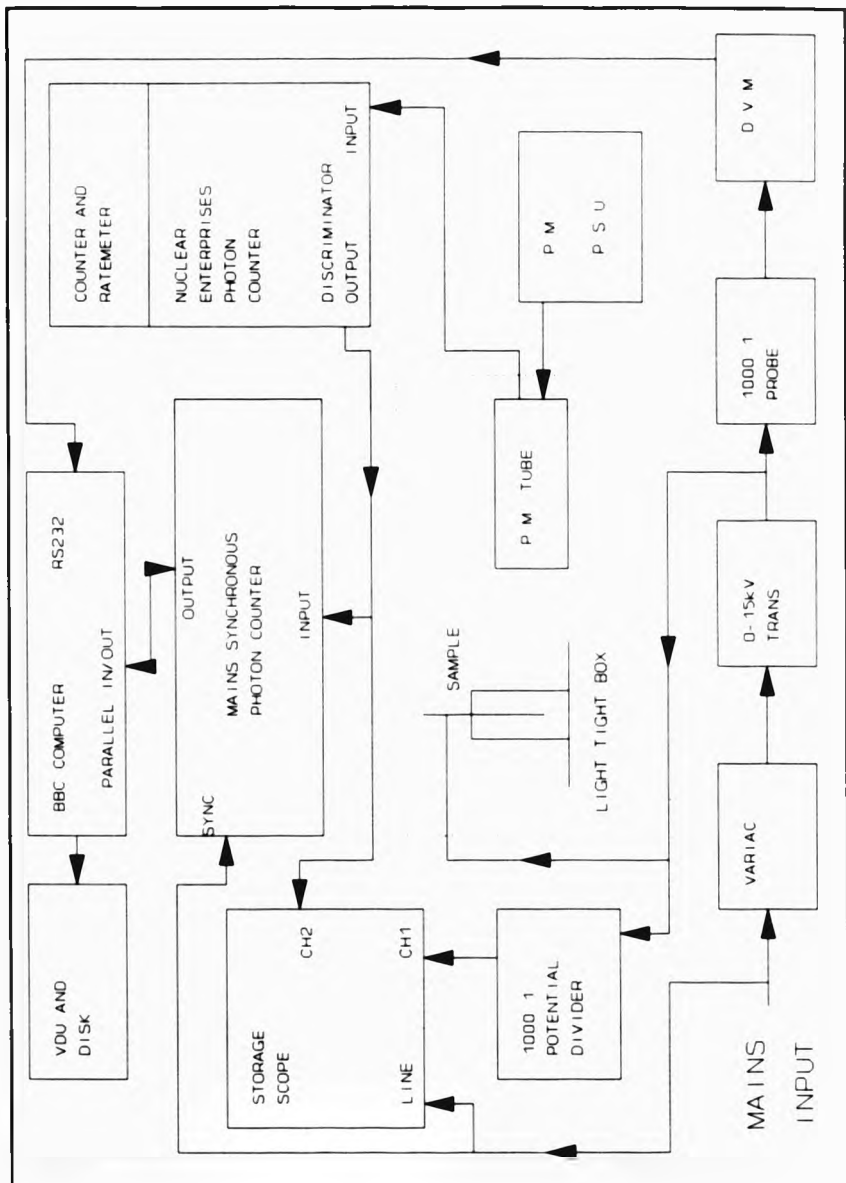


Figure 5.2. Experimental arrangement.

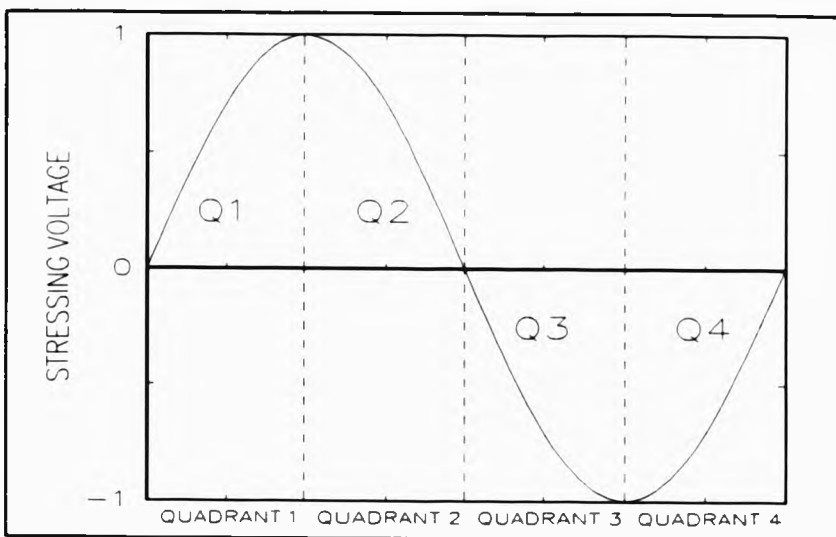


Figure 5.3. Light emission phase with respect to stressing voltage waveform.

figure 5.3. The synchronisation was derived from the mains supply. The count time (integration time) can be set within the range 1 second to 99 seconds and each counter can count up to a maximum of 1024 photons. A BBC model B microcomputer was used to control and read the four counters using a parallel data interface and to monitor the stressing voltage by reading the digital voltmeter display contents via a RS232 serial data link. The light emission measurements can be taken at intervals of 1 minute or more and at the end of each measurement the data is displayed on the computer screen and stored on floppy disk. Each data record uses 35 bytes of the available storage space on the floppy disk. An unused disk has a capacity of 200K bytes, and so if an 100 second measurement is taken every 2 minutes, then the system can record up to 12000 minutes (2 weeks) of light emission data without interruption. Hence, this system is suitable for both short term step ramp tests as well as long term stressing tests.

5.2.3. Mains Synchronous Photon Counter

In order to minimise development time a BBC model B microcomputer having good input/output facilities, was used to control the mains synchronous photon counter and to display and record the measured data. The BBC microcomputer is equipped with a parallel input/output port having 8 data lines, and two control bits, CB1 and CB2. CB2 was configured for output and the 8 data lines and CB1 for input.

A schematic of the mains synchronous counter is shown in figure 5.4. The synchronisation is derived from the 240V a.c. mains and is converted to a TTL logic signal. A zero phase detection circuit and the associated start/stop flip-flop ensures that photon counting commences and halts at the beginning of quadrant 1 (see figure 5.3). With the start/stop flip-flop in the start mode, the 50Hz synchronisation triggers the series of monostables M1 to M4 which generate the four time window signals corresponding to the four quadrants of the stressing cycle (see figure 5.3). These four window signals, time gate the discriminated photon pulses to four separate 12 bit binary counters. As only 8 data lines are available to communicate with the BBC microcomputer, the two least significant bits of the four counters were discarded and the next 8 bits used. Each counter can therefore count up to 1023 photons with an error of 4 photon counts. This error will be much less than the error associated with using photon counting techniques to measure the low intensity light emission.

The control circuit is based around a 5 stage Johnson counter. Successive pulsing of CB2, will switch one of its 10 output lines to logic high state in turn, ^{with} the remaining outputs in logic low states. These (up to 10) outputs are used to control the operation of the mains synchronous photon counter when instructed to by the BBC microcomputer. On switch on, the Johnson counter is initially reset such that the first of the 10 output lines is logic high and the rest low, the 'ready' state. In this state, the mains synchronous counter does nothing except illuminates a light emitting diode (on the front panel) and waits for a 'start' pulse on CB2. Once this happens, the second output line of the Johnson counter switches to logic high, triggering a monostable to reset all the counters and after a delay, longer than the reset pulse length, the start/stop flip-flop is set to start mode. Phase resolved photon pulses are

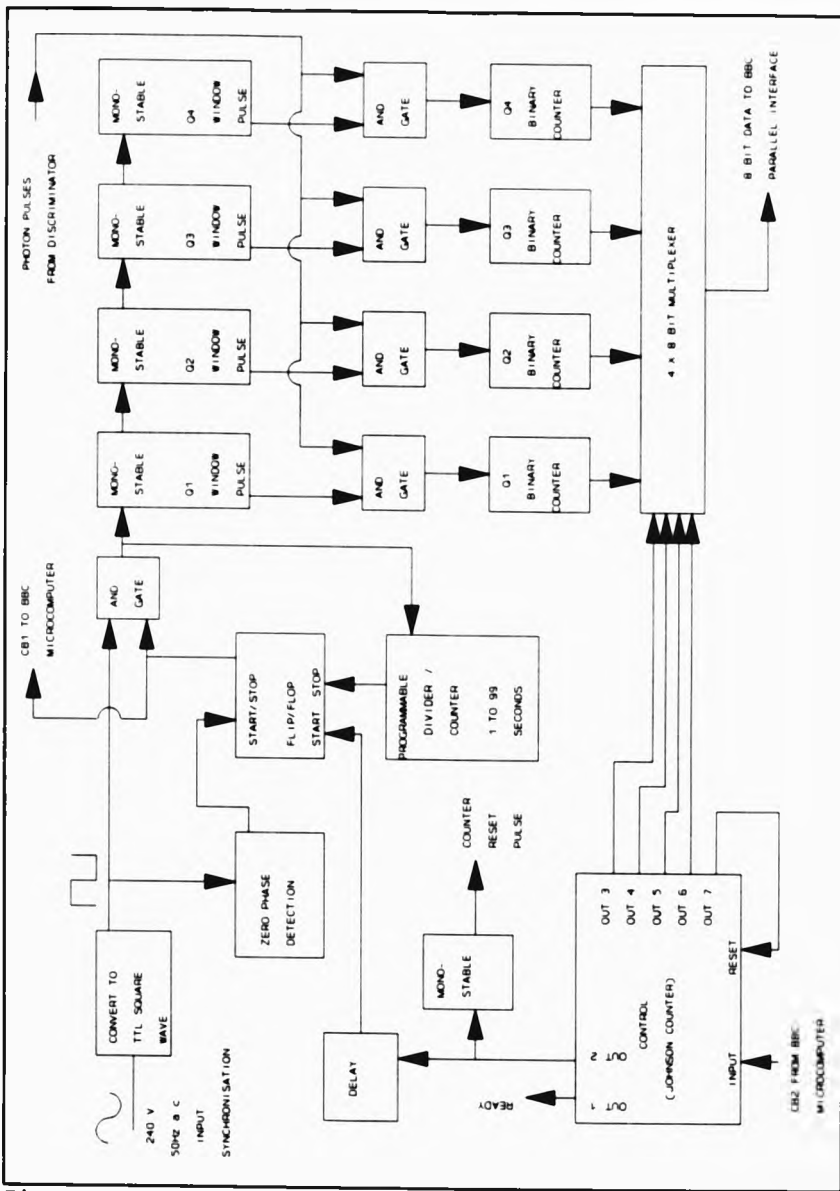


Figure 5.4. Mains synchronous photon counter.

then counted on the four quadrant counters. Simultaneously, the time gated synchronisation pulses are counted on a programmable counter until after a preset number of pulses, corresponding to a time interval between 1 and 99 seconds, a stop pulse is generated forcing the start/stop flip-flop into its stop state. This stop pulse is also used to signal the BBC microcomputer that photon counting has terminated (via CB1). Once the BBC microcomputer has received this pulse, it generates four further pulses on CB2, switching the third, fourth, fifth and sixth output lines of the Johnson counter, logic high in turn. These four lines control the 4 into 1, 8-bit multiplexer, presenting the contents of the four quadrant counters onto the 8-bit data bus in turn to be read by the BBC microcomputer. One further pulse on CB2, sets the seventh output line logic high, which forces the Johnson counter to reset, back into the ready state to await the next start pulse on CB2.

The mains synchronous photon counter was built from both TTL and CMOS logic gates. There is no reason why the system cannot be extended to include say 16 counters, to increase the phase resolution. However, 4 counters is sufficient to measure phase changes and any phase ambiguities can be removed by comparing with the phase distribution built up on the storage oscilloscope.

5.2.4. Detection System Performance

The detectability of the mains synchronous photon counting system depends on the light collection efficiency of the optics, the quantum efficiency and dark count of the photomultiplier and the absorption of light through the resin sample. Both the quantum efficiency and absorption are wavelength dependent. In the case of CT200 resin, the resin strongly absorbs below 400nm, and for the photomultiplier, the quantum efficiency of the photocathode falls below 2% above 600nm. Hence light will only be efficiently detected within this wavelength range. The spectral range of the light detection system is shown in figure 5.5 where the sample absorption and quantum efficiency has been combined and plotted against wavelength.

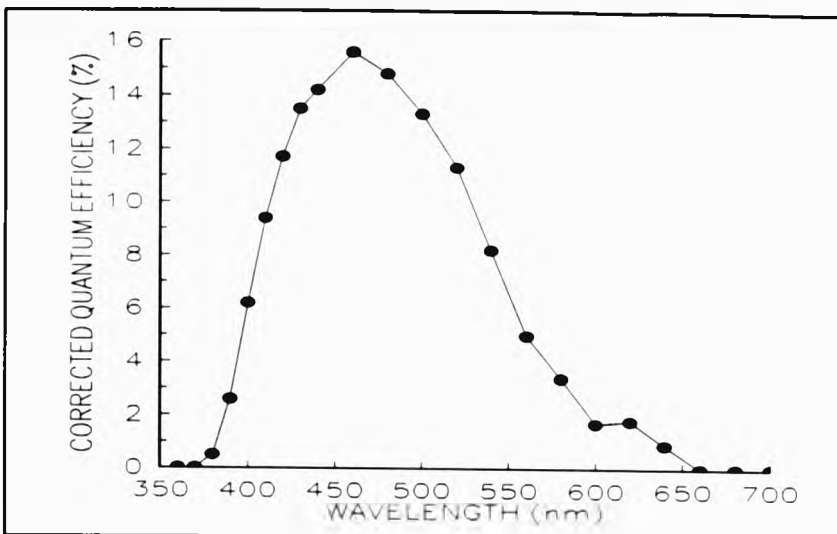


Figure 5.5. Spectral sensitivity of the light detection system.

The light collection efficiency of the optics i.e. the ratio of the solid angle of the lens aperture to 4π was calculated giving a value of 5%. Assuming the emitted photons have a wavelength of 460nm, (i.e. at the peak of figure 5.5), the overall photon detection efficiency is 0.8%. This corresponds to one photon being detected for every 125 photons emitted from the pin-tip. For other wavelengths, the detection efficiency will be less than 0.8%. The EMI 9789B photomultiplier has a dark count of 1.2 photon counts per second and so for a signal to noise ratio of 1:1, 150 photons will have to be emitted from the pin-tip region every second.

Before the mains synchronous photon counting system was used various tests were undertaken to ensure that,

- 1) the synchronisation remains in phase with the stressing voltage over the full range of stressing voltage 0-15kV rms,
- 2) no systematic mains correlation exists in the threshold detected photon pulses,

3) the dead time of the mains synchronous photon counter is not excessive and

4) that no spurious discharges occur from the high voltage electrodes and connections that could be detected on the photon counter.

5.3. Step Ramp Light Emission Results

Some twenty samples of CT200 epoxy and polyester resin with varying purity levels and embedded tungsten or Ogura pins were examined. The pin-tip radii ranged from $0.08\mu\text{m}$ to $5\mu\text{m}$. Each sample was subjected to a number of step-ramp stress tests until pin-tip/resin interface failure occurred or a large ($100\mu\text{m}$) electrical tree had grown. A standard step-ramp stressing test was used for all samples where the voltage was incremented by 300V rms every 6 minutes. The step length of 6 minutes was determined by the requirement of counting a sufficient number of photons to give a counting error of $\pm 5\%$. Within this time, 3 individual measurements of the light intensity are taken, each with a 99 second integration time. An example of light emission measured for a CT200 sample with pin-tip radius $0.2\mu\text{m}$ is shown in figure 5.6. The light emission in each of the 4 quadrant counters and the stressing voltage is plotted against time. The fluctuations in the light emission for stressing voltages less than 6kV rms , are within the statistical error associated with photon counting and therefore not significant. However for stressing voltages above 6kV rms , the fluctuations become significant and a rapid rise in the light emission intensity is observed.

Collation of the step-ramp data sets show that three distinct types of light emission response occur on increasing the applied voltage.

1) Type A, where a steady-state (independent of time over a period of three times the integration time of the photon counter) low level light emission was observed in the range 1 to 8 photon counts/sec at constant stress. Some 90% of the emitted light appears in quadrant 3 of the mains cycle and 10% in quadrant 1 as shown in figure 5.7(a).

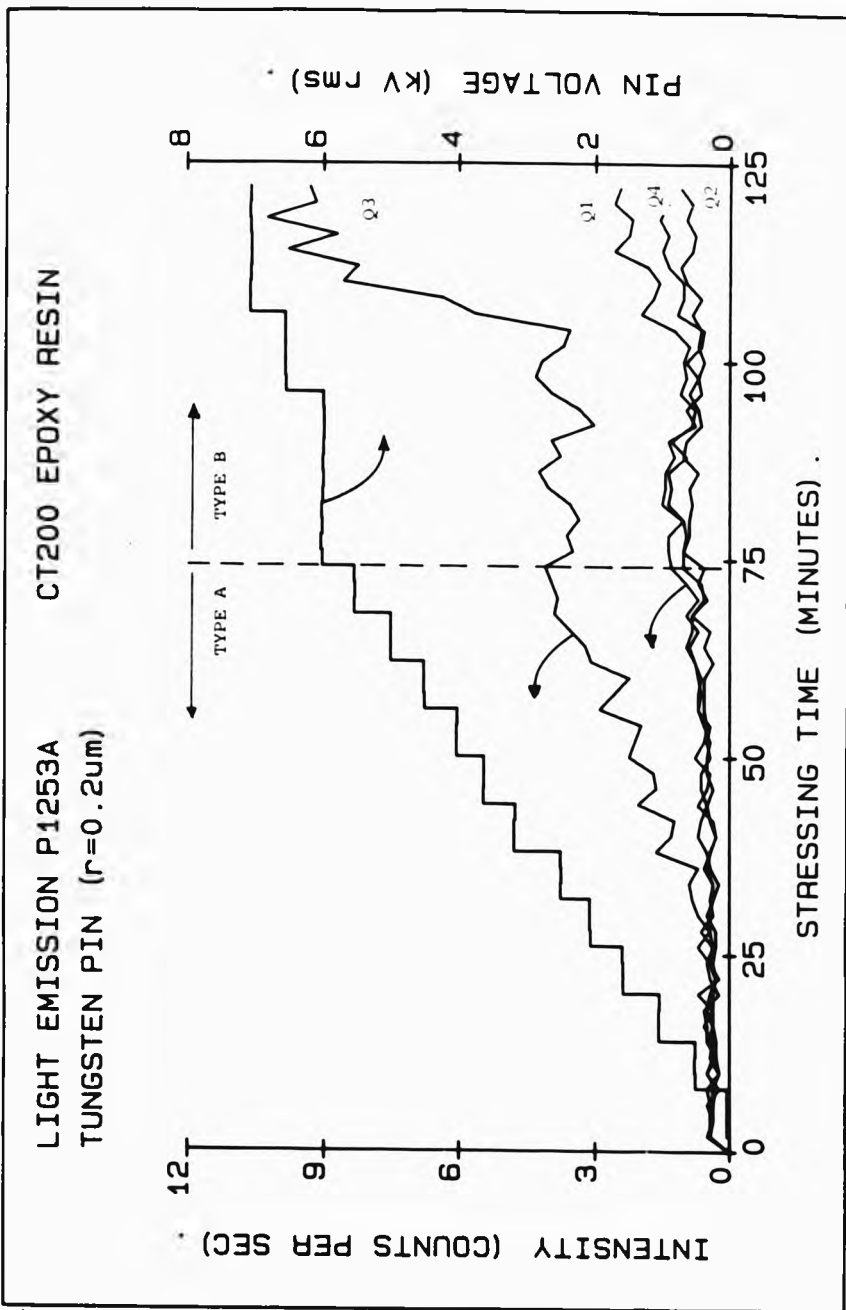
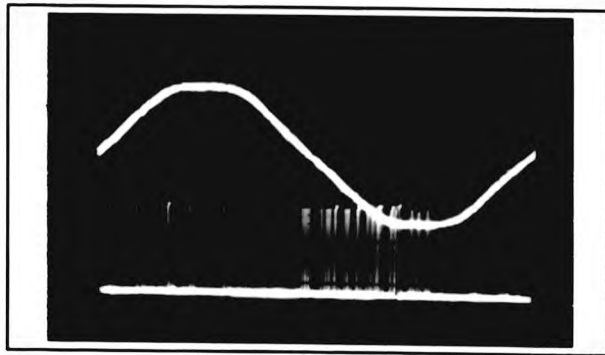
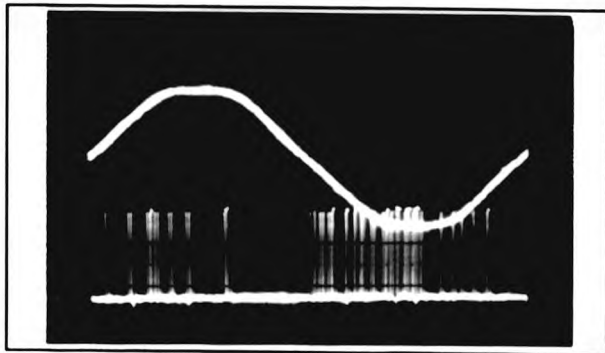


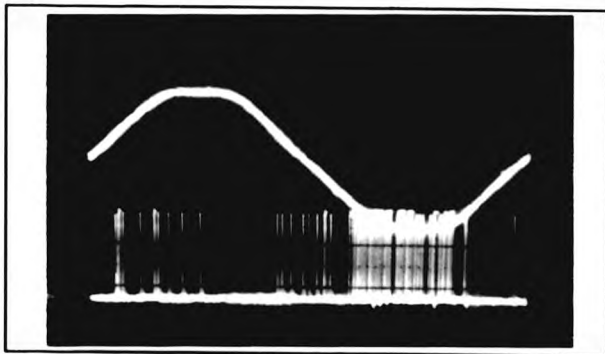
Figure 5.6. Step ramp light emission response.



(a)



(b)



(c)

Figure 5.7. Oscilloscope photographs showing the phase of the three types of light emission. (a) Type A, (b) Type B and (c) Type C.

2) Type B. The light emission fluctuates with time, decreasing after a initial surge. The measured intensity was generally in the range 10-20 photon counts/second with 70% in quadrant 3 and 30% in quadrant 1. (see figure 5.7(b)).

3) Type C. The light intensity is relatively large (> 25 photon counts/second), fluctuates rapidly with periods of quiescence and increases with time at constant stress. During this increase, a phase change occurs from the centre of quadrant 3 towards quadrant 4. (see figure 5.7(c)).

From optical microscopic examination of the pin-tip/resin interface, Type A emission is associated with initial charge injection with no observable microscopic defects (or obvious damage), Type B with the formation of micro-channels $2\text{-}5\mu\text{m}$ long and less than $1\mu\text{m}$ wide, and Type C with the existence of large channels greater than $10\mu\text{m}$ long, larger than $2\mu\text{m}$ wide.

For tungsten pins of radius ranging from $0.08\mu\text{m}$ to $0.25\mu\text{m}$, a small (spherical) bush-like failure always occurs first in BOTH resins, whilst for larger pins (both tungsten and Ogura steel) of radius ranging from $2.5\mu\text{m}$ to $5\mu\text{m}$, a $2\mu\text{m}$ crack or line failure always occurs first.

5.3.1. Type A Emission - Field Limiting Space Charge Model

Baumann et al. [93] claim to have shown experimentally that in an epoxy resin, using the pin-plane geometry and a ramped a.c. voltage (V) at 500Hz, the square root of the electroluminescent intensity (I), varies linearly with voltage. This is stated to be in agreement with the field limiting space charge (FLSC) model of Hibma and Zeller [1], (see appendix 7) with a threshold step increase in the carrier mobility when a material dependent critical (threshold) field is reached. Extrapolating to zero I on a \sqrt{I} versus V plot enables the threshold voltage to be determined. Typical plots of \sqrt{I} (having subtracted the dark count per second) are shown in Figure 5.8, for CT200 sample PJ159A and polyester sample RC1312C both with embedded tungsten pins. The data points at the highest voltages are in the region of Type B behaviour. Extrapolation of the straight line to zero intensity enables evaluation of the threshold

voltage, $V_{A,t}$. The best fit to the data is not always a linear relation at high or low stress as shown by the dotted line.

A summary of the values of $V_{A,t}$ obtained by extrapolation from the initial step ramp test for a series of samples is shown plotted against pin-tip radius in Figure 5.9. The corresponding threshold field, $E_{A,t}$, is shown in figure 5.10, with the electric field at the pin-tip, E , calculated from Mason's expression [96] assuming no space charge effects,

$$E = \frac{2 \cdot V}{r \cdot \ln(4d/r)} \quad (5.1)$$

where r is the pin-tip radius and d is the pin-plane separation. The abscissa is plotted as a log function merely to expand the data points along the axis. It is found that $V_{A,t}$ and $E_{A,t}$ depend only on the pin-tip radius and are independent of the type of resin, purity level of the resin and the type of pin used. For small pin-tip radii ($< 0.3 \mu\text{m}$), $V_{A,t}$ values are constant having a limiting value, $V_{A,t}$, of 1.1 ± 0.5 kV, whilst the

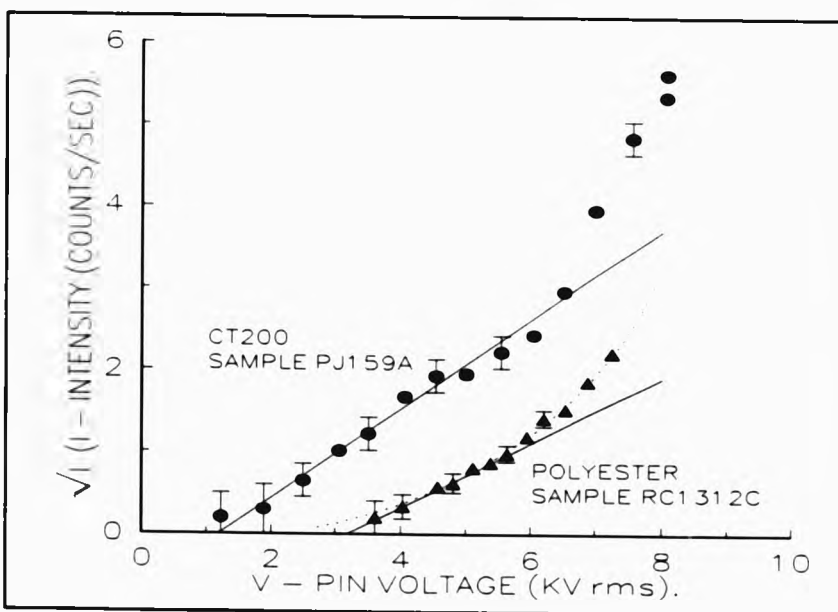


Figure 5.8. FLSC Plot.

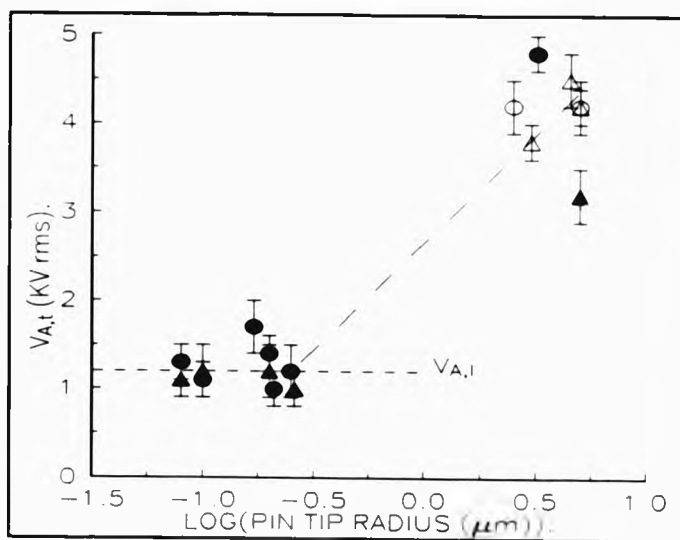


Figure 5.9. Type A threshold Voltages. Symbols, circles - CT200, triangles - polyester, filled - tungsten pin, empty - Ogura pin.

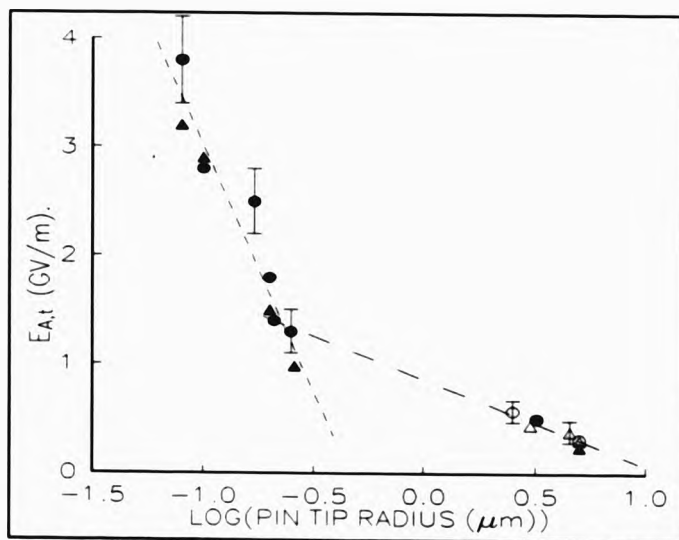


Figure 5.10. Type A threshold fields. Symbols, circles - CT200, triangles - polyester, filled - tungsten pin, empty - Ogura pin.

corresponding $E_{A,t}$ values depend strongly on pin-tip radius. Hibma and Zeller, [1], also found that for small pin-tip radii, less than $3\mu\text{m}$, considerably higher critical fields were obtained. They suggested two possible explanations for this,

- i) lack of active sites for charge injection and carrier multiplication by impact ionization.
- ii) due to the small distances involved, a critical distance for charge trapping of mobile charge carriers may be required.

Another possible explanation for this, is the space charge blunting effect [96], which limits the field enhancement at the pin-tip for small pin-tip radii. However, this would not be in agreement with the FLSC concept.

5.3.2. Type A Emission - Charge Carrier Injection Mechanisms

Assuming that the emitted light intensity I , (counts per second above noise) is directly proportional to the injection current and that the electric field, E_{max} , at the pin-tip is calculable from equation 1, then it is possible to assess alternative charge carrier injection mechanisms (Fowler-Nordheim and Schottky injection, as described in appendix 7).

1) Fowler-Nordheim (F-N) charge tunnelling injection is well documented [9,97] and the injection current - field relationship is,

$$I \propto E^2 \cdot \exp\left[-\frac{8\pi(2m^*)^{1/2}\phi^{3/2}}{3eh} \cdot \frac{1}{E}\right] \quad (5.2)$$

where m^* is the effective mass of the charge carrier and ϕ the interface barrier height [97]. Plotting $\ln(I/E^2)$ against $1/E$ should give a linear relationship from which ϕ , can be evaluated if a value for the carrier effective mass is assumed.

2) Schottky (thermionic) charge injection is also well documented [9,97], where the injection current - field relationship is

$$I = \exp\left[\frac{q}{kT} \sqrt{\frac{qE}{4\pi\epsilon_0\epsilon_r}}\right] \quad (5.3)$$

where ϵ_r is the relative dielectric permittivity, q the carrier charge. A plot of $\ln(I)$ is a linear function of \sqrt{E} , enabling ϵ_r to be evaluated [97].

Typical F-N and Schottky plots are shown in Figures 5.11 and 5.12 respectively. An assessment of such plots for a number of different specimens is given in table 5.1, together with the corresponding value of E when 1KV is applied to the pin. ϕ is calculated assuming that the carrier effective mass is equal to the mass of an electron.

It is found that Schottky plots appear to fit the data when E is less than 0.5 GV/m, and F-N plots when E is greater than 1.0 GV/m. It has been pointed out by O'Dwyer [97], that at very low temperatures there will be no thermionic emission (Schottky emission) over the potential barrier. At higher temperatures thermionic emission will dominate at low applied fields, whilst at very high fields, tunnelling emission (F-N) will dominate. The condition for this, found by Good and Muller [98], is

$$E > \phi^{1/2} T \quad (5.4)$$

with E in MV/m, ϕ in eV and T in deg.K. Assuming $\phi = 1\text{eV}$, then for F-N emission, $E > 0.3\text{GV/m}$, agreeing reasonably well to that found above experimentally.

It is worth noting that in the literature only two sets of data of light emission as a function of field have been examined analytically in terms of the injection mechanisms described above. Laurent et al. [92] using a pin-plane geometry with polyethylene showed that their data fitted F-N rather than Schottky emission. They did not evaluate ϕ , but their data gives a value of $\phi = 0.52\text{eV}$.

Kojima et al. [91], using $12\mu\text{m}$ PET films in a plane-plane geometry found that their data fitted a F-N plot but leads to a value of $\phi = 0.05\text{eV}$. However, according to the above thermionic emission criterion (equation 4), their data should be in the Schottky regime as their maximum field is of the order of 0.08GV/m .

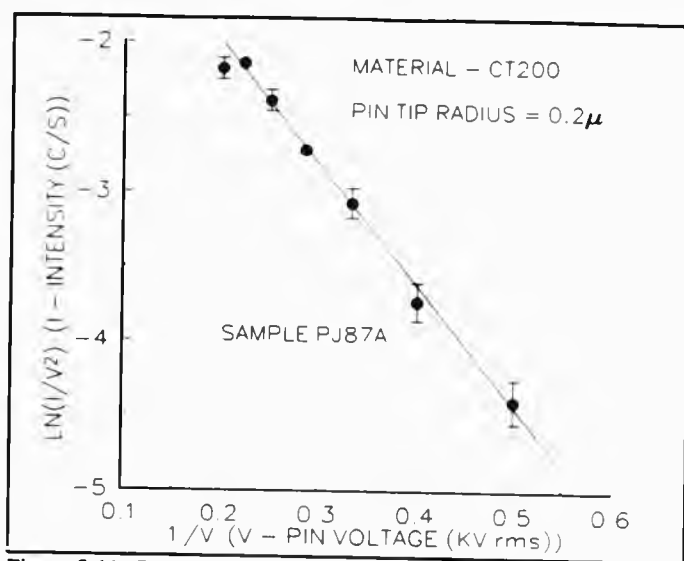


Figure 5.11. F-N Plot.

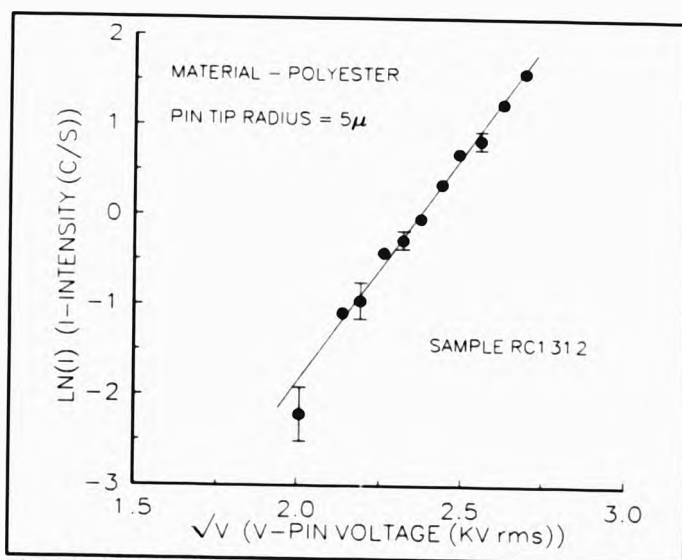


Figure 5.12. Schottky Plot.

Table 5.1. Charge injection mechanism results

Sample	Material	Pin Type	Pin Radius [μm]	F-N Plot ϕ [eV]	Schottky ϵ_r	E (at 1kV rms) [GV/m]
P1259	CT200	Tungsten	0.25	0.73	no fit	1.050
RC1312	Polyester	Tungsten	5.00	no fit	5.3	0.073
RC164	Polyester	Tungsten	0.08	1.30	no fit	2.940
P1253	CT200	Tungsten	0.21	0.63	no fit	1.270
P1256	CT200	Ogura	2.50	no fit	4.6	0.134
PJ159	CT200	Tungsten	0.08	1.50	no fit	2.940
PJ87A	CT200	Tungsten	0.20	1.28	no fit	1.270

5.3.3. Type B Emission

A value for the threshold voltage for Type B emission, $V_{B,1}$, may be obtained using the criteria of the sudden increase in the light emission during the stressing voltage step ramp and its subsequent decay, and associated change in the phase distribution.

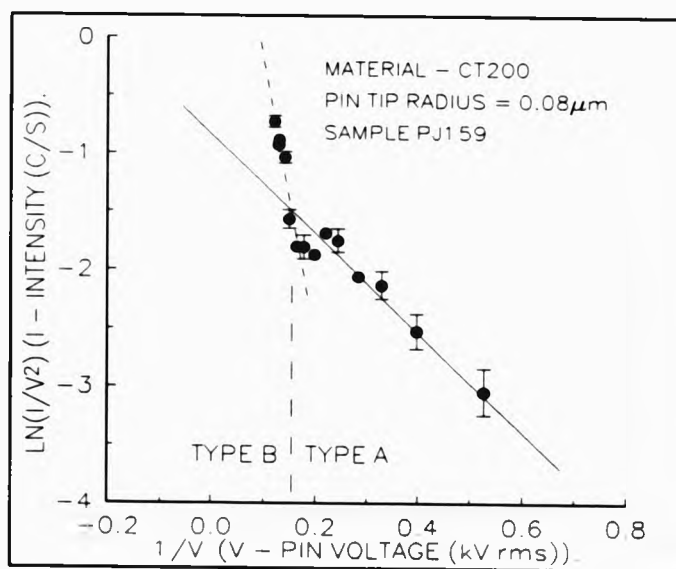


Figure 5.13. Determination of threshold voltage for Type B emission, $V_{B,1}$, from F-N plot.

Such a change in the light emission characteristics is shown in figure 5.6. This threshold voltage may alternatively be obtained from F-N, Schottky, or FLSC plots where a departure from linearity is observed above this threshold. An example is shown in figure 5.13, where departure from F-N behaviour is found at a voltage of 6kV rms.

Figure 5.14 shows the threshold voltage for Type B emission, $V_{B,1}$, plotted against pin-tip radius for all samples tested. The abscissa is plotted as a log function merely to expand the data points along the axis. $V_{B,1}$ is clearly a function of the resin type and in the case of the polyester samples, also the pin-tip radius. For small pin-tip radii ($<0.5\mu\text{m}$), Type B threshold values are $6\pm 1\text{KV}$ for CT200 and $2.5\pm 0.5\text{KV}$ rms for polyester resin. The corresponding values of $E_{B,1}$, the threshold field for Type B emission, calculated using equation 1, are shown in figure 5.15. Clearly, $E_{B,1}$ depends on material type and the pin-tip radius. The fact that for small pin-tip radii ($<0.3\mu\text{m}$), $V_{B,1}$ is constant and not $E_{B,1}$, (the same behaviour that was found for the $V_{A,1}$ and $E_{A,1}$ values), suggests that space charge blunting effects occur which limit the field enhancement for pin-tip radii less than $0.3\mu\text{m}$.

It is quite clear from the above results for Type A and Type B light emission that measurement of the critical field for charge injection (our $E_{A,1}$), does not describe a material dependent parameter for the onset of dielectric aging as proposed by Baumann et al. [93]. Instead, it is considered that their material dependent critical field can be associated with $E_{B,1}$, given the superior sensitivity of the light emission detection system used in this work. The large variation in the critical fields of supposedly identical samples, obtained by Hibma and Zeller [1], (their curious Type I and Type II samples) can be explained as due to the variable quality of the pin-tip resin interface.

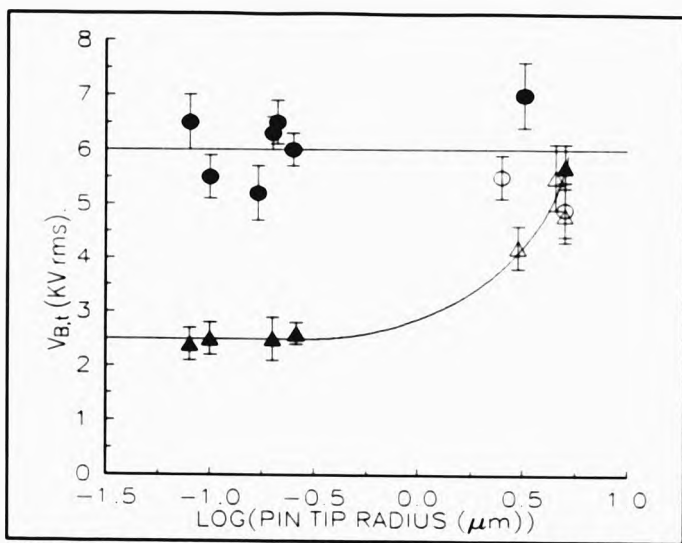


Figure 5.14. Type B Threshold Voltages. Symbols, circles - CT200, triangles - polyester, filled - tungsten pin, empty - Ogura pin.

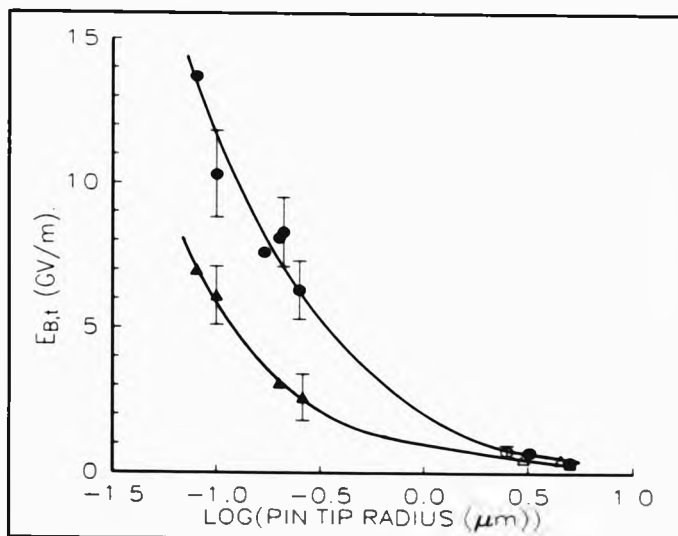


Figure 5.15. Type B threshold fields. Symbols, circles - CT200, triangles - polyester, filled - tungsten pin, empty - Ogura pin.

5.3.4. Type C Emission

Once a tree of size 10-20 μm is present, then a third form of light emission, Type C, is observed. The emission is relatively large > 30 photon counts per second and shows large fluctuations with short periods of quiescence and generally increases in time at constant a.c. voltage stress. Associated with this is a phase shift in the emitted light from quadrant 3 towards quadrant 4, shown in figure 5.7(c), such that the emission originally in quadrant 3 for Type A and B is nearly in phase with the stressing voltage waveform.

5.3.5. Discussion - Step Ramp Results

Due to the general poor understanding that currently exists and the paucity of good experimental data in the literature on light emission from solid polymers during charge injection and the early stages of electrical treeing, it is necessary to assess our results with some care.

The FLSC model of Hibma and Zeller [1] (see appendix 7) has been applied to both charge injection and light emission studies [93]. Their experimental results show that the FLSC model is only valid for pin-tip radii greater than 3 μm and for applied voltages between V_c and $2V_c$, where V_c is the material dependent critical voltage for charge injection. Assessment of our data using this model gives threshold voltages for Type A emission independent of the material type and only dependent on the pin-tip radius. However, the range of pin-tip radii used in our study vary from 0.1 μm to 5 μm .

Alternatively Schottky and F-N emission models (see appendix 7) may be used to interpret the Type A data. F-N behaviour is found to be closely followed at very high fields and Schottky behaviour at lower fields as predicted theoretically. Also, the values obtained for ϕ , the potential barrier height and ϵ_r , the relative dielectric permittivity, see table 5.1, are realistic. In both these models a material dependent threshold field is not required. It is worth noting that theoretical data derived from the F-N equation will give an approximate straight line (over the limited range of V_c

to $2V_c$) on a FLSC plot allowing an apparent threshold field to be obtained. Our high-field experimental data is in agreement with this, whilst it is possible to obtain a partial fit to the FLSC model, the F-N fit is much more convincing. The extrapolated value of $V_{A,0}$, obtained from the FLSC plots and the limiting value $V_{A,L}$, for small pin-tip radii, have no real physical significance. These are obtained by extrapolating to zero intensity, the limited region of linear behaviour on the FLSC plot, due to F-N or Schottky charge injection behaviour. These values are therefore not relatable to threshold voltages or fields for charge injection. However, the limiting value of $V_{A,0}$, for pin tip radii less than $0.3\mu\text{m}$, $V_{A,L}$, may be due to the space charge blunting effect mentioned earlier. Those sets of data found not to fit either F-N or FLSC model were found to follow the Schottky behaviour. However, it is for these data sets that the FLSC model should be applicable as they are obtained from samples with the larger pin-tip radii, greater than $2.5\mu\text{m}$. Hence, we are not convinced that there is any experimental evidence (from the work reported here and in the literature) for a material dependent threshold field/voltage for charge injection and subsequent light emission.

Careful examination of the voltage threshold data in the literature for the onset of what is called electroluminescence, shows that in all cases where the FLSC model is not used, the threshold is obtained by voltage ramping and determining the voltage at which light emission is first observed [94,95]. The noise level of the detection systems used vary from 10 to well over 50 counts per second with very limited collection optics. Hence it would appear that the threshold voltage is in practice determined by the signal detection sensitivity of the system used. This also seems to be true for threshold voltages determined from charge injection measurements. Thus it is not surprising that there is confusion in the literature [99] regarding the correlation (or otherwise) of threshold voltage/fields for charge injection and electroluminescence.

Recalling that the bulk of the data in the literature is for polyethylene, the recent work of Hozumi et al. [100], using transmission electron microscopy to examine initial tree growth is relevant. They find that the starting point of tree growth is a convex shaped defect of $0.01\mu\text{m}$ to $0.1\mu\text{m}$ in size, from which a channel of $0.1\mu\text{m}$



diameter grows. Constrictions with a period of $0.05\mu\text{m}$ to $0.1\mu\text{m}$ are also observed. These channels exhibit carbonization at their surfaces indicating exposure to high temperature and filamentary thermal breakdown. Their work suggests that initial tree growth is via micro-discharges in micro-channels whose size is well below the limit of observation by optical microscopy. Hence the view [3,94,95,99,101] that the light emitted, before the appearance of an optically visible tree, is purely electroluminescence is not well founded.

From the step-ramp tests, material dependent thresholds are found for Type B emission which is known to be associated with material damage in which the resulting defects are smaller than $5\mu\text{m}$ in extent. The behaviour of the threshold values with pin-tip radius suggests that space charge plays a significant role in the process of tree initiation. Precisely what role remains unclear, although from our results, it would seem to limit the field enhancement at the pin-tip for tip radii less than $0.3\mu\text{m}$. More knowledge of the charge transport processes and the relationship between the local field in the vicinity of the pin-tip and the applied voltage will be required to explain the transition from Type A to Type B behaviour.

It is possible that a material dependent threshold field exists for electron avalanches to occur within the resin leading to the formation of micro-channels and the occurrence of micro-discharges. Alternatively, Poole-Frenkel trap lowering may lead to a negative differential resistance region in the field-mobility relationship [1], once a material dependent critical field is exceeded. This could possibly change the injected charge characteristics from a radially symmetric space charge region to a pulsed filamentary case. The large current densities in these filaments may well contribute to the initiation of electrical trees [9] and a change in the light emission behaviour.

Once tree channels greater than approximately $10\mu\text{m}$ are formed, the characteristics of the light emission change and Type C emission is observed. The observed change in the phase of the emission with respect to the stressing voltage is probably influenced by the accumulation and the spatial distribution of charge within the tree channels.



It is also found that for a sample with a poor interface already present, in the form of a $3\mu\text{m}$ crack produced during resin cure, or on recycling the stress after the appearance of microchannels, or even when a large $100\mu\text{m}$ tree has grown, all three types (A,B and C) of emission can still be observed but over lower voltage ranges, as illustrated in table 5.2, for polyester sample RC11/1 and CT200 sample PJ87. The fact that the FLSC model criteria still gives discernable values for the critical field for charge injection, even though a large defect is present at the pin-tip, questions its usefulness as a technique to extrapolate material dependent parameters characterizing their resistance to electrical breakdown.

Table 5.2. Repeated stress cycling

SAMPLE/STRESS cycle NO.	$V_{A,i}$ (kV)	$V_{B,i}$ (kV)	$V_{C,i}$ (kV)	Form of Failure
RC11/1	4.2	4.8	5.5	none
RC11/3	3.2	3.5	5	$45\mu\text{m}$ tree
RC11/5	2.8	3	4	$90\mu\text{m}$ tree
RC11/7	2.4	2.6	3	$130\mu\text{m}$ tree
PJ87/1	1.4	6.3	-	none
PJ87/4	1.2	4.0	7.2	$80\mu\text{m}$ tree

5.4. Long Term Voltage Stressing Tests

Whilst step ramp a.c. tests are a quick method for determining electrical strength and predicting insulator lifetimes, they are not necessarily representative of insulator service conditions where the insulators are expected to withstand high electrical stress for some considerable time. Also the material dependent threshold fields (e.g. our $V_{B,i}$) obtained from these tests while useful, do not take into account any long term failure or degradation mechanisms which will be of obvious importance for the prediction of the service life of real insulation systems.

In order to understand more fully the physical processes governing tree initiation (Type A to Type B transition), a series of long term stressing experiments were undertaken.

5.4.1. Experimental

A series of CT200 pin-plane samples having pin-tip radii of around $0.1\mu\text{m}$ and pin-plane spacing of 3mm , were subjected to an initial step ramp voltage stress up to approximately 80% of the threshold voltage for Type B emission, $V_{B,t}$, found using figure 5.14 from the step ramp tests. The samples were then continuously stressed at this voltage and the light emission measured every two minutes with an integration time of 99 seconds. To see how stress interruption may affect the light emission behaviour, two of the samples were subjected to stress interruption times of 17 hours or 65 hours before stress continuation at the same voltage.

5.4.2. Light Emission Results

The light emission behaviour of four of the samples are shown in figures 5.16, 5.17, 5.18 and 5.19 for samples P134/2, P139/1, P139/3 and P140/2 respectively. Plotted is the pin voltage and light emission intensity in quadrants 1, 2 and 3 of the stressing cycle against time. Quadrant 4 intensity was not plotted for clarity but exhibits the same intensity and temporal behaviour as quadrant 2.

These results show that Type A to Type B transition does occur in time, when the samples are stressed below the Type B threshold field for Type B behaviour obtained from the short term step ramp tests.

The long term light emission behaviour of these samples share a number of common features. Firstly a Type A region where the electroluminescent intensity initially increases exponentially to a constant level. This increase is shown plotted in figure 5.20 along with the two other samples that were also stressed continuously (i.e. no stress interruption). The electroluminescent intensity rises for the three samples were normalised such that they can be directly compared. The function fitted was a single exponential function with a time constant of 5 hours. The similarity of the three plots suggest that this increase is an intrinsic property of CT200 resin. For sample P139/1, where the electrical stress was interrupted for 17 and 65 hours during the initial electroluminescent increase, the intensity was found to drop on re-establishment of

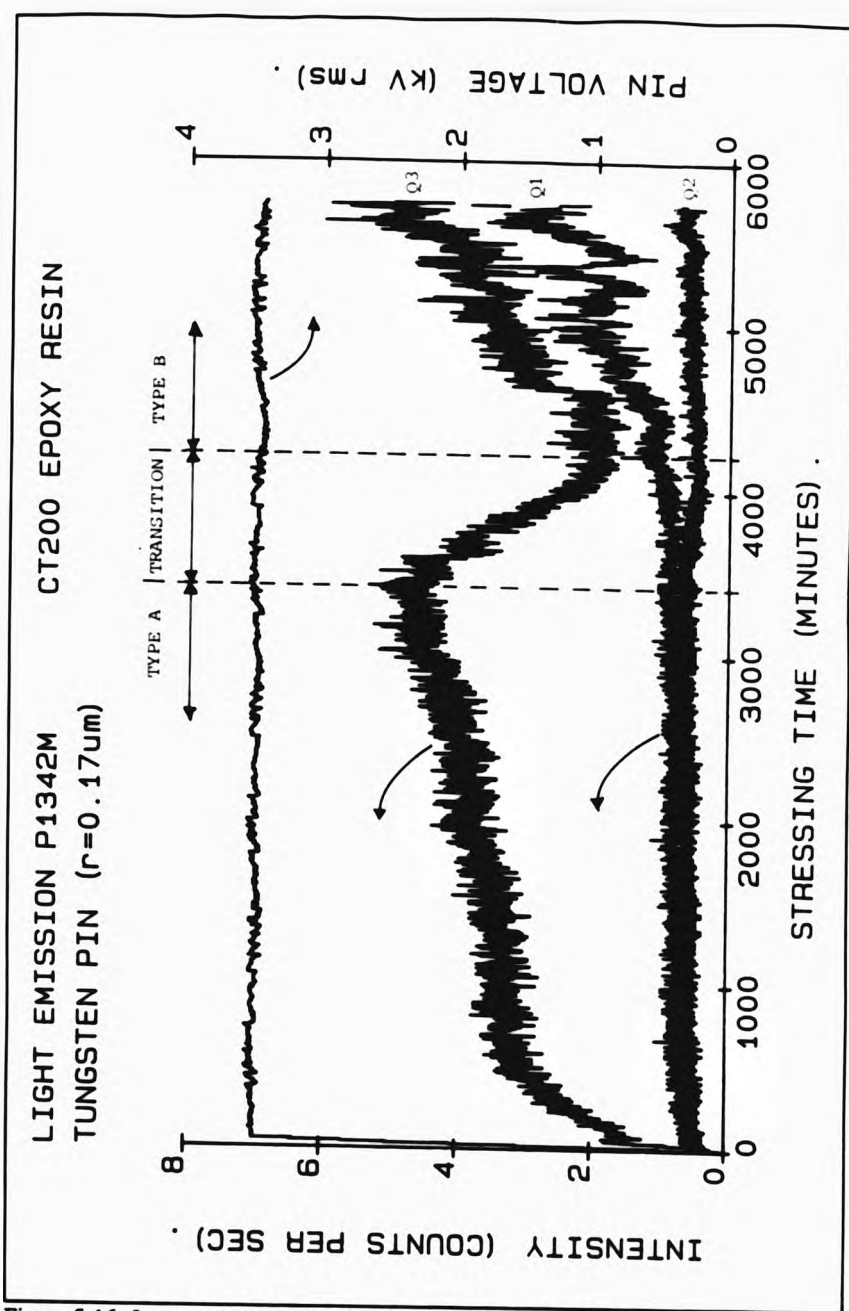


Figure 5.16. Long term light emission for CT200 sample P134/2.

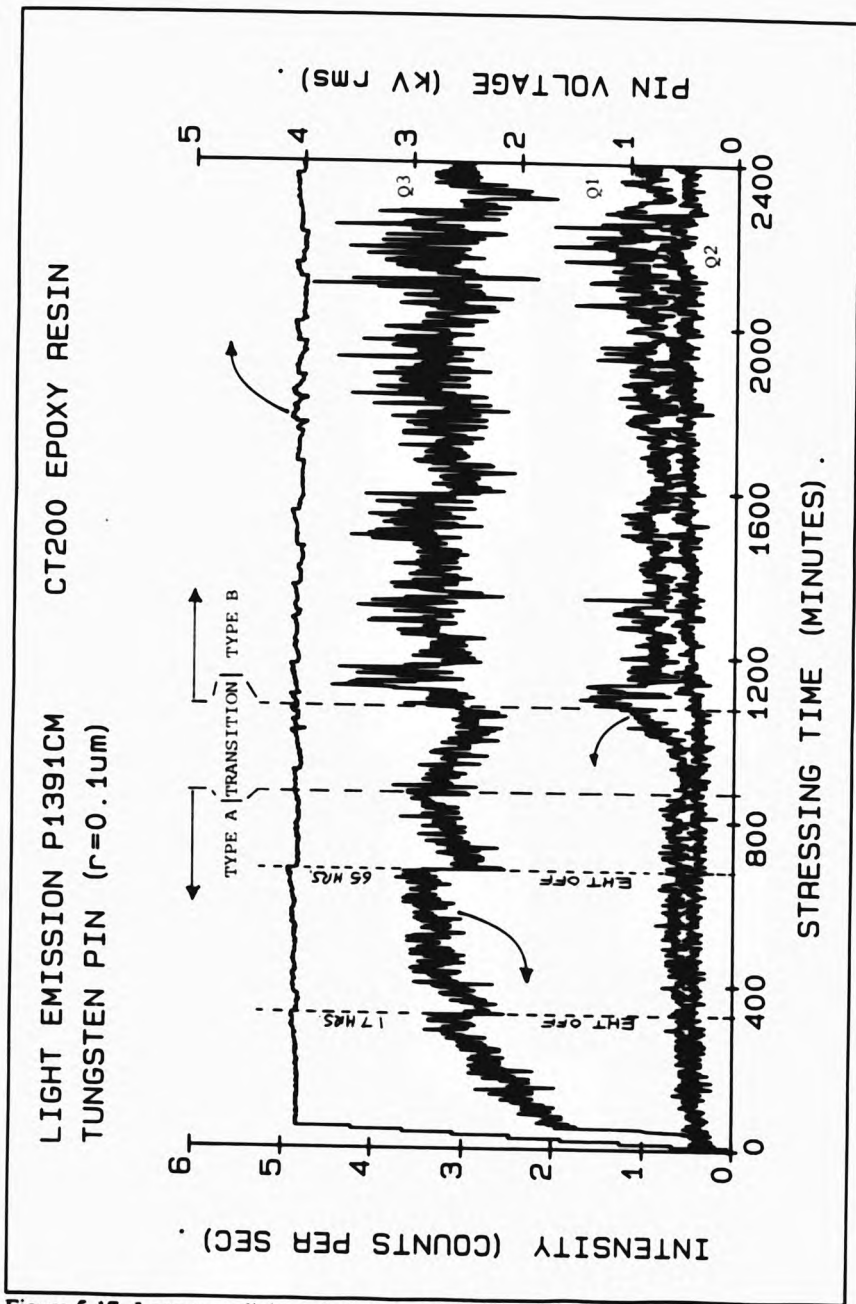


Figure 5.17. Long term light emission for CT200 sample P139/1.

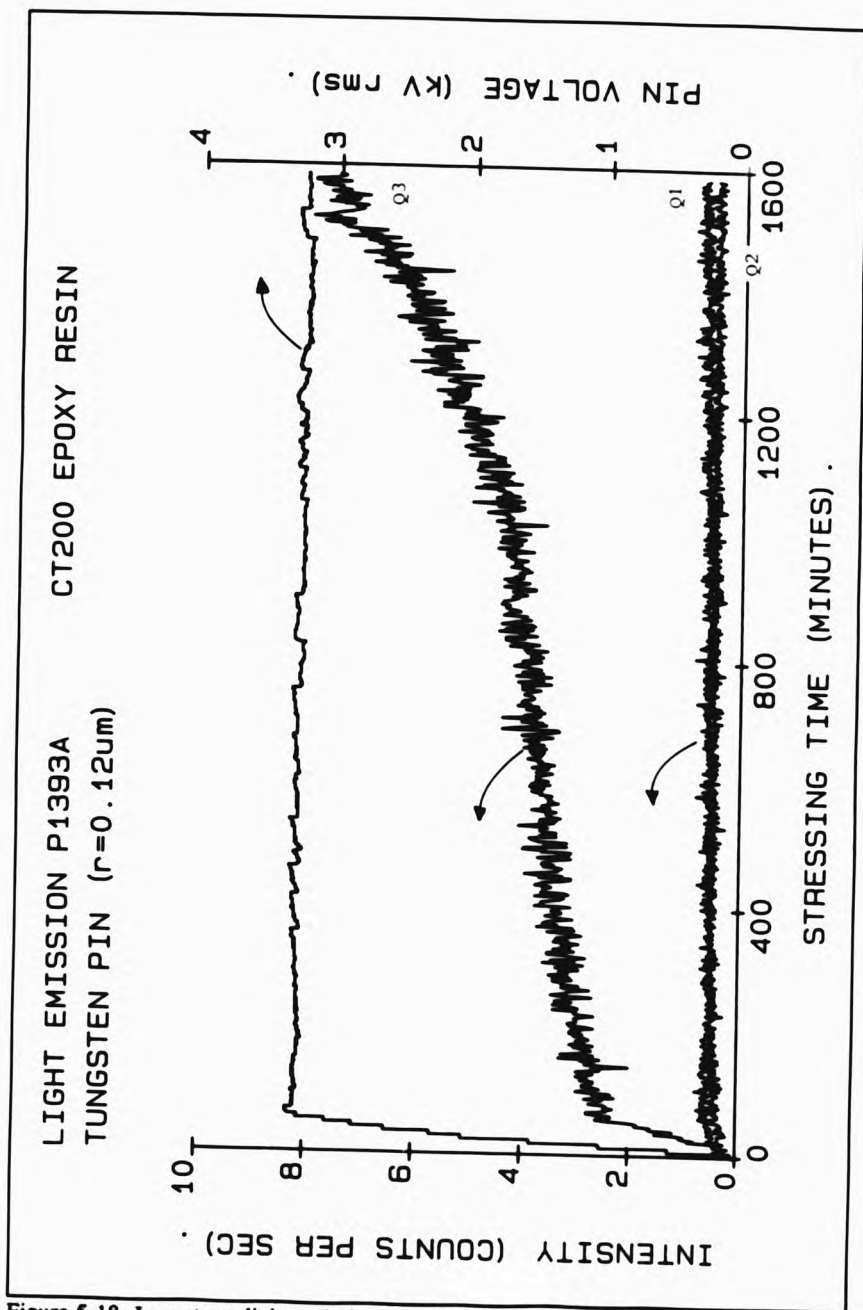


Figure 5.18. Long term light emission for CT200 sample P139/3.

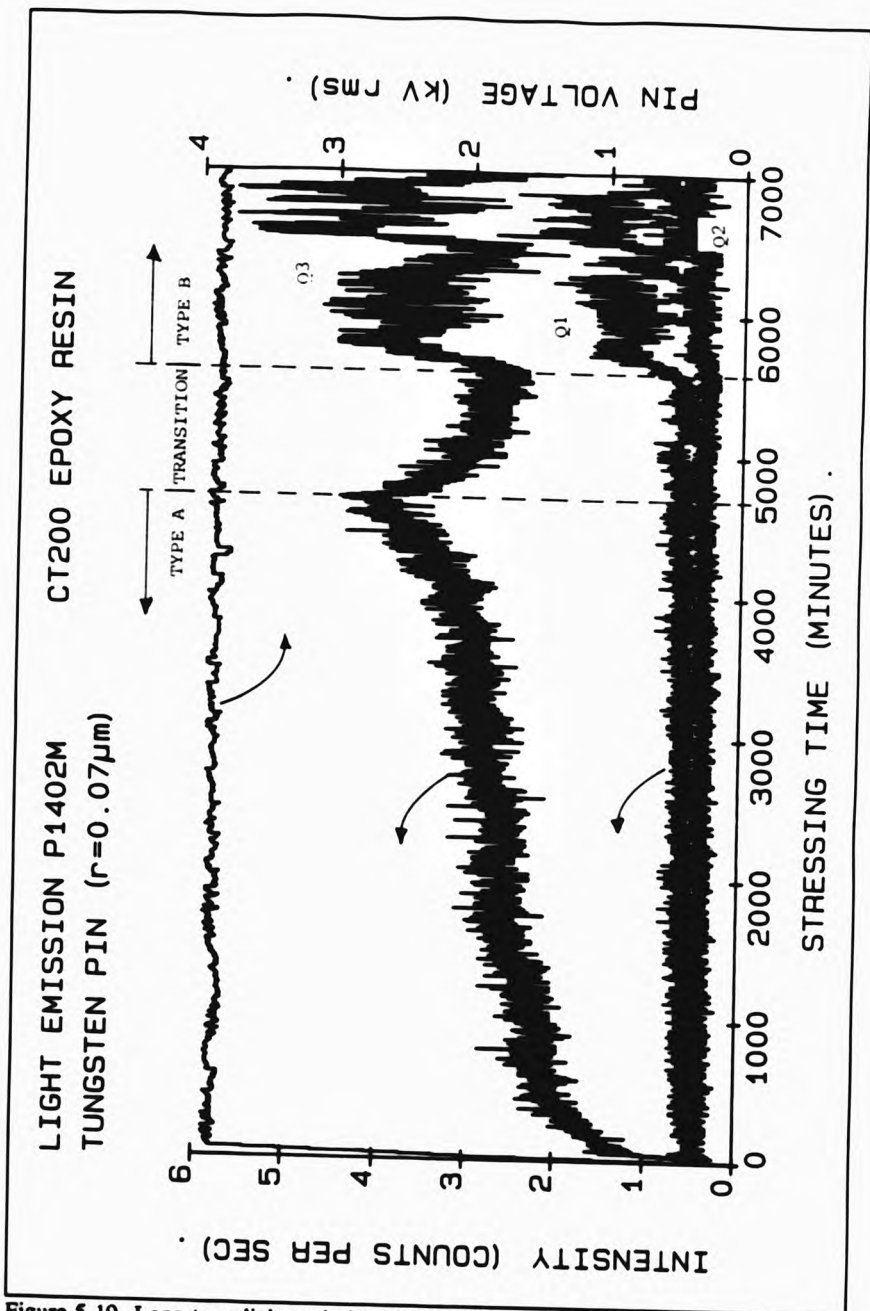


Figure 5.19. Long term light emission for CT200 sample P140/2.

the stressing voltage, below the level on interruption. The magnitude of this drop was found to depend on the interruption time as shown in figure 5.21 along with the results from another sample. After this initial drop in intensity the electroluminescence increases at a rate similar to the initial rise.

Further changes in the electroluminescent behaviour occur in time. A second but in general slower increase in the Type A light emission intensity is observed, for the non-interrupted samples, before a sudden and sharp decrease in the light emission intensity marking the transition from Type A to Type B behaviour. The magnitude of these intensity changes and the stressing time required, depend on the individual samples, e.g. the initial state of the pin-resin interface condition and the actual electrical stress condition at the pin-tip. Sample P139/3, where the stress was interrupted before the transition region, was examined by optical microscopy and no observable material damage was found at the pin-tip.

After the transition region, Type B behaviour is observed. The difference in phase and temporal behaviour between Type A and B light emission can be clearly seen.

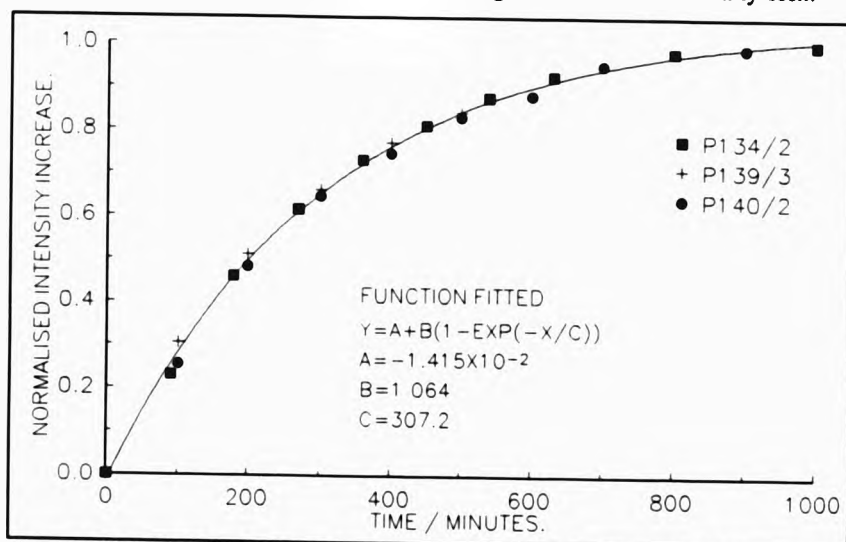


Figure 5.20. Initial Type A electroluminescence intensity increase in CT200 epoxy resin.

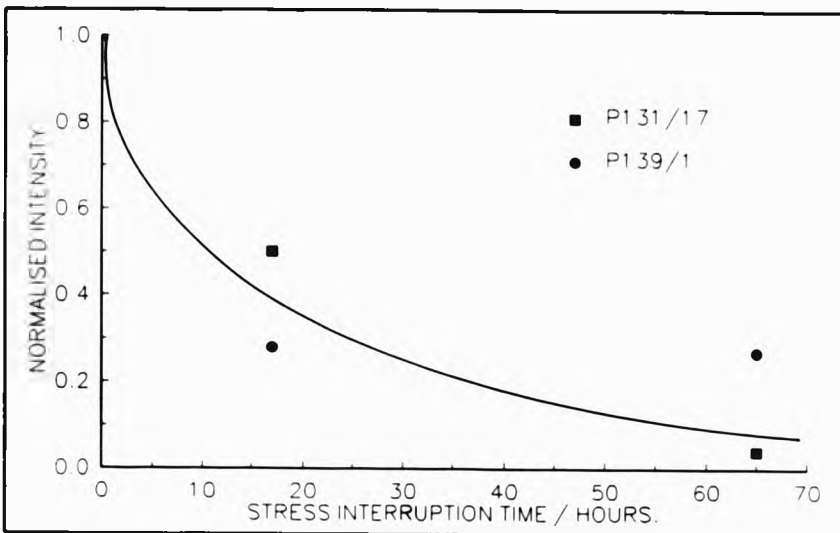


Figure 5.21. Decrease in the Type A electroluminescent intensity after stress interruption.

5.4.3. Long Term Voltage Stressing - Discussion

A generalised schematic of the long term light emission behaviour is shown in figure 5.22.

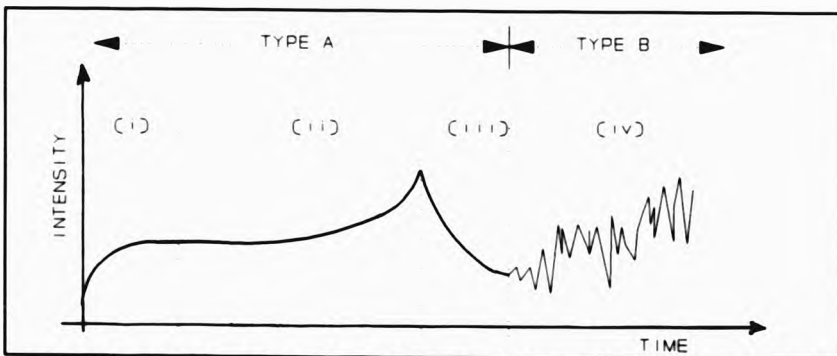
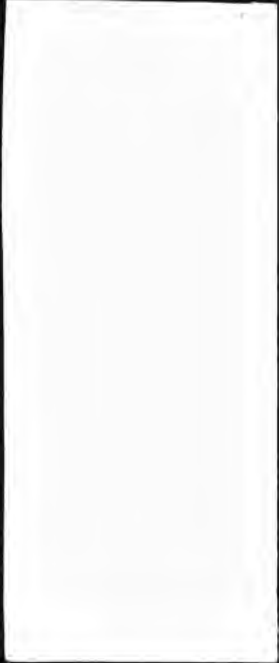


Figure 5.22. General schematic of the long term light emission behaviour in CT200 epoxy resin with the different light emission regions indicated.



The initial long time constant exponential rise in the Type A electroluminescent intensity, region (i) in figure 5.22 and the intensity drop after stress interruption suggest that charge storage in the resin is responsible for the observed electroluminescence behaviour. How this may occur will be discussed in detail in section 5.6, where a deep trap recombination model will be proposed.

The magnitude and time required for the second but generally slower increase in the electroluminescence, region (ii) in figure 5.22, was found to be sample dependent and therefore not intrinsic to CT200. A possible explanation for this is material degradation at the pin-tip resin interface, where the injected charge carriers, above a critical energy, break bonds in the resin network. Such a process has been discussed by Tanaka and Greenwood [102]. To account for the intensity increase, bond breakage then leads to an increase in the number of deep trap recombination centres. Sample P139/3 was interrupted here and found not to have any observable microscopic damage at the pin-tip. Hence, if deterioration has occurred, then its extent must be less than the optical resolution, i.e. less than $1\mu\text{m}$. This is therefore consistent with the above process where damage first occurs at the molecular level.

A transition region, (iii) in figure 5.22, occurs before the onset of Type B behaviour where the electroluminescent intensity decreases sharply. The magnitude of this drop is sample dependent and is therefore not intrinsic to CT200 resin. The most likely explanation for this is interface failure and a reduction in the amount of charge injected into the bulk of the resin. Type B behaviour, region (iv) in figure 5.22, occurs after the transition region with the formation of microchannels at the pin-tip.

From these long term stressing tests a scheme for tree initiation in CT200 epoxy resin can be formulated. The pin-tip resin interface is first weakened by injected space charge. Interface failure then follows once sufficient deterioration has occurred and possibly facilitated by the high mechanical compressive and shear stresses that exist at the pin-tip (see chapter 4). Microchannels form at the failed interface again possibly facilitated by the high mechanical stresses at the pin-tip as a prelude to tree propagation.

5.5. Simultaneous CCD-Photomultiplier Measurement of the Light Emission

The use of a photomultiplier and mains synchronous detection techniques has shown that the Type A light emission behaviour was found to follow the Schottky or Fowler-Nordheim charge injection mechanisms depending on the magnitude of the applied electric field. No evidence was found for a material dependent threshold voltage/field for light emission and therefore charge injection. In order to substantiate these conclusions and to determine the spatial distribution of the emitted light at the pin-tip, an ultra-sensitive liquid nitrogen cooled charge coupled device (CCD) camera was used in conjunction with the existing photomultiplier, to simultaneously record the emitted light.

5.5.1. Experimental

A Wright Instruments liquid nitrogen cooled CCD camera utilising a thinned and UV coated CCD chip, EEV CCD02, was used in a back-to-back arrangement with the photomultiplier, shown in figure 5.23, to simultaneously record the intensity and spatial distribution of the emitted light from the test sample. The CCD has negligible dark noise compared with the readout noise of 10 electrons per pixel. The light collection efficiency of the CCD optics is 2.5% and the CCD chip has a quantum efficiency of 80%. Assuming the emitted light falls equally on 5 CCD pixels and an integration (exposure) time of 100 seconds, then the CCD camera is approximately 4 times as sensitive as the photomultiplier. For a CCD integration time of 1000 seconds, the detectability increases to approximately 40 times that of the photomultiplier. The CCD chip has 385 x 578 pixels each of size $22\mu\text{m} \times 22\mu\text{m}$. The CCD optics has a magnification of X15 using a 25mm microscope objective and hence the spatial resolution is $1.5\mu\text{m}$ per pixel.

Standard pin-plane CT200 samples with embedded etched tungsten pins of pin-tip radii around $0.08\mu\text{m}$ were electrically stressed by applying an initial step ramp up to approximately 80% of the threshold field for Type B behaviour, obtained from the short term step ramp tests. Continuous long term stressing then continued at this voltage.

5.5.2. Step Ramp Tests

The results of simultaneous measurement of the light emission intensity for sample P144/19 using both the photomultiplier and the CCD camera with a 1000 second integration time are shown in figure 5.24 plotted against pin voltage. The higher sensitivity photodetection of the CCD camera shows that light emission is maintained at voltages 2.5 times lower than when first detected using the photomultiplier. This supports the view that ^{no} experimental evidence currently exists for a material threshold voltage/field for charge injection and subsequent light emission.

CCD spatial imaging of the pin-tip region, see figure 5.25 (a), (b) and (c) for sample P144/2 (CT200 sample with a $0.09\mu\text{m}$ embedded tungsten pin) at 3kV, 4kV and 5kV rms respectively, reveals that the majority, (60%) of the Type A light emission emanates from an area less than $3\mu\text{m}$ from the pin-tip, with maximum emission occurring at the pin-tip and light still detectable some $10\mu\text{m}$ into the resin.

This would suggest that injected charge is concentrated at the pin-tip and extends at least $10\mu\text{m}$ into the resin.

5.5.3. Long Term Stressing

Long term stressing of these samples has shown that the light emission area increases in time, principally along the pin-tip as shown in figure 5.26 (a), for sample P144/2 stressed at 5kV + 3.5 hours. From this it is found that 60% of the light emission is from an area less than $4.5\mu\text{m}$ from the pin-tip. Damage accumulation was therefore probably occurring throughout the whole stressing time principally along the cone and at the pin-tip. This can be seen more clearly in figure 5.26 (b) for sample P144/2 stressed at 5kV + 6.5 hours.

5.5.4. Light Emission from Tree Channels

Continuous CCD imaging (with short integration times of 10 seconds) of the Type C light emission was performed on a mature $160\mu\text{m}$ tree grown in CT200 (sample

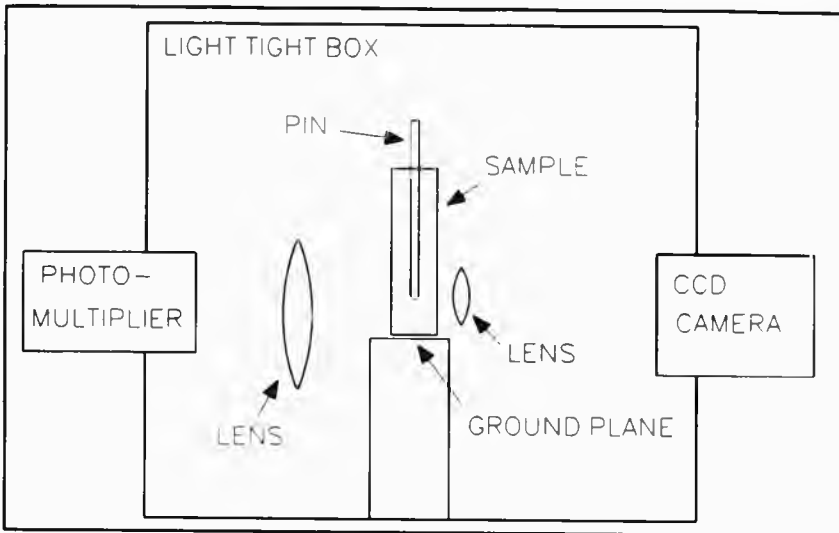


Figure 5.23. Back to back CCD and photomultiplier experimental arrangement.

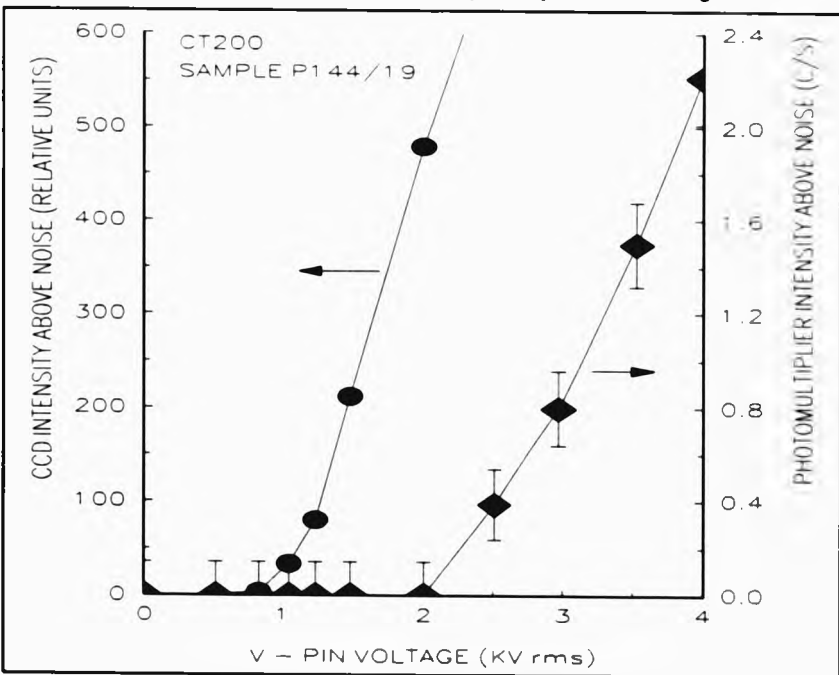
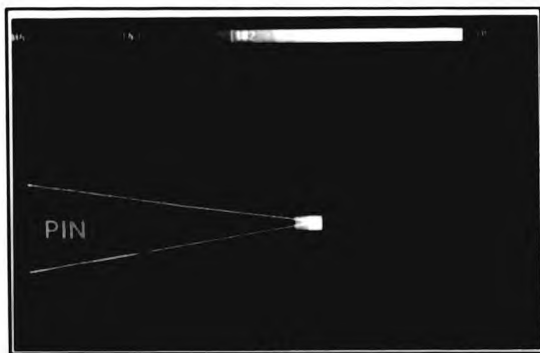
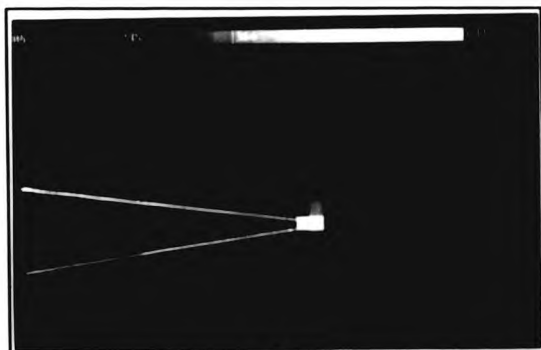


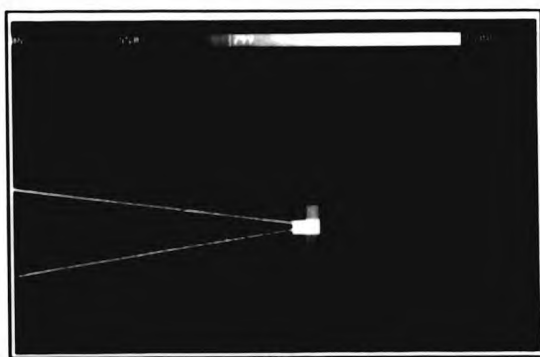
Figure 5.24. Simultaneous measurement of the light emission using the photomultiplier and a liquid nitrogen cooled CCD camera.



(a)

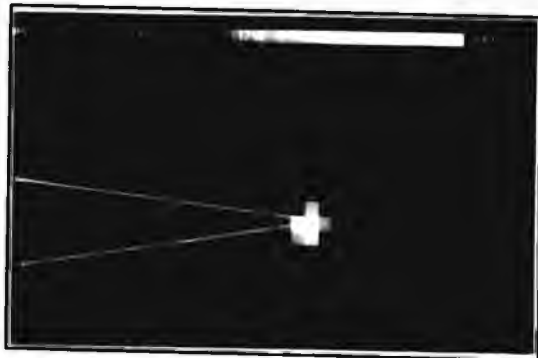


(b)

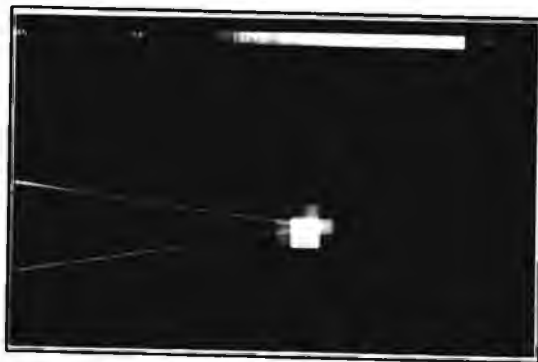


(c)

Figure 5.25. CCD images of the Type A light emission. Pin voltages, (a) 3kV rms, (b) 4kV rms and (c) 5kV rms.



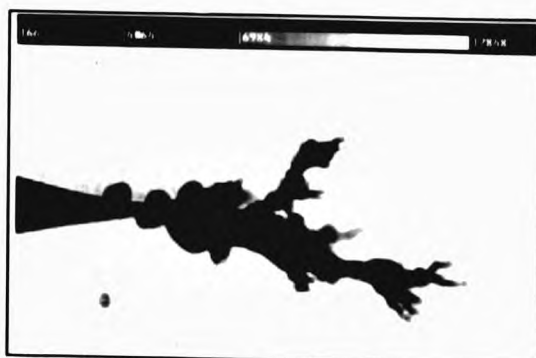
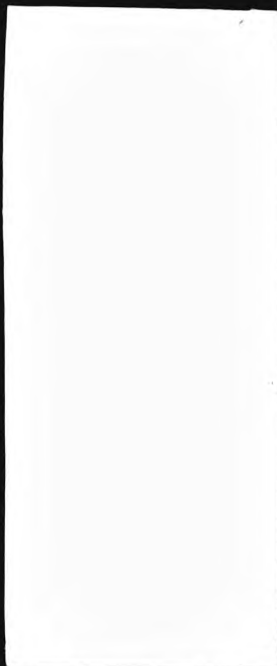
(a)



(b)

Figure 5.26. Long term light emission behaviour. (a) 5kV + 3.5 hours, (b) 5kV + 6.5 hours.

P131/17 with pin voltage 5kV rms). Discharges occur throughout the tree, as shown in figure 5.27(a), (b) and (c), the same image was used for figures 5.27(b) and (c), with the grey scales on the former set to show the whole region of light emission whilst for the latter, the grey scales were set to show just the brightest regions. The discharging was found to switch on and off in time and the overall activity was found to decrease with time with periods of quiescence dominating after approximately 10 minutes. Random bursts of discharge activity occurred after this time. If the discharge activity is associated with tree growth, then the mechanisms of passivation and the random switching behaviour of discharges will be of fundamental importance in predicting tree growth times.



(a)



(b)



(c)

Figure 5.27. CCD imaging of the light emission in a $160\mu\text{m}$ long tree. (a) electrical tree. Grey scales adjusted to show (b) discharge activity in whole of tree and (c) the brightest regions.

5.6. Discussion

It was concluded from the short term step ramp tests (see section 5.3) that the electroluminescence is governed by charge injection. Depending on the applied electric field either Schottky or Fowler-Nordheim injection behaviour is observed. The mechanisms for electroluminescence and the role of charge injection and space charge formation on electrical tree initiation are as yet unresolved. This is due mainly to insufficient knowledge of i) the electronic states in synthetic resins, ii) the high field transport processes and iii) lack of quantitative light emission measurements in the literature. What follows is a brief discussion on some of the likely physical processes involved leading to a proposed deep trap recombination model for electroluminescence in order to explain the observed measurements.

5.6.1. Electronic States in an Synthetic Resin

Little is known of the actual electronic states of amorphous synthetic resins, the simple periodic lattice model for a crystalline insulator is not suitable. However, localised acceptor and donor states will exist in the synthetic resin, distributed around energies E_a and E_d corresponding to the conduction/forbidden band transition energy and forbidden/valence band transition energy respectively in a simple crystalline insulator model [35]. The band gap i.e. $E_a - E_d$, is likely to be in the range 4-8eV. The actual energy distributions of the localised acceptor and donor states are unknown but are likely to extend well into the region between E_a and E_d . These localised states arise due to the non-periodic nature of the amorphous polymer with the appearance of chain defects, ends and impurities. Electron and hole injection as well as charge transport may occur via these sites.

5.6.2. Shallow Trap Transport and the Phase Relationship of the Electroluminescence

Shallow trap hopping is the likely high field charge transport process in synthetic resins. If the traps sites are Coulombic, i.e. charged when empty, Poole-Frenkel trap lowering [9,97] occurs when an electric field is applied. The trap barrier height

energy reduction, $\Delta\phi$, for a range of electric fields is shown in table 5.3, along with the conductivity enhancement, σ/σ_0 .

Table 5.3. Poole-Frenkel trap lowering and conductivity enhancement

Electric Field E	$\Delta\phi = 2 \cdot (e^3 \cdot E / \epsilon)^{0.5}$	$\sigma/\sigma_0 = \exp(\Delta\phi/2k_0T)$
1.0 GV/m	4.3 eV	5×10^{35}
0.1 GV/m	1.3 eV	8×10^{10}
10.0 MV/m	0.43 eV	4×10^3
1.0 MV/m	0.13 eV	1×10^1

It can be seen from table 5.3 that significant conductivity enhancement occurs when the magnitude of the electric field exceeds 0.1GV/m, provided that such an extrapolation is valid. The corresponding value for the Poole-Frenkel trap lowering is 1.3eV. Coulombic traps originally of energy below this value will no longer be available for charge trapping hence, for a distribution of trap energy levels, the number of traps available will depend on the local electric field. This raises the possibility of a field dependent mobility for the charge carriers. For non-coulombic traps, i.e. neutral when empty, Poole-Frenkel trap lowering does not apply. Poole-Frenkel trap lowering is not essential for the following argument below.

Richard Hare [103] of National Power has recently used a computer model to solve the continuity, transport and Poisson equations for charge injection under well defined boundary conditions in the pin-plane geometry using prolate spheroidal coordinates. A FLSC model with the low mobility controlled by shallow trap hopping and a generalised Fowler-Nordheim/Schottky charge injection law, was used to determine the injection current and resulting space charge spatial distribution. It was shown that when an alternating electric voltage is applied to the pin, the local electric field at the pin-tip leads the applied voltage phase by approximately 45 degrees. More importantly Hare's calculation of the current density at the pin-tip shows two peaks located in quadrants 1 and 3, reproduced here in figure 5.28 (with kind permission of Richard Hare). This is exactly what is found from the light emission measurements.

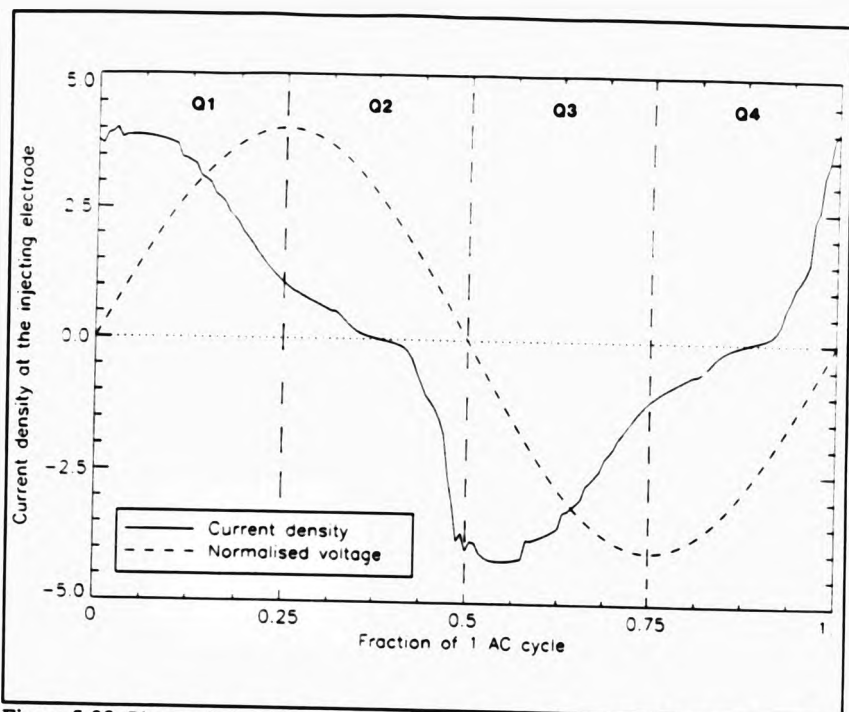


Figure 5.28. Phase relationship between applied voltage and current density at the pin-tip calculated using Richard Hare's model.

Space charge therefore accounts for the phase relationship between the emitted light and the applied alternating voltage. The phase relationship arises due to the space charge forming a reverse electric field which opposes the driving field due to the alternating voltage applied to the pin. However, the formation of space charge itself cannot explain the initial exponential rise in the electroluminescent intensity. To do this a charge carrier recombination model is proposed below, where the electroluminescent intensity depends upon the amount of charge stored in deep traps in the resin.

5.6.3. Deep Trap Recombination Model

The majority of injected charge carriers, for example electrons injected into the resin during the negative half cycle of the alternating stressing waveform, will occupy the shallow trapping sites responsible for controlling bulk charge transport. Some

however, may find their way into the deeper trap sites in the resin, such that they are not removed during the opposite half cycle of the stressing voltage. These occupied deep trap sites may then act as recombination centres and have a finite probability of recombining with holes injected during the positive half cycle of the stressing voltage with each recombination emitting a photon and giving rise to the observed electroluminescence. If only a fraction of all the deep trapped electrons recombine with holes during one cycle, then on subsequent stressing cycles, the total number of deep trapped electrons will increase, leading to an increase in the number of recombination centres and electroluminescent intensity.

The same situation arises for the injected holes during the positive half cycle of the stressing voltage, some of these will occupy deep hole trap sites and act as recombination centres for injected electrons. Due to the symmetry of the two cases, i.e. deep trapped electrons or holes, only one charge carrier is considered in the analysis below.

This situation can be modelled by assuming, at a fixed a.c. stressing voltage, V , applied to the pin, the local field at the pin-tip is such that N_c charge carriers are injected during each stressing cycle. The injected charge occupying the shallow traps are completely removed during the opposite half cycle. Let D represent the total number of deep traps available for charge trapping, each one having a trapping probability P , per cycle. Once filled these traps can only be emptied by recombination of probability P , per cycle. This probability will depend on the amount of counter-charge injected on the opposite half cycle. The electroluminescent intensity will be proportional to $C.P$, where C represents the number of occupied deep traps.

Let C_n be the amount of charge trapped in the deep traps in stressing cycle n .

For the first half cycle of stressing cycle n , the total charge trapped is given by

$$C_{n-1/2} = C_{n-1} + P_r N_c (D - C_{n-1}) D. \quad (5.5)$$

On the second half cycle of cycle n , the number left after recombination is given by

$$C_n = C_{n-1} \cdot (1 - P_r). \quad (5.6)$$

The amount of charge trapped after the n^{th} stressing cycle is therefore

$$C_n = C_{n-1} + \frac{P_r N_c (D - C_{n-1})}{D} - P_r C_{n-1} - \frac{P_r P_r N_c (D - C_{n-1})}{D}. \quad (5.7)$$

Re-arranging to form the differential equation,

$$C_n - C_{n-1} = \frac{\Delta C}{\Delta n} = C_{n-1} \left(\frac{P_r P_r N_c}{D} - P_r - \frac{P_r N_c}{D} \right) + P_r N_c (1 - P_r). \quad (5.8)$$

Let $y = C_n$, $x = n$, $A = (P_r + P_r N_c / D - P_r P_r N_c / D)$ and $K = P_r N_c (1 - P_r)$ then the differential equation

$$dy/dx + A \cdot y = K, \quad (5.9)$$

has the solution,

$$y = E \cdot \exp(-A \cdot x) + K/A, \quad (5.10)$$

where E is a constant of integration. Hence,

$$C = E \cdot \exp \left[- \left(P_r + \frac{P_r N_c}{D} - \frac{P_r P_r N_c}{D} \right) n \right] + \frac{P_r N_c (1 - P_r)}{P_r + P_r N_c / D - P_r P_r N_c / D}. \quad (5.11)$$

If $C = C_0$, when $n = 0$, then,

$$E = C_0 - \frac{P_r N_c (1 - P_r)}{P_r + P_r N_c / D - P_r P_r N_c / D}. \quad (5.12)$$

As the electroluminescent intensity is proportional to C , then an exponential rise to a constant level is predicted with a time constant, t_c , given by,

$$t_c = 1/(P_r + P_r N_c/D - P_r P_r N_c/D). \quad (5.13)$$

If $P_r \gg P_r N_c/D$, then the exponential rise is deep trap recombination dominated.

If $P_r < P_r N_c/D$, then the exponential rise is deep trap filling dependent.

Assuming that the exponential rise is deep trap recombination dominated then the solution reduces to

$$C = \frac{P_r N_c (1 - P_r)}{P_r} \cdot (1 - \exp(-P_r n)), \quad (5.14)$$

with a time constant,

$$t_c = 1/P_r. \quad (5.15)$$

5.6.4. Deep Trap Recombination Model - Discussion

The deep-trap-recombination-dominated solution of the model is shown graphically in figure 5.29 for different values of C_0 , the initial quantity of trapped charge. For zero initial trapped charge, an exponential rise to a constant level is predicted. However if the initial quantity of trapped charge is high (i.e. higher than the steady state value) then an exponential decrease to a constant level with the same time constant is predicted. Shimizu, in his PhD thesis [104], describes the electroluminescent behaviour of anthracene and naphthalene doped polyethylene. He found that the electroluminescent intensity decreases with time to a constant level with a time constant of 5 minutes. This model described above can be used to explain his findings if the anthracene or naphthalene act as charge donors in the resin.

The time constant observed experimentally for CT200, is approximately 5 hours. Hence P_r has the approximate value 1×10^{-4} per cycle. P_r will depend on the amount of counter charge injected into the resin and the cross-section for recombination.

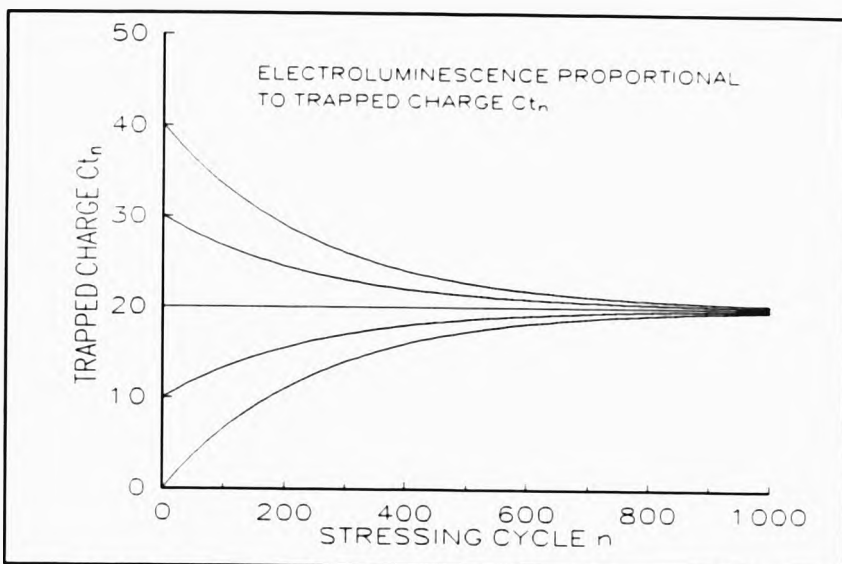


Figure 5.29. Deep trap recombination model, evolution of trapped charge, C_t , for different values of initial trapped charge C_{t_0} .

An estimate of the amount of charge injected into the resin, N_i , may be obtained by considering the following. For pin-plane sample, P134/2 (see section 5.4), with pin-tip radius, $0.17\mu\text{m}$ and pin-plane distance, 2mm , the maximum field at the pin-tip, E_{max} , will have a value of 5GV/m when 3.5 kV rms is applied to the pin. Consider a sphere of space charge of radius $5\mu\text{m}$ situated adjacent to the pin-tip. The amount of charge distributed homogeneously within the sphere, Q , to give an electric field of E_{max} at the sphere surface is given by

$$Q = 4\pi\epsilon_0\epsilon_r^2 E_{\text{max}}^2 \quad (5.16)$$

For the values above and $\epsilon_r=4$, the number of charges injected into the space charge sphere is 3.5×10^8 and corresponds to a charge density of $7 \times 10^{17}\text{ cm}^{-3}$. This corresponds only to the space charge region required to oppose the applied field to limit further injection. Shimizu [104], considering a $10\mu\text{m}$ long, $10\mu\text{m}$ radius cylinder of space charge, calculates the density of injected charge to be $2.42 \times 10^{16}\text{ cm}^{-3}$ for $E_{\text{max}}=2.8\text{GV/m}$. This corresponds to 1.25×10^8 charges being injected for $E_{\text{max}}=5\text{GV/m}$ (by simple scaling) and agrees well with the estimate above.

If it is assumed that at steady state, C is approximately equal to N_c , then using the values calculated above for the number of charges injected per cycle, $N_c = 3.5 \times 10^4$ and recombination probability, $P_r = 1 \times 10^{-6}$, the electroluminescent intensity, given by $C \cdot P_r$, is 350 photons per cycle. From experiment, (sample P134/2 see section 5.4), approximately 12 photons per cycle are emitted over the full solid angle assuming all photons have a wavelength at the maximum sensitivity of the light detection system (see section 5.2.4). Considering photons of other wavelengths, then 12 photons represents the lower limit for the number of photons emitted per cycle and is consistent with the theoretical argument, i.e. less than 350 photons per cycle. At steady state, $C = P_r \cdot N_c / P_r$, and hence P_r is approximately equal to P_r . As we are considering the deep-trap-recombination-dominated solution ($P_r \gg P_r \cdot N_c / D$), then the number of deep traps available for filling, D , must be much greater than N_c , the number of charges injected, i.e. $D \gg 350 \times 10^4$. The density of deep traps must therefore be much greater than $7 \times 10^{17} \text{ cm}^{-3}$. This is in agreement with Kao and Hwang [105], who quote Milnes [106], giving the value 10^{19} cm^{-3} for the Coulombic trap density in an imperfect large band gap insulator. Hence it would appear that this model describes reasonably our experimental observations.

It may be possible to test this model experimentally by pre-stressing the samples with high d.c. voltages applied to the pin. If a long enough pre-stressing period is given it may be possible to store enough charge such that a decreasing exponential behaviour is observed. Pre-stressing with just one polarity in this way, will just affect the light emission on one half cycle only. A sample pre-stressed with the opposite polarity will affect the opposite half cycle. Pre-stressing with a higher voltage a.c. is not practical as material damage is likely to occur.

5.7. Conclusions

Measurement of the light emission during the early stages of electrical breakdown has been shown to be a sensitive probe of

- 1) charge injection processes,
- 2) degradation of the pin-tip/resin interface,

- 3) interface failure,
- 4) the occurrence of microdischarges as a prelude to tree propagation (tree initiation),
- 5) the partial discharge activity in growing tree channels.

Collation of all light emission results obtained so far suggest that the initiation of electrical treeing breakdown may be described in the following stages.

1) Experimentally immeasurable electroluminescence occurs as soon as an electric field is applied. At sufficiently high fields electroluminescence can be detected experimentally and found principally in the first negative quadrant (quadrant 3) of the voltage stressing cycle. The electroluminescence and hence the injection current is described by either F-N or Schottky emission depending on the magnitude of the field at the pin-tip as determined by the sample geometry and applied voltage. For the materials examined in this work an interfacial barrier height for charge injection across the metal/resin interface of the order of 1eV is found. There is no field (or voltage) threshold for this behaviour which we term Type A emission.

Simultaneous CCD imaging and photomultiplier photodetection has confirmed that the light detected by the photomultiplier does emanate from the pin-tip region of the pin-plane samples. The extra (X40 for CCD exposure time of 1000 seconds) sensitivity of the CCD camera over the photomultiplier supports the view that no experimental evidence currently exists for a material dependent threshold voltage or field for electroluminescence and therefore charge injection. The majority of the electroluminescence and hence the injected charge is concentrated at the pin-tip ($< 3\mu\text{m}$) and extends at least $10\mu\text{m}$ in to the resin.

2) On further increase in the field a material dependent threshold voltage occurs, associated with the onset of micro-partial discharges and a corresponding change in the emitted light behaviour, which we call Type B emission. Once this occurs, micro-channels have formed, growth ensues and eventually breakdown channels are observed by optical microscopy. The low level electroluminescence is rapidly masked by the light emission from discharges in the growing micro-channels. This light emission fluctuates in time with an increasing contribution to the total emitted light in

quadrant 1 (the first positive voltage quadrant). The FLSC model will not be applicable at this stage of breakdown and the threshold field for Type B, should not be associated with the critical field of the FLSC model.

Long term stressing of samples in the Type A region, i.e. below the threshold for Type B emission obtained from the short term step ramp tests, has shown that an eventual transition to Type B behaviour occurs. In this case, it is considered that slow material degradation at the pin-tip due to continual charge injection/extraction weakens the pin/resin interface. Interface failure then occurs followed by the formation of microchannels and Type B light emission behaviour.

Zeller and Schneider's model for electrofracture [4] may be applicable here. In this case an additional mechanical compressive stress is produced due to the local electric field acting on the space charge near the pin-tip. The resulting cumulative stress may exceed the yield stress of the resin and hence form the first tree channels. However, their calculations assume that the FLSC model is valid, i.e. it is assumed that a material dependent critical field exists throughout the space charge region and that the pin-tip radius is greater than $3\mu\text{m}$ [93]. The work described in this chapter suggests that this might not be so and if we consider Schottky and Fowler-Nordheim charge injection mechanisms, the formation of a stable space charge region may in the limit, reduce the local field to zero at the pin-tip, to prevent further injection. In this case no additional compressive mechanical stress will arise. The real situation is probably between the two cases above. Further complications arise; the long term light emission behaviour suggests that slow material degradation occurs prior to interface failure, this may reduce the yield stress of the resin at the pin-tip during voltage stressing. In CT200 epoxy resin, the residual internal mechanical stress RIMS at the pin-tip after sample manufacture, is found to be near the compressive strength of the resin and relaxes slowly with time, (see chapter 4). The electrostatic energy required for crack formation will depend on whether the additional stress due to the space charge contributes or reduces the mechanical stress in the resin at the pin-tip. Alternatively, the slow material degradation may simply reduce the compressive strength of the resin to below the RIMS value, leading to crack formation. In both these cases, the time and field dependence for crack formation will depend on the age

of the sample due to the RIMS relaxation. The role of electrofracture therefore remains inconclusive and a comprehensive experimental study of the field-time dependence of tree initiation in samples having a range of mechanical stress conditions will be required in order to confirm or refute these suggestions.

The Type B threshold value obtained from the step ramp tests should be used with caution as it will depend on the actual stressing time as well as the stress condition at the pin-tip.

3) Once the breakdown channels are greater than about $10\mu\text{m}$, more conventional discharge characteristics appear. These include rapid fluctuations of the emitted light interspersed with quiescence which we call Type C emission. On reducing the stress to zero and repeating the same voltage stressing cycle, all three stages can again be found but the transitions from Type A to Type B to Type C occur at lower voltages.

Further changes in the emitted light characteristics occur on increasing the stressing voltage which are associated with tree growth. Passivation of the electrical discharge activity in the tree is likely to occur after a period of time with just the occasional burst of activity occurring in time. The mechanisms of passivation and the random switching behaviour of discharges are therefore of fundamental importance in predicting tree growth times and the time to failure of the insulation.

The physical mechanisms governing the transition from Type A to Type B behaviour (tree initiation) are as yet unresolved. However, the fractal dimension of the initial failure is found to be dependent on the pin-tip radius and independent of the material, the smaller radii producing a higher dimension. This suggests that the formation of space charge and therefore the magnitude of the field enhancement (determined principally by the pin-tip radius) is playing a major role in the formation of the initial failure.

Chapter 6

Tree Initiation and Growth in CY1311 Epoxy Resin

6.1. Introduction

It has been shown in chapter 4 that CT200 epoxy resin has high compressional RIMS, which is near the compressional strength of the material. As a result, the success rate for manufacturing pin-plane samples with good quality pin-resin interfaces is rather low. This is particularly true for Ogura pins due to the larger shank diameter. Another disadvantage, is that the high RIMS make this material less useful for tree growth studies under differing mechanical stress conditions as rather large externally applied stresses will be required to reduce the compressive stress at the pin-tip through zero and into a tensile stress condition. Although this system has disadvantages as a model system, it is widely used in industry for real insulation systems and for this reason alone it is worthy of study.

This is not necessarily true for polyester resin, which is not widely used in real insulation systems. As a model material, this resin suffers from a number of serious disadvantages making it unsuitable for serious study. The most serious is the tensional RIMS which results from resin cure. Because of this the production rate of samples with good interfaces is poor and much less than CT200. Also, the RIMS is observed to increase by 100% in the first 50 days after manufacture which will be significant in long term electrical breakdown studies. Hence, polyester resin is not ideally suited as a model material.

Because of the difficulties with the two resin systems above, some other resin systems were investigated and from this, a new model resin system was identified. This resin system, the CY1311 epoxy resin system from Ciba Geigy, is used for encapsulating electronic circuits and so knowledge of its electrical breakdown mechanisms and performance may be of interest to the electronics industry. Once cured, this resin has a rubbery nature and at room temperature, it is approximately 20°C above its glass transition temperature. With no elevated temperature post cure, a low RIMS is obtained, with a high yield of pin-plane samples with good interfaces.

making them suitable for both tree initiation and tree growth studies. An additional advantage is that tree growth is rapid at relatively low applied voltages.

In this chapter, an investigation of tree growth in CY1311 epoxy resin using various non-invasive optical techniques will be described. The effect of sample age, RIMS, externally applied mechanical stress, voltage and pin-plane geometry on tree growth was assessed. CCD imaging of the light emission during tree growth was also used to elucidate tree growth mechanisms in this material.

6.1.1. Background

Electrical treeing in synthetic polymers has recently been comprehensively reviewed by Dissado and Fothergill [9]. Electrical treeing can be split into three different stages.

- 1) Tree initiation, where void formation at a region of high field enhancement occurs. The physical mechanisms leading to tree initiation have been addressed in chapter 5 and will not be discussed here.
- 2) Tree growth stage, where fine hollow channels form due to partial discharge activity. These grow slowly and tend to branch, forming tree shaped structures. Tree growth, as it propagates across the pin-plane region, can be split into 3 distinct regions [9]. a) an initial fast growth region near the pin-tip which slows and is followed by, b) a slower tree propagation region. As the tree grows near to the plane electrode, the tree growth rate increases which identifies region c) the runaway stage of tree growth.
- 3) Final breakdown stage. Once the growing tree crosses the inter-electrode gap, large discharge currents can flow causing catastrophic failure of the insulation.

Many physical parameters influencing tree growth have been identified. The most obvious is voltage, Kelen and Larsson [107], have shown that the tree growth rate in epoxy pin-plane samples subjected to different alternating voltages, increases with

applied voltage. Auckland et al. [108], using pin-plane unsaturated polyester specimens and stressing frequencies of 50Hz and 1kHz, have shown that the form of trees grown at the higher frequency differ significantly compared with tree grown under 50Hz stress. Cooper and Stevens [10], investigated the effect of differing post cure temperature on tree growth in unsaturated polyester resin. They found that the average tree fractal dimension increases from 1.08 to 1.45 with increasing post cure temperature and relates to a factor of three increase in static tensile modulus and a 12°C rise in the glass transition temperature. The corresponding characteristic time for tree propagation obtained from a Weibull analysis, increased from 9 to 39 hours. The influence of mechanical stress has also been reviewed in chapter 4.

Tree growth behaviour has been investigated by many authors. Noto and Yoshimura [14], have studied tree growth in polyethylene pin-plane samples using different alternating voltages and frequency. They find that the tree growth rate increases with frequency, but behaves in a complex way with voltage. As the applied voltage is increased, the tree growth also increases. However, above a critical voltage, the tree growth rate decreases when the test voltage is increased further, due to an increasing gas pressure in the growing tree channels suppressing the partial discharge activity. Above a second critical voltage, the tree growth rate increases again with voltage. This, they explain is due to an increase in diffusion of the decomposition gases into the polyethylene.

Ieda and Nawata [13], have also observed this effect in polyethylene, and came to the same conclusion. They also compared the tree growth rates at two different temperatures and found that it was significantly more rapid at 80°C compared with tree growth at 30°C. This, they concluded was due to the higher gas diffusion rate at the higher temperature. Further evidence for this effect has been published by McMahon [109], he found that the time to failure of high molecular weight, low density polyolefin resin, is significantly reduced if vented pins are used or the applied voltage is interrupted, suggesting that the build up of decomposition gas and subsequent decay during stress interruption plays a significant role.

Densley [82], has pointed out that the time to failure variation with applied voltage, can be correlated with the transition between different electrical tree shapes and therefore cannot be accounted for by gas pressure effects alone. Alternative mechanisms of discharge suppression have been proposed. Olyphant [17], has suggested that semi-conducting decomposition products on the walls of tree channels, can suppress the discharges. However, he also finds that final catastrophic breakdown does not always occur instantly the tree crosses from pin to plane and that conductivity measurements of specimens with trees spanning the inter electrode gap are no different from newly cast specimens. Auckland et al. [110], investigating the electrical strength of narrow tubules in perspex, have suggested that charge accumulating on the tubule walls increases its electric strength and stifles electrical avalanches.

Few authors have attempted to map the electrical discharge activity in growing tree channels. Shibuya et al. [2], used an image intensifier tube to detect the light emission from trees growing in CT200 epoxy resin. They found that light is emitted from tree trunks, tree tips and from the surrounding resin. The light emission was found to decrease on prolonged constant voltage application. Stress interruption over a period of several hours led to an increase in the light emission intensity on reapplication of the stressing voltage. Laurent and Mayoux [6], have also used an image intensifier tube to detect the light emission from electrical trees grown in polyethylene. During the growth of a bush type tree or the initial growth of a branch type tree, the light emission is observed throughout the tree. The light emission from the bush or foot of the branch-type tree, ceases when the tree reaches a certain size and the remaining light emission appears as isolated spots at the growing tree tips. They suggest that the local extinction of discharge activity can be explained by variations in the surface conductivity of the channel walls rather than an increase in the pressure of the decomposition gases or the presence of trapped wall charge.

6.2. Effect of Material Age on Tree Growth Behaviour

Preliminary experiments on standard pin-plane CY1311 epoxy resin samples which had been electrically stressed at a constant 5kV rms have shown that the form of tree



grown changes with sample age. For samples 5 to 30 days old from the start of the cure procedure, the tree growth is of the form shown in figure 6.1. Here, the tree form can be described as an open structure on the macroscopic level with microscopic secondary branching existing along the length of each of the main tree channels. This type of tree will be described as a 'monkey puzzle' tree due to its structural similarity with real 'monkey puzzle' trees, although a closer examination of these electrical trees under high magnification reveals a closer similarity to the creeping rhizome of the 'rabbit's foot' fern (*Davallia canariensis*).

Samples of age between 30 and 40 days, show 'monkey puzzle' form only in a limited region, 130-300 μ m from the pin-tip, then a fine branch tree structure forms with few leaders as shown in figure 6.2.

After 40 days, no 'monkey puzzle' tree growth is observed as shown in figure 6.3, instead a fine branch structure grows forming a dense 'bush' near the pin-tip with few leading branches.

The change in tree growth characteristics with age of sample is likely to be due to incomplete cure of the resin as the samples were not subjected to an elevated temperature post cure.

6.3. Detailed Tree Growth Study using Video Recording Techniques

The rapid electrical tree growth found in CY1311 epoxy resin makes this a useful material for electrical breakdown study. As was shown above, this material exhibits some interesting tree growth characteristics which may help elucidate some of the tree growth mechanisms. The most efficient way of continuously monitoring the tree growth is to record this on video tape which can then be analysed at a later date. An additional plus, is that video frames are recorded at a rate of 25 per second, with each of these composed of 2 interlaced fields, giving a time resolution of 1/50th of a second i.e. one cycle of the stressing voltage. Fast events such as the initial rapid tree growth or the final breakdown once the tree has crossed the insulator can be



Figure 6.1. Tree growth in CY1311 epoxy resin. Sample age less than 30 days.

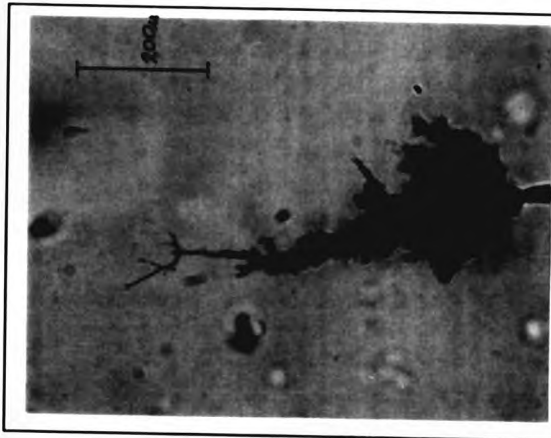


Figure 6.2. Tree growth in CY1311 epoxy resin. Sample age between 30 and 40 days.

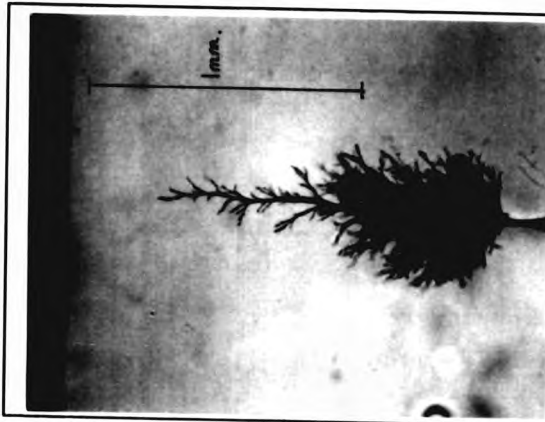


Figure 6.3. Tree growth in CY1311 epoxy resin. Sample age greater than 40 days.



captured. Also, the use of time lapse methods will enable the long term tree growth characteristics to become more apparent.

6.3.1. Experimental

To record on video tape, the tree growth in CY1311 epoxy resin, a 2 metre optical bench microscope was used, as shown in figure 6.4. This has essentially the same arrangement as the circular polariscope described in section 4, but without the circular polarisers and the screen replaced by a Sony colour CCD camera. This arrangement has the advantage that changes in the mechanical stress distribution may also be monitored during electrical stressing, by the inclusion of two circular or crossed polarisers.

Three different objective lenses were used to alter the microscope magnification allowing an image extent of $300\mu\text{m}$, $800\mu\text{m}$ and 3mm across the vertical height of the video frame. Each magnification was determined by placing a graticule in the object plane of the microscope. These calibration and tree growth images were recorded on a Sony U-matic SP video recorder. All samples were held in the object plane of the

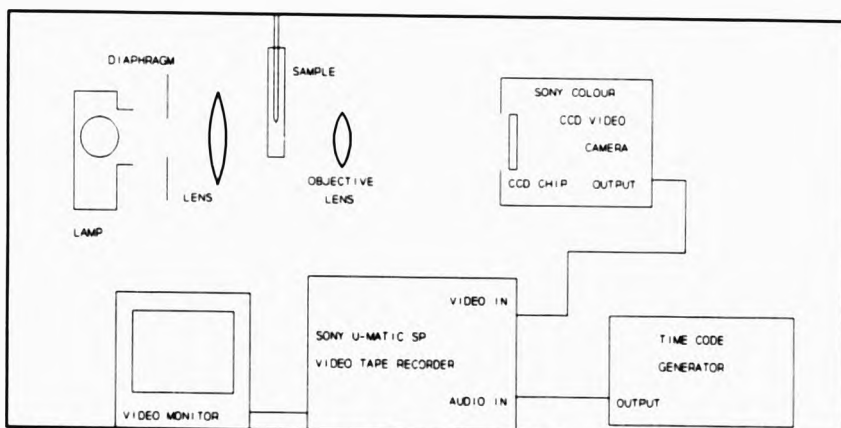


Figure 6.4. Experimental arrangement for the video study of tree growth.

microscope by suspension in order to minimise induced mechanical stress. Elapsed time from the start of voltage stressing was recorded on the audio channel of the video recorder using a time code generator.

Pin-plane CY1311 epoxy resin samples with embedded tungsten pins were continuously electrically stressed at 5kV rms and the tree growth recorded continuously for the first 20 minutes. After this initial period, the tree growth was recorded for one minute, at time intervals depending on the rate of tree growth, enabling a time lapse sequence of events to be edited during the slower phase of tree growth. Once the tree had grown close to the plane electrode, continuous recording was again used to capture the final breakdown events.

6.3.2. Results

The maximum radial extent of the growing tree with time as measured on the video monitor, for each of the samples are shown plotted using log-log axes in figure 6.5, for samples C11/11/2, C11/11/3, C11/11/5 and C11/9/7. The first three of these samples are from the same sample preparation and were 11-13 days old before use. The fourth, was from an earlier preparation, having an age of 46 days. Figure 6.6 shows a series of images of the tree growth at various times during electrical stressing for sample C11/11/3. The images were obtained from the video tape using a Mitsubishi video printer.

6.3.3. Discussion

The tree growth behaviour of samples C11/11/2 and C11/11/3 show very similar characteristics, as can be seen from the radial extent graphs. For these two samples, the tree growth behaviour can be split into three distinct regions.

The first region is characterized by rapid tree growth of fine tree channels, as shown in figures 6.6(a) and 6.6(b) for sample C11/11/3. This rapid tree growth virtually stops once the tree radial extent reaches 120 μ m, figure 6.6(c), marking the beginning

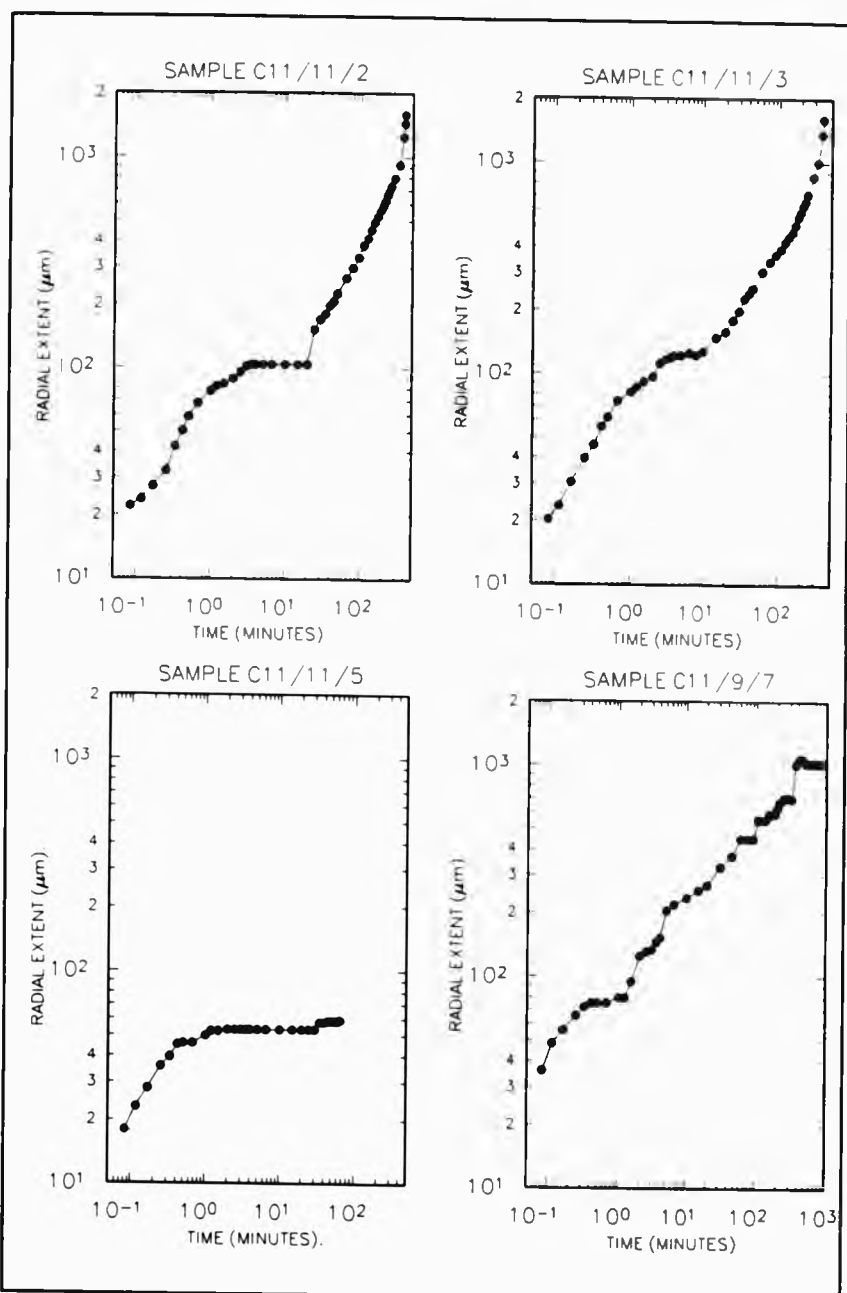


Figure 6.5. Tree growth behaviour in 4 different CY1311 epoxy resin samples. Stressing voltage - 5kV rms.

of the second tree growth region.

The leading branches back thicken at their tips, forming the beginning of the 'monkey puzzle' tree form, as shown in figure 6.6(d). The tree radial extent then starts to increase again as 'monkey puzzle' tree growth ensues as shown in figure 6.6(e). The tree growth rate increases as the tree grows towards the plane electrode while branches other than the leading one continue to grow also, but at a slower rate than the leading branch, (see figures 6.6(f) to 6.6(i)).

As the tree accelerates towards the plane electrode the 'monkey puzzle' structure opens as shown in figure 6.6(j), forming the third region of tree growth behaviour. This is characterized by separate tree channels which branch and grow towards the plane electrode, figure 6.6(k).

When the first tree channel reaches the plane electrode, catastrophic breakdown does not occur immediately and other tree branches continue to grow to the earth plane. In figure 6.6(l), a streamer discharge occurred through one of these tree channels and caused local damage. Catastrophic breakdown occurred soon after. In the case of sample C11/11/2, breakdown did not occur even after one hour of further stressing after the tree had bridged the electrodes.

For the third sample from the same batch as the two discussed above, C11/11/5, tree growth stopped once the tree reached a radial extent of $60\mu\text{m}$ (figure 6.5). Very little additional growth occurred after the next 60 minutes and stressing was abandoned after this time. It seems therefore that 'monkey puzzle' tree growth occurs only after the tree radial extent exceeds approximately $100\mu\text{m}$ otherwise tree passivation occurs. This can also be seen in the radial extent graphs, in figure 6.5, that for sample C11/11/2, where the initial tree growth reached $105\mu\text{m}$, a longer period of passivation and tree back filling occurred compared with sample C11/11/3, where the initial tree grew to $120\mu\text{m}$. These results suggest that two important factors control the variation in the time to failure in these samples, firstly, the period of passivation after the initial tree growth phase and secondly, the delay in catastrophic breakdown after the tree has crossed the pin-plane region.

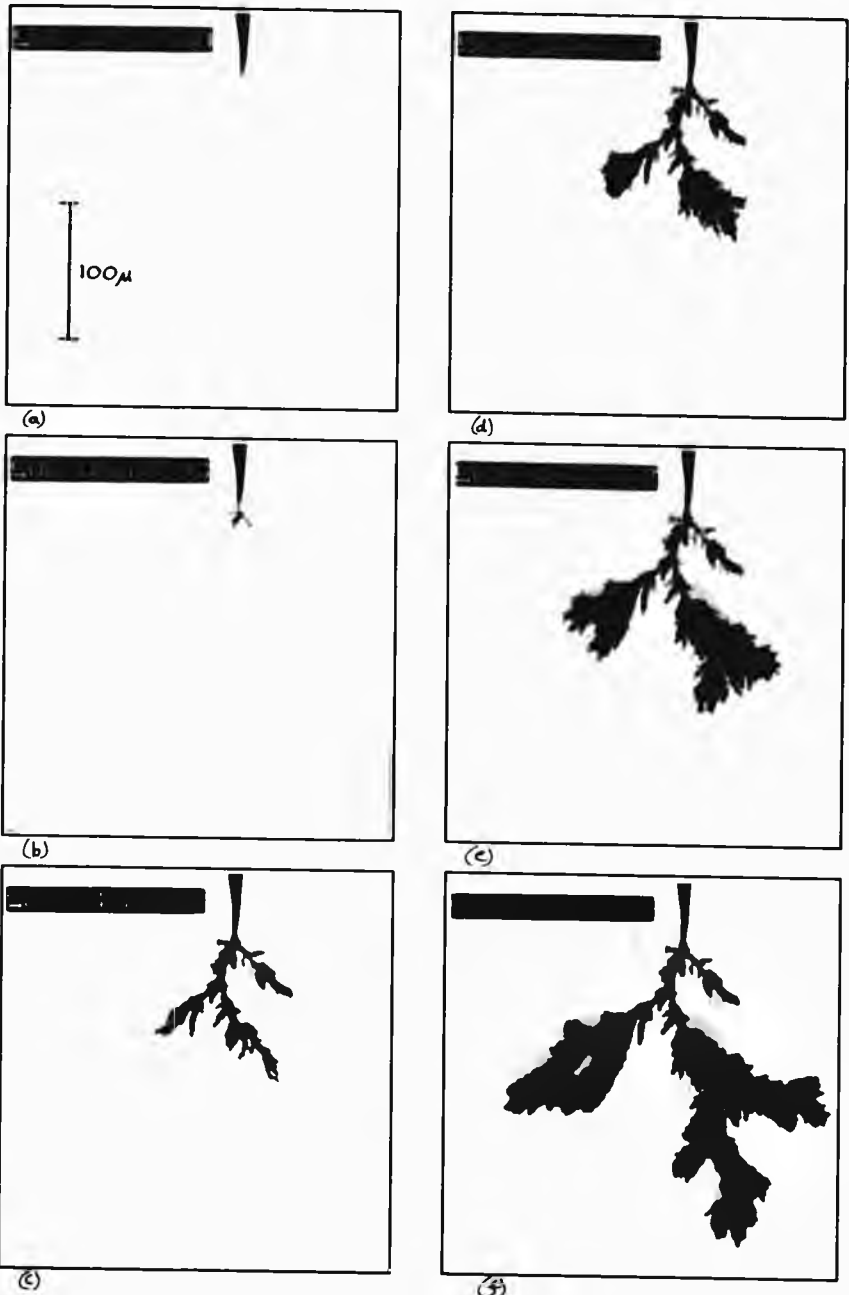


Figure 6.6(a) to (f). Tree growth for sample C11/11/3.

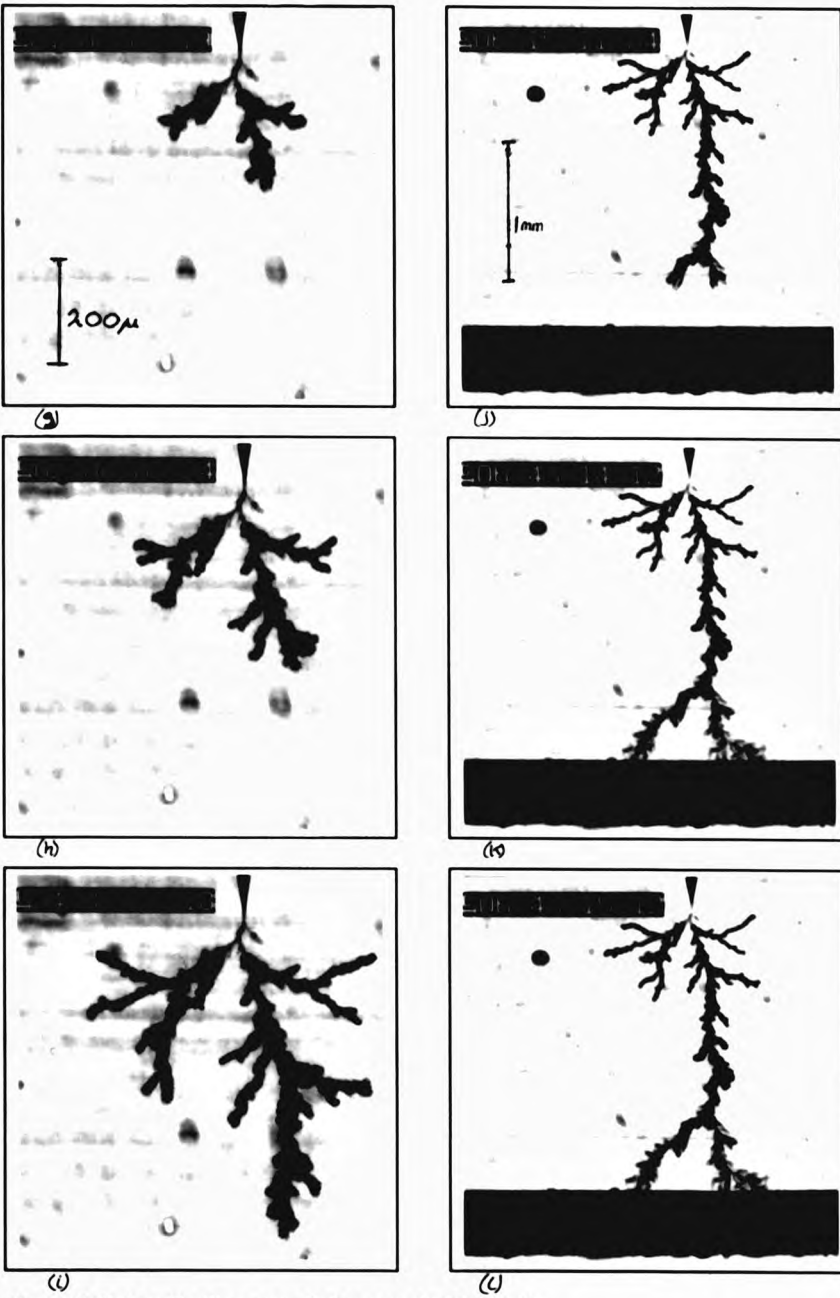


Figure 6.6(g) to (l). Tree growth for sample C11/11/3.



Sample C11/9/7, which is an older sample, did not exhibit 'monkey puzzle' tree growth. Instead, a fine tree structure developed whose growth can be characterised by random side branching and subsequent passivation, resulting in a stop/start tree growth behaviour; this is reflected in its radial extent behaviour, shown in figure 6.5, after an initial rapid growth to $80\mu\text{m}$.

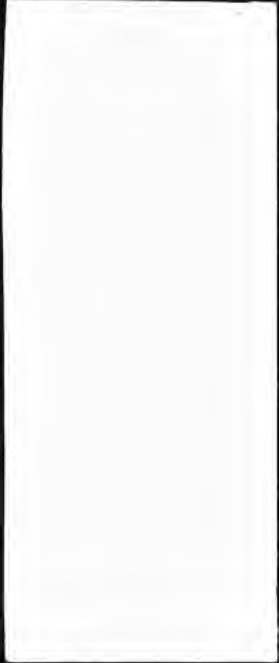
The different character of 'monkey puzzle' tree growth and the fine branched initial rapid growth region, suggest that different tree growth mechanisms may be responsible not only for samples of different age, but also for the different tree growth regions within the pin-plane space. This will be pursued further in sections 6.5 and 6.6.

6.4. Effect of RIMS and Externally Applied Mechanical Stress on Tree Initiation and Growth

It was shown in section 4 that the RIMS in CY1311 epoxy resin pin-plane samples changes with time from cure in a complex way. Initially the resin is in a state of compression in the pin-plane space along the pin axis direction. Absorption of water vapour forces the plane region into a state of tension after approximately 40 days, producing a band of zero RIMS within the pin-plane region perpendicular to the pin axis direction. The tensional stress at the plane increases with age forcing the zero stress position (ZSP) to move slowly towards the pin.

6.4.1 Experimental

Observing the sample through cross polarisers with the polarisation direction 45° to the pin axis direction, a black fringe can be seen marking the ZSP. This technique was used to monitor both the tree growth and the ZSP of sample C11/9/7, (the 46 day old sample used in the video tree growth experiments of the previous section). Using the symmetrical beam bending technique, it is possible to add either tensile or compressive stress to the pin-plane space, with the effect of moving the ZSP towards or away from the pin-tip. The tree growth in sample C11/9/7 was recorded along with the ZSP to observe the effect of zero stress on tree growth behaviour.



A series of 6 CY1311 pin-plane samples of age 18 to 20 days, 3 having embedded tungsten pins of tip radius $0.1\mu\text{m}$ and the others having embedded Ogura pins of tip radius $2\mu\text{m}$, have been used to assess the effect of applied tensile (+ve) and compressive (-ve) mechanical stress on tree initiation and growth. The stress was applied using the symmetric beam bending technique described in section 4, and the stress estimated using the Shibuya model [2], applied to the local linear behaviour near the pin-tip (by plotting distance from the pin-tip against the reciprocal of the measured optical retardation). A stressing voltage of 5kV rms was used throughout. The (arbitrary) criteria for the tree initiation time was the time after the test voltage was reached for a $3\pm 1\mu$ crack to form at the pin-tip, assessed by visual microscopic observation.

6.4.2. Results

The radial extent of the electrical tree and ZSP are plotted against time in figure 6.7. Tree growth stops as it approaches the ZSP after 30 hours. The symmetrical beam bending technique was used to move the ZSP away from the pin-tip after 125 hours and tree growth immediately continued until the tree again reached the new ZSP where it again stopped growing. Applying additional mechanical stress after 220 hours to move the ZSP out of the sample, breakdown occurs rapidly with respect to the original time scale.

The effect of externally applied mechanical stress on tree initiation and time to failure are shown in table 6.1. Two of the samples were unstressed, leaving just a small compressive RIMS at the pin-tip. The data in general indicates that a compressive (-ve) stress at the pin-tip significantly increases the initiation time and time to failure, and the addition of a tensile (+ve) stress reduces the initiation time and significantly increases the time to failure. More work is required to establish the detail.

6.4.3. Discussion

These results along with the effect of a zero stress region, suggest that tree growth is influenced by the magnitude of the stress ^{and its} distribution along the pin axis direction in

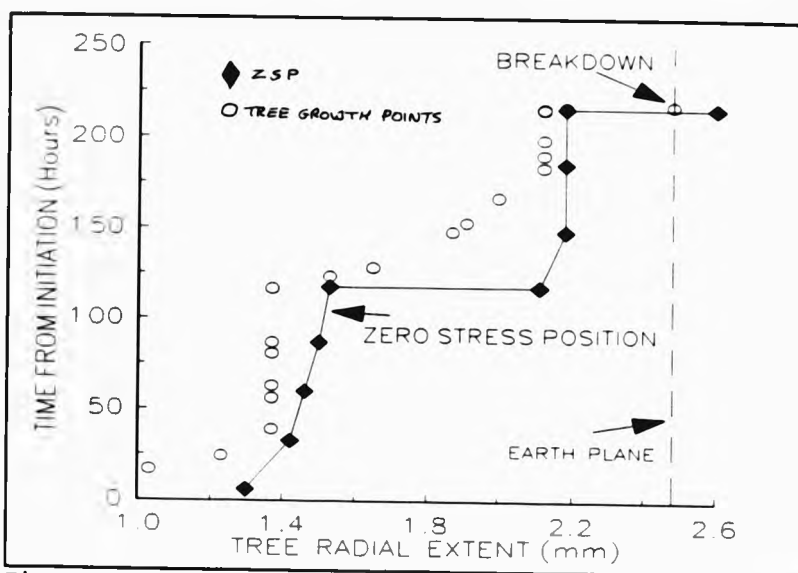


Figure 6.7. Effect of a zero stress region on tree growth.

a complex way. High compressive or tensile stress regions, or a region of zero stress which marks a transition from a region of tensile to compressive stress is found to impede tree growth compared with samples of low RIMS. The ZSP therefore acts as a barrier to tree growth, suggesting that orientation of the

Table 6.1. Initiation and Failure Times as a Function of Total Mechanical Stress.

S(max) (N/m ²)	Initiation Time	Failure Time
Tungsten Pins (radius 0.1 μm)		
-4.7 X 10 ⁴	40 +/- 1 sec.	1240 min.
-0.7 X 10 ⁴	8 +/- 1 sec.	230 min.
+4.8 X 10 ⁴	3 +/- 1 sec.	1320 min.
Ogura Pins (radius 2 μm)		
-7.3 X 10 ⁴	1260 +/- 5 min.	-
-0.7 X 10 ⁴	360 +/- 5 min.	-
+9.8 X 10 ⁴	48 +/- 1 min.	-

epoxy network influences its electrical strength, being a maximum when the network is completely random. Another interesting feature shown in figure 6.7, is that the growing electrical tree exerts an additional compressive stress in the pin-plane region, as the ZSP is observed to move away from the pin-tip as the tree approaches it.

The tree initiation times may be related to the amount of damage required for the pin-resin interface to de-bond. This will be higher for compressive stresses as the resin is being pressed onto the pin-tip whilst for tensile stresses the resin is effectively being pulled from the pin-tip.

6.5. The Effect of Voltage and Pin-Plane Spacing on Tree Initiation and Growth in CY1311 Resin

It was suggested in the video tree growth study that different tree growth mechanisms may be responsible for the 3 regions of different growth behaviour. Further, for the early samples, 'monkey puzzle' tree growth only ensued if the initial rapid tree growth exceeded $100\mu\text{m}$ before passivation. In an attempt to understand the reasons for this, the effect of both stressing voltage and pin-plane geometry on the early stages of tree growth were investigated.

6.5.1. Experimental

A set of pin-plane CY1311 epoxy resin samples were used to determine the effect of voltage (V) and pin-plane spacing (d) on tree initiation and growth. A series of CY1311 epoxy samples containing embedded tungsten pins of essentially the same pin-tip radius (r) of $0.11 \pm 0.1\mu$ with either an approximately constant pin-plane spacing (d) of $1.8 \pm 0.2\text{mm}$, or a range of d varying from 0.8 mm to 2.6 mm were used.

All the tests were performed between 13 and 18 days from sample manufacture, i.e., the centre of the time span in which the material is in compression throughout the pin-plane region and a 'monkey puzzle' type tree growth occurs. Samples were mounted on the circular polariscope (see section 4) taking care not to introduce



additional mechanical stress when clamping. With the circular polarisers removed, the initiation time and radial extent of the tree after 1 hour were determined. The arbitrary criteria for the initiation time was the time after the test voltage was reached for a $3 \pm 1 \mu$ crack to form at the pin-tip, as assessed by visual microscopic observation. The voltage was initially applied by linear ramping, taking approximately 2 seconds to reach the final test voltage.

6.5.2. Results

Figure 6.8 shows the initiation time and the radial extent (Re) of the tree after 1 hour stressing versus applied voltage. In both cases a sudden change occurs at a particular voltage indicating that a (different) critical voltage may exist for rapid initiation and rapid growth of the tree. In both cases the individual samples show a remarkable consistency in their behaviour which we suggest is due to the similarity of the residual mechanical stress field in all the samples.

Figure 6.9 shows the initiation time and the tree radial extent after 1 hour as a function of the pin-plane spacing. The fixed test voltage (3.20kV rms) was chosen merely to facilitate the measurement of the initiation time. The strong dependence of both initiation time and the tree radial extent on the pin-plane spacing show that both parameters are field driven.

6.5.3. Discussion

The actual field at and in the region of the pin-tip is not simply determinable and depends in a complex way on V , r , d , sample geometry (slab in this work) and the magnitude and distribution of the injected space charge. It is useful to explore if the above data may be used to separate or gauge the significance of any of these parameters. Plots (not illustrated) of the initiation time and the tree radial extent versus $E'(\max)$ (the maximum field at the pin-tip assuming no space charge) show a completely uncorrelated behaviour. Figure 6.10 shows the initiation time and figure 6.11, the tree radial extent as a function of the average applied field (i.e. V/d). Both

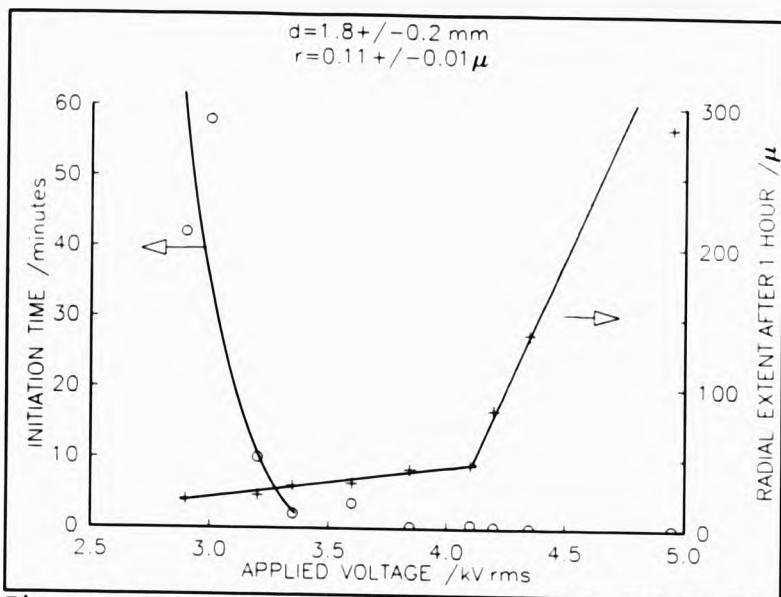


Figure 6.8. The initiation time and radial extent as a function of voltage in CY1311 resin.

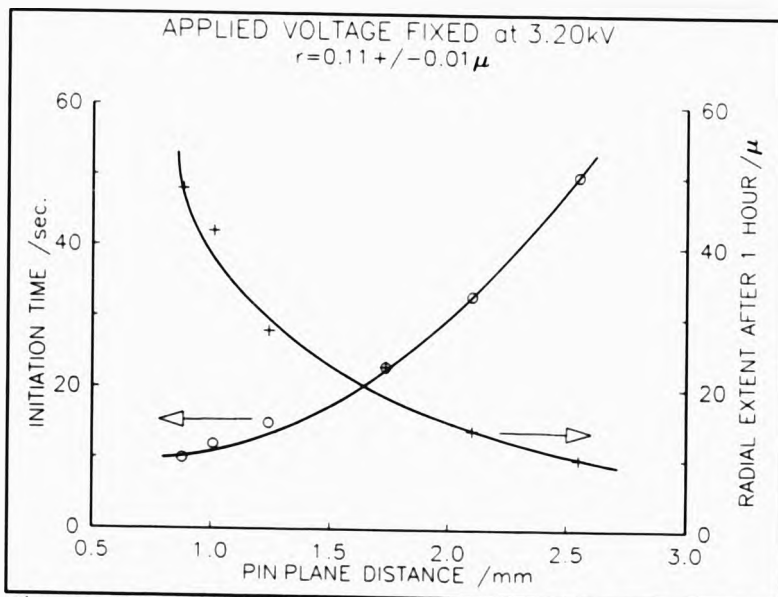


Figure 6.9. The initiation time and radial extent as a function of pin-plane spacing for CY1311 resin.

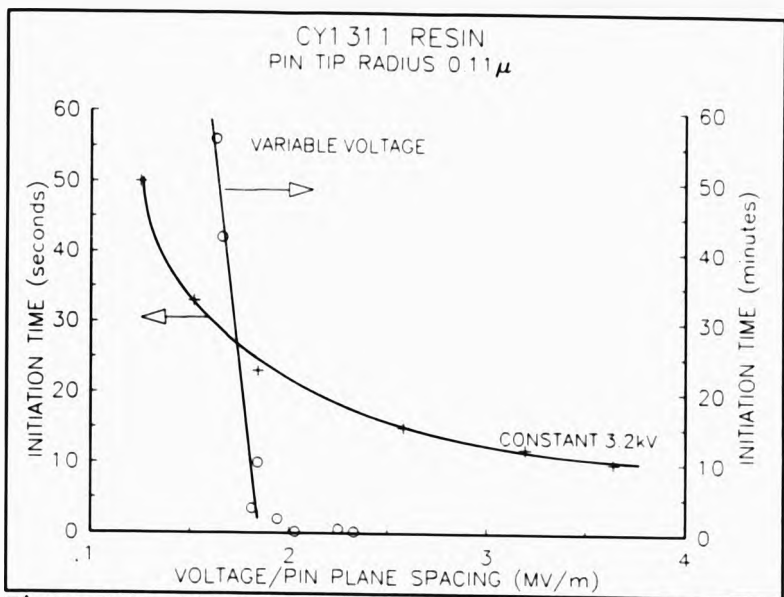


Figure 6.10. The initiation time as a function of average field.

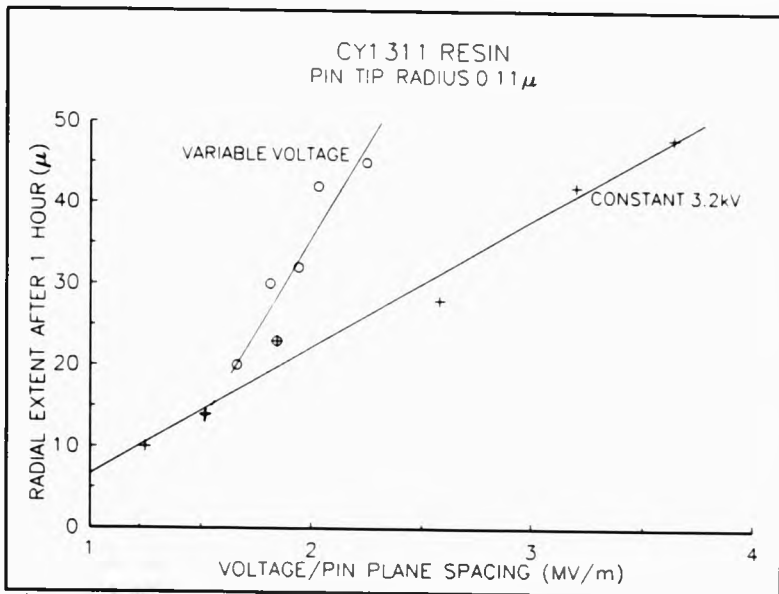


Figure 6.11. The radial extent as a function of average field.

the constant applied voltage (3.20 kV) with variable d and the approximately constant d (1.64 - 2.01 mm) with variable voltage data are shown separately. The values of V/d have been calculated from individual values of d for each sample, and the variable voltage data spans 2.9 kV to 4.2 kV. The reduced scatter in these plots suggest that the average field (V/d), may be a more realistic controlling parameter, rather than just the applied voltage alone.

Figures 6.10 and 6.11 both show that V and d are not separable parameters but play different roles in their contribution to the electric field in the region of the pin-tip. The voltage plays the more dominant role in that small changes can produce large changes in initiation times or tree radial extent whilst proportionally similar changes in d have a weaker effect. Figure 6.10 also suggests that a threshold field for initiation may exist as a material parameter as given by the variable voltage curve, whilst changes in d at constant voltage modify smoothly the magnitude of the field enhancement in the region of the pin- tip. Further data using a range of pin-tip radii and other resin materials are required to confirm these suggestions.

The radial extent after 1 hour decreases by over 50% with an increase in the pin-plane spacing from 1mm to 2.5mm. Hence, the pin-plane geometry is playing an important role in the initial tree growth. Neglecting space charge effects, Mason's expressions [97] for the electric field enhancement and electric field along the pin axis direction, can be used as a basis for modelling the initial tree growth. The maximum field at the pin-tip, E_{max} , is given by,

$$E_{max} = \frac{2V}{r \cdot \ln(1 + 4d/r)} \quad (6.1)$$

The electric field along the pin axis direction, E_z , can be calculated from,

$$E_z = \frac{E_{max}}{1 + 2z/r} \quad (6.2)$$

where d is the pin-plane spacing, r is the pin radius, V is the peak stressing voltage, and where z is the distance from the pin-tip along the pin axis direction towards the plane.

A simple model describing the general form of tree passivation can be constructed by assuming that damage can only be formed above a critical field E_{crit} ; if this damage is conducting it will in turn modify the local field condition by reducing the pin-plane separation and increasing the apparent pin-tip radius. This model therefore has some of the features of the model proposed by Bahder et al. [111]. The essential difference is that to model channel growth, the Bahder model assumes a constant radius of curvature to calculate the field enhancement at the channel tip [9]. The model proposed here, says nothing about the growth mechanism, only that it is a field driven process.

The model is constructed as follows, the maximum field at the pin-tip, E_{max} , may be calculated using equation 6.1. From equation 6.2, the distance along the z axis, z_c , where the electric field is equal to a material dependent critical field, E_{crit} , can then be determined. If it is assumed that material damage occurs over part of this distance, say one tenth, and that the damage can be approximated as an spherical extension of the pin-tip, then the pin-plane distance is reduced by z_c and the pin radius increases by z_c .

Repeating this procedure with the new values of d and r , it is found that after many repetitions, the new r value, which is a measure of the radial extent of material damage, increases rapidly before converging to a fixed value. This is shown in figure 6.12, for a pin voltage of 3.2kV rms, pin radius of $0.1\mu\text{m}$, a critical field of 17MV/m and for various pin-plane spacings ranging from 1mm to 3mm. Although this simple model over estimates the tree radial extent at tree passivation, the functional behaviour of the tree radial extent with pin-plane separation is the same as that found experimentally.

The initial tree growth therefore may be considered to be driven by the high electric field that exists at the pin-tip and determined by the sample geometry as well as the

applied voltage. This explains the differences in the radial extent of the initial tree growth phase of notionally similar samples used in the video tree growth study. In table 6.2, the radial extent of the initial tree growth before passivation is tabulated along with the pin-plane separation for the three samples used in the video tree growth study. Samples C11/11/2 & 3 having similar pin-plane separation, have the

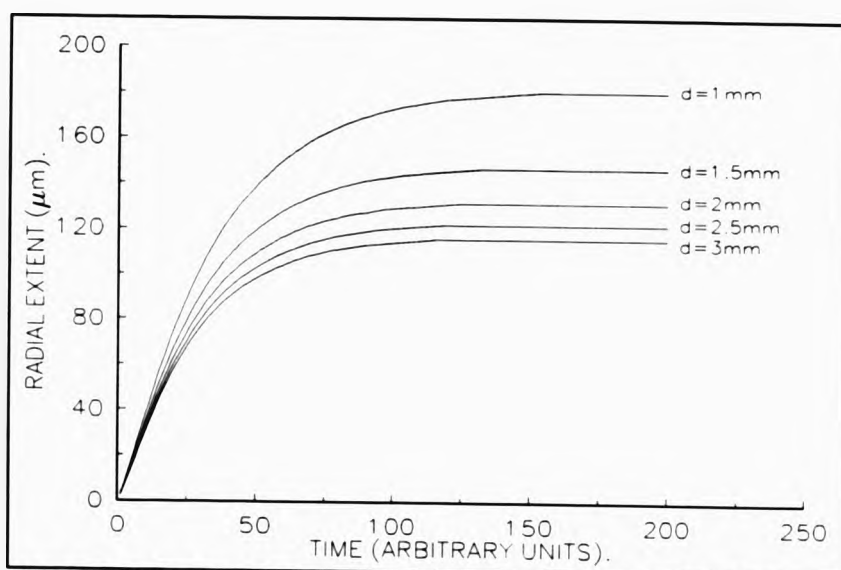


Figure 6.12. Results from the initial tree growth model.

Table 6.2. Effect of pin-plane distance in initial tree growth for the samples used in the video tree growth study

SAMPLE	PIN-PLANE SEPARATION (mm)	RADIAL EXTENT OF INITIAL TREE GROWTH (μm)
C11/11/2	1.86 +/- 0.05	105 +/- 1
C11/11/3	1.93 +/- 0.05	120 +/- 1
C11/11/5	2.50 +/- 0.05	60 +/- 1

largest tree radial extent of initial tree growth before passivation, whilst sample C11/11/5 with the significantly larger pin-plane separation, has the smallest radial extent of tree growth before passivation.

The results of this simple model, shown in figure 6.12, can be directly compared with the radial extent versus time behaviour measured during the video tree growth study. The radial extent of samples C11/11/2, 3 and 5, are reproduced in figure 6.13, using a linear axis, for the first 5 minutes of tree growth. These show a remarkable similarity to the predicted tree growth behaviour of the simple tree growth model.

This field driven degradation model can also be used to explain the tree growth behaviour observed by Yoshimura et al. [112] in crosslinked polyethylene, and in particular by Ieda and Nawata [13] in polyethylene at 30°C and 80°C. The predicted tree growth using the model for a hypothetical sample with pin-plane distance of 3mm, material dependent critical field of 11MV/m and voltages ranging from 6 to 16kV rms is shown in figure 6.14. This behaviour mirrors the 80°C polyethylene data where an inflection in the tree extension versus time behaviour occurs at the higher voltages. This suggests that the tree growth is solely driven by the electric field. As soon as the initial growth reaches half the pin-plane distance, runaway tree growth ensues and the tree rapidly accelerates towards the plane electrode.

The lower temperature behaviour, similar to the lower voltage predictions in figure 6.14, can be explained by an increase in the critical breakdown field as the temperature is lowered from 80°C to 30°C. However, a decomposition gas pressure effect is observed in the 30°C polyethylene data, suggested by the reduction in tree extension and change in tree character for voltages greater than 12kV. This is likely to be real, unless samples of widely differing pin-plane separation were used for their measurements.

These results demonstrate that the pin-plane geometry can influence electrical tree initiation and the early stages of tree growth. The pin-plane distance is a crucial parameter controlling tree growth, passivation and hence, the time to failure. The video tree growth study has shown that 'monkey puzzle' tree growth in samples less

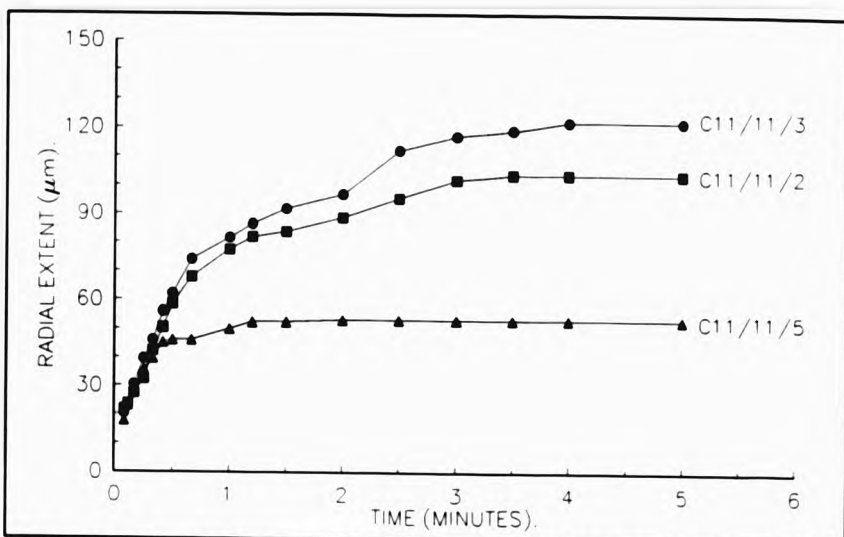
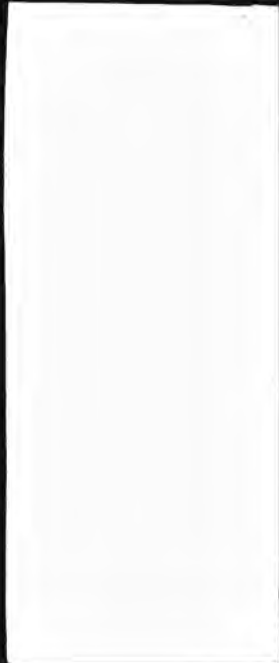


Figure 6.13. The early growth of electrical trees in CY1311 epoxy resin with time, from the video tree growth data.

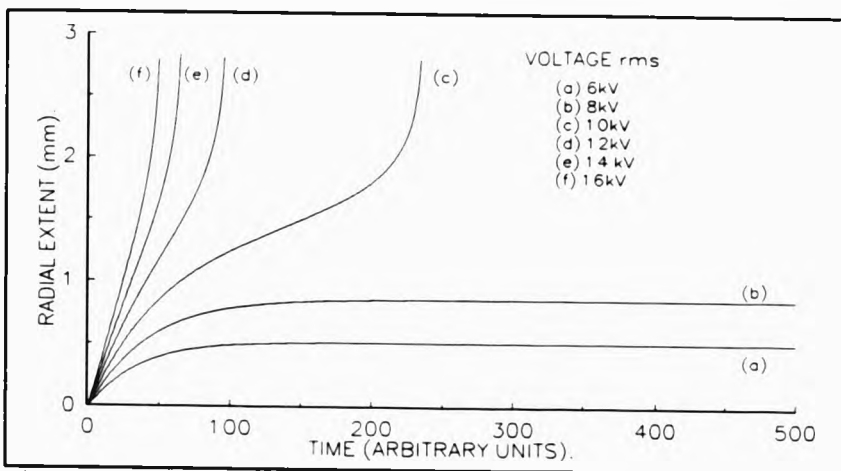


Figure 6.14. Tree growth model predictions for various voltages.

than 30 days old, only ensues once the initial tree radial extent exceeds $100\mu\text{m}$ otherwise passivation of the tree growth occurs. The reason why 'monkey puzzle' tree growth requires a minimum initial tree length will be addressed in the next

section as part of a more general inquiry into the tree growth mechanisms in CY1311 epoxy resin.

6.6. CCD Imaging of Light Emission during Tree Growth

The observation that the form of tree growth in CY1311 epoxy resin depends on age and the region within the pin-plane space are suggestive that different tree growth mechanisms may be responsible. So far, only the consequences of these growth mechanisms (the electrical trees) have been examined in detail and in order to gain further insight into the tree growth dynamics, the electrical discharge activity within the growing trees must be determined. This has usually been done by spatially detecting the light emission from the growing tree channels using a image intensifier tube, for example, Shibuya [2] or Laurent and Mayoux [6]. Recently, high sensitivity charge coupled device (CCD) cameras have become available, which offer much higher sensitivity and linearity than an image intensifier tube. In this section a Peltier cooled CCD camera was used to image the light emission and hence the electrical discharge activity from the different types of growing trees which are observed in CY1311 epoxy resin.

6.6.1 Experimental

The experimental arrangement is shown in figure 6.15. A Wright Instruments Peltier cooled CCD camera was used to detect and image the light emission. The CCD chip has 600 by 400 pixels, each of size $25\mu\text{m} \times 25\mu\text{m}$. The light collection optics used a 50mm, F1.4, camera lens, and the image-lens and object lens distance set to give a X5 optical magnification. Each pixel of the CCD chip therefore represents an object area of $5\mu\text{m} \times 5\mu\text{m}$. The CCD quantum efficiency is 15% over the spectral range 500nm to 900nm, and the dark noise, 0.1 electrons per pixel per second. The CCD readout electronics has a noise level of 10 electrons per pixel and so an exposure time of 100 seconds will give optimum sensitivity. For exposure times less than this, sensitivity will be reduced due to the fixed readout noise.

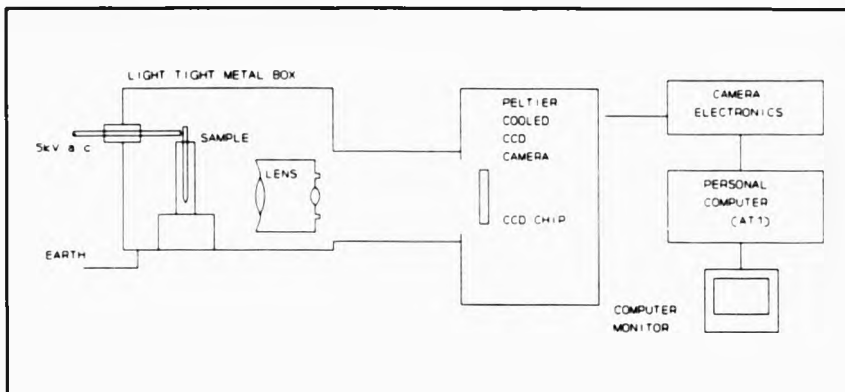


Figure 6.15. CCD imaging experimental arrangement.

CY1311 epoxy resin pin-plane samples with embedded tungsten pins were used. The stressing voltage was 5kV rms for all samples to ensure rapid tree initiation and growth. An exposure time of 1 second was used in order to capture the quickly changing light emission.

6.6.2 Results

Images of the light emission during tree growth are too numerous to include here. Instead only those images relating to significant tree growth events will be reproduced.

Figure 6.16(a), (b) and (c), show colour enhanced images of the light emission during all stages of tree growth in a CY1311 resin sample of age 13 days, and a pin-plane spacing of 1mm. A continuous light emission is observed from the growing tree at the pin-tip for the first two minutes.

After this time, the tree was approximately $100\mu\text{m}$ in length and a switching light emission behaviour was observed, where the light emission throughout the whole tree switches on and off randomly over periods of seconds. The intervals of no light emission become more prolonged with time. This switching behaviour can be identified with passivation of the initial tree growth as observed during the video tree

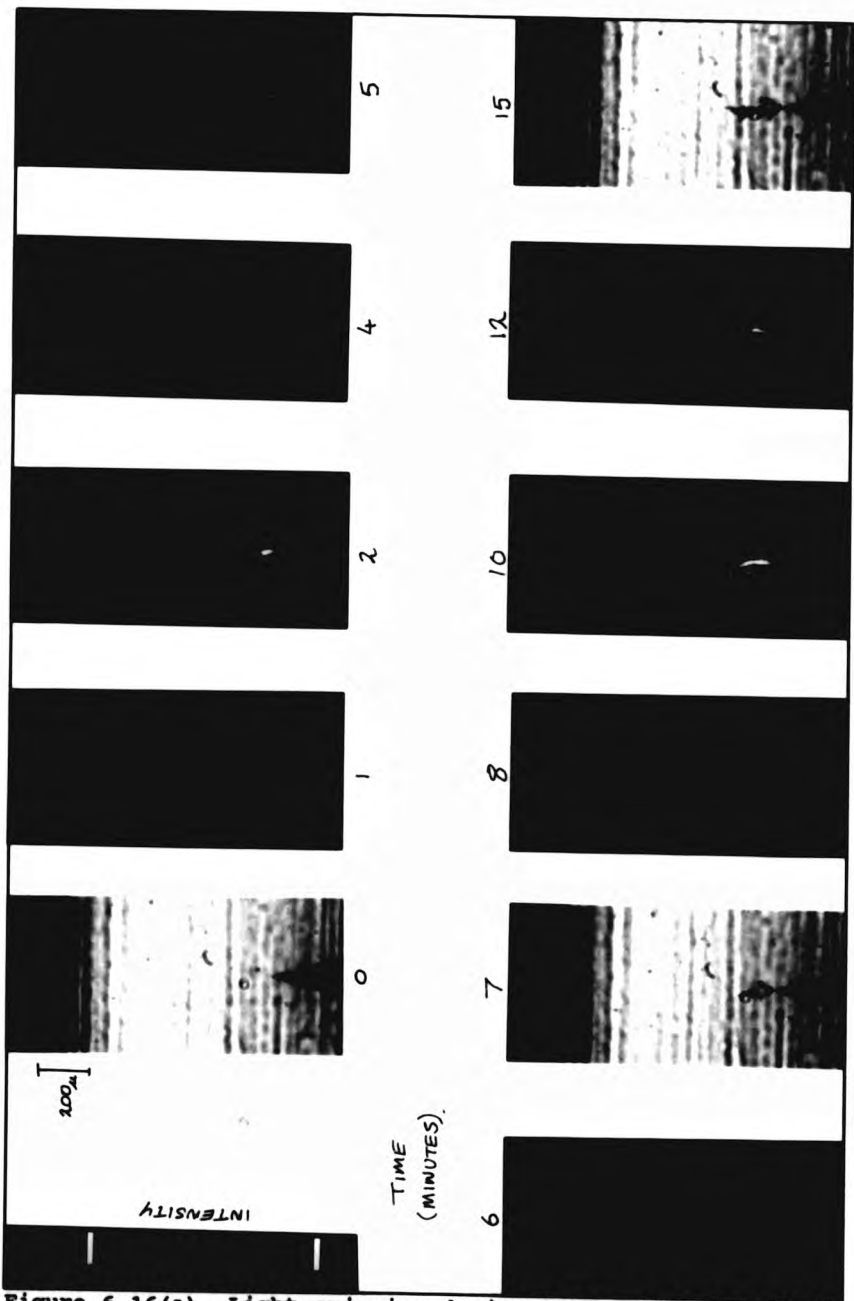


Figure 6.16(a). Light emission during tree growth in CY1311 epoxy resin.

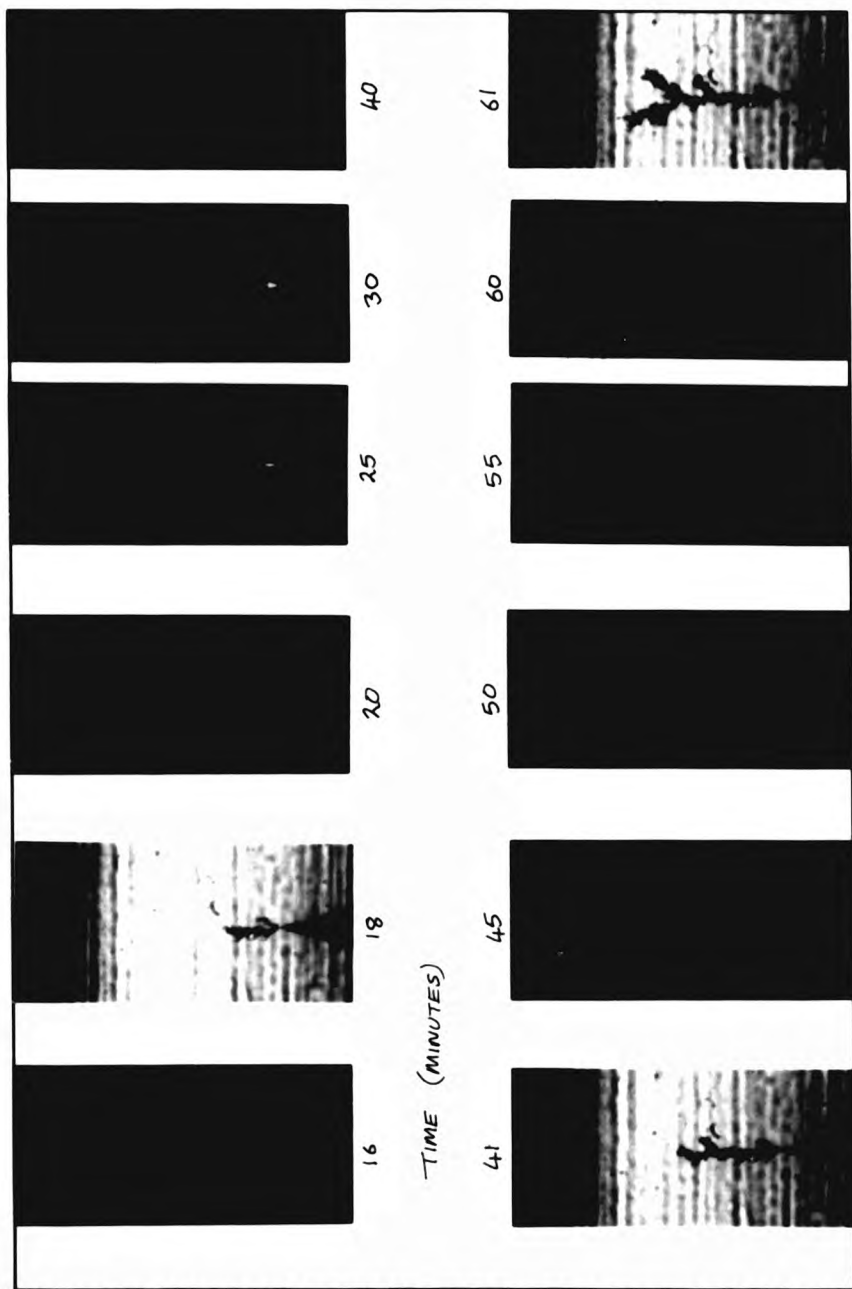


Figure 6.16(b). Light emission during tree growth in CY1311 epoxy resin.

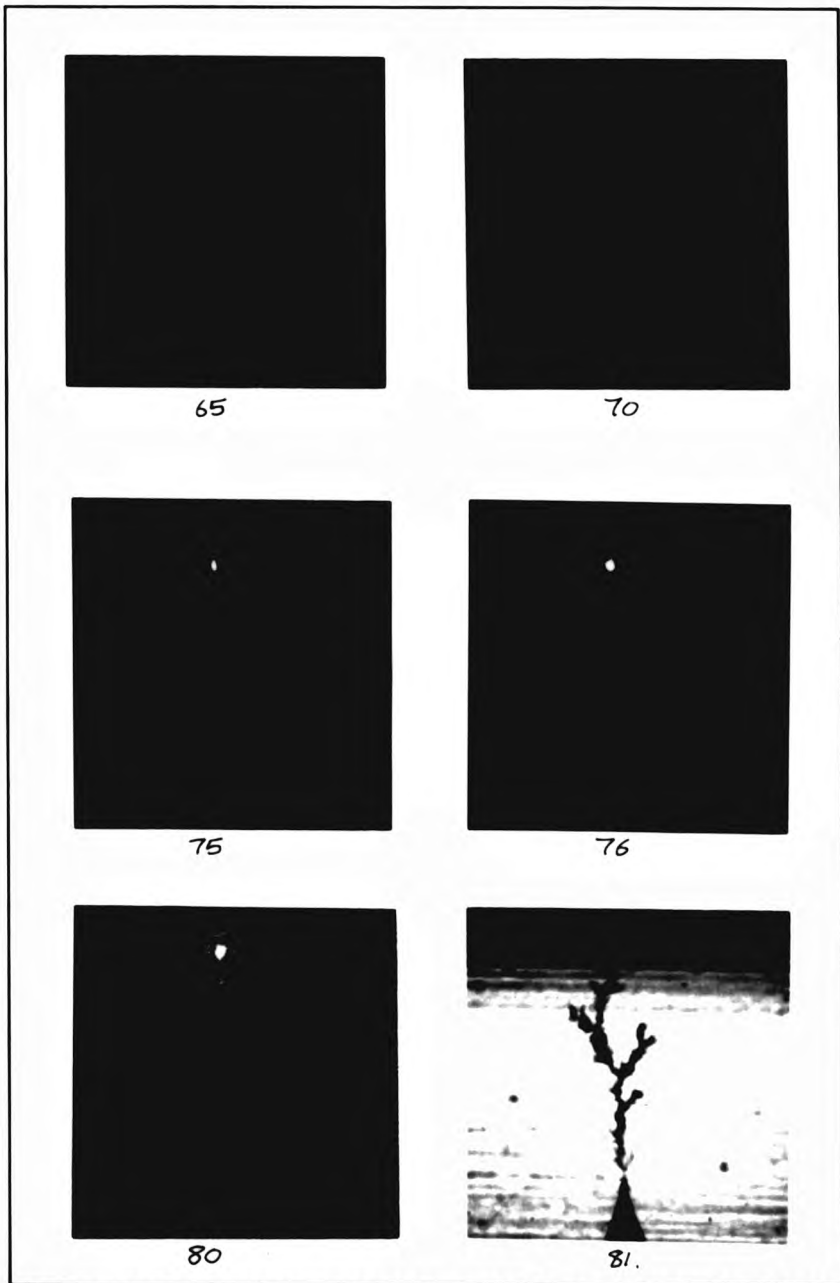
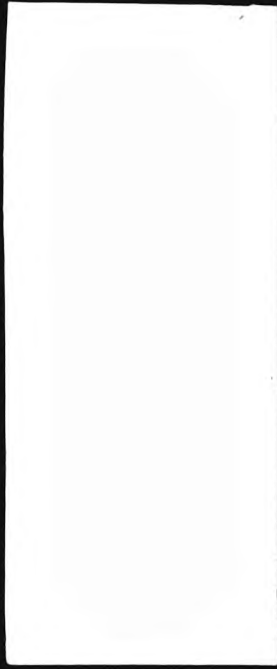


Figure 6.16(c). Light emission during tree growth in CY1311 epoxy resin.



growth study.

After 15 minutes the light emission separated into two cores, one core in the initial tree at the pin-tip and the second originating from the leading tree tip. This second light emission core is associated with back filling of the leading branch to form the beginning of the 'monkey puzzle' tree structure. The light emission core at the tree extremity, slowly moves away from the pin-tip towards the ground plane as the leading tree branch grows.

The light emission from the pin-tip switches off after 36 minutes, leaving just the one light emission core at the extreme of the growing tree.

During tree bifurcation, the single light emission core splits into two, initially with similar intensities, which grow away from each other with similar growth rates.

Further tree bifurcations are observed, the light emission cores splitting as new tree branches grow. All tree branches are found to grow at a rate which appears proportional to the intensity of their light emission core.

The light emission from the leading branch increases in intensity as the branch grows at an increasing rate towards the ground plane. Even after 80 minutes, light emission is observed at the ends of all growing tree branches.

The light emission was also imaged for older CY1311 epoxy samples which do not exhibit 'monkey puzzle' type tree growth. In this case, light emission is observed throughout the growing tree as shown in figure 6.17. The more intense light emission was found in the larger channels near the pin-tip and light emission just noticeable at the ends of the fine tree channels. This mode of light emission behaviour is similar to that observed during the initial rapid tree growth found in all samples as well as the light emission from the 160 μ m tree grown in CT200 described in the previous chapter.



Figure 6.17. Light emission from electrical trees grown in CY1311 epoxy resin with a sample age greater than 40 days.

6.6.3. Discussion

Use of CCD detection techniques to image the light emission behaviour in electrical trees has been used to determine the electrical discharge activity for different types of electrical tree growth in CY1311 epoxy resin.

For samples less than 30 days old exhibiting 'monkey puzzle' tree growth behaviour, the electrical discharge activity is localised at the growing tree tips. This type of discharge activity is very similar to that found by Laurent and Mayoux [6], in polyethylene. As CY1311 resin samples were not subjected to an elevated temperature post cure, it is believed that 'monkey puzzle' tree growth is associated with incomplete cure of the resin. This suggests the tentative idea that unreacted chemical species in the partially cured resin, enters the gas phase at the tree tip perhaps by local heating, which then breaks down in the high field to sustain the local discharge. The discharge activity causes further erosion of the incompletely cured resin, accessing fresh resin where the process continues. The fact that separate regions of light emission are observed at the ends of all growing tree tips and that tree bifurcation only occurs within these regions, suggest that either surface conductivity of the tree channel walls or the presence of trapped wall charge plays an essential role. If the resin has cured sufficiently, as is the case with samples greater than 40 days old, then this growth mechanism does not occur and tree growth will

proceed via a different mechanism. This explains the differences in the tree character with material age.

It is also found that the rate of tree growth appears proportional to the light emission intensity. As further tree bifurcations occur, the light emission in all but the leading branch diminishes, with a subsequent decrease in the tree branch growth rate. The localised light emission in the leading branch is found to increase in intensity as it accelerates towards the plane electrode. This is consistent with a field driven process.

The initial rapid tree growth found in all samples is driven by the high electric field at the pin-tip. The discharge activity occurs throughout the tree and hence is similar to the tree growth found in the older samples, greater than 40 days old, where 'monkey puzzle' tree growth is not observed. This suggests that the same tree growth mechanism is responsible. Passivation of the initial tree occurs once the tree extends beyond the high field enhancement region near the pin-tip. Passivation is associated with the switching behaviour of the discharge activity throughout the tree where periods of quiescence are interdispersed with random pulses of discharge activity. The resulting tree growth will therefore be intermittent and rather slow.

The requirement that the initial tree radial extent must exceed $100\mu\text{m}$ before the onset of 'monkey puzzle' tree growth can now be explained. Firstly, the initial tree growth rate must be sufficiently slow or even stop for the slower 'monkey puzzle' tree growth process to operate. This requirement is met when the initial tree growth passivates as the tree grows out of the high field enhancement region, and will depend on the applied voltage and pin-plane separation. Secondly, the radial extent must be sufficiently large, to allow a separate local discharge activity to be sustained at the tree tip, which initially causes back filling of the leading branches before the onset of 'monkey puzzle' tree growth. For older samples greater than 40 days old, 'monkey puzzle' tree growth does not occur, and tree growth continues via the same mechanism as the initial tree growth. As the electrical discharge behaviour has large periods of quiescence interdispersed with random bursts, the tree growth is characterized by passivation and random side branch tree growth.

6.7. Conclusions

CY1311 epoxy resin has been shown to be a useful material for the study of electrical tree initiation and growth in synthetic resins. Various non-evasive optical techniques have been used to monitor the tree growth behaviour in this resin and have highlighted a number of important factors governing tree initiation and growth.

- 1) Tree form depends on the age of the material. For samples of age less than 30 days 'monkey puzzle' tree growth occurs (see figure 6.1), whilst for samples greater than 40 days, a fine branch structure grows forming a dense bush (see figure 6.3). For samples of age between these limits composite structures are formed (see figure 6.2).
- 2) From the video tree growth study, three different regions of tree growth behaviour have been identified as the tree grows from the pin to the plane electrode. An initial rapid tree growth is observed at the pin-tip followed by slower mid region, which is then followed by a more rapid tree growth region as the tree approaches the plane electrode.
- 3) The effect of RIMS and externally applied mechanical stress has been assessed and it is found that high tensile or compressive mechanical stress, or a region of zero RIMS which marks the transition from a region of tensile to compressive stress, impede tree growth. Tree initiation times are also found to vary, a high tensile stress reduces the initiation time, whilst a large compressive stress will increase the initiation time.
- 4) Electrical tree initiation and early stages of tree growth depend on the applied voltage, V , and the pin-plane separation, d . Combining these two parameters to form a new parameter, V/d , (effectively the average field), reduces significantly the scatter in the tree initiation times, suggesting that this parameter may be a better descriptor for the field dependence of tree initiation, as it takes into account differences in the pin-plane separation in the different samples. The radial extent of the initial tree growth before passivation, depends inversely on the value of d . A model of tree

growth is proposed which explains this behaviour. This model assumed that damage can only be formed above a critical field and if conducting, will in turn modify the local field condition. Passivation occurs when the field at the extremity of the damage fall below the critical field.

5) CCD imaging of the light emission during tree growth reveals that two different tree growth mechanisms are responsible for the different tree characteristics with age of material. The differences in the tree growth mechanisms can be explained as due to incomplete cure of the resin for samples less than 30 days old.

6) The light emission during 'monkey puzzle' tree growth was found to be located at the tips of the growing branches with an intensity which appears proportional to the growth rate. During tree bifurcation, the localised light emission splits into 2 separate regions each associated with a tree channel which then grow away from each other.

7) The initial tree growth must exceed a critical length (dependent on voltage and pin-plane spacing) before 'monkey puzzle' tree growth ensues, otherwise substantial periods of tree passivation will occur.

Chapter 7

Final Discussion and Overall Conclusions

The work presented in this thesis has demonstrated that non-evasive optical techniques can be successfully used to quantitatively assess resin inhomogeneity (microstructure) and the residual internal mechanical stress in pin-plane resin samples. Further non-evasive optical techniques were successfully used to probe resin degradation mechanisms during electrical tree initiation in pin-plane samples and to clarify some of the factors that cause or can influence tree growth. In the following sections, the achievements and key results will be discussed.

7.1. Material Characterization

Before any serious studies on the effect of material properties on tree initiation and growth can be undertaken, techniques to quantitatively characterise these material parameters need to be developed. Two such techniques to characterise resin inhomogeneity and residual internal mechanical stress in pin-plane samples are presented here for the first time. Whilst residual internal mechanical stress has been shown to have a significant affect on electrical treeing, the influence of resin inhomogeneity has yet to be fully investigated.

7.1.1. Resin Microstructure

Light scattering measurements and subsequent analysis has shown that microstructure exists in both CT200 epoxy and unsaturated polyester resins. In both resin systems, the microstructure was found to be inhomogeneities having a log-normal size distribution of modal diameter $0.01\mu\text{m}$ and geometric mean standard deviation ranging from 0.7 to 1.0. The inhomogeneity relative refractive index value for best fit was 1.01 corresponding to density fluctuations of 2% within the resin. However, due to the insensitivity of light scattering theory to changes in relative refractive index, the density fluctuations could be as high as 20%.

The microstructure concentration in CT200 epoxy resin samples was found to vary by up to 2 orders of magnitude, depending on the sample preparation technique. Microgelation occurs after filtration of the uncured resin when the butanone solvent is removed and before the resin is cured. Insignificant additional microstructure forms during resin cure. By controlling the sample preparation procedure, fully cured CT200 samples can be prepared covering a wide range of microstructure concentration and opens the way for a comprehensive quantitative investigation of resin morphology on tree growth for the first time. Significant microstructure exists in the material supplied by the manufacturer, formed during the manufacture process. Hence, unless quality control is high during the manufacturing process, different batches of notionally the same material may contain a wide range of microstructure concentration. This may have important consequences in industry, where large quantities are used, as the microstructure content of the as supplied resin may influence its mechanical and electrical properties.

Significant microstructure is also found in the polyester resin and is due to microgel particles in the 'as received' resin with the microgel concentration depending on batch and microstructure which formed during the cure reaction. The full power of the non-evasive light scattering technique was utilised to investigate microstructure formation during polyester resin cure. It was found that the observed microstructure results from an inhomogeneous cure reaction arising essentially from the non-stoichiometric excess of styrene monomer and the early gelation in this resin.

7.1.2. Residual Internal Mechanical Stress

Polarised light measurements to determine the residual internal mechanical stress (RIMS) in pin-plane samples has shown that in the case of CT200 epoxy resin, a compressive stress exists within the material with the maximum stress at the pin-tip. This mechanical stress is near the compressive strength of the material and failure often occurs near the pin-tip, with the formation of microscopic cracks which relax the surrounding stress. This explains the low production success rate when manufacturing samples with good pin-resin interfaces. The RIMS forms as a result of the different thermal expansion coefficients of the metal pin and resin as the samples



cool after post cure at 150°C. The magnitude of the stress at the pin-tip is found to decrease with time, with a time constant of approximately 4 years. This occurs as a result of structural relaxation (physical ageing) of the materials. The age of the sample is an important parameter in electrical breakdown studies.

For unsaturated polyester resin, the RIMS is found to be tensile due to the large volume shrinkage that occurs during resin cure. This explains the loss of adhesion between the metal pin and resin which is found to occur in the majority of polyester samples as the tensile nature of the RIMS is effective at pulling the resin away from the pin. The RIMS is also found to increase by 100% in 50 days due to structural relaxation, making this resin less attractive than CT200 for both tree initiation and growth studies.

Pin-plane samples made from CY1311 epoxy resin (a flexible material cured at room temperature) were found to have very low RIMS which changed from compression to tension with age. The compressive RIMS arising from an exothermic cure reaction and the tensile RIMS which occurs at the sample plane is due to water vapour absorption and subsequent swelling of the resin.

A symmetric beam bending technique has also been developed to apply a known compressive or tensile stress to pin-plane samples without destroying the stress symmetry which is required for correct analysis of the polarised light. When the pin shank diameter is less than 7% of the sample thickness the overall mechanical stress, i.e. RIMS plus externally applied stress is simply additive. This is not the case for larger pin shank diameters. Using this technique, the effect of mechanical stress, i.e. both RIMS and externally applied stress, on tree initiation and growth may be studied quantitatively for the first time.

7.2. Electrical Breakdown Studies

Electrical tree initiation in CT200 epoxy and unsaturated polyester resin has been studied in detail using ultra sensitive synchronous light emission detection techniques. For the bulk of the work an ultra sensitive photomultiplier tube having a dark count

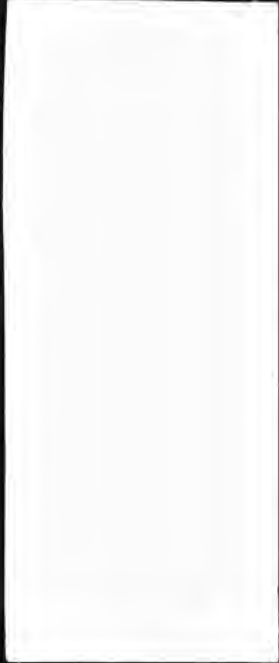
of 1.2 photon counts per second was used. To complement these results, a liquid nitrogen cooled charge coupled device (CCD) camera was utilised. Having a sensitivity 40 times that of the photomultiplier, this was used to detect and spatially resolve the light emission during tree initiation.

Tree initiation and growth in CY1311 epoxy resin^{has been investigated} using a range of non-invasive optical techniques. Video recording of the tree growth was utilised to extract which would otherwise be missed if just photographic recording was used. Tree growth was examined over a range of sample age, stressing voltages, pin-plane spacings and mechanical stress. Partial discharge activity within the growing tree channels was recorded by spatially detecting the faint light emission using a Peltier cooled CCD camera.

7.2.1. Electrical Tree Initiation in CT200 Epoxy and Polyester Resin

Quantitative light emission studies of the tree initiation and early growth stages of electrical failure in CT200 epoxy and unsaturated polyester resins has been undertaken. From short term step ramp tests, it has been shown that 3 types of light emission are observed consistently and relate to:

- 1) Electroluminescence due to charge injection, where a steady light emission is observed and can be described by either a Schottky or Fowler-Nordheim process depending on the magnitude of the electric field at the pin tip. No evidence is found for a material dependent threshold voltage or field for charge injection and electroluminescence. No material damage is observed at the pin tip in the short term.
- 2) Pulsating light emission with a material dependent threshold voltage, which is associated with micro-discharge activity and where microchannels are formed.
- 3) Rapidly fluctuating light emission, whose intensity increases with time and first appears when the tree channels are greater than about $10\mu\text{m}$; this is associated with partial discharge activity and tree growth.



In addition, longer term voltage stressing of CT200 epoxy resin in the electroluminescence region reveals some interesting reversible and non-reversible light emission behaviour. The initial reversible behaviour of the electroluminescent intensity has led to the development of a deep trap charge carrier recombination model for the mechanism of electroluminescence. The irreversible light emission behaviour has been used to interpret the key steps leading to tree initiation. An eventual transition from electroluminescence to micro-discharge behaviour (tree initiation) is found to occur, via. material degradation due to continued charge injection and extraction, followed by interface failure, (i.e. debonding of the pin-resin interface) which in turn is followed by micro-channel formation and tree growth.

The extra X40 sensitivity of the CCD camera over the photomultiplier extends the view that no experimental evidence currently exists to indicate that a material dependent voltage or field threshold exists for charge injection and electroluminescence. CCD imaging of the electroluminescence, has shown that the electroluminescence and hence, injected charge, is concentrated at the pin tip and extends at least $10\mu\text{m}$ into the resin. Imaging of the light emission within a mature $160\mu\text{m}$ tree in CT200 epoxy resin, has shown that the mechanisms of passivation and the random switching behaviour of discharges will be of fundamental importance in the prediction of tree growth times.

7.2.2. Tree Growth in CY1311 Epoxy Resin

Detailed tree initiation and growth studies in CY1311 epoxy resin samples has highlighted some of the factors that influence electrical breakdown in this material. Sample age, voltage, pin-plane spacing, mechanical stress and a region of zero internal mechanical stress between the pin and plane electrodes all have a significant effect on electrical tree growth. The early rapid tree growth, near the pin electrode, was found to be driven by the high electrical field. Tree growth slows and passivation of partial discharges can occur as the tree grows away from the high electrical field enhancement region which exists near the pin-tip. CCD imaging of the light emission during tree growth has shown that at least two different tree growth

mechanisms can occur depending on the age of the sample and leads to a very different form of tree growth.

7.3. Concluding Remarks

The non-evasive optical material characterization techniques developed in this work will contribute significantly to the study of electrical breakdown in synthetic resin insulation by opening the way for a comprehensive quantitative study of the effect of resin morphology and mechanical stress on tree initiation and growth. The effect of resin morphology and other material parameters, especially fracture toughness are worthy of study and will lead not only to a better understanding of the resin itself, but also, the mechanisms of electrical failure.

Measurement of the light emission during all stages of electrical breakdown is a sensitive probe of the physical mechanisms responsible for tree initiation and growth. Recent advances in ultra-sensitive CCD imaging techniques is likely to make this a powerful tool in the study of electrical breakdown and the extra sensitivity over more traditional detection techniques may open the way for a full spectroscopic study of the low intensity light emission during tree initiation and growth.

The large variability in the resin microstructure, internal mechanical stress and tree growth found in supposedly similar samples, gives rise to serious concerns as to the usefulness of previous studies of electrical breakdown in resin insulation where these factors have not been fully considered. Only after a comprehensive study of the inter-relationships between the many resin parameters that influence tree initiation and growth, can the mechanisms of tree growth be fully understood and lead to the development of useful models for insulator lifetime prediction. It is hoped that the work described in this thesis will at least in part contribute to a fuller understanding of the electrical breakdown mechanisms and the ultimate electrical integrity of insulation systems based on cast resin materials.

References

1. Hibma, T., and Zeller, H.R., 1986, *J. Appl. Phys.*, 59(5), p1614.
2. Shibuya, Y., 1976, Ph.D. Thesis, University of Salford, U.K.
3. Bamji, S.S., Bulinski, A. and Densley, R., 1988, *J. Appl. Phys.*, 61(2), p694.
4. Zeller, H.R. and Schneider, W.R., 1984, *J. Appl. Phys.*, 56(2), p455.
5. Shibuya, Y., Zoledziowski, S. and Calderwood, J.H., 1978, *Proc. IEE.*, 125(4), p352.
6. Laurent, C. and Mayoux, C., 1980, *IEEE Trans. Elec. Insul.*, EI-15(1), p33.
7. Dissado, L.A. and Sweeney, P.J.J., 1992, *Proc. 4th Int. Conf. on Cond. and Break. in Solid Diel.*, Sestri Levante, Italy, p328.
8. Fruth, B. and Niemeyer, L., 1992, *IEEE Trans. Elec. Insul.*, EI-27(1), p60.
9. Dissado, L.A. and Fothergill, J.C., 1992, "Electrical Degradation and Breakdown in Polymers", Ed. Stevens, G.C., Publ. Peter Peregrinus Ltd. (IEE).
10. Cooper, J.M. and Stevens, G.C., 1990, *J. Phys. D: Appl. Phys.*, 23, p1528.
11. Hozumi, N., Ishida, M., Okamoto, T. and Fukagawa, H., 1990, *IEEE Trans. Elec. Insul.*, EI-25(4), p707.
12. Schirr, J., 1972, *Proc. Int. Sym. High Volt. Tech.*, Munich, p457.
13. Ieda, M. and Nawata, M., 1972, *CEIDP, National Academy of Science*, p143.
14. Noto, F. and Yoshimura, N., 1974, *Ann. Rep. Conf. Elec. Insul. & Diel. Phenom.*, p207.
15. Ieda, M. and Nawata, M., 1977, *IEEE Trans. Elec. Insul.*, EI-12(1), p19.
16. McMahon, E.J. and Perkins, J.R., 1972, *Ann. Rep. CEIDP*, p133.
17. Olyphant, M., 1963, *IEEE Trans. PAS*, PAS-82, p1106.
18. Laurent, C., Mayoux, C. and Noel, S., 1983, *J. Appl. Phys.*, 54(3), p1532.
19. Mie, G., 1908, *Ann. Phys.*, 25, p377.
20. Stevens, G.C. and Richardson, M.J., 1983, *Polymer*, 24, p851.

21. Stevens, G.C., "Structural Adhesives: Developments in Resins and Primers", Ed. Kinloch, A.J., Elsevier Applied Science Publishers, 1986.
22. Liddell, P., Ph.D Thesis (CNA), "An Investigation of Local Inhomogeneities in Amorphous Polymers using Light Scattering Techniques", 1979.
23. Mark, H.F. et al, (ed), 1988, "Polyesters to Polypeptide Synthesis" (Encyclopedia of Polymer Science and Engineering vol 12), New York: Wiley.
24. Yang, Y.S. and Lee, L.J., 1988, Polym. Proc. Engin., 5(3 & 4), p327.
25. Perkins, E.A., Ph.D Thesis (CNA), "Investigation of Defect Formation and Growth in Epoxy Resin using Light Scattering Methods", 1989.
26. Ciba Geigy data sheet, No.C.123a, CY1311/HT1300 epoxy resin system, November 1982.
27. Racich, J.L. and Koutsky, J.A., 1976, J. Appl. Polym. Sci., Vol.20, p2111.
28. Yamini, S. and Young, R.J., 1980, J. Mats. Sci., Vol.15, p1823.
29. Morgan, R.J. and O'Neal, J.E., 1977, J. Mats. Sci. Vol.12, p1966.
30. Morgan, R.J., Mones, E.T. and Steele, W.J., 1982, Polymer, Vol.23, p295.
31. Misra, S.C., Manson, J.A. and Sperling, L.H., 1978, Org. Coat. Plast. Chem. Prepr., Vol.39, p152.
32. Wu, W-L., Hu, J-T. and Hunston, D.L., 1990, Polym. Eng. Sci., Vol.30(14), p835.
33. Stevens, G.C., Perkins, E. and Champion, J.V., 1988, 5th Int. Conf. Diel. Mats. Meas. Appl. 27-30 June, IEE Conf. Publ. No. 289, p234.
34. Tanaka, Y., Ohnuma, N., Katsunami, K. and Ohki, Y., 1991, IEEE Trans. Elec. Insul., Vol.26(2), p258.
35. Lewis, T.J., 1990, J. Phys. D: Appl. Phys., Vol.23, p1469.
36. Cartier, E. and Pfluger, P., 1987, IEEE Trans. Elec. Insul., Vol.22(2), p123.
37. Mijovic, J.S. and Koutsky, J.A., 1979, J. Appl. Polym. Sci., Vol.23, p1037.
38. Aspbury, P.J. and Wake, W.C., 1979, Brit. Polym. J., Vol.11, p17.
39. Gupta, V.B., Drzal, L.T., Adams, W.W. and Omlor, R., 1985, J. Mats. Sci., Vol.20, p3439.
40. Yang, Y.S. and Lee, L.J., 1988, Polymer, Vol.29, p1793.

41. Dusek, K., Plestil, J., Lednický, F. and Lunak, S., 1978, *Polymer*, Vol.19, p393.
42. Matyi, R.J., Uhlmann, D.R. and Koutsky, J.A., 1980, *J. Polym. Sci. Polym. Phys. Ed.*, Vol.18, p1053.
43. Uhlmann, D.R., 1979, *Farad. Disc. Chem. Soc.*, 'Organisation of Macromols. in the Condensed Phase', Vol.68, p87.
44. Wu, W-L. and Bauer, B.J., 1985, *Polym. Comms.*, Vol.26, p39.
45. Bai, S.J., 1985, *Polymer*, Vol.26, p1053.
46. Bogdanova, L.M., Belgovskii, I.M., Irzhak, V.I. and Rosenberg, B.A., 1981, *Polym. Bull.*, Vol.4, p119.
47. Stevens, G.C., Champion, J.V. and Liddell, P., 1982, *J. Polym. Sci. Polym. Phys. Ed.*, Vol.20, p327.
48. Dusek, K. and Prins, W., 1969, *Adv. Polym. Sci.*, Vol.6, p1.
49. Zimm, B.H., Price, F.P. and Bianchi, J.P., 1958, *J. Phys. Chem.*, Vol.62, p979.
50. Dusek, K., Galina, H. and Mikes, J., 1980, *Polym. Bull.*, Vol.3, p19.
51. Funke, W., 1982, *Plast. Rubb. Process. Appl.*, Vol.3(3), p243.
52. Ghaemy, M., Billingham, N.C. and Calvert, P.D., 1982, *J. Polym. Sci. Polym. Lett. Ed.*, Vol.20, p439.
53. Bell, J.P., 1982, *J. Appl. Polym. Sci.*, Vol.27, p3503.
54. Kerker, M., 'The Scattering of Light and Other Electromagnetic Radiation', Academic Press, 1969.
55. Van de Hulst, H.C., 'Light Scattering by Small Particles', Dover Publications, 1957.
56. Bohren, C.F. and Huffman, D.R., 'Absorption and Scattering of Light by Small Particles', Wiley Interscience, 1983.
57. Bayvel, L.P. and Jones, A.R., 'Electromagnetic Scattering and its Applications', Applied Science Publishers, 1981.
58. Asano, S. and Yamamoto, G., 1975, *Appl. Opt.*, Vol.14(1), p29.
59. Asano, S. and Sato, M., 1980, *Appl. Opt.*, Vol.19(6), p962.
60. Holland, A.C. and Gagne, G., 1970, *Appl. Opt.*, Vol.9(5), p1113.

61. Pinnick, R.G., Carroll, D.E. and Hofmann, D.J., 1976, *Appl. Opt.*, Vol.15(2), p384.
62. Coumou, D.J., Mackor, E.L. and Hijmans, J., 1964, *Trans. Far. Soc.*, Vol.60, p1539.
63. Ahad, E. and Jennings, B.R., 1970, *J. Phys. D: Appl. Phys.*, Vol.3, p1509.
64. Hariharan, P., 'Optical Holography Principles, Techniques and Applications', Cambridge University Press, 1986.
65. Lowenthal, S. and Joyeux, D., 1971, *J. Opt. Soc. Am.*, Vol.61(7), p847.
66. Ohtsuka, Y. and Imai, Y., 1979, *J. Opt. Soc. Am.*, Vol.69(5), p684.
67. Bevington, P.R., 'Data Reduction and Error Analysis for the Physical Sciences', McGraw-Hill, 1969.
68. Szymansky, W. and Wagner, P.E., 1983, *J. Aerosol Sci.*, Vol.14(3), p396.
69. Sato, T., Yabuzaki, T. and Ogawa, T., 1982, *Japan. J. Appl. Phys.*, Vol.21(11), p1599.
70. Phillips, D.L., 1962, *J. Ass. Comput. Mach.*, Vol.9, p84.
71. Twomey, S., 1963, *J. Ass. Comput. Mach.*, Vol.10, p97.
72. Chow, L.C. and Tien, C.L., 1976, *Appl. Opt.*, Vol.15(2), p378.
73. Backus, G. and Gilbert, F., 1970, *Philos. Trans. R. Soc. London*, Vol.266, p123.
74. Post, M.J., 1976, *J. Opt. Soc. Am.*, Vol.66(5), p483.
75. Wickramasinghe, N.C., 'Light Scattering Functions for Small Particles with Applications in Astronomy', Adam Hilger, 1973.
76. 'CRC Handbook of Chemistry and Physics', Ed. Weast, R.C., 60th ed., CRC press, 1980.
77. Newman, F.H. and Searle, V.H.L., 'The General Properties of Matter', Edward Arnold Publishers, 1962.
78. Nakanishi, k., Hirabayashi, S., and Inuishi, Y., 1979, *IEEE Trans.*, EI-14(6), p306.
79. Campoccia, A., and Schifani, R., 1988, *IEEE Trans.* EI-23(3), p419.
80. Billing, J.W., and Groves, D.J., 1974, *Proc. IEE.*, 121 (11), p1451.

81. Densley,R.J., 1979, IEEE Trans., EI-14(3), p148.
82. Arbab,M.N., and Auckland,D.W., 1989, IEE Proc., 136 (A), p73.
83. Auckland,D.W., McNicol,A.A., and Varlow,B.R., 1990, J.Phys.D: Appl.Phys., 23, p1608.
84. Kuske,A., and Robertson,G., 1977, "Photoelastic Stress Analysis", Wiley, New York.
85. Kihara,T., Kubo,H., and Nagata,R., 1979, Applied Optics, 18(3), p321.
86. Timoshenko,S. and Goodier,J., 1951, "Theory of Elasticity", 2nd.Ed. McGraw Hill, New York.
87. Ciba Geigy, Advance Information Sheet for Photoelastic Stress Analysis, No. M.5b, Febuary 1973.
88. Longhurst,R.S., 1984, "Geometrical and Physical Optics", 3rd Ed., Longman, London.
89. Rudd,J.F. and Andreas,R.D., 1960, J.Appl.Phys., 31, p818.
90. Kong,E.S, Wilkes,G.L, McGrath,J.E., Banthia,A.K., Mohajer,X. and Tant,M.R., 1981, Polm.Eng.Sci., 21(14), p943.
91. Kojima,K., Takai,Y., and Ieda,A., 1982, J.Appl.Phys., 21(6), p860.
92. Laurent,J., Mayoux,C., and Noel,S., 1985, J.Appl.Phys., 58(11), p4346.
93. Baumann,T., Fruth,B., and Stucki,F., 1987, Proc.Fifth Int.Symp.High Volt.Eng.,Braunschweig, p1.
94. Bamji,S.S., Bulinski,A.T., and Densley,R., 1988, J.Appl. Phys., 63(12), p5841.
95. Lebey,T., Laurent,C., and Mayoux,C., 1988, Proc.21st. Symp.Elec.Ins.Mat., p45.
96. Mason,J.H., 1955, Proc.IEE, 102C, p254.
97. O'Dwyer,J.J., 1973, "The Theory of Electrical Conduction and Breakdown in Solid Dielectrics", Clarendon Press.
98. Good,R.H. and Muller,W., 1956, "Field Emission", Handbuch der Physik, Vol.21, Springer Verlarg.
99. Lebey,T. and Laurent,C., 1988, Sec.Int.Conf.Prop.Appl. Diel.Mat., 2, p582.

100. Hozumi,N., Okamoto,T., Fukagawa, H., 1988, *Jpn.J.Appl.Phys.*, 27(7), p1230.
101. Stone,G.C. and Van Heeswijk,R.R., 1988, *Conf.Elec.Ins. Diel.Phen.*, p376.
102. Tanaka,T., and Greenwood,A., 1978, *IEEE Trans. PAS*, PAS-97(5), p1749.
103. Hare,R., and Budd,C., 1992, *Proc.6th Int.Conf.Diel.Mats. Meas.Appl.*, Manchester, UK, p81.
104. Shimizu, Ph.D. Thesis, 1979, "Treeing Phenomena of Polymeric Materials at Low Temperature", Nagoya University.
105. Kao,K.C.,Hwang,W, 1981, 'Electrical Transport in solids', Pergamon Press.
106. Milnes,A.G., 1973, "Deep Impurities in Semiconductors", Wiley, New York.
107. Kelen,A. and Larsson,L., 1967, *Acta Polytechnica Scandinavia*, Vol. EL16, p133.
108. Auckland,D.W., Cooper,J.M. and Varlow,B.R., 1992, *IEE Proc.-A*, Vol.139(1), p9.
109. McMahon,E.J., 1978, *IEEE Trans. Elec. Insul.*, Vol. EI-34 No.4, p277.
110. Auckland,D.W., Borishade,A.B. and Cooper,R., 1975, *Conf. on Diel. Mats. Meas. and Appl.*, IEE Conf. Pub. No.129, p15.
111. Bahder,G., Garrity,T., Sosnowski,M., Eaton,R. and Katz,C., 1982, *IEEE Trans. Power Appar. & Sys.*, PAS-101, p1379.
112. Yoshimura,N., Hamman,M.S.A.A., Nishida,M. and Noto,F., 1978, *Ann. Rep. Conf. Elec. Insul. & Diel. Phenom.*, p342.

Appendix 1

Rayleigh Theory

For particles small compared with the wavelength (less than wavelength/20) the particle is considered to be an induced dipole, placed at the centre of the particle, whose direction is parallel to the incident light polarisation. The induced dipole oscillates at the frequency of the incident light and will radiate light in all directions forming the scattered light. For unpolarised incident light [54], the scattered intensity per unit incident intensity, I_u , is given by

$$I_u = \frac{8\pi^4 a^6}{r^2 \lambda^4} \left(\frac{n_1^2 - n_2^2}{n_1^2 + 2n_2^2} \right)^2 (1 + \cos^2 \theta) \quad (A1.1)$$

Where, a , is the scatterer radius, n_1 , is the medium refractive index, n_2 , is the scatterer refractive index, λ , is the incident light wavelength in the medium, r , is the scatterer to detector distance and θ , is the angle of scatter.

For vertically polarised light [54], and horizontal scattering plane, then the scattered intensity per unit incident intensity is given by

$$I_v = \frac{16\pi^4 a^6}{r^2 \lambda^4} \left(\frac{n_1^2 - n_2^2}{n_1^2 + 2n_2^2} \right)^2 \quad (A1.2)$$

When measuring the scattered light it is customary to use the Rayleigh ratio, $R(\theta)$, which is defined as the energy scattered by a unit volume in the direction θ per steradian, when the medium containing the scatterers is illuminated with unit intensity [54]. $R(\theta)$ is therefore given by

$$R(\theta) = r^2 \cdot N \cdot I_v \quad (A1.3)$$

Where N is the number of scatterers per unit volume. Hence,

$$R(\theta) = \frac{16\pi^4 a^6}{\lambda^4} \left(\frac{n_1^2 - n_2^2}{n_1^2 + 2n_2^2} \right)^2 \cdot N. \quad (\text{A1.4})$$

If the scatterers are anisotropic, then a correction needs to be made, which is known as the Cabbanes factor [54]. For vertically polarised incident light the Cabbanes factor, C_v , is given by,

$$C_v = 6 / (6 - 7\Delta_v), \quad (\text{A1.5})$$

where Δ_v is the depolarisation, i.e. the ratio of the horizontal and vertical components of the scattered light. Hence,

$$R(\theta) = \frac{16\pi^4 a^6}{\lambda^4} \left(\frac{n_1^2 - n_2^2}{n_1^2 + 2n_2^2} \right)^2 C_v N. \quad (\text{A1.6})$$

We note that for Rayleigh scatterers, the scattered light is isotropic in this case for vertically polarised incident light and that the scattered intensity is related to the forth power of the wavelength.

Appendix 2

Mie Theory

The formal solution of the scattering properties by a homogeneous sphere of arbitrary radius and refractive index was formulated by Mie in 1908 [19]. The resulting formulae are called the Mie formulae and result from the solution of Maxwell's equations with the appropriate boundary conditions [54,55,56,57].

The Mie formulae give the scattering properties for a sphere of radius a , and refractive index m , for plane polarised incident light of wavelength, λ , from two parameters, X and m [55].

$$X = 2\pi a/\lambda, \quad (\text{A2.1})$$

$$m = n - ik. \quad (\text{A2.2})$$

Where n and k are the real and imaginary parts of the refractive index. X is called the size parameter and is the ratio of the circumference of the sphere to the wavelength of the incident light. Assuming that the spheres are non-absorbing, ie. $k=0$, and if the spheres of refractive index m_1 are in a medium of refractive index m_2 [55], then the two parameters become

$$X = 2\pi a m_2/\lambda, \quad (\text{A2.3})$$

$$m = m_1/m_2, \quad (\text{A2.4})$$

and then m is called the relative refractive index of the scatterer.

The formal solutions take the form of infinite series which have to be evaluated in order to calculate the scattering properties. The Mie formulae [56] are,

$$S_1(\theta) = \sum_{n=1}^{\infty} \frac{2n+1}{n(n+1)} (a_n \pi_n(\cos \theta) + b_n \tau_n(\cos \theta)), \quad (\text{A2.5})$$

$$S_2(\theta) = \sum_{n=1}^{\infty} \frac{2n+1}{n(n+1)} (b_n \pi_n(\cos \theta) + a_n \tau_n(\cos \theta)), \quad (\text{A2.6})$$

$$Q_{\text{sca}} = \frac{2}{x^2} \sum_{n=1}^{\infty} (2n+1) (|a_n|^2 + |b_n|^2), \quad (\text{A2.7})$$

$$Q_{\text{ext}} = \frac{2}{x^2} \sum_{n=1}^{\infty} (2n+1) \text{Re}(a_n + b_n), \quad (\text{A2.8})$$

where, $S_1(\theta)$ and $S_2(\theta)$ are the scattering matrix elements for vertically and horizontally polarised incident light, Q_{sca} is the scattering efficiency of the sphere and Q_{ext} is the extinction efficiency. The coefficients a_n and b_n are defined by

$$a_n = \frac{x \Psi'_n(y) \Psi_n(x) - y \Psi'_n(x) \Psi_n(y)}{x \Psi'_n(y) \xi_n(x) - y \xi'_n(x) \Psi_n(y)}, \quad (\text{A2.9})$$

$$b_n = \frac{y \Psi'_n(y) \Psi_n(x) - x \Psi'_n(x) \Psi_n(y)}{y \Psi'_n(y) \xi_n(x) - x \xi'_n(x) \Psi_n(y)}, \quad (\text{A2.10})$$

$$y = mx. \quad (\text{A2.11})$$

The functions Ψ_n and ξ_n are the Riccati-Bessel functions, (primes denote differentiation with respect to the argument) which are defined in terms of Bessel functions [56], J_n 's.

$$\Psi_n(z) = \left(\frac{\pi z}{2}\right)^{1/2} J_{n+1/2}(z), \quad (\text{A2.12})$$

$$\xi_n(z) = \left(\frac{\pi z}{2}\right)^{1/2} [J_{n+1/2}(z) + i(-1)^n J_{-n-1/2}(z)]. \quad (\text{A2.13})$$

$\pi_n(\cos\theta)$ and $\tau_n(\cos\theta)$ are angle dependent functions [56] and are defined by

$$\pi_n(\cos\theta) = P'_n(\cos\theta), \quad (\text{A2.14})$$

$$\tau_n(\cos\theta) = \cos\theta \cdot \pi_n(\cos\theta) - \sin^2\theta \frac{d}{d\cos\theta} \pi_n(\cos\theta). \quad (\text{A2.15})$$

Where $P_n(\cos\theta)$ are Legendre polynomials.

The scattered intensity $I_s(\theta)$, is related to $S_1(\theta)$ and $S_2(\theta)$ [55] by

$$I_s = \frac{|S_1(\theta)|^2}{k^2 r^2} I_0, \quad (\text{A2.16})$$

for perpendicular polarisation

$$I_s = \frac{|S_2(\theta)|^2}{k^2 r^2} I_0, \quad (\text{A2.17})$$

for parallel polarisation.

Where I_0 is the incident intensity and parallel and perpendicular refer to the scattering plane. For perpendicular polarisation it will only be necessary to consider $S_1(\theta)$. The Rayleigh ratio is therefore given by

$$R(\theta) = \frac{|S_1(\theta)|^2}{k^2} N. \quad (\text{A2.18})$$

The angular distribution of scattered light (the light scattering envelope) is found to differ significantly from the isotropic case of Rayleigh scatterers. For scatterers of size greater than the incident light wavelength, most of the scattered light falls into a lobe in the forward direction (low scattering angles). The angular width of this lobe decreases with increasing scatterer size.

Appendix 3

Calibration of the Light Scattering Equipment

In order to determine the concentration of scatterers from the light scattering data, it is necessary to calibrate the light scattering measurement system as described below.

Standard liquids of known Rayleigh ratio and depolarisation were used. Table A3.1 below lists the liquids used along with their Rayleigh ratio at 90°, $R(90)$, and their depolarisation, Δ_u . These values were obtained from reference [62], no indication as to their actual error.

TABLE A3.1 Rayleigh Ratios for Standard Liquids

LIQUID	$R(90)$ (cm^{-1})	Δ_u
TOLUENE	18.4×10^{-6}	0.48
BENZENE	15.8×10^{-6}	0.42
CCl_4	5.38×10^{-6}	0.042

The data in Table A3.1 was obtained using unpolarised incident light of wavelength 546nm. Hence corrections for vertically polarised incident light and a wavelength of 632.8nm will have to be made to this data.

The correction required for vertically polarised incident light is found by considering the following argument. The unpolarised scattered intensity due to unpolarised incident light, R_{uu} , can be considered to be composed of two contributions. These are the unpolarised scattered light due to horizontally polarised incident light, R_{hu} , and unpolarised scattered light due to vertically polarised incident light, R_{vu} . This may be written as

$$R_{uu} = R_{hu} + R_{vu} \quad (\text{A3.1})$$

Now, the depolarisation is defined as, $\Delta_u = R_{vu}/R_{hu}$, substituting into the equation above and rearranging gives

$$R_{vu} = R_{uu} / (1 + \Delta_u) \quad (\text{A3.2})$$

Now, R_{uu} is measured for unit incident intensity, half of which is composed of horizontally polarised light and half vertically polarised. Hence, the equation above for R_{vu} must be re-normalised for unit intensity as shown below.

$$R_{vu} = 2 \cdot R_{uu} / (1 + \Delta_u) \quad (\text{A3.3})$$

To correct for vertically polarised light, all R(90) values in table A3.1 should be multiplied by the factor $2/(1 + \Delta_u)$.

As all the liquids listed in table A3.1 are Rayleigh scatterers, a wavelength to the power 4 correction has to be made. The correction factor is given by $0.546^4/0.6328^4$, which is equal to 0.5535. Table A3.2 below gives the corrected R(90)'s for vertically polarised incident light and a wavelength of 632.8nm.

TABLE A3.2 Corrected Rayleigh Ratios for Standard Liquids

LIQUID	CORRECTED R(90) (cm ⁻¹)
TOLUENE	13.76 X 10 ⁻⁶
BENZENE	12.32 X 10 ⁻⁶
CCL ₄	5.72 X 10 ⁻⁶

Two further corrections due to the geometry of the light scattering goniometer have to be made. The first is to compensate for the variation in the scattering volume with scattering angle, θ . The correction factor required is $\sin(\theta)$. The second correction factor is due to the lens effect of the cylindrical scattering cell which has the effect of decreasing the scattering volume as seen by the detector [63]. The correction factor required is n^2 , the index matching fluid refractive index.

The calibration constant, CC, can now be determined. Light scattering measurements for a scattering angle of 90° are taken for toluene, which has been repeatedly filtered through 0.05µm filters to remove dust or dirt which may cause spurious scattering. The measured scattered intensity, $I_m(90)$, is determined from

$$I_m(\theta) = \frac{\text{scattered intensity}}{\text{incident intensity}} \cdot \sin(\theta), \quad (\text{A3.4})$$

where the incident intensity is the simultaneous measurement of the incident light from the second channel of the photon counter and compensates for any fluctuations in the laser intensity. The calibration constant, CC, can be calculated from

$$CC = R(90) / I_m(90) \cdot n_l^2. \quad (\text{A3.5})$$

Where R(90) is the corrected Rayleigh ratio for toluene. On repeated measurement of the scattered light the error in the calibration constant was found to be approximately 10%.

The other two liquids from table A3.2, benzene and CCl₄, may be used to check the calibration. Tabulated below in table A3.3, are the measured R(90)'s for these two liquids together with the corrected R(90)'s from table A3.2.

TABLE A3.3 Calibration Results

LIQUID	MEASURED R(90) (cm ⁻¹)	R(90) FROM TABLE A3.2 (cm ⁻¹)
BENZENE	(12 +/- 3) X 10 ⁻⁶	12.32 X 10 ⁻⁶
CCl ₄	(6 +/- 1) X 10 ⁻⁶	5.72 X 10 ⁻⁶

Table A3.3 shows good agreement between the measured and corrected Rayleigh ratios. The large measurement errors of around 20% are due to measurement of the low intensity scattered light. As stated above, the calibration constant is determined to an accuracy of 10%. Also measurement of the scattered light for either Benzene or CCl₄, gives an additional error of 10%, consequently yielding a combined error of 20% in the measured Rayleigh ratio. The intensity of scattered light from resin samples will be much higher than from these liquids, with a corresponding reduction in the measurement error. Hence, the accuracy in determining scatterer concentrations from resin samples will depend mainly by the error in the calibration constant, i.e. around 10%.

Appendix 4

Laser Speckle Reduction

The HeNe laser used as the light source emits highly coherent light. The coherence length of this laser is approximately 30cm and high spatial coherence exists across the width of the laser beam (TEM₀₀ single transverse mode). Scatterers in the scattering volume of size 0.2mm X 0.2mm X the path length through the laser beam (see section 3.3.), will therefore act as coherent sources of scattered light. In solids, where the scatterers remain in fixed position relative to each other, speckle will be observed in the scattered light. This has the effect of reducing the quality of the measured data by superimposing noise on the data. In liquids however, the scatterers move relative to each other causing speckle in the scattered light to move relative to the detection system. Time averaging of the detected light can be used to reduce the speckle noise to arbitrary low levels.

Formation of the speckle can be explained by examining the first order statistics of speckle patterns [64], assuming that we can approximate the 3 dimensional scattering volume by a 2 dimensional diffuser of size 0.2mm X 0.2mm, which is illuminated by a coherent source of laser light. The complex amplitude at any point in the far field of the diffuser is the sum of the complex amplitudes of the scattered light from each of the n individual scatterers in the object. The complex amplitude in the far field of the diffuser is given by

$$a \exp(-i\phi) = \sum_{n=1}^n a_n \exp(-i\phi_n). \quad (A4.1)$$

Assuming that all the moduli, a_n , of the individual complex amplitudes are equal, while the phase shifts, ϕ_n , after subtracting integral multiples of 2π , are randomly distributed over the interval 0 to 2π , the statistics reduce to the well known random-walk problem. Providing n is large, the joint probability density function of the real, A_r , and imaginary, a_i , parts of the complex amplitude, is given by

$$P_{r,i}(a_{r,i}) = (1/2\pi\sigma^2) \exp[-(a_r^2 + a_i^2)/2\sigma^2], \quad (A4.2)$$

where σ^2 is a constant. The probability function of the intensity is then,

$$P(I) = (1/2\sigma^2) \exp(-I/2\sigma^2). \quad (A4.3)$$

The mean value of the intensity is

$$\langle I \rangle = 2\sigma^2, \quad (A4.4)$$

While its second moment is

$$\langle I^2 \rangle = 2\langle I \rangle^2. \quad (A4.5)$$

The variance of the intensity is

$$\sigma^2 = \langle I^2 \rangle - \langle I \rangle^2 = \langle I \rangle^2. \quad (A4.6)$$

The signal to noise ratio can be defined as

$$S/N = \langle I \rangle / \sigma = 1. \quad (A4.7)$$

If the detector aperture is larger than the speckle size, then spatial averaging of the speckle noise will result. The speckle size at the detector depends on the light collection optics and can be calculated using the second order statistics of speckle patterns [64]. The autocorrelation function, $R(\Delta x, \Delta y)$, of the intensity in the speckle pattern is determined by the complex amplitude of the scattered waves at the observation plane, $a(x, y)$, which are related to the complex amplitude $A(x_1, y_1)$, at the scattering surface by the Fresnel-Kirchhoff integral. The result is,

$$R(\Delta x, \Delta y) = \langle I \rangle^2 \frac{\left| \iint_{-\infty}^{\infty} |A(x_1, y_1)|^2 \exp\{i(2\pi/\lambda z)(x_1 \Delta x + y_1 \Delta y)\} dx_1 dy_1 \right|^2}{\left(\iint_{-\infty}^{\infty} |A(x_1, y_1)|^2 dx_1 dy_1 \right)^2}. \quad (A4.8)$$

For a square scattering surface, of edge length L , the average dimensions of the speckle calculated from the equation above, are,

$$\delta x = \delta y = \lambda z / L. \quad (A4.9)$$

For, $\lambda = 0.6328 \mu\text{m}$, $z = 500 \text{mm}$ and $L = 0.2 \text{mm}$, the speckle size observed at the detector surface of the light scattering goniometer is 1.6mm, defined by the two pin

holes (see section 3.3.). The detector aperture is less than 1mm and so no spatial averaging of the speckle noise occurs.

Hence, with no speckle reduction techniques employed, the signal to noise ratio of the measured data will be around 1:1 and a method of speckle reduction will be necessary. Reduction of the speckle noise in the scattered light from solid samples can be achieved by reducing the spatial coherence of the incident laser light. The phase of the light across the laser beam can be scrambled by a moving diffuser using techniques described in references [65,66], to reduce speckle noise in holographic images. In these particular cases, expanded laser beams were used and the technique will be much more difficult in the light scattering case due to the small width of the laser beam, approximately 1mm diameter. The effect of phase scrambling will be to move the speckle across the detector aperture and speckle noise reduction achieved by time averaging.

The method of speckle noise reduction employed is as follows. The phase scrambling material, vibrated vertically in the incident laser beam is shown in figure A4.1. A moving coil transducer and function generator were used to provide the vibration. Careful selection of the phase scrambling material is required. The material is required to have a random phase shift profile with a phase autocorrelation length less than the width of the laser beam. However if the autocorrelation length is too small, substantial scattering of the laser light will result, leading to a broadening of the laser beam. Two suitable materials have been identified. 1) sellotape, where its optical axis is aligned vertically to prevent depolarisation of the laser beam, and 2) perspex, where one side was roughened using course emery paper and re-polished. Best results were obtained using the perspex phase scrambler with a 50Hz triangular vibration waveform and a linear displacement of 3mm. A signal to noise ratio of 10:1 in the measured scattered light is obtained using this technique.

The accuracy with which the scattered intensity can be measured is limited by speckle noise, which is around 10% of the measured intensity if this speckle reduction technique is used.

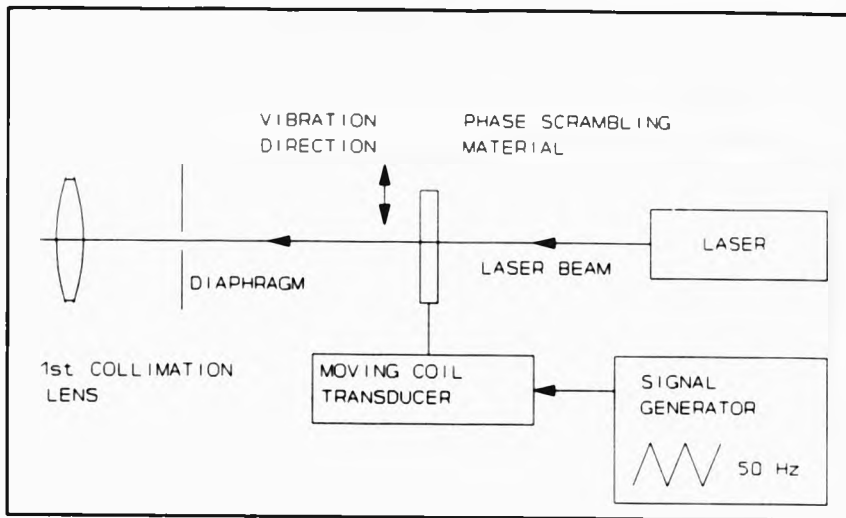


Figure A4.1. Laser Speckle Reduction Technique.

Appendix 5

Computation of Mie Formulae

The computational procedure for calculating the Mie formulae involves extensive use of recurrence relations. Care must be taken to prevent round off errors associated with the storage of numbers with a finite number of digits, from accumulating and yielding incorrect results. The computer program was written in VAX Fortran and double precision variables were employed throughout to minimise the risk of round off error.

The series for $S_1(\theta)$, $S_2(\theta)$, Q_{ms} and Q_{em} , see appendix 2, converge, the number of terms for convergence will depend on the value of the size parameter, x . Bohren and Huffman [56] give the number of terms for convergence as the nearest integer to

$$x + 4x^{1/3} + 2. \quad (\text{A5.1})$$

Calculation of the coefficients a_n and b_n , may be simplified [75] by use of the logarithmic derivative $A_n(y)$, defined as,

$$A_n(y) = \psi'_n(y) / \psi_n(y). \quad (\text{A5.2})$$

and using the recurrence relations for Bessel functions gives

$$a_n = \frac{\left(\frac{A_n(y)}{m} + \frac{n}{x}\right) \text{Re}\{\xi_n(x)\} - \text{Re}\{\xi_{n-1}(x)\}}{\left(\frac{A_n(y)}{m} + \frac{n}{x}\right) \xi_n(x) - \xi_{n-1}(x)}, \quad (\text{A5.3})$$

$$b_n = \frac{\left(mA_n(y) + \frac{n}{x}\right) \text{Re}\{\xi_n(x)\} - \text{Re}\{\xi_{n-1}(x)\}}{\left(mA_n(y) + \frac{n}{x}\right) \xi_n(x) - \xi_{n-1}(x)}. \quad (\text{A5.4})$$

To generate $A_n(y)$, Wickramasinghe [75] gives

$$A_n(y) = -\frac{n}{y} + \left(\frac{n}{y} - A_{n-1}(y)\right)^{-1}, \quad (\text{A5.5})$$

with

$$A_0(y) = \cos y / \sin y. \quad (A5.6)$$

This upwards recurrence relation is unstable. A better method is to calculate the $A_n(y)$'s by downwards recurrence. Bohren and Huffman [56], give the recurrence relation

$$A_{n-1}(y) = \frac{n}{y} - \frac{1}{A_n(y) + n/y}, \quad (A5.7)$$

with a starting term of $0+i0$, and starting fifteen terms higher than required for convergence of Mie formulae. Successive more accurate lower terms are generated.

To generate ξ_n , the recurrence relation

$$\xi_n(x) = \frac{2n-1}{x} \xi_{n-1}(x) - \xi_{n-2}(x) \quad (A5.8)$$

is used together with

$$\xi_0(x) = \sin x + i \cos x, \quad \xi_{-1}(x) = \cos x - i \sin x, \quad (A5.9)$$

and can be computed by upwards recurrence.

The angle dependent functions, π_n , and τ_n , are determined from the following recurrence relations [75],

$$\pi_n(\cos \theta) = \cos \theta \cdot \frac{2n-1}{n-1} \pi_{n-1}(\cos \theta) - \frac{n}{n-1} \pi_{n-2}(\cos \theta), \quad (A5.10)$$

$$\tau_n(\cos \theta) = \cos \theta \cdot [\pi_n(\cos \theta) - \pi_{n-2}(\cos \theta)] - (2n-1) \sin^2(\theta) \cdot \pi_{n-1}(\cos \theta) + \tau_{n-2}(\cos \theta). \quad (A5.11)$$

The angle dependent functions can now be computed by upwards recurrence with,

$$\pi_0(\cos \theta) = 0, \quad \pi_1(\cos \theta) = 1, \quad \pi_2(\cos \theta) = 3 \cos \theta, \quad (A5.12)$$

$$\tau_0(\cos \theta) = 0, \quad \tau_1(\cos \theta) = \cos \theta, \quad \tau_2(\cos \theta) = 3 \cos 2\theta. \quad (A5.13)$$

The Mie formulae may now be calculated.

Appendix 6

Least Squares Fitting

The method of least squares compares the measured data with a theoretical model in which one or more parameters are allowed to vary [67]. The technique is to determine optimum values of the parameters by minimising χ^2 , where,

$$\chi^2 = \sum_{n=1}^N \frac{(f_n - y_n)^2}{\sigma_n^2} \quad (A6.1)$$

N is the number of data points in the data set, f_n is the theoretical value obtained from the parameters, y_n is the measured data value and σ_n is the standard deviation or error in the n^{th} measured data value. For a best fit then, the difference between each measured value and theoretical value called the residual, should be on average equal to the standard deviation associated with the measured data point. χ^2 should therefore give a value equal to the number of data points. This will of course only be true provided that the error estimates, σ_n , for the data values are reasonable and that the theory used can adequately explain the measured data. For scattered light data of resin samples, the error in the measured data is due to the speckle noise, see appendix 4, which was found to be 10% of the measured value. The minimum value of χ^2 can therefore be used as a measure of how good the data fits the theory.

Errors in the parameters may be estimated from the curvature of the χ^2 values around the minimum value [67]. The standard deviation in parameter P is given by

$$\sigma_P^2 = \frac{2}{\partial^2 \chi^2 / \partial P^2} \quad (A6.2)$$

where,

$$\frac{\partial^2 \chi^2}{\partial P^2} = \frac{\chi^2(P + \Delta P) - 2\chi^2(P) + \chi^2(P - \Delta P)}{\Delta P^2} \quad (A6.3)$$

and P is the optimised value of the parameter and ΔP is a small increment in the parameter. All other parameters remain fixed at their optimum values. Errors in the other parameters can be found in a similar way. The errors calculated therefore represent 65% confidence limits.

For the least squares fitting analysis, a VAX computer and NAG library subroutine E04FDF was used. This subroutine requires a user defined subroutine incorporating the theory to be fitted, to calculate the residuals for each of the measured data elements in the data set, for given values of the parameters. The NAG subroutine repeatedly calls this user defined subroutine, making adjustments to the parameters until a minima in χ^2 is found.

Appendix 7

Charge Carrier Injection Mechanisms and the Field Limiting Space Charge Model

Schottky Charge Injection

Schottky (thermionic) charge injection is well documented (see references [9,97]). For a charge carrier, i.e. an electron, to escape from the surface of a metal, it must have sufficient energy to overcome a potential barrier which is defined by the work function of the metal, an image force which attracts the electron back to the metal and the applied electric field. This situation is illustrated in figure A7.1. With no field applied, the energy required by the electron to escape from the metal is equal to the work function, ϕ . These electrons must have an energy greater than $E_F + \phi$ and therefore be in the high energy tail of the electron distribution. Electron emission will therefore be dependent on the temperature of the metal. When an electric field is applied, the image potential is modified by the addition of a further potential due to the applied electric field and the barrier height is therefore reduced by $\Delta\phi$. Barrier height reduction therefore depends on the applied field. The emission current density j , has been calculated and is given below, from reference [97].

$$j = AT^2 \exp\left\{ \frac{-(\phi - e^{3/2} E^{1/2} / \epsilon^{1/2})}{k_0 T} \right\}. \quad (\text{A7.1})$$

Where A is the Richardson-Dushman constant, T is the temperature, ϕ is the work function, e is the charge on an electron, E is the electric field, ϵ is the permittivity of the dielectric and k_0 is the Boltzmann constant.

Fowler-Nordheim Charge Injection

Fowler-Nordheim (tunnelling) injection is well described (see references [9,97]). If the applied electric field is increased, the width of the potential barrier width, Δx , will decrease. With a sufficiently high electric field, the barrier width becomes small enough for electron tunnelling to occur through the barrier. The situation is shown graphically in figure A7.2. Here electrons of energy E_F can pass (tunnel) through the

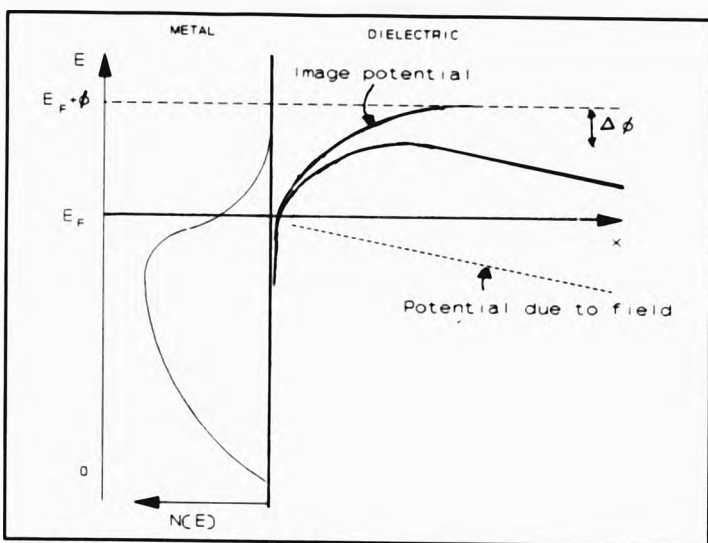


Figure A7.1. Schottky potential barrier.

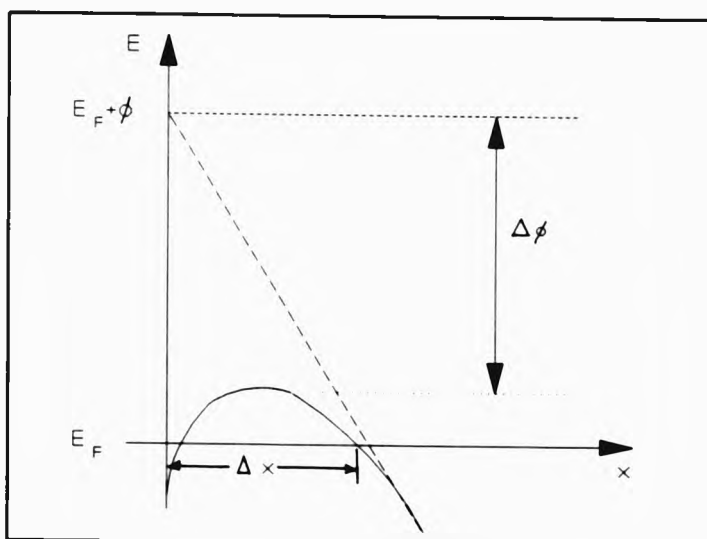


Figure A7.2. Fowler-Nordheim potential barrier.

barrier without requiring the additional energy ϕ . The emission current density, j , is given below, (from reference [97]).

$$j = (e^3 E^2 / 8\pi h \phi) \exp(-8\pi (2m^*)^{1/2} \phi^{3/2} / 3 h e E). \quad (A7.2)$$

Where, m^* is the effective mass of the charge carrier and h is the Planck constant.

Field Limiting Space Charge Model

The field limiting space charge (FLSC) model of Hibma and Zeller [1], is based on the assumption that the mobility of the charge carriers in the dielectric increases by orders of magnitude once a critical field E_{crit} is exceeded, where E_{crit} is a material parameter. Irrespective of the mechanism of charge injection across the metal-dielectric interface, no significant charge injection occurs when the field is less than E_{crit} due to the immobility of the localised charge at the interface. However, for fields greater than E_{crit} , the much increased mobility allows the injected charge to move away from the electrode and distribute itself in the space charge region near the electrode. A constant field E_{crit} is required at the electrode and throughout the space charge region. For this model then, a material dependent threshold field for charge injection is predicted.



THE BRITISH LIBRARY
BRITISH THESIS SERVICE

**ELECTRICAL BREAKDOWN AND STRUCTURAL
CHARACTERIZATION IN SYNTHETIC RESINS
USING OPTICAL TECHNIQUES**

TITLE ..

STEPHEN JOHN DODD

AUTHOR

DEGREE

AWARDING BODY **City of London Polytechnic (CNAM)**

DATE **(1992)**

THESIS
NUMBER

THIS THESIS HAS BEEN MICROFILMED EXACTLY AS RECEIVED

The quality of this reproduction is dependent upon the quality of the original thesis submitted for microfilming. Every effort has been made to ensure the highest quality of reproduction.

Some pages may have indistinct print, especially if the original papers were poorly produced or if the awarding body sent an inferior copy.

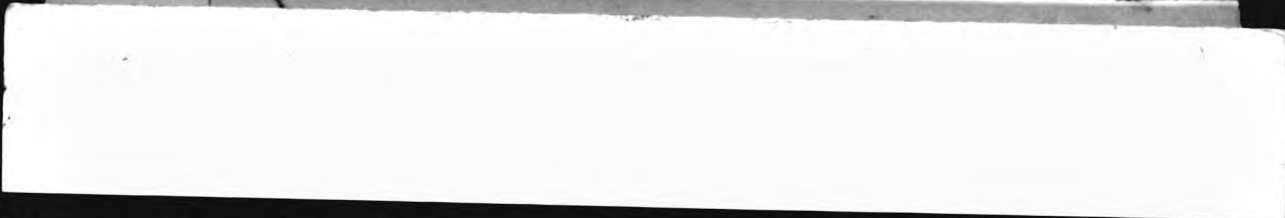
If pages are missing, please contact the awarding body which granted the degree.

Previously copyrighted materials (journal articles, published texts, etc.) are not filmed.

This copy of the thesis has been supplied on condition that anyone who consults it is understood to recognise that its copyright rests with its author and that no information derived from it may be published without the author's prior written consent.

Reproduction of this thesis, other than as permitted under the United Kingdom Copyright Designs and Patents Act 1988, or under specific agreement with the copyright holder, is prohibited.

1	2	3	4	5	6	REDUCTION X	20
cms						CAMERA	5
						No. of pages	



DX



172356

